SEMIANNUAL STATUS REPORT

TO THE NATIONAL AERONAUTICS AND SPACE ADMINISTRATION

DYNAMICS OF THE SOLID EARTH PROGRAM

NASA GRANT NAG 5-1921

"Lithospheric Dynamics Near Plate Boundaries"

for the period
15 March - 14 September 1992

Principal Investigator: Sean C. Solomon
Department of Earth, Atmospheric, and Planetary Sciences
Massachusetts Institute of Technology
Cambridge, MA 02139

TABLE OF CONTENTS

SUMMARY

This is a Progress Report on research conducted between 15 March 1992 and the present under NASA Grant NAG 5-1921, entitled "Lithospheric Dynamics near Plate Boundaries." This grant has supported the research of one Investigator (S. C. Solomon), one Research Staff (R. E. Reilinger), and two Ph. D. students (M. Simons, C. J. Wolfe) on behalf of the NASA DOSE (Dynamics of the Solid Earth) Program.

The focus of the research during the first grant year has been on several problems broadly related to the nature and dynamics of time-dependent deformation and stress along major seismic zones, with an emphasis on western North America but with additional work on seismic zones in oceanic lithosphere as well. The principal findings of our research to date are described in the accompanying papers and abstract. The first three are reprints of recently published papers supported by this project. The next two are preprints of two papers submitted for publication. The last is an abstract of a paper presented at the 1992 Fall AGU Meeting in San Francisco.

APPENDIX 1

Global Positioning System measurements of deformations associated with the 1987 Superstition Hills earthquake: Evidence for conjugate faulting

by S. Larsen, R. Reilinger, H. Neugebauer, and W. Strange

Published in *J. Geophys. Res., 97,* 4885-4902, 1992.

JOURNAL OF GEOPHYSICAL RESEARCH, VOL. 97, NO. B4, PAGES 4885–4902, APRIL 10, 1992

Global Positioning System Measurements of Deformations Associated With the 1987 Superstition Hills Earthquake: Evidence for Conjugate Faulting

SHAWN LARSEN[1]

Seismology Laboratory, California Institute of Technology, Pasadena

ROBERT REILINGER

Earth Resources Laboratory, Massachusetts Institute of Technology, Cambridge

HELEN NEUGEBAUER AND WILLIAM STRANGE

National Geodetic Survey, NOAA, Rockville, Maryland

Large station displacements observed from Imperial Valley global positioning system (GPS) campaigns are attributed to the November 24, 1987, Superstition Hills earthquake sequence. Thirty sites from a 42-station GPS network established in 1986 have been reoccupied during 1988 and/or 1990. Displacements at three sites within 3 km of the surface rupture approach 0.5 m. Eight additional stations within 20 km of the seismic zone are displaced at least 10 cm. This is the first occurrence of a large earthquake (M_S 6.6) within a preexisting GPS network. Best-fitting uniform slip models of rectangular dislocations in an elastic half-space indicate 130 ± 8 cm right-lateral displacement along the northwest-trending Superstition Hills fault and 30 ± 10 cm left-lateral displacement along the conjugate northeast-trending Elmore Ranch fault. The geodetic moments are 9.4×10^{25} dyn cm and 2.3×10^{25} dyn cm for the Superstition Hills and Elmore Ranch faults, respectively, consistent with teleseismic source parameters. The data also suggest that postseismic slip along the Superstition Hills fault is concentrated at shallow depths. Distributed slip solutions using singular value decomposition indicate near uniform displacement along the Elmore Ranch fault and concentrated slip to the northwest and southeast along the Superstition Hills fault. A significant component of nonseismic secular displacement is observed across the Imperial Valley, which is attributed to interseismic plate-boundary deformation.

1. INTRODUCTION

The global positioning system (GPS) is rapidly becoming one of the most important geodetic tools for studying tectonic deformation [e.g., *Larsen*, 1991]. By recording signals from Earth orbiting satellites it is possible to determine three-dimensional coordinates of geodetic monuments with high accuracy [e.g., *King et al.*, 1985; *Wells et al.*, 1987]. The station displacement or deformation between surveys is measured when observations are repeated. GPS can be used to monitor secular deformation such as that associated with plate motion or to record strain fluctuations from seismic and volcanic activity. In its final configuration scheduled for the mid 1990s, 21 satellites will be deployed in six orbital planes (with three additional satellites used as active spares). When GPS becomes fully operational, it will be possible to continuously determine three-dimensional positions anywhere on or near the Earth. The available satellite constellation during the period of this study was optimized for North America, making GPS-based geodetic research in California practical.

On November 24, 1987, two moderate earthquakes separated by 12 hours occurred in the northwest section of the Imperial Valley region of southern California. The first event was located on a northeast-trending seismic lineament and was followed 12 hours by rupture along the northwest-trending Superstition Hills fault. What makes this earthquake sequence significant from a GPS standpoint is that it occurred spatially and temporally within a preexisting GPS network. This network was established in the Imperial Valley in 1986, with partial resurveys in 1988 and 1990. Fifteen stations are located within 20 km of the rupture zone; three stations are within 3 km.

We compute GPS determined displacements in the Imperial Valley between 1986 and 1990. Observed station movements of up to 0.5 m are attributed to the Superstition Hills earthquake sequence. The earthquake-induced displacements are inverted to estimate seismic slip and the geodetic moment along the rupture planes. In addition, there is a large component of deformation which cannot be explained by the seismic disturbance. We assume this to be, in part, a manifestation of ongoing relative motion between the Pacific and North American plates.

2. IMPERIAL VALLEY SEISMICITY AND TECTONICS

The Imperial Valley region of southern California is a complex transition zone between crustal spreading in the Gulf of California and right-lateral transform motion along the San Andreas fault (Figure 1) [*Lomnitz et al.*, 1970; *Elders et al.*, 1972]. The valley is 4–12 million years old and has been filled by up to 15 km of late Cenozoic sediments

[1]Now at Scientific Software Division, Lawrence Livermore National Laboratory, Livermore, California.

Paper number 92JB00128.
0148-0227/92/92JB-00128$05.00

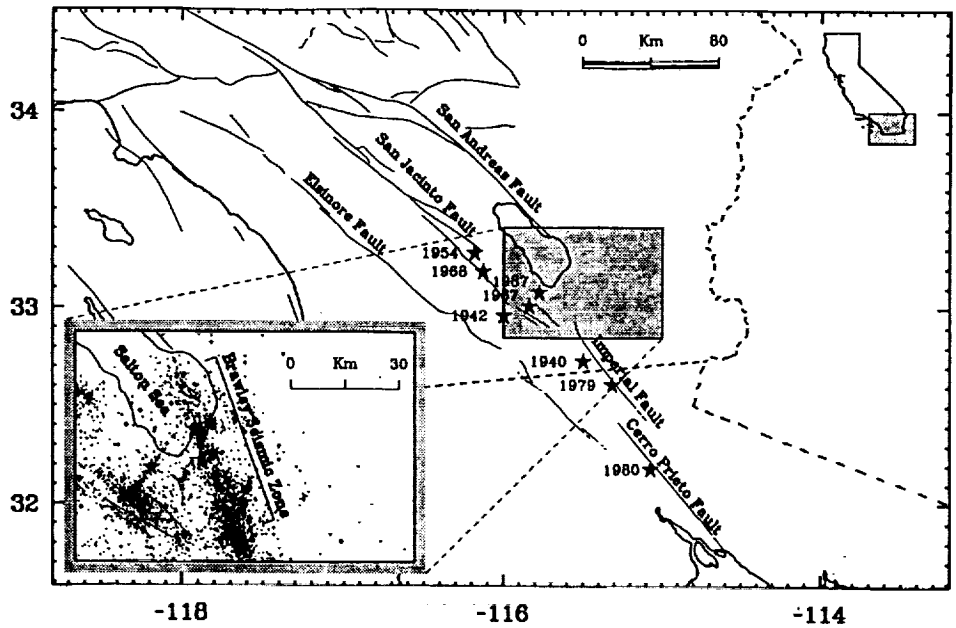

Fig. 1. Seismicity and major fault systems of the Imperial Valley. The Brawley Seismic Zone is the region of anomalously high activity between the northern Imperial and southern San Andreas faults. The valley represents a transition zone between crustal spreading in the Gulf of California to the south and right-lateral transform motion along the San Andreas system.

[*Larson et al.*, 1968; *Moore and Buffington*, 1968; *Ingle*, 1974; *Fuis et al.*, 1982]. The major fault systems and structural grain of the valley trend to the northwest, roughly parallel to the direction of plate motion.

The Imperial Valley is one of the most seismically active regions of California (Figure 1). Much of this activity occurs along the Imperial fault and within the Brawley Seismic Zone [*Johnson and Hill*, 1982]. Several large earthquakes have occurred in and near the Imperial Valley since 1940 (Figure 1). The Imperial fault ruptured with a M_S 7.1 event in 1940 and a M_L 6.6 event in 1979 [*U.S. Geological Survey*, 1982]. Segments of the San Jacinto fault system broke with a M_L 6.2 earthquake in 1954 and a M_L 6.5 event in 1968 (Borrego Mountain). The most GPS relevant episode of seismic activity occurred in 1987 along the Superstition Hills segment of the San Jacinto fault system, with a M_S 6.2 earthquake on a northeast-trending seismic lineament followed 12 hours by a M_S 6.6 event on the Superstition Hills fault.

Terrestrial geodetic measurements show that a significant fraction of the Pacific-North American relative plate motion is accommodated across the Imperial Valley. New global plate model estimates (NUVEL-1) [*DeMets et al.*, 1987; *DeMets et al.*, 1990] predict the rate of motion between the North American and Pacific plates averaged over the last 3 million years is 4.7 cm/yr oriented N39.6° W (at Imperial Valley coordinates: 33.0° N, 115.5° W). Dislocation models of triangulation measurements spanning this region suggest 4.3 cm/yr of plate-boundary deformation between 1941 and 1986 [*Snay and Drew*, 1988]. Trilateration measurements made by the U.S. Geological Survey (USGS) between 1973 and 1989 show 3.69 ± 0.11 cm/yr relative movement between stations on opposite sides of the valley [*Lisowski et al.*, 1991]. The orientations of the displacements are approximately N40° W, although this direction depends upon a priori assumptions [e.g., *Prescott*, 1981]. Very long baseline interferometry (VLBI) measurements indicate 3.33 ± 0.12 cm/yr movement between stations on opposite sides of the Salton Trough [*Ward*, 1990]. In addition, the terrestrial measurements suggest that deformation is concentrated in a narrow 20-km-wide zone along the Imperial fault [*Snay and Drew*, 1988], while it is distributed over a region at least 50 km wide to the north [*Prescott et al.*, 1987*b*; *Lisowski et al.*, 1991]. Presumably, deformation is transferred from the Imperial fault, which acts as the primary strain release mechanism near the U.S.-Mexico border, to distributed shear along the San Andreas, San Jacinto, and Elsinore faults.

3. Superstition Hills Earthquake Sequence

On November 24, 1987 (0154 UT), a M_S 6.2 earthquake occurred along a northeast-trending seismic lineament northeast of the Superstition Hills fault (Figure 2) [*Magistrale et al.*, 1989]. The focal mechanism and aftershock sequence, which extended for 26 km into the Brawley Seismic Zone, are consistent with left-lateral strike slip motion on a vertical fault. Seven foreshocks were recorded in the 22 min prior to the main event, including two with $M_L > 4.0$. Surface rupture consisted of a complex pattern of northeast-trending left-lateral offsets ranging in length from 1.5 to 10 km, and with maximum displacements between 3 and 13 cm [*Budding and Sharp*, 1988; *Hudnut et al.*, 1989*a*]. The maximum cumulative displacement across all surface breaks was about 20 cm. We refer to this northeast-trending lineament as the Elmore Ranch fault, although more precisely this name refers only to the longest of the surface fractures.

Twelve hours after the Elmore Ranch event (1315 UT), a M_S 6.6 earthquake occurred along the northwest-trending Superstition Hills fault. The epicenter was near the intersection of the Elmore Ranch and Superstition Hills faults.

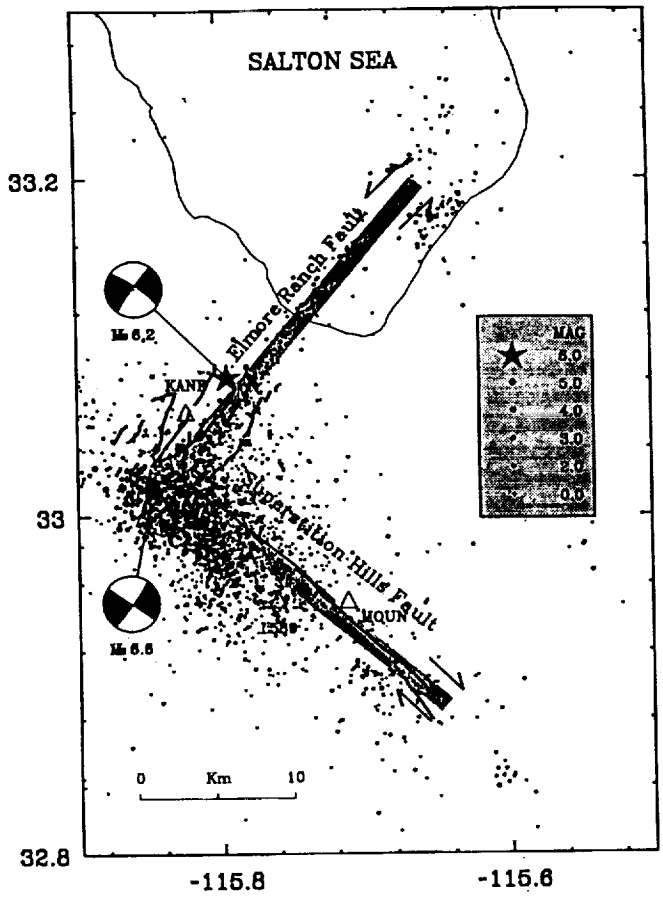

Fig. 2. Seismicity and surface faulting associated with the November 24, 1987, Superstition Hills earthquake sequence. A M_S 6.2 event occurred along a northeast-trending structure (referred to here as the Elmore Ranch fault) and was followed by 12 hours with a M_S 6.6 event along the northwest-trending Superstition Hills fault. The focal mechanisms, aftershock distribution, and surface offset measurements are consistent with left-lateral strike-slip motion along the Elmore Ranch fault and right-lateral strike-slip motion along the Superstition Hills fault. A significant amount of postseismic slip was observed along the surface trace of the Superstition Hills fault, while activity essentially ceased on the Elmore Ranch fault after the M_S 6.6 event. The shaded strips along each fault indicate the geometrical extent of the dislocations used to model the geodetic displacements. GPS stations L589, KANE, and MOUN are shown by triangles.

Strong ground motion and teleseismic data suggest the rupture process for this second event consisted of multiple subevents [*Bent et al.*, 1989; *Frankel and Wennerberg*, 1989; *Hwang et al.*, 1990; *Wald et al.*, 1990]. Surface rupture extended 24 km along the previously mapped trace of the fault [*Williams and Magistrale*, 1989]; up to 50 cm right-lateral displacement was measured. The aftershock pattern was concentrated slightly to the west of the fault and did not extend the length of the surface rupture. *Magistrale et al.* [1989] suggested the aftershock sequence was highly correlated with basement structure. Both the Superstition Hills and Elmore Ranch events triggered sympathetic surface offsets along the Imperial, San Andreas, and Coyote Creek faults [*McGill et al.*, 1989; *Hudnut and Clark*, 1989].

Significant afterslip was recorded along the surface rupture of the Superstition Hills fault [*Williams and Magistrale*, 1989]. No afterslip was measured along any of the surface ruptures associated with the Elmore Ranch event. In fact, seismic activity essentially stopped along this segment after the initiation of the second mainshock.

One of the most interesting aspects of this earthquake sequence is the conjugate geometry of faulting [*Johnson and Hutton*, 1988]. That is, two surface ruptures oriented nearly perpendicular to each other. As discussed below, this type of fault interaction may be typical of Imperial Valley tectonics and may dictate the mode of stress/strain transfer from one fault system to another.

4. GPS Observations

The signal structure broadcast from each GPS satellite consists of two carrier phase signals modulated by a navigational message and pseudorandom codes. The two carrier frequencies, known as the L1 and L2 phases, are broadcast at 1575.42 MHz (L1) and 1227.60 MHz (L2). This is equivalent to wavelengths of about 19 cm for the L1 and 24 cm for the L2. The navigational message contains the satellite coordinates (broadcast ephemeris), clock parameters, satellite health, and general system status. The pseudorandom codes are accurate time marks which allow GPS receivers to determine the transmission time of the signal. When scaled by the speed of light, the pseudorange, or the time-biased satellite-receiver distance is computed. If measurements from at least 4 GPS satellites are available, and if the satellite coordinates are known (usually with the broadcast ephemeris), the three-dimensional receiver position and the satellite-receiver time offset can be determined. The positioning accuracy with the pseudorange is $\sim$ 1–100 m, depending on whether the P or C/A code is used, the receiver type, length of observation, and the static or kinematic behavior of the instrument. The pseudorange is used for civilian and military navigation. For highly accurate geodetic positioning, however, the carrier phase measurements are used in a postprocessing mode. That is, the data collected in the field are brought back to the office or laboratory for analysis, usually with a robust computer software system. More complete details about the global positioning system, including theoretical aspects and processing methods, are found in the works by *King et al.* [1985], *Wells et al.* [1987], *Rocken* [1988], and *Dixon* [1991].

GPS Surveys: Data Collection and Processing

The GPS data for this study were collected during four Imperial Valley field campaigns from 1986 to 1990 (Table 1). A total of 46 stations in or near the valley have been occupied at least once during this interval; 30 sites have been reoccupied since 1986 (Figure 3). TI-4100 GPS receivers supporting GESAR software were used during 1986 and 1988, while Trimble 4000SST instruments were used during the 1990 survey. A comprehensive discussion regarding the data collection and processing methods is given by *Larsen* [1991].

TABLE 1. Imperial Valley GPS Campaign Summary

Year	Month	Days	Stations	Organization
1986	May/June	20	42	NGS
1988	February/March	9	19	UNAVCO
1988	March/April	6	21	NGS
1990	April	1	3	UNAVCO/RCFC

Abbreviations are NGS, National Geodetic Survey; UNAVCO, University Navstar Consortium; and RCFC, Riverside County Flood Control.

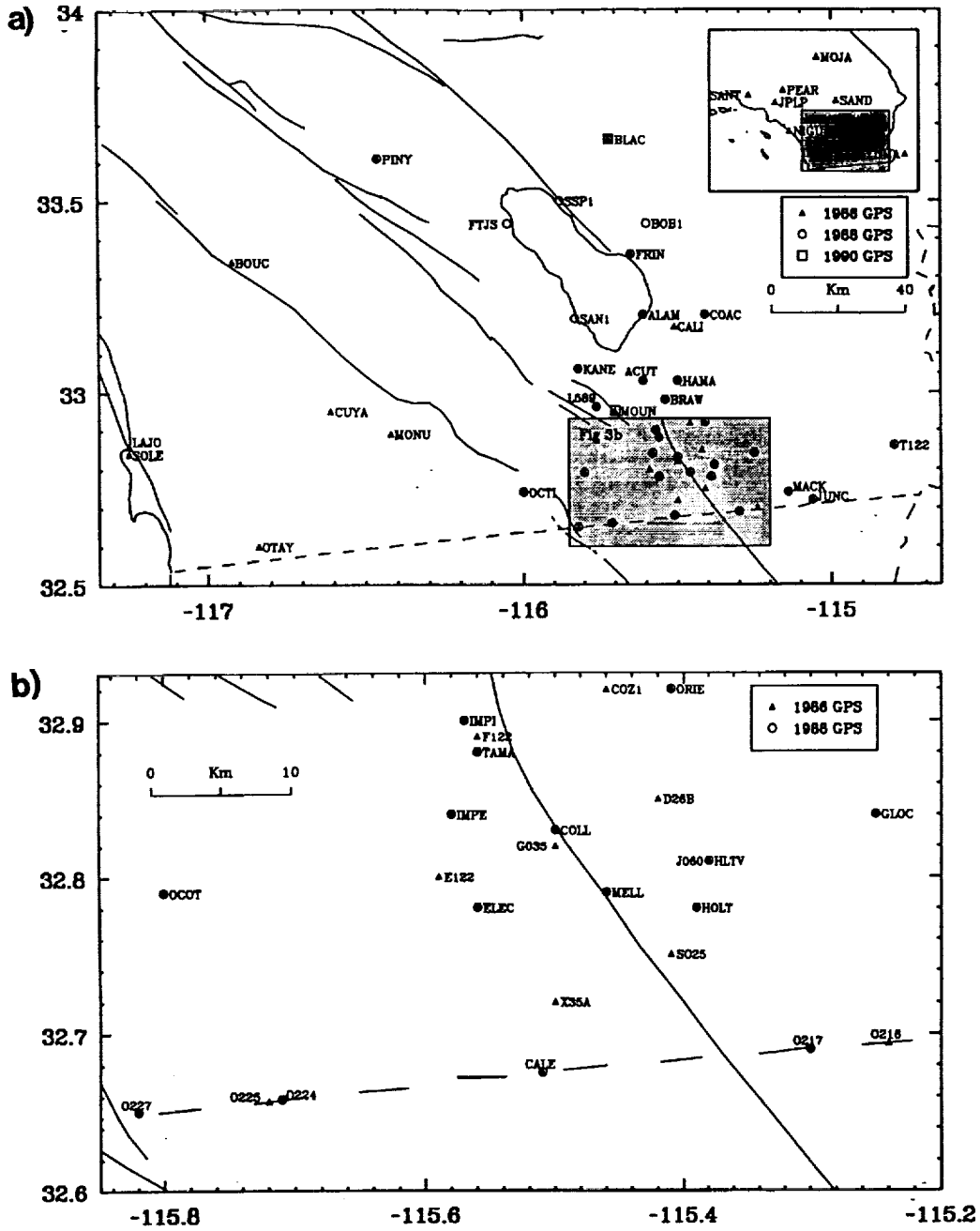

Fig. 3. (*a*) Imperial Valley and other GPS stations surveyed in 1986, 1988, and/or 1990. (*b*) Central-southern Imperial Valley GPS stations surveyed in 1986, 1988, and/or 1990.

The National Geodetic Survey (NGS) occupied 54 sites in southern California in May/June 1986; 42 stations were located in or near the Imperial Valley. Most marks were observed at least 2 days, although redundant baselines were relatively uncommon (i.e., simultaneous occupation of the same station-station pair for 2 or more days). GPS surveying at this time was still at an "experimental stage" (this was one of the first GPS networks established to investigate crustal motions). The scheduled 4.5 hour daily occupations were somewhat less than the 6–8 hour sessions typical of more recent southern California campaigns. There was less than 2 hours each day when more than three satellites were simultaneously tracked, and there was a scheduled 1 hour gap for one satellite during the middle of the measurement session (PRN 6). Less than 2 hours of data were collected at several sites. The GPS observations were processed with the GPS22 software at the National Geodetic Survey. Satellite orbital information was provided by the NSWC (Naval Surface Weapons Center). A tropospheric delay parameter was solved at each station, constrained by surface meteorological measurements. Ambiguities were fixed to the nearest integer. The data were generally noisy and reduction was unusually tedious. Each of the 20 days of observation was processed separately, and the daily solutions were combined into a single set of station coordinates using DYNAP (DYNamic Adjustment Program) [*Drew and Snay*, 1989]. All co-

ordinates were computed in the WGS-72 reference frame and transformed to WGS-84 [*Defense Mapping Agency*, 1987]. Due to relatively poor data quality and limited observations, the 1986 campaign is about an order of magnitude less precise than the more recent surveys. The accuracy of these measurements is believed to be of the order of 1 ppm (parts per million).

In February/March 1988, university field crews (M.I.T., Caltech, Lamont) with assistance from the University Navstar Consortium (UNAVCO), observed for 9 days reoccupying 15 of the Imperial Valley marks, and establishing four new stations along the Salton Sea. Most monuments were occupied for 2 days (one was observed 3 days, one for 4 days, and two for 1 day). The scheduled nightly observation scenario lasted 7.5 hours, with a total of seven satellites tracked. In March/April 1988 the NGS reoccupied 21 of the 1986 stations (seven of these were observed by the university crews a month earlier). Most sites were occupied only 1 day. The daily observation period was 6.0 hours, and seven satellites were tracked each day.

Data from both 1988 campaigns were processed with the Bernese GPS analysis software (version 3.0), from the University of Bern in Switzerland. For each survey, all data were combined into a simultaneous multiday solution. Orbital parameters were estimated using CIGNET observations (Cooperative International GPS Network) from Mojave (California), Westford (Massachusetts), and Richmond (Florida) [e.g., *Chin*, 1988]. The coordinates of these fiducial sites were held fixed to values well determined from VLBI and satellite laser ranging (M. Murray and R. King, Massachusetts Institute of Technology interoffice memorandum, 1988). Multiple 3-day satellite arcs were used [e.g., *Lichten and Border*, 1987; *Davis et al.*, 1989; S. C. Larsen et al., Strain accumulation in the Santa Barbara channel: 1971–1987, submitted to *Journal of Geophysical Research*, 1992]. Surface meteorologic data (temperature, pressure, relative humidity) were used to constrain a Saastamoinen atmospheric model [*Saastamoinen*, 1973]; independent tropospheric zenith delay parameters were estimated at each station. We experimented with fixing ambiguities but found mixed results, therefore ambiguities were left unresolved in the final analysis. The Cartesian coordinates estimated for both 1988 surveys were combined and adjusted using least squares to obtain a single set of station positions.

GPS observations were made at station MOUN (Mound) in 1986. Unfortunately, field investigation during early 1988 revealed that this station was destroyed; the monument and supporting concrete base had been completely uprooted from the ground. The site is located about 1 km from the surface rupture of the Superstition Hills fault and we attribute its destruction to the 1987 earthquake. Unless a suitable reference marker is available, destroyed monuments usually cannot be tied to previous surveys because of the high accuracy required for crustal motion research. If the

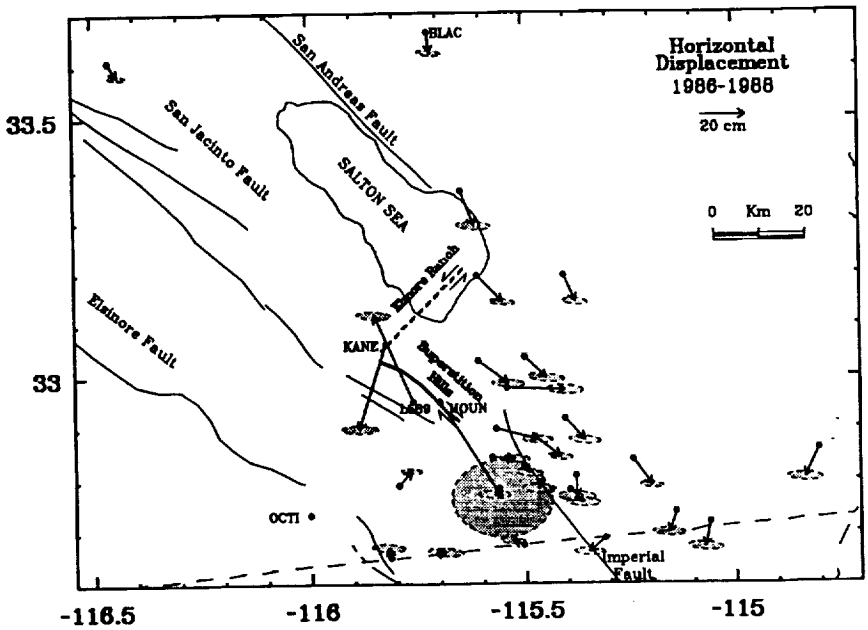

Fig. 4. Imperial Valley GPS station displacements between 1986 and 1988. The displacement at MOUN is from 1986 to 1990. All movements are relative to station OCTI. OCTI is chosen as the reference because it is the site most distant from the 1987 earthquake zone that was observed in 1986 and in both 1988 campaigns. Vertical movements are excluded in the analysis because the uncertainty in this direction is much larger (10–50 times) than the suspected tectonic displacements. The observed displacements are attributed to the 1987 Superstition Hills earthquake sequence, secular plate-boundary deformation across the Imperial Valley, and measurement error. Movements near the 1987 rupture zone approach 0.5 m. Error ellipses are estimated by multiplying the formal errors by a variance factor, determined so the average error scales as 1 ppm (parts per million). The east-trending uncertainty is about 4 times larger than the north-trending uncertainty. The north-trending displacement components are reliable indicators of seismic (and nonseismic) deformation, but this feature is partially obscured by the large longitudinal errors. The anomalous southwest-trending apparent movements for the southeastern-most stations are attributed to measurement error. Station MOUN was reset between surveys so it has an unusually large uncertainty.

suspected deformation is significantly large, however, useful information may be recovered if the monument (or a substitute) is reset in approximately the same location. Site inspection at MOUN clearly showed the position of the old monument and in April 1990 a rebar rod acting as a temporary benchmark was set at approximately the same location. We estimate the temporary mark was reset within 0.15 m of the previous monument. The seismic displacement at MOUN is about 0.5 m, so reoccupation of this site should retrieve a tectonic signal larger than the estimated uncertainty.

The 1990 survey was conducted to establish the displacement of the reset MOUN relative to its 1986 position. This "mini-campaign" included stationary GPS receivers at only three sites (Table 1). Data were collected for only 1 night; a total of nine satellites were tracked during the scheduled 7.0-hour experiment. The 1990 campaign was processed with the Trimvec software, available from the receiver manufacturer (Trimble Navigation, Sunnyvale, California). High positioning accuracy was not required because MOUN was reset between surveys. The orbits were given by the broadcast ephemeris, and surface meteorological data were used to constrain a tropospheric delay model.

Station Displacements 1986–1988

GPS station displacements for the interval 1986 to 1988 are shown in Figure 4 and listed in Table 2. The displacement at MOUN is for the period 1986 to 1990. All movements and uncertainties are made relative to station OCTI. OCTI is selected as the reference because it is the site most distant from the 1987 seismic zone that was occupied in 1986 and in both 1988 campaigns. Only the horizontal components are shown. The vertical displacement is excluded in the analysis because the error in this direction is significantly larger (10–50 times) than the suspected tectonic deformation. The method used to formulate uncertainties is discussed below. The observed displacements can be decomposed into three components: (1) seismic deformation due to the Superstition Hills earthquake sequence; (2) secular deformation due to the Pacific-North American relative plate motion; and (3) measurement error, which we believe is most apparent in the east-trending direction.

The GPS displacement vectors suggest considerable deformation between 1986 and 1988 (or 1990). A significant fraction of this movement is attributed to the 1987 Superstition Hills earthquake sequence. Stations nearest the seismic rupture zone (KANE, L589, and MOUN) show movements of up to 0.5 m. In fact, the 13-km KANE-L589 baseline was shortened by 70 cm. The orientations of the displacements are consistent with conjugate faulting (i.e., right-lateral rupture along the Superstition Hills fault and left-lateral rupture along the Elmore Ranch fault). Other stations near the active fault system also appear to have been affected by the 1987 event.

There is an additional tectonic displacement component due to the relative motion between the North American and Pacific plates. Stations east of the Imperial fault tend to be moving south or southeast relative to sites on the other side of the valley. *Larsen* [1991] estimated the magnitude of this deformation by decomposing the displacements into their north and east-trending components and plotting them separately on cross-sections perpendicular to plate motion (Figure 5). The displacements were adjusted to remove the effect of the 1987 earthquake sequence. The north-trending movements indicate a differential motion of 8.1 ± 1.4 cm between stations on opposite sides of the valley, which is equivalent to a right-lateral deformation rate of 5.9 ± 1.0

TABLE 2. Station Displacements 1986–1988

Station	N, cm	σ_N	E, cm	σ_E
OCTI	0.0	0.0	0.0	0.0
L589	38.1	1.7	−17.2	7.6
KANE	−37.2	1.7	−11.7	8.1
MOUN	−42.3	16.7	27.3	22.5
OCOT	6.4	1.1	5.6	4.6
COAC	−11.7	1.3	5.1	5.5
ALAM	−11.7	1.3	11.2	5.8
GLOC	−11.3	1.2	8.5	5.2
BLAC	−9.0	1.2	1.0	5.2
ORIE	−9.2	1.6	8.9	7.3
FRIN	−15.3	1.7	5.8	7.6
CALE	2.0	1.3	−4.9	5.6
TAMA	−8.6	1.3	11.4	5.5
O217	−6.0	1.6	−7.3	6.8
COLL	−3.0	1.4	2.2	6.0
HAMA	−9.3	1.7	9.8	8.2
PINY	−6.2	1.0	4.0	4.1
BRAW	−0.9	1.9	26.2	8.1
HOLT	−5.4	1.8	5.9	7.5
MELL	−2.8	1.8	−0.5	7.5
IMPE	−0.7	1.6	10.1	6.7
IMPI	−4.8	1.6	18.9	6.7
ACUT	−9.9	1.6	13.2	7.2
ELEC	−2.7	1.6	−2.1	6.9
HLTV	−9.0	2.1	0.3	8.4
MACK	−9.1	1.7	−3.4	7.5
O227	4.4	1.7	09.9	7.4
T122	−12.6	1.8	−6.3	7.8
JUNC	−11.0	1.8	−2.3	7.9
O224	0.6	1.7	3.0	7.9

MOUN displacement is 1986–1990.

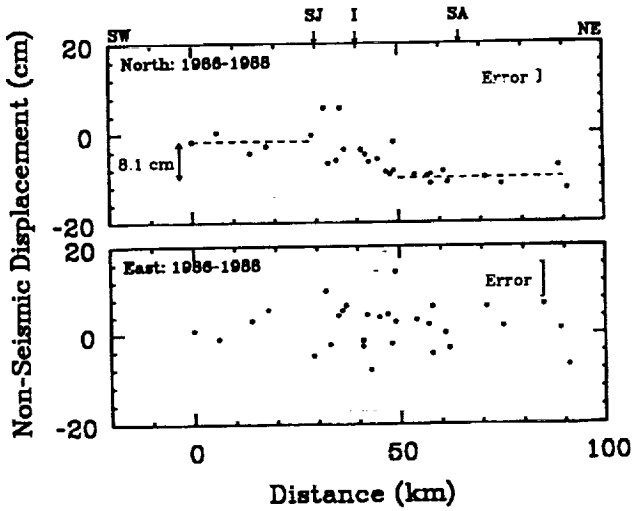

Fig. 5. The north and east-trending GPS displacement components for the 1986–1988 interval [*Larsen*, 1991]. All distances are computed relative to OCTI on a cross section trending N50° E, perpendicular to the plate motion direction. The displacements were adjusted to remove the effect of the 1987 earthquake sequence. Stations with seismic adjustments greater than 4 cm (in the component plotted) are shown as open circles, other sites as solid circles. The average displacement error for each component (bracket) includes uncertainties from the seismic adjustment. The 8.1 ± 1.4 cm north-trending offset between stations on opposite sides of the valley is equivalent to 5.9 ± 1.0 cm/yr right-lateral motion oriented N40° W. The large scatter for the east-trending component is presumably due to measurement error in the 1986 survey.

cm/yr oriented N40° W (average over 1.79 years). This rate is strongly influenced by measurement error and unmodeled seismic effects and is probably not significantly different than the 3.69±0.11 cm/yr rate obtained with terrestrial geodesy [*Lisowski et al.*, 1991]. The scatter is too large in the east-trending components to make a similar comparison.

Also evident in Figure 4 are unusual movements with no obvious tectonic explanation. Most notable are the southwest-trending vectors (as opposed to southeast) for those sites east of the Imperial fault near the border. It appears that the entire network has undergone a systematic clockwise rotation. We investigated this possibility by assuming the network could be rotated (and translated) in terms of an outer coordinate solution by minimizing the displacement component perpendicular to the structural axis of the valley (N40° W) [e.g., *Prescott*, 1981]. Stations KANE, L589, and MOUN were not included in the solution. The applied adjustment did not remove the anomalous displacements, and in fact, made the apparent deformation less uniform. Although these unusual movements cannot be attributed to a simple coordinate rotation, they can be explained by large east-trending systematic errors in the 1986 data. This is consistent with the longitudinal elongation of the computed error ellipses (see below) and explains the large scatter for the east-trending components (Figure 5). The north-trending displacements are apparently reliable indicators of tectonic deformation (for our data), but they are partially obscured by the large longitudinal errors.

Station Displacements 1988–1988 (February–April)

Seven GPS sites were occupied during both 1988 campaigns; calculated site displacements for this 1 month interval are shown in Figure 6 (late February to early April). An adjustment (simple translation) is applied to all movements so that the sum of the vector displacements is zero. Error ellipses are not shown because the figure itself is a representation of uncertainty. Measurable tectonic deformation is not expected during this 1-month period; the apparent movements (averaging 1.6 cm) are an indication of the short-term repeatability with GPS. Short baseline (~ 50 km) horizontal precisions computed from GPS repeatability studies are generally at the sub-centimeter level [e.g., *Dong and Bock*, 1989], but these tests usually involve multiple occupations of the same network over a consecutive 4- to 5-day interval. The seven stations shown in Figure 6 were not all observed simultaneously [*Larsen*, 1991], so the repeatability is somewhat degraded. Nevertheless, at this level of precision the 1 to 5 cm/yr deformation rates across major tectonic structures in southern California should be resolvable in as short as 1 year. In addition, the relatively good reliability indicated for the 1988 data suggests that east-trending errors in the 1986 data account for much of the anomalous nonseismic movement observed between 1986 and 1988 (Figure 4).

Note that the 2.9 cm apparent displacement observed at KANE is to the west-southwest. This might suggest left-lateral afterslip along the Elmore Ranch fault. However, while postseismic offsets were significant along the Superstition Hills fault, almost all Elmore Ranch activity ceased after the initiation of the Superstition Hills event [*Williams and Magistrale*, 1989; *Magistrale et al.*, 1989; *Hudnut et al.*, 1989*a*]. As mentioned above, the observed displacements in Figure 6 probably indicate measurement error, although postseismic deformation cannot be ruled out.

GPS Errors

Formal estimates of GPS uncertainty almost always underestimate variances derived from repeatability studies. We estimate more realistic and illustrative errors by multiplying the formal covariance matrix calculated with each GPS solution by a variance factor, which scales as the aver-

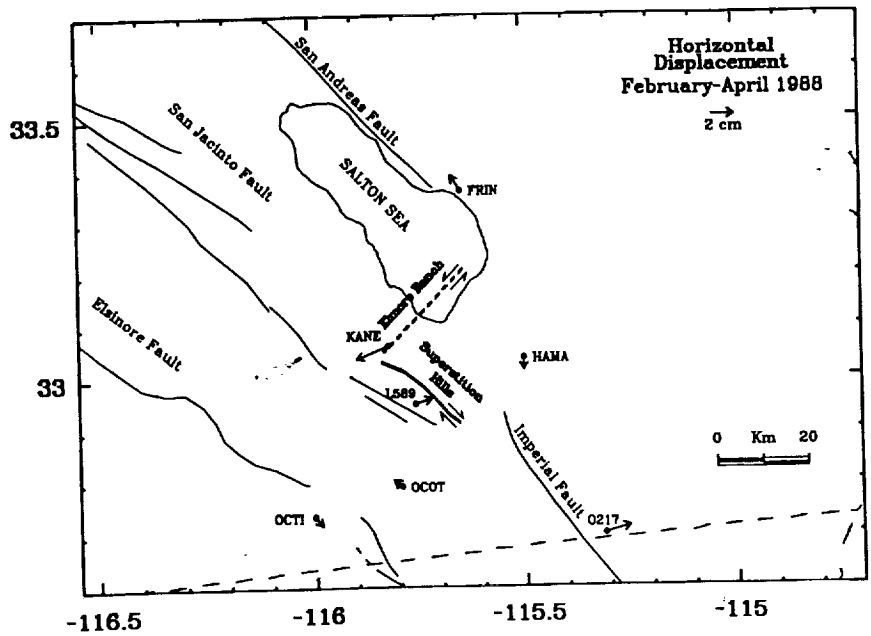

Fig. 6. Imperial Valley GPS station displacements between February/March 1988 and March/April 1988. Error ellipses are not shown because the figure itself is a representation of uncertainty. Measurable tectonic motion is not expected over this 1-month period; the apparent movements likely indicate the repeatability (precision) of the 1988 data. The displacement at KANE could represent postseismic deformation from the 1987 earthquake sequence.

age baseline length. We select a variance factor for the 1986 data so that the average baseline error is 1 ppm. Residuals from the DYNAP adjustment are consistent with this level of uncertainty. The 1988 errors are assumed negligible by comparison, since these data were processed robustly using orbit improvement techniques (not possible with the 1986 campaign). In general, the measurements reported here are not sufficiently redundant to develop reliable statistics. However, based on those cases where repeat measurements have been made, the errors given in this study appear to represent conservative 1 sigma estimates. Although this method is somewhat ad hoc, it allows for self consistent errors and maintains the relationship between north and east-trending uncertainties. Notably, the east-trending errors are about 4 times larger than the north-trending errors. This is due to the north-south ground track of the satellite orbits.

A potential error source is from the different processing schemes used for data reduction; the 1986 campaign was analyzed with the GPS22 software, while the Bernese software was used for the 1988 surveys. Comparison tests have shown that different software systems agree at levels comparable to short-term repeatability ($\sim$ 1 cm) [e.g., *Larsen*, 1991].

Station MOUN was reset between the 1986 and 1990 surveys, so the uncertainty in setting the new mark at the previous location is the primary source of error. Field inspection indicated this uncertainty to be about 15 cm (in all directions), which adds to the GPS measurement error.

5. MODELING

Theory

Simple dislocation theory is often used to model seismically induced geodetic deformation. The Earth is considered a homogeneous isotropic elastic half-space with no stress applied to the free surface. The displacement field u_k for a dislocation Σ in the medium is given by

$$u_k = \frac{1}{8\pi\mu}\int\int_{\Sigma} \nabla u_i w_{ij}^k v_j d\Sigma \tag{1}$$

where ∇u_i is the discontinuity, w_{ij}^k are the displacement Green's functions due to a set of strain nuclei, and v_j are the direction cosines of the normal to the surface element $d\Sigma$ [*Steketee*, 1958; *Chinnery*, 1961]. Analytical solutions to this integral are rather complex but have been simplified for special cases of dislocation or fault geometry [e.g., *Chinnery*, 1961; *Savage and Hastie*, 1966; *Mansinha and Smylie*, 1967]. General expressions of the displacement field for rectangular strike and dip-slip faults of arbitrary inclination have been computed by *Mansinha and Smylie* [1971] and *Okada* [1985]. Arbitrary slip directions can be designed by the superposition of strike and dip-slip dislocations.

The strain/stress within a medium is computed by differentiating the displacement field. For the displacement u_k, where u is a function of the geometrical coordinates x_i, the strain tensor components are given by

$$\epsilon_{ij} = \frac{1}{2}\left(\frac{\partial u_i}{\partial x_j} + \frac{\partial u_j}{\partial x_i}\right). \tag{2}$$

In an isotropic medium the stress tensor σ is given by

$$\sigma_{ij} = \lambda\theta\delta_{ij} + 2\mu\epsilon_{ij} \tag{3}$$

where θ is the dilatation $\left(\theta = \sum_{i=1}^{3}\epsilon_{ii}\right)$. We assume the medium is a Poisson solid with $\lambda = \mu = 2.8\times10^{11}$ dyn cm^{-2}.

A rectangular dislocation within an elastic half-space will create a spatially dependent stress tensor σ throughout the volume. The force acting at a point along an arbitrarily oriented plane in the medium is computed by multiplying σ by the outward normal vector to the plane ($\mathbf{N}_n$). That is, the traction vector T is given by

$$\mathbf{T} = \sigma\mathbf{N}_n. \tag{4}$$

If we assume the plane is coincident with a fault, then the forces generated on this secondary structure due to an initial dislocation are determined by calculating the traction vectors at selected points along the fault. The normal (σ_n), strike-slip (σ_s), and dip-slip (σ_d) stresses on the fault plane are computed by

$$\begin{aligned} \sigma_n &= \mathbf{T}\cdot\mathbf{N}_n \\ \sigma_s &= \mathbf{T}\cdot\mathbf{N}_s \\ \sigma_d &= \mathbf{T}\cdot\mathbf{N}_d \end{aligned} \tag{5}$$

where $\mathbf{N}_n$, $\mathbf{N}_s$, and $\mathbf{N}_d$ are the normal vectors perpendicular, along strike, and along dip to the fault plane. Analytic solutions for the stress and strain fields due to a dislocation within a medium are given by *Chinnery* [1963], *Alewine* [1974], and *Iwasaki and Sato* [1979].

Inverse Methods

Inversion of seismically generated geodetic displacements can yield fault-rupture parameters, such as the slip distribution along a fault plane [e.g., *Ward and Barrientos*, 1986; *Harris and Segall*, 1987; *Segall and Harris*, 1987; *Snay*, 1989]. We employ a method similar to that outlined by *Segall and Harris* [1987]. Singular value decomposition (SVD) [e.g., *Lanczos*, 1961; *Jackson*, 1972; *Menke*, 1984] and elastic dislocation theory are used to invert the Imperial Valley GPS measurements for seismic slip along the Superstition Hills and Elmore Ranch faults.

The relationship between surface deformation and slip along a rectangular dislocation is defined by equation (1). The rupture plane is modeled as a set of nonoverlapping rectangular dislocations. That is, the fault plane is partitioned into multiple subelements or subfaults. The slip distribution along the seismically active fault is given as the discrete approximation of slip along each subelement. The normal equations which govern surface displacement resulting from such slip are given by

$$\mathbf{A}^g m^f = d^g \tag{6}$$

where the superscripts g and f refer to geodetic observation and fault slip, respectively. Each row of $\mathbf{A}^g$ is determined from (1), and is a function of subfault geometry and station location. The slip distribution m_f is defined by $m^f = [m_1, m_2, \cdots, m_n]^T$, where m_i is the slip along the ith subfault. The data vector d^g contains the geodetic observables. In theory, each GPS station displacement adds three rows to $\mathbf{A}^g$ and three elements to d^g, corresponding to the vertical and two horizontal components. For this study, however, the less accurate vertical observations are ignored, since the uncertainty in this direction is many times larger than the expected deformation. The horizontal displacement components dominate in strike-slip environments.

Surface rupture is easily included into (6) by considering measurements of surface displacement as geodetic observation. The offsets are modeled as a priori slip information on

the surface intersecting subfaults. Equation (6) becomes

$$\mathbf{A}m^f = \begin{bmatrix} \mathbf{A}^g \\ \mathbf{A}^s \end{bmatrix} m^f = \begin{bmatrix} d^g \\ d^s \end{bmatrix} = d \tag{7}$$

where d_i^s are the discrete approximations of surface slip along the fault trace, and $\mathbf{A}_{ij}^s = 1$ if subfault element j corresponds to surface slip offset i, otherwise $\mathbf{A}_{ij}^s = 0$.

The GPS displacements shown in Figure 4 and listed in Table 2 are not connected to an external reference but are defined relative to the displacement at OCTI. OCTI was selected as a reference because it is the most distant station from the 1987 earthquake sequence, that was occupied in 1986 and in both 1988 GPS campaigns. However, any use of the GPS displacements as a criteria for evaluating the effect of the earthquakes will be affected by measurement error and tectonic deformation at OCTI. This ambiguity is circumvented if displacement-offset terms are estimated in addition to fault slip parameters. Equation (7) is rewritten

$$\mathbf{A}m = \mathbf{A} \begin{bmatrix} m^f \\ m^o \end{bmatrix} = d \tag{8}$$

where m_i^o is the ith displacement component (i.e., north and east component) uniformly added to all station movements. These (two) displacement-offset terms account for any seismic, nonseismic, or error-induced motion at OCTI, which we have assumed to be zero.

The singular value decomposition of A is given by

$$\mathbf{A} = \mathbf{U}\lambda\mathbf{V}^T \tag{9}$$

where U is a matrix of eigenvectors spanning the data space, V is a matrix of eigenvectors spanning the parameter space, and λ is a diagonal matrix of singular values. Without loss of generality, this is written

$$\mathbf{A} = \mathbf{U}_p\lambda_p\mathbf{V}_p^T \tag{10}$$

where p refers to the nonzero singular values. If the normal equations of (8) are normalized to have unit variance [e.g., *Segall and Harris*, 1987], the generalized inverse of (8) and (10) is given by

$$\mathbf{A}^{-1} = \mathbf{V}_p\lambda_p^{-1}\mathbf{U}_p^T \tag{11}$$

[*Lanczos*, 1961; *Menke*, 1984]. In practice it is often necessary to restrict the volume of the parameter space by considering only the k largest singular values, setting all others to 0.

The generalized solution to (8) for the k largest singular values is given by

$$m = \mathbf{A}_k^{-1}d + \mathbf{V}_0\alpha_0 \tag{12}$$

where $\mathbf{V}_0$ are eigenvectors spanning the null space of the model and α_0 is a vector of arbitrary coefficients. The volume of the model space not constrained by observation is defined by $\mathbf{V}_0\alpha_0$. This term is not influenced by the geodetic data and is thus arbitrary. Often it is the minimum-length solution $m = \mathbf{A}_k^{-1}d$ which is of interest (the coefficients of α_0 are 0). However, some other solution criteria can be satisfied by carefully designating the coefficients of α_0.

For high-resolution fault models where the rupture plane is partitioned into numerous subfaults, it is necessary to apply some type of smoothing constraint over the dislocation surface to prevent the slip distribution from taking on an oscillatory pattern. *Segall and Harris* [1987] showed that the "roughness" of fault slip could be minimized by considering smoothness as an a priori constraint utilized from the model null space through the coefficients of α_0 (equation (12)). They used a smoothing matrix T, with coefficients determined from the discrete approximation of the Laplacian operator $\nabla^2 = \partial^2/\partial x^2 + \partial^2/\partial y^2$, where x and y are the fault distances along strike and dip, respectively. The boundary conditions around the lower and lateral edges of the dislocation are assumed to be null slip, so that the applied smoothing operator causes the calculated fault offset to tend toward zero along these boundaries. Because the Superstition Hills and Elmore Ranch faults ruptured the surface, the upper boundary is considered an unconstrained dislocation. The estimated fault slip is given by

$$m = [\mathbf{I} - \mathbf{V}_0(\mathbf{V}_0^T\mathbf{T}^T\mathbf{T}\mathbf{V}_0)^{-1}\mathbf{V}_0^T\mathbf{T}^T\mathbf{T}]\mathbf{A}_k^{-1}d \tag{13}$$

[*Segall and Harris*, 1987, equation (13)]. A similar formulation for utilizing fault smoothness over the model null space is given by *Harris and Segall* [1987]; an alternate method considering fault smoothness as quasi-data is provided by *Snay* [1989].

For overconstrained solutions (more independent data than parameters), if $k = p$ then SVD is equivalent to simple least squares. This is advantageous since the solution provided by (12) can be utilized for either uniform dislocations or for detailed parameterizations where the fault plane is partitioned into multiple subelements.

Simple dislocation theory has the advantage that the displacement and stress/strain fields for simple fault ruptures can be computed almost instantaneously. The inverse problem of using geodetic data to calculate the slip distribution along a fault plane is also straightforward. However, we have assumed the Earth can be modeled as a homogeneous half-space. Crustal layering or inhomogeneities in the Earth can introduce nonexistent structure into half-space models [*Savage*, 1987]. The Imperial Valley may be especially susceptible since it is a sediment-layered basin overlying basement. While low-resolution schemes such as the average slip over the fault plane will not be seriously affected, attempts to resolve detailed properties may be badly contaminated by artifacts of Earth structure.

Uniform Seismic Slip

We model rupture along the Superstition Hills and Elmore Ranch faults as strike-slip dislocations along vertical planes extending from the surface to 10 km depth. Each dislocation approximately coincides with the mapped surface rupture and/or aftershock distribution. The geometrical parameters for the modeled faults are listed in Table 3. In this section the Superstition Hills and Elmore Ranch faults are modeled as uniform dislocations, with no slip variation allowed on the rupture planes.

To best utilize the GPS computed movements shown in Figure 4, it is necessary to remove the secular deformation from the displacement field. The best example of secular motion is provided by USGS trilateration measurements between 1973 and 1989 [e.g., *Prescott et al.*, 1987*a*; *Prescott et al.*, 1987*b*; *Lisowski et al.*, 1991]. The observed plate-boundary deformation across the Salton Trough is 3.69±0.11 cm/yr at an orientation roughly parallel to the direction of plate motion (N40° W). The deformation northwest of the Imperial Valley is concentrated in a zone at least 50 km wide

TABLE 3. Parameters for Modeled Dislocations

	Superstition Hills	Elmore Ranch
Length, km	25	25
Width, km	10	10
Strike	N50° W	N40° E
Dip	90	90
Depth, km	0	0
Latitude, ° N	32.9569	33.1078
Longitude, ° E	−115.7431	−115.7505

Latitude and longitude are coordinates at top center of dislocation. Depth is depth to top of fault.

TABLE 4. Inverse Models of Seismic Slip

Model	Fault	Subfaults Strike	Subfaults Dip	Slip, cm	Moment, $\times 10^{25}$ dyn cm
Model 1	SH	1	1	130. ± 8.	9.4
Model 1	ER	1	1	−30. ± 10.	2.3
Model 2a	SH	10	5		9.9
Model 2a	ER	10	5		5.9
Model 2b	SH	10	5		8.4
Model 2b	ER	10	5		7.0

Abbreviations are SH, Superstition Hills fault and ER, Elmore Ranch fault.

[*Prescott et al.*, 1987*b*], indicating distributed shear across the San Andreas and San Jacinto faults. Unfortunately, the strain distribution in the Imperial Valley is not as well constrained because of relatively sparse electronic distance measurement (EDM) coverage. However, observations from a dense triangulation network indicate 4.3 cm/yr differential velocity across the valley from 1941 to 1986 [*Snay and Drew*, 1988]. While the slightly larger rate (compared to EDM) may be insignificant considering the increased uncertainties with triangulation data, the measurements indicate that deformation is concentrated in a narrow 20-km-wide zone about the Imperial fault. Therefore the following empirical approach is used to model and remove the secular deformation from the GPS observations. The differential velocity across the Salton Trough is assumed to be 3.69 cm/yr. Running along the axis of the trough (coincident with the Imperial fault) is a transition zone, where the strain gradient is defined by simple shear with displacements oriented N40° W. The transition zone north of the Imperial fault is 50 km wide; to the south it is 20 km wide.

A uniform slip model computed by inverting the GPS displacements (minus the secular deformation), indicates 130±8 cm right-lateral slip along the Superstition Hills fault and 30 ± 10 cm left-lateral slip along the Elmore Ranch fault (Model 1, Table 4). Two slip parameters and two displacement-offset terms (equation (8)) were solved (the entire model space was searched). The corresponding moments are 9.4×10^{25} dyn cm (Superstition Hills) and 2.3×10^{25} dyn cm (Elmore Ranch). The displacement residuals are shown in Figure 7 (observed minus calculated). The largest residuals trend in the longitudinal direction and are especially noticeable for the southeastern-most sites. This reconfirms our speculation for large east-trending errors. However, the residual vectors at the three stations nearest the seismogenic zone are unusually large. The large residual at MOUN is easily explained since this station was reset between surveys. Station KANE is located within the complex fracture zone of the Elmore Ranch fault (~ 100 m from a mapped trace), and is therefore especially sensitive to shallow slip. Solutions without KANE are not significantly different, however. The residual at L589 is significantly larger than the average residual computed at the other stations. Field inspection here (and at KANE) revealed no evidence that the monument had been disturbed. The large residual suggests additional slip not modeled by the uniform dislocations assumed for Model 1.

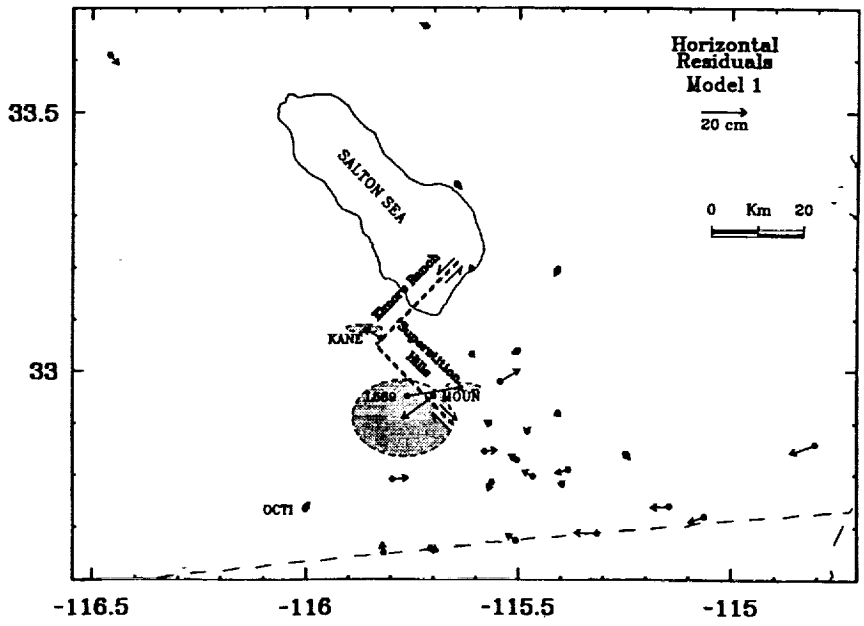

Fig. 7. The residuals (observed minus calculated) for the best fit solution to Model 1. Errors ellipses not shown are presented in Figure 4. The large east-trending residuals for the southeastern stations are suggestive of measurement error. The residual at MOUN is attributed to the benchmark being reset between surveys. The unusually large discrepancy at L589 (and KANE) suggest additional seismic deformation not modeled by the uniform slip dislocations used for Model 1.

Seismic Slip Distribution

To estimate the seismic slip distribution, it is necessary to partition the rupture planes into multiple regions or subfaults (Model 2). The divisions must be sufficiently dense as to provide reasonable slip resolution. We choose 10 subfault elements in the horizontal and 5 in the vertical, so that each fault is partitioned into 50 subregions. Each dislocation element is 2.0 km wide (vertical) and about 2.5 km long (2.4 km for Superstition Hills and 2.6 km for the Elmore Ranch fault). The slip distribution along both rupture planes is constrained to be sufficiently smooth (equation (13)). The GPS displacements (minus the secular deformation) are adjusted by the displacement-offset terms estimated with Model 1.

A priori surface slip information is added to Model 2. Surface slip along the Superstition Hills fault extends (nearly) the entire length of the modeled fault plane (Figure 8) [*Williams and Magistrale*, 1989]. The mapped offset is broken into two fairly continuous strands, one spanning the northwestern half and the other the southeastern half of the fault. These strands overlap near the faults midsection; surface slip initiates on the southeastern strand where it dies out on the northwestern strand. We refer to this break in the rupture pattern as a slip ambiguity. The cumulative surface offset for both strands is averaged over 2.4 km segments (the horizontal dimension of each subfault), which are used as a priori slip estimates for the surface fault elements corresponding to each segment. Surface rupture along the Elmore Ranch fault is confined to the southwest (Figure 8). Recall that the mapped surface breaks occurred along several nearly parallel strands (Figure 2) [*Hudnut et al.*, 1989a]. We take the cumulative surface offset for all strands averaged over 2.6 km segments and use this as a priori slip for the surface subfault elements. Where no rupture is mapped (to the northeast), the surface-intersecting fault partitions are assigned 0 slip. The a priori uncertainty for each surface slip estimate is assumed to be 10 cm.

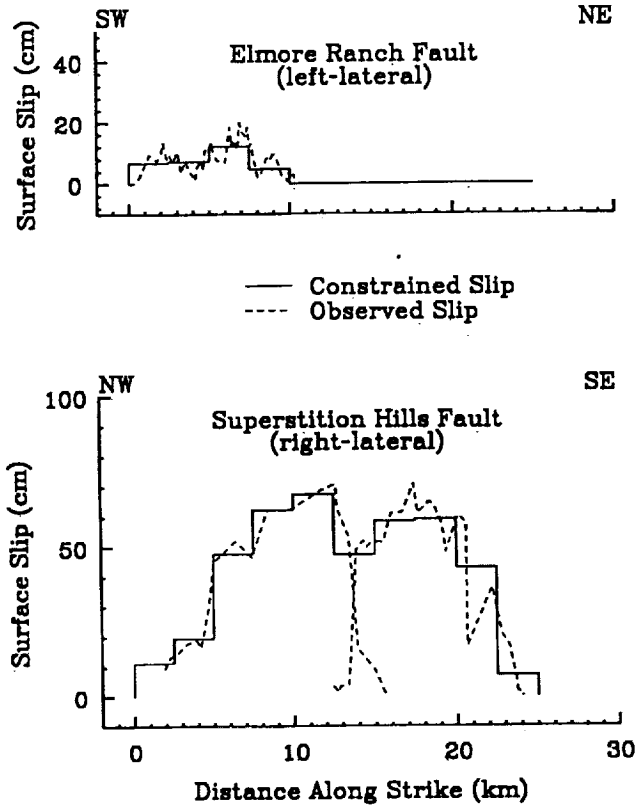

Fig. 8. Observed surface slip along the Superstition Hills and Elmore Ranch faults (dashed lines), as of January 26, 1988 (1 month prior to the GPS observations) [*Williams and Magistrale*, 1989]. A discrete approximation to the surface slip was used to constrain the uppermost subfault elements in Models 2a and 2b (solid lines). The Elmore Ranch measurements are the cumulative slip from multiple surface breaks across a 10-km-wide zone. Superstition Hills slip is broken into two strands, overlapping near the faults midsection (the discrete approximation corresponds to the cumulative slip on both strands).

The number of independent parameters estimated through singular value decomposition depends on the number of singular values k utilized in equation (12). A trade-off exists between solution variance and resolution [e.g., *Menke*, 1984]. Large k produce highly resolved models at the expense of increasing solution uncertainty. Correspondingly, small k yield low variance solutions but do not provide detailed resolution. A total of 100 subfault elements are used for Model 2 (50 for each fault). If $k = 100$, then slip along each subfault will be determined uniquely. Because of limited geodetic coverage, however, it is practical to consider only the first few eigenvectors of the parameter space defined by the geodetic observations. Therefore each solved parameter is a function of some combined slip over multiple subfault elements. This property is fundamental of singular value decomposition when used to solve under-determined or poorly determined problems [e.g., *Jackson*, 1972]. It is necessary to determine the k which maximizes the resolution without allowing the solution to become too oscillatory or unstable.

The geodetic moment, solution instability, and model residual calculated for different values of k are shown in Figure 9. The moment is a function of the average slip along the fault planes, while solution instability is determined from the standard deviation of slip for each subfault element. An instability of 0 (stable) indicates uniform slip along the fault planes, while high values indicate an oscillatory or unstable solution. The rms defines the agreement between model and observation and is calculated by rms $= \sum(o_i - c_i)^2/\sigma_i^2$ where o_i is the observed, c_i is the calculated, and σ_i is the uncertainty assigned to the ith observation.

The first 20 singular values correspond to the a priori slip estimates for the surface-intersecting subfaults (Figure 9). The solution becomes increasingly oscillatory after $k = 30$ as is indicated by the instability. The rms is significantly reduced beyond $k = 20$, but only improves marginally with increasing k. The solution fit for $k > 20$ is slightly better than that for Model 1. Also evident is the relatively large moment estimates for the Elmore Ranch fault. This is because the far-field displacements are nearly identical for two perpendicular faults with opposite slip orientations. Since we are using only the first few eigenvectors of the model space, the slip between the two faults is strongly correlated. The larger slip along the Superstition Hills fault is being mapped onto the Elmore Ranch fault plane producing higher moments.

The estimated seismic slip distribution along the Superstition Hills and Elmore Ranch faults for $k = 23$ and $k = 27$ are shown in Figure 10. We refer to these solutions as Models 2a and 2b, respectively (Table 4). Although both faults are partitioned into 50 elements, the fault rupture is not

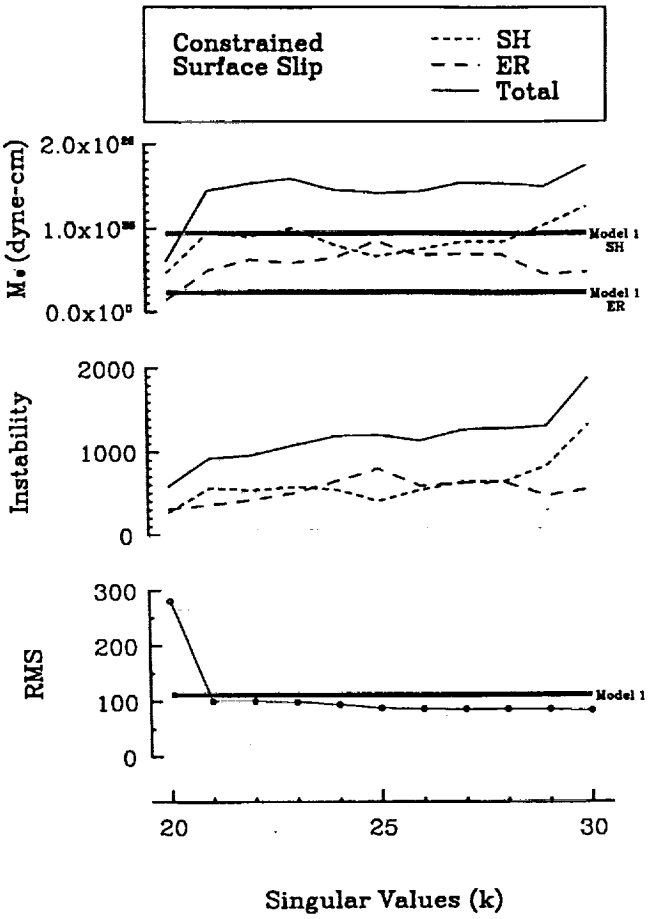

Fig. 9. The geodetic moment, standard deviation of subfault slip (instability), and solution rms calculated for different singular values (k). Shown are solutions constrained by surface slip measurements ($20 \leq k \leq 30$).

as resolved as the contours suggest since all but the first few (nonsurface) model space eigenvectors are ignored. The solution suggests fairly uniform rupture along both fault planes for $k = 23$. The dislocation may be slightly concentrated to the southwest along the Elmore Ranch fault. The apparent "bullseye" pattern is due to the smoothness constraint, which requires zero slip along the lateral edges and lower boundaries (the upper boundaries are constrained by the surface slip). There is little difference in the slip distribution for $k = 21$ through $k = 26$. However, there is a noticeable change in the dislocation pattern starting with $k = 27$. While slip along the Elmore Ranch fault remains fairly uniform, displacement along the Superstition Hills fault becomes concentrated to the northwest and to the southeast. This change is significant and is caused by the GPS displacement at one station. Recall the large residual for L589 in Model 1 (Figure 7). This discrepancy is nearly eliminated beginning with $k = 27$. Therefore the observed displacement at L589 can be satisfied by concentrated rupture at each end of the Superstition Hills fault. It is assumed that the observed GPS displacement at L589 is seismically generated and not contaminated by an unusually large measurement error. The slip deficit near the center of the fault roughly corresponds to the slip ambiguity observed at the surface (Figure 8).

The model resolution for $k < 27$ is very limited. In fact, the similar solutions obtained for $20 < k < 27$ suggests that the most significant feature is the combined moment on both fault planes (or average slip). When $k = 27$, it is possible to distinguish slip along the Superstition Hills fault, primarily from the measured displacement of L589. Due to the limited data, it is doubtful any additional features can be resolved without making the solution unstable (high variance). There is little resolution with depth since surface (geodetic) data are poorly equipped to distinguish slip in this direction.

Independent solutions made without constraining the up-

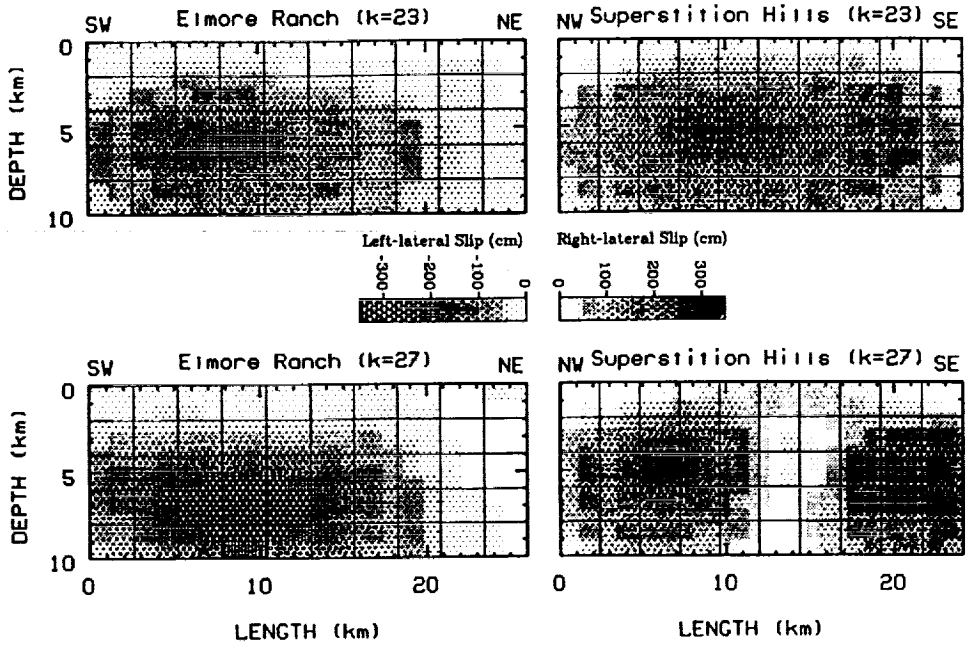

Fig. 10. Slip distribution along the Superstition Hills and Elmore Ranch faults computed using singular value decomposition. Each fault is partitioned into the 50 sub-elements indicated by the grid spacing. Shown are solutions for $k = 23$ and $k = 27$ constrained by measurements of surface offset.

per subfault elements by surface offset measurements are presented by *Larsen* [1991] and are not duplicated here. In general, the constrained and unconstrained slip distributions are similar. Notably, the unconstrained solutions also reveal concentrated slip on the northwestern and southeastern segments of the Superstition Hills fault. This emphasizes that the calculated slip discrepancy near the faults midsection is not simply an artifact of incorporating measurements of surface offset into the model.

6. GEOPHYSICAL IMPLICATIONS

Conjugate Faulting

The most prominent feature of the Superstition Hills earthquake sequence is the conjugate relationship exhibited by near-simultaneous ruptures along right-lateral northwest and left-lateral northeast-trending faults. In the context of the Imperial Valley, the northeast-trending structures are termed "cross faults" [e.g., *Hudnut et al.*, 1989*a*]. Conjugate and cross-fault seismicity seems to be a fairly typical phenomenon for this region (Figure 11) and may dictate the strain transfer mechanism between faults. The 1981 Westmorland earthquake (M_L 4.1) is a prime example of cross-fault tectonics. The mainshock and aftershock sequence are clearly mapped onto a northeast-trending lineament. Other examples are associated with the Imperial fault. The largest aftershock (M_L 5.8) following the 1979 Imperial Valley earthquake (M_L 6.6) was located near the town of Brawley [*Johnson and Hutton*, 1982]. The focal mechanism and following seismicity suggested left-lateral slip along a vertical northeast-trending fault. *Reilinger and Larsen* [1986] found that rupture along an identical conjugate structure successfully modeled geodetic observations within the Brawley Seismic Zone. A large (M_L 5.5) aftershock was also recorded near Brawley following the 1940 earthquake [*Neumann*, 1942]. Due to the sparse seismic data, neither the mechanism nor location were precisely determined, although we speculate this event occurred along the same northeast-trending feature as the large 1979 aftershock. Of historical interest are Imperial Valley earthquake pairs during 1915 (M_L 6.3, M_L 6.3) and 1927 (M_L 5.8, M_L 5.5) [*Beal*, 1915; *Toppozada et al.*, 1978]. In each case the second shock followed the first by about 1 hour, contrasting with the 12-hour interval between the 1987 events. It is not known which fault(s) ruptured during these earthquake sequences, but conjugate fault interaction is possible.

Rupture on the Superstition Hills fault was almost certainly triggered by the Elmore Ranch event (occurring 12 hours earlier) suggesting some mechanism of stress transfer between the two faults. Figure 12 shows the normal (σ_n) and strike-shear (σ_S) stress components instantaneously applied to the Superstition Hills fault due to a 30 cm left-lateral Elmore Ranch dislocation (Model 1). Tension and right-lateral shear are considered positive, both tending to induce failure on the rupture plane. Also shown is a Coulomb failure stress (σ_c), here given by $\sigma_c = \sigma_s + \mu\sigma_n$, where μ is the coefficient of internal friction. We assume $\mu = 0.75$ [e.g., *Hudnut et al.*, 1989*b*]; different values do not significantly alter our results. Positive σ_c indicate stress-loading leading to shear failure. Failure will occur if the preexisting stress on the fault plane plus σ_c is greater than some critical value (the inherent shear strength).

The Coulomb failure relation assumes that the Earth behaves as a linearly elastic material. Near the limiting state of failure, however, the stress distribution will not be governed by elastic stress/strain laws. Nevertheless, the qualitative form of the function will still be valid. That is, increased right-lateral shear and/or tension moves the Superstition Hills fault closer to failure.

We assume that the Superstition Hills rupture plane was at or near failure at the time of the Elmore Ranch event. The initial shock generated an increase in the Coulomb fail-

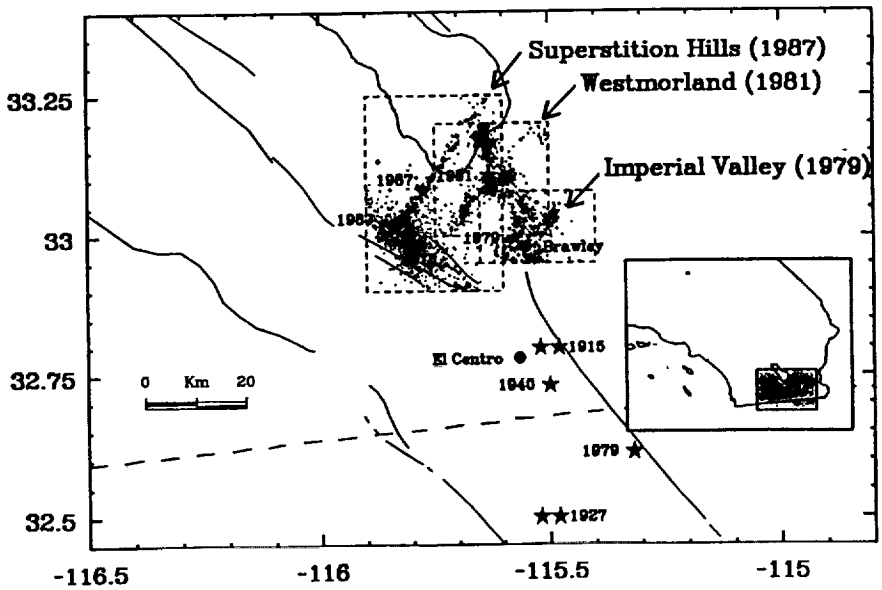

Fig. 11. Known and/or potential conjugate/cross-fault seismic episodes in the Imperial Valley since 1900. Seismic release on (left-lateral) northeast-trending structures was observed in 1979, 1981, and 1987. Earthquake pairs or mainshock/aftershock sequences suggestive of conjugate faulting were observed in 1915, 1927, and 1940. This suggests conjugate/cross-fault interaction is typical for the Imperial Valley.

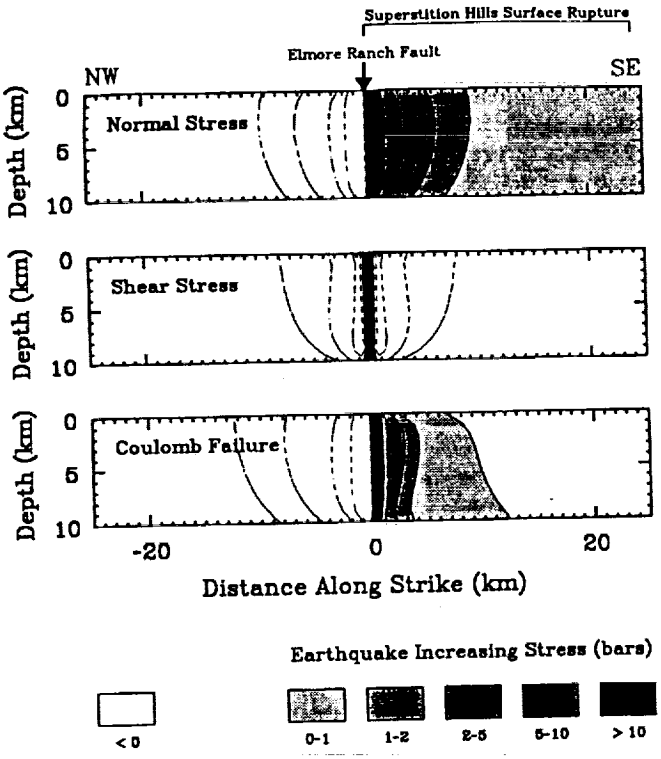

Fig. 12. Strike-shear (right-lateral positive) and normal stress change (dilatation positive) induced on the Superstition Hills fault due to a 30-cm left-lateral Elmore Ranch dislocation (Model 1). Also shown is the Coulomb failure stress change, where positive values indicate an increased potential for rupture (earthquake inducing stress). The northwest third of the 1987 Superstition Hills rupture plane underwent a stress change tending it toward failure with the maximum change calculated in the epicentral region near the intersection with the Elmore Ranch fault. There was no rupture to the northwest where the Coulomb failure stress was negative (reduced earthquake potential). The magnitude of the stress change (in bars) is comparable to typical earthquake stress drops.

ure potential along the Superstition Hills fault (Figure 12), possibly advancing it past its failure threshold. This is seen mostly as a combination of increased tension (earthquake inducing) countered by left-lateral shear (earthquake inhibiting). The increase is maximized along the northwest boundary of the rupture plane, near the nucleation point of the second event. Presumably, rupture began where the applied stress was greatest and then propagated to the southeast. Northwestward rupture is prohibited because the increase in compressive forces tends to inhibit shear failure along this segment of the plane. The magnitude of the Coulomb stress increase near the Superstition Hills epicentral zone is comparable to typical earthquake stress drops (~ 10 bars if $\mu = 0.75$).

In Coulomb analysis the angle ϕ between two conjugate ruptures is given by $\phi = \tan^{-1}(\mu)$, or $\phi = 53°$ if $\mu = 0.75$. In addition, slip on conjugate faults should be equal for the coaxiality of stress and strain. However, the Superstition Hills and Elmore Ranch faults are nearly orthogonal, with considerably greater slip on the Superstition Hills. The failure pattern in the Imperial Valley may be strongly governed by preexisting zones of weakness, so rupture geometry may not follow a strict Coulomb behavior. Also, it has been theoretically shown and experimentally demonstrated that the principal axes of stress and strain are not coaxial during faulting of a frictional material [*Mandl and Fernandez-Luque*, 1970; *Drescher*, 1976].

The one to several hour delay recorded between events during observed and suspected conjugate episodes in the Imperial Valley is significant from an earthquake failure perspective. Shown in Figure 13 are potential scenarios for earthquake ruptures involving conjugate-mainshock interaction, such as that observed for the Superstition Hills events. We assume faults fail by an undefined mechanism when they are at or above some critical stress level. The regional strain acting over several years brings a fault near this critical failure point. A stress increase is induced along part of the fault plane due to rupture on a conjugate structure (e.g., Figure 12), which may or may not be sufficient to push the stress state past its critical threshold. In the case of Earthquake 1 (Figure 13*a*), the stress change caused by the conjugate event is not enough to induce failure. Some form of time dependent stress transfer onto the fault is activated and eventually the critical level is reached. A mechanism involving postseismic viscous creep along the Elmore Ranch fault has been suggested for the 1987 Superstition Hills sequence [*Given and Stuart*, 1988]. If this scenario is valid, we would also expect failure modes such as that indicated by Earthquake 2. Here the instantaneous stress applied to the fault from the conjugate event pushes the stress state past the critical level and rupture is immediate. In this case, failure

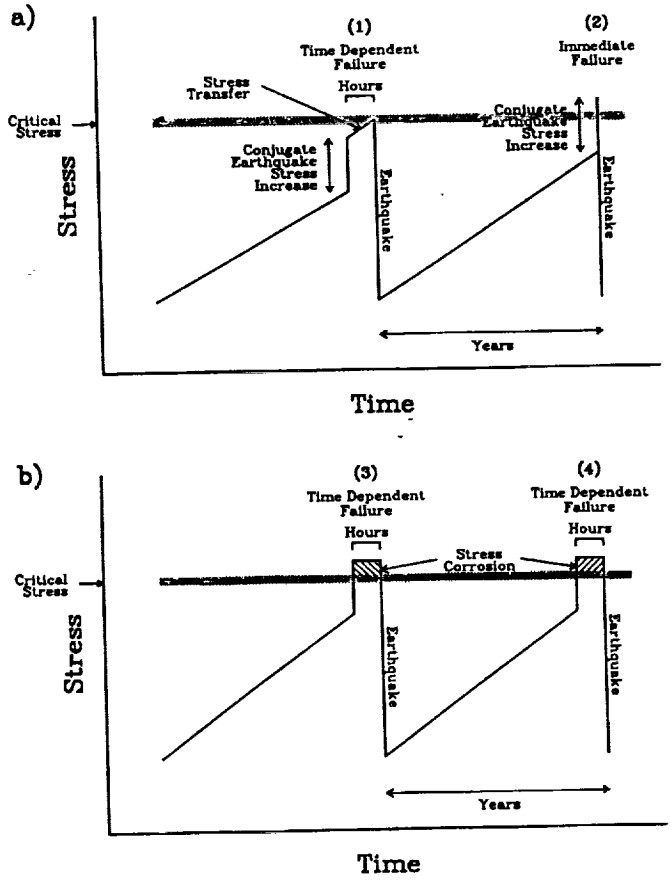

Fig. 13. Schematic of potential earthquake failure processes in the Imperial Valley. (*a*) Earthquake failure occurs after some critical stress is reached. (*b*) Earthquake failure occurs following a time dependent delay after critical stress is exceeded.

along the two perpendicular fault planes will occur simultaneously. However, this behavior is not observed in the Imperial Valley. Conjugate episodes characteristically have been separated by one to several hours. This suggests that the critical stress level can be exceeded without immediate failure. Therefore some time dependent mechanism must be active on the fault plane. We loosely refer to this as "stress corrosion" (Figure 13*b*) [e.g., *Das and Scholz*, 1981]. This does not exclude the occurrence of stress transfer due to nonseismic deformation. In fact, work hardening along the fault plane during this load transfer may allow the stresses to increase during the time interval between events. In the case of Earthquakes 3 and 4, it is suggested that the critical stress level must be exceeded for a period of one to several hours before failure occurs. *Hudnut et al.* [1989*b*] proposed fluid diffusion as an alternate mechanism, whereby the effective normal stress was reduced (made more positive) due to pore-fluid infiltration into the rupture plane thus increasing the Coulomb failure stress. This process involves action on the fault plane and cannot be explained by stress transfer alone. Regardless of cause, the temporal and geometric relationship exhibited by conjugate fault interaction is seemingly typical of Imperial Valley tectonics and is likely an important factor for the potential prediction of large earthquakes and aftershocks.

Moment and Slip Distribution

The geodetic (GPS) source parameters for the Superstition Hills and Elmore Ranch earthquakes are listed in Table 4 and the slip distribution is shown in Figure 10. The seismic moment is best defined by Model 1, while the slip distribution is best expressed by Model 2b. The GPS measured coseismic displacements are directly proportional to the combined effect of the Elmore Ranch and Superstition Hills events, although we have attempted to resolve slip between each fault. The calculated slip is a function of the coseismic offset, as well as 3–4 months of postseismic slip (plus 1.5 years of preseismic movement, if any). The average left-lateral Elmore Ranch dislocation is about 30 cm, with a fairly uniform distribution along the fault plane. In the case of the Superstition Hills fault, the average right-lateral dislocation is about 130 cm, with concentrated slip along the northwest and southeast sections of the fault. Because the GPS sampling frequency is so low (years), the calculated source parameters contain the total coseismic moment, including several months of postseismic slip.

The GPS moments are compared with estimates made through seismic and other geodetic studies (Table 5). Forward and inverse models using teleseismic and strong-motion recordings are used to constrain source parameters, as well as investigate complexities of the Superstition Hills rupture process [*Dziewonski et al.*, 1989; *Bent et al.*, 1989; *Sipkin*, 1989; *Frankel and Wennerberg*, 1989; *Wald et al.*, 1990; *Hwang et al.*, 1990]. The teleseismic moments are similar to the GPS estimates, while the strong ground motion data suggest significantly lower moments. The high-frequency strong-motion measurements are dominated by energy around 1 s and conceivably miss a sizable portion of the long-period energy release; these near-field seismic solutions may underestimate the total moment release.

Geodetic measurements from Pinyon Flat observatory are used to constrain planer and curved dislocation models for the Superstition Hills and Elmore Ranch faults [*Agnew and Wyatt*, 1989]. The data are obtained from long-base strain and tiltmeters, as well as a borehole dilatometer. The best fit planer models to all observations are significantly lower than those calculated with the GPS and teleseismic data (Table 5), although a 70% moment increase for the Superstition Hills fault is obtained when the strain meter data are excluded. The low moment estimate may be due to a number of factors [*Agnew and Wyatt*, 1989]: (1) measurement quality, particular with the strain meter, (2) rheologic differences between Superstition Hills and Pinyon Flat, and (3) strain meter-dilatometer sensitivity to the nodal deformation plane roughly on azimuth with the observatory.

Geodolite observations from the Salton Trough EDM network were made in early December (1987), several days after the Superstition Hills sequence [*Lisowski and Savage*, 1988]; the last previous occupation was in January 1987. Simple dislocation models with 40 cm left-lateral slip along the Elmore Ranch fault and 120 cm right-lateral slip along the Superstition Hills fault best fit the observations. The estimated moment for the Superstition Hills event is comparable to that obtained with the GPS displacements (Table 5).

The discrepancies in Table 5 are largely attributed to the alternate methodologies, observations, and parameters used to constrain each model. However, for those calculations which include moment estimates for both the Superstition Hills and Elmore Ranch events, the ratio between the two ruptures is fairly constant. This illustrates internal consistency with each method. More importantly, it suggests that postseismic slip along the Superstition Hills fault is probably confined to the shallow segment of the rupture plane. Since seismic activity on the Elmore Ranch fault essentially ceased after the Superstition Hills event, if postseismic slip occurred in mass along a large fraction of the Superstition Hills rupture plane, the GPS moment ratio would be considerably larger.

TABLE 5. Moment Comparison

Method	Moment, $\times 10^{25}$ dyn cm				Reference
	SH	ER	Total	Ratio	
GPS (Model 2)	9.4	2.3	11.7	4.1	this study
Teleseismic	7.2	1.4	8.6	5.1	*Dziewonski et al.* [1989]
Teleseismic	10.0	2.3	12.0	4.3	*Sipkin* [1989]
Teleseismic	10.8	2.7	13.5	4.0	*Bent et al.* [1989]
Teleseismic	8.0				*Hwang et al.* [1990]
Strong motion	5.2				*Wald et al.* [1990]
Strong motion	1.8				*Frankell and Wennerberg* [1989]
Pinyon Flat (Planar-A)	3.7	0.8	4.3	4.6	*Agnew and Wyatt* [1989]
EDM	9.3				*Lisowski and Savage* [1988]

Abbreviations are SH, Superstition Hills fault and ER, Elmore Ranch fault.

While the epicenter and aftershock sequence for the Superstition Hills event were concentrated along the northwestern portion of the fault, seismic and surface slip data suggest significant moment release on the southeastern portion of the Superstition Hills fault [*Wald et al.*, 1990; *Bent et al.*, 1989; *Hwang et al.*, 1990; *Williams and Magistrale*, 1989]. An exception is the strong ground motion study of *Frankel and Wennerberg* [1989], where slip is confined to the northwest. However, if their analysis is strongly dependent on high-frequency data, this suggests rupture along the southeastern segment was dominated primarily by low-frequency energy release. The GPS data also indicate slip along the southeastern segment of the fault, and further suggest a displacement null near the fault's midsection. This slip deficiency may be related to the ambiguity observed in the surface offset along the center of the fault (Figure 8).

Deformation Across the Imperial Valley

The 1986–1988 GPS station displacements indicate significant nonseismic movement across the Imperial Valley, which is attributed to the ongoing motion between the Pacific and North American plates. *Larsen* [1991] showed that this movement could be modeled by a differential velocity of 5.9 ± 1.0 cm/yr across the valley. This rate is heavily influenced by measurement error and unmodeled seismic effects, however, and is probably not significantly different than the 3.69 ± 0.11 cm/yr rate obtained with EDM observations from 1973–1989 [*Lisowski et al.*, 1991]. In fact, in the present study the EDM rate is used to remove the secular displacement component from the 1986–1988 data. Alternatively, accelerated deformation is not without precedence and cannot be ruled out. GPS observations between 1988 and 1989 indicate 5.2 ± 0.9 cm/yr displacement across the Imperial Valley [*Larsen and Reilinger*, 1992]; triangulation observations suggest a rate of 6.2 cm/yr between 1941 and 1954 [*Snay and Drew*, 1988], although this is attributed to postseismic deformation following the 1940 Imperial Valley earthquake. Increased deformation following the 1979 earthquake is not observed in the EDM observations [*Savage et al.*, 1986]. In any case, additional GPS measurements will better constrain the current deformation.

7. CONCLUSIONS

Station movements computed from four Imperial Valley GPS campaigns indicate large crustal displacements during the periods 1986–1988 and 1986–1990. Much of the deformation is attributed to the 1987 Superstition Hills earthquake sequence. Eleven sites near the seismic rupture zone are displaced at least 10 cm. The Superstition Hills and Elmore Ranch faults are modeled as rectangular dislocations of uniform slip in an elastic half-space. The best fit model to the GPS observations requires 130 cm right-lateral offset along the northwest-trending Superstition Hills fault and 30 cm left-lateral offset along the conjugate northeast-trending Elmore Ranch fault. The estimated geodetic moments are 9.4×10^{25} dyn cm and 2.3×10^{25} dyn cm for the Superstition Hills and Elmore Ranch faults, respectively. These moments are consistent with those obtained from teleseismic data, suggesting that postseismic slip along the Superstition Hills fault was concentrated near the surface. The slip distribution along each fault is investigated by partitioning the rupture planes into 50 subelements and utilizing singular value decomposition to estimate the slip along each subfault. Measurements of surface offset are used to constrain slip on the shallow elements of the fault plane. The estimated slip distribution along the Elmore Ranch fault is fairly uniform. Slip along the Superstition Hills fault appears to be concentrated to the northwest and the southeast, with a displacement drop near the fault's midsection.

In addition, the 1986–1988 GPS observations suggest a nonseismic differential velocity across the Imperial Valley of 5.9 ± 1.0 cm/yr due to the relative motion between the North American and Pacific plates. The observed rate is heavily influenced by unmodeled seismic effects and measurement error and is not significantly different than the 3.69 ± 0.11 cm/yr rate obtained from EDM measurements. Regardless, the observed seismic and secular deformations clearly emphasize the importance of future GPS study in the Imperial Valley.

Acknowledgments. The field support provided by so many people was invaluable. In particular, we thank John Beavan, Lewis Gilbert, Ken Hudnut, Michael Jackson, James Stowell, and Mike Bevis. We also thank William Young and Gerald Dole at the Riverside County Flood Control District and Gerald Stayner at the Riverside County Survey Department for providing support for the 1990 mini-campaign. Ken Hudnut processed the 1990 data. Reviews by Michael Lisowski, Roger Denlinger, Hiroo Kanamori, Kerry Sieh, and William Prescott substantially improved the manuscript. We thank Liz Henderson for formatting the text for *JGR*. This work is supported by USGS grants 14-08-0001-G1679, 14-08-001-G1354, and 14-08-0001-G1774, and by NASA contract NAG-5-814.

REFERENCES

Agnew, D.C., and F.K. Wyatt, The 1987 Superstition Hills earthquake sequence: Strains and tilts at Pinyon Flat observatory, *Bull. Seismol. Soc. Am., 79*, 480–492, 1989.

Alewine, R.W., Application of linear inversion theory toward the estimation of seismic source parameters, Ph.D. thesis, 303 pp., Calif. Inst. of Technol., Pasadena, 1974.

Beal, C.H., The earthquake in the Imperial Valley, California, June 22, 1915, *Bull. Seismol. Soc. Am., 5*, 130–149, 1915.

Bent, A.L., D.V. Helmberger, R.J. Stead, and P. Ho-Liu, Waveform modeling of the November 1987 Superstition Hills earthquakes, *Bull. Seismol. Soc. Am., 79*, 500–514, 1989.

Budding, K.E., and R.V. Sharp, Surface faulting associated with the Elmore Ranch and Superstition Hills, California, earthquake of 24 November 1987 (abstract), *Seismol. Res. Lett., 59*, 49, 1988.

Chin, M., CIGNET report, GPS Bulletin, Global Positioning System Subcomm. of Comm. VIII, Int. Coord. of Space Technol. for Geod. and Geodyn., Natl. Geod. Surv., Rockville, Md., 1988.

Chinnery, M.A., The deformation of the ground around surface faults, *Bull. Seismol. Soc. Am., 51*, 355–372, 1961.

Chinnery, M.A., The stress changes that accompany strike-slip faulting, *Bull. Seismol. Soc. Am., 53*, 921–932, 1963.

Das, S., and C.H. Scholz, Off-fault aftershock clusters caused by shear stress increase?, *Bull. Seismol. Soc. Am., 71*, 1669–1675, 1981.

Davis, J.L., W.H. Prescott, J.L. Svarc, and K.J. Wendt, Assessment of global positioning system measurements for studies of crustal deformation, *J. Geophys. Res., 94*, 13,635–13,650, 1989.

Defense Mapping Agency, Department of Defense world geodetic system 1984, *DMA TR 8350.2*, 122 pp., Def. Mapp. Agency, Washington, D.C., 1987.

DeMets, C., R.G. Gordon, S. Stein, and D.F. Argus, A revised estimate of Pacific-North America motion and implications for western North America plate boundary zone tectonics, *Geophys. Res. Letts., 14*, 911–914, 1987.

DeMets, C., R.G. Gordon, D.F. Argus, and S. Stein, Current plate motions, *Geophys. J. Int., 101*, 425–478, 1990.

Dixon, T.H., An introduction to the Global Positioning System and some geological applications, *Rev. Geophys., 29*, 249–276, 1991.

Dong, D., and Y. Bock, Global positioning system network analysis with phase ambiguity resolution applied to crustal deformation studies in California, *J. Geophys. Res., 94*, 3949–3966, 1989.

Drescher, A., An experimental investigation of flow rules for granular materials using optically sensitive glass particles, *Geotechnique, 26*, 591–601, 1976.

Drew, A.R., and R.A. Snay, DYNAP: Software for estimating crustal deformation from geodetic data, *Tectonophysics, 162*, 331–343, 1989.

Dziewonski, A.M., G. Ekström, J. H. Woodhouse, and G. Zwart, Centroid-moment tensor solutions for October–December 1987, *Phys. Earth Planet. Inter., 54*, 10–21, 1989.

Elders, W.A., R.W. Rex, T. Meidav, P.T. Robinson, and S. Biehler, Crustal spreading in southern California, *Science, 178*, 15–24, 1972.

Frankel, A., and L. Wennerberg, Rupture process of the M_S 6.6 Superstition Hills earthquake determined from strong-motion recordings: Application of tomographic source inversion, *Bull. Seismol. Soc. Am., 79*, 515–541, 1989.

Fuis, G.S., W.D. Mooney, J.H. Healey, G.A. McMechan, and W.J. Lutter, Crustal structure of the Imperial Valley region, *U.S. Geol. Surv. Prof. Pap., 1254*, 25–50, 1982.

Given, D.D., and W.D. Stuart, A fault interaction model for triggering of the Superstition Hills earthquake of November 24, 1987 (abstract), *Seismol. Res. Lett., 59*, 48, 1988.

Harris, R.A., and P. Segall, Detection of a locked zone at depth on the Parkfield segment of the San Andreas fault, *J. Geophys. Res., 92*, 7945–7962, 1987.

Hudnut, K., and M. Clark, New slip along parts of the 1968 Coyote Creek fault rupture, California, *Bull. Seismol. Soc. Am., 79*, 451–465, 1989.

Hudnut, K.W., L. Seeber, T. Rockwell, J. Goddmacher, R. Klinger, S. Lindvall, and R. McElwain, Surface ruptures on cross-faults in the 24 November 1987 Superstition Hills, California, earthquake sequence, *Bull. Seismol. Soc. Am., 79*, 282–296, 1989*a*.

Hudnut, K.W., L. Seeber, and J. Pacheco, Cross-fault triggering in the November 1987 Superstition Hills earthquake sequence, southern California, *Geophys. Res. Lett., 16*, 199–202, 1989*b*.

Hwang, L.J., H. Magistrale, and H. Kanamori, Teleseismic source parameters and rupture characteristics of the 24 November 1987, Superstition Hills earthquake, *Bull. Seismol. Soc. Am., 80*, 43–56, 1990.

Ingle, J.C., Paleobathymetric history of Neogene marine sediments, northern Gulf of California, in *Guidebook to the Geology of Peninsular California*, pp. 121–138, AAPG-SEPM-SEG, Pacific Sections, Stanford Univ., Stanford, CA, 1974.

Iwasaki, T., and R. Sato, Strain field in a semi-infinite medium due to an inclined rectangular fault, *J. Phys. Earth, 27*, 285–314, 1979.

Jackson, D.D., Interpretation of inaccurate, insufficient and inconsistent data, *Geophys. J. R. astr. Soc., 28*, 97–107, 1972.

Johnson, C.E., and D.P. Hill, Seismicity of the Imperial Valley, *U.S. Geol. Surv. Prof. Pap., 1254*, 14–24, 1982.

Johnson, C.E., and L.K. Hutton, Aftershocks and preearthquake seismicity, *U.S. Geol. Surv. Prof. Pap., 1254*, 59–76, 1982.

Johnson, C.E., and L.K. Hutton, Tectonic implications of the November 24, 1987, Superstition Hills earthquakes, Imperial Valley, CA (abstract), *Seismol. Res. Lett., 59*, 48, 1988.

King, R.W., E.G. Masters, C. Rizos, A. Stolz, and J. Collins, Surveying with GPS, Monogr. 9, 128 pp., Sch. of Surv., The Univ. of New South Wales, Kensington, Australia, 1985.

Lanczos, C., *Linear Differential Operators*, D. Van Nostrand, New York, 1961.

Larsen, S.C., Geodetic measurement of deformation in southern California, Ph.D. thesis, 351 pp., Calif. Inst. of Technol., Pasadena, 1991.

Larsen, S.C. and R.E. Reilinger, GPS measurements of strain accumulation across the Imperial Valley, California: 1986–1989, *J. Geophys. Res.*. in press, 1992.

Larson, P.A., H.W. Menard, and S.M. Smith, Gulf of California: A result of ocean-floor spreading and transform faulting, *Science, 161*, 781–784, 1968.

Lichten, S.M., and J.S. Border, Strategies for high-precision Global Positioning Systems orbit determination, *J. Geophys. Res., 92*, 12,751–12,762, 1987.

Lisowski, M., and J.C. Savage, Deformation associated with the Superstition Hills, California, earthquakes of November 1987 (abstract), *Seismol. Res. Lett., 59*, 35, 1988.

Lisowski, M., J.C. Savage, and W.H. Prescott, The velocity field along the San Andreas fault in central and southern California, *J. Geophys. Res., 96*, 8369–8389, 1991.

Lomnitz, C., F. Mooser, C.R. Allen, J.N. Brune, and W. Thatcher, Seismicity and tectonics of northern Gulf of California region, Mexico: Preliminary results, *Geofis. Int., 10*, 34–48, 1970.

Magistrale, H., L. Jones, and H. Kanamori, The Superstition Hills, California, earthquakes of 24 November, 1987, *Bull. Seismol. Soc. Am., 79*, 239–251, 1989.

Mandl, G., and R. Fernandez-Luque, Fully developed plastic shear flow of granular materials, *Geotechnique, 20*, 277–307, 1970.

Mansinha, L., and D.E. Smylie, Effect of earthquakes on the Chandler wobble and the secular polar shift, *J. Geophys. Res., 72*, 4731–4743, 1967.

Mansinha, L., and D.E. Smylie, The displacement fields of inclined faults, *Bull. Seismol. Soc. Am., 61*, 1433–1440, 1971.

McGill, S.F., C.R. Allen, K.W. Hudnut, D.C. Johnson, W.F. Miller, and K.E. Sieh, Slip on the Superstition Hills fault and on nearby faults associated with the 24 November 1987 Elmore Desert Ranch and Superstition Hills earthquakes, southern California, *Bull. Seismol. Soc. Am., 79*, 362–375, 1989.

Menke, W., *Geophysical Data Analysis: Discrete Inverse Theory*, Academic, San Diego, Calif., 1984.

Moore, D.G., and E.C. Buffington, Transform faulting and growth of the Gulf of California since late Pliocene, *Science, 161*, 1238–1241, 1968.

Neumann, F., United States earthquakes, 1940, in *U.S. Coast and Geod. Surv. Ser., 647*, 74 pp., Washington, DC, 1942.

Okada, Y., Surface deformation due to shear and tensile faults in a half-space, *Bull. Seismol. Soc. Am., 75*, 1135–1143, 1985.

Prescott, W.H., The determination of displacement fields from geodetic data along a strike slip fault, *J. Geophys. Res., 86*, 6067–6072, 1981.

Prescott, W.H., J.C. Savage, and M. Lisowski, Crustal strain, in National Earthquake Hazards Reduction Program, Summaries of Technical Reports, *U.S. Geol. Surv. Open File Rep., 87-374*, 272–280, 1987*a*.

Prescott, W.H., M. Lisowski, and J.C. Savage, Velocity field along the San Andreas fault in southern California (abstract), *Eos Trans. AGU, 68*, 1506, 1987*b*.

Reilinger, R.E., and S.C. Larsen, Vertical crustal deformation associated with the 1979 $M = 6.6$ Imperial Valley, California earthquake: Implications for fault behavior, *J. Geophys. Res., 91*, 14,044–14,056, 1986.

Rocken, C., The global positioning system: A new tool for tectonic studies, Ph.D. thesis, 365 pp., Univ. of Colo., Boulder, 1988.

Saastamoinen, J., Contributions to the theory of atmospheric refraction, *Geodesy, 107*, 13–34, 1973.

Savage, J.C., Effect of crustal layering upon dislocation modeling, *J. Geophys. Res., 92*, 10,595–10,600, 1987.

Savage, J.C., and L.M. Hastie, Surface deformation associated with dip-slip faulting, *J. Geophys. Res., 71*, 4897–4904, 1966.

Savage, J.C., W.H. Prescott, and G. Gu, Strain accumulation in southern California, 1973-1984, *J. Geophys. Res., 91*, 7455–7473, 1986.

Segall, P., and R. Harris, Earthquake deformation cycle on the San Andreas fault near Parkfield, California, *J. Geophys. Res., 92*, 10,511–10,525, 1987.

Sipkin, S.A., Moment-tensor solutions for the 24 November 1987 Superstition Hills, California, earthquake, *Bull. Seismol. Soc. Am., 79*, 493–499, 1989.

Snay, R.A., Enhancing the geodetic resolution of fault slip by introducing prior information, *Manuscr. Geod., 14*, 391–403, 1989.

Snay, R.A., and A.R. Drew, Supplementing geodetic data with prior information for crustal deformation in the Imperial Valley, California, 30 pp., Tech. Rep. Ser., Univ. of Stuttgart, 1988.

Steketee, J.A., On Volterra's dislocations in a semi-infinite medium, *Can. J. Phys., 36*, 192–205, 1958.

Toppozada, T.R., D.L. Parke, and C.T. Higgins, Seismicity of California 1900–1931, in *Calif. Div. of Mines and Geol. Spec. Rep., 135*, 39 pp., Sacramento, CA, 1978.

U.S. Geological Survey The Imperial Valley, California, earthquake of October 15, 1979, in *U.S. Geol. Surv. Prof. Pap., 1254*, 451 pp., Washington, DC, 1982.

Wald, D.J., D.V. Helmberger, and S.H. Hartzell, Rupture process of the 1987 Superstition Hills earthquake from the inversion of strong motion data, *Bull. Seismol. Soc. Am., 80*, 1079–1098, 1990.

Ward, S.N., Pacific-North America plate motions: New results from very long baseline interferometry, *J. Geophys. Res., 95*, 21,965–21,981, 1990.

Ward, S.N., and S.E. Barrientos, An inversion for slip distribution and fault shape from geodetic data observations of the 1983, Borah Peak, Idaho, earthquake, *J. Geophys. Res., 91*, 4909–4919, 1986.

Wells, D., N. Beck, D. Delikaraoglou, A. Kleusberg, E.J. Krakiwsky, G. Lachapelle, R.B. Langley, M. Nakiboglu, K. Schwarz, J.M. Tranquilla, and P. Vanicek, *Guide to GPS Positioning*, Canadian GPS Associates, Fredericton, N. B., Canada, 1987.

Williams, P.L., and H.W. Magistrale, Slip along the Superstition Hills fault associated with the 24 November 1987 Superstition Hills, California, earthquake, *Bull. Seismol. Soc. Am., 79*, 390–410, 1989.

S. Larsen, Science Software Division, L-279, Lawrence Livermore National Laboratory, Livermore, CA 94550.

H. Neugebauer and W. Strange, National Geodetic Survey, NOAA, Rockville, MD 20852.

R. Reilinger, Earth Resources Laboratory, Massachusetts Institute of Technology, Cambridge, MA 01239.

(Received January 25, 1991;
revised January 13, 1992;
accepted January 14, 1992.)

APPENDIX 2

Global Positioning System measurements of strain accumulation across the Imperial Valley, California: 1986-1989

by S. Larsen and R. Reilinger

Published in *J. Geophys. Res.*, *97*, 8865-8876, 1992.

JOURNAL OF GEOPHYSICAL RESEARCH, VOL. 97, NO. B6, PAGES 8865–8876, JUNE 10, 1992

Global Positioning System Measurements of Strain Accumulation Across the Imperial Valley, California: 1986–1989

SHAWN LARSEN[1]

Seismological Laboratory, California Institute of Technology, Pasadena

ROBERT REILINGER

Earth Resources Laboratory, Massachusetts Institute of Technology, Cambridge

Global Positioning System (GPS) data collected in southern California from 1986 to 1989 indicate considerable strain accumulation across the Imperial Valley. Displacements are computed at 29 stations in and near the valley from 1986 to 1988, and at 11 sites from 1988 to 1989. The earlier measurements indicate 5.9 ± 1.0 cm/yr right-lateral differential velocity across the valley, although the data are heavily influenced by the 1987 Superstition Hills earthquake sequence. The 1988–1989 GPS displacements are best modeled by 5.2 ± 0.9 cm/yr of valley crossing deformation, but rates calculated from 15 years of terrestrial geodetic measurements (3.7 ± 0.1 cm/yr) fit the data nearly as well. The relatively high GPS rates are suspect because some measurements, especially the east-trending displacements, have large errors. There is evidence from GPS and very long baseline interferometry observations that the present strain rate along the southern San Andreas fault is smaller than the long-term geologic estimate, suggesting a lower earthquake potential than is currently assumed. Correspondingly, a higher earthquake potential is suggested for the San Jacinto fault.

INTRODUCTION

The Global Positioning System (GPS) is rapidly becoming one of the most important tools to study tectonic deformation. Signals from Earth-orbiting Navigation Satellite Time And Ranging (NAVSTAR) satellites are inverted to obtain three-dimensional coordinates of geodetic monuments with high precision. For crustal deformation studies, the relative position (or baseline) between stations is often measured. Under optimal conditions, the typical accuracy for a 50-km baseline is about 1 cm in the horizontal and 3 cm in the vertical [e.g., *Davis et al.*, 1989]. The accuracy is significantly degraded under poor observing conditions. GPS measurements can be used to monitor the secular deformation associated with plate motion, or to record the rapid strain fluctuations due to seismic and volcanic activity. GPS technology is ideally suited for crustal motion research since, unlike conventional geodesy, intersite visibility is not required, stations can be separated by long distances (> 100 km), and it is possible to measure three-dimensional deformation.

A prime location for GPS studies is the Imperial Valley of southernmost California (Figure 1). The valley is one of the most tectonically active regions in the state and has been the site of several large earthquakes. GPS monitoring was initiated in the Imperial Valley in 1986 with resurveys in 1988 and 1989. GPS station displacements from 1986 to 1988 have been discussed by *Larsen et al.* [1992]. These measurements illustrate the effect of the 1987 Superstition Hills earthquake sequence. In the present study we incorporate the 1989 GPS observations. Significant station displacements are observed across the Imperial Valley between 1986 and 1989. These movements are attributed in part to the relative motion between the North American and Pacific plates.

SEISMICITY AND TECTONICS

The Imperial Valley (Figure 1) is a complex transition zone between crustal spreading in the Gulf of California and right-lateral transform motion along the San Andreas fault [*Lomnitz et al.*, 1970; *Elders et al.*, 1972]. The valley is 4–12 million years old and is filled by up to 15 km of late Cenozoic sediments [*Larson et al.*, 1968; *Moore and Buffington*, 1968; *Ingle*, 1974; *Fuis et al.*, 1982]. The structural axis of the valley and its major fault systems trend to the northwest, roughly parallel to the Pacific-North American plate motion. A significant fraction of the relative plate displacement may be accommodated across the valley.

The Imperial Valley is one of the most seismically active regions of California with much of the activity occurring along the Imperial fault and in the Brawley Seismic Zone [*Johnson and Hill*, 1982]. Several large earthquakes have occurred in and near the Imperial Valley since 1940. The Imperial fault ruptured with a M_S 7.1 event in 1940 and a M_L 6.6 event in 1979 [*U.S. Geological Survey*, 1982]. Segments of the San Jacinto fault system broke with a M_L 6.2 earthquake in 1954 and a M_L 6.5 event in 1968 (Borrego Mountain). The most GPS relevant episode of seismic activity occurred recently along the Superstition Hills segment of the San Jacinto fault system [e.g., *Magistrale et al.*, 1989]. On November 24, 1987, a moderate (M_S 6.2) earthquake occurred along a northeast-trending seismic lineament; 12 hours later a larger event (M_S 6.6) occurred along the northwest-trending Superstition Hills fault. What makes this earthquake sequence so significant from a GPS standpoint, is that it occurred within a preexisting GPS network.

[1]Now at Scientific Software Division, Lawrence Livermore National Laboratory, Livermore, California.

Paper number 92JB00428.
0148-0227/92/92JB-00428$5.00

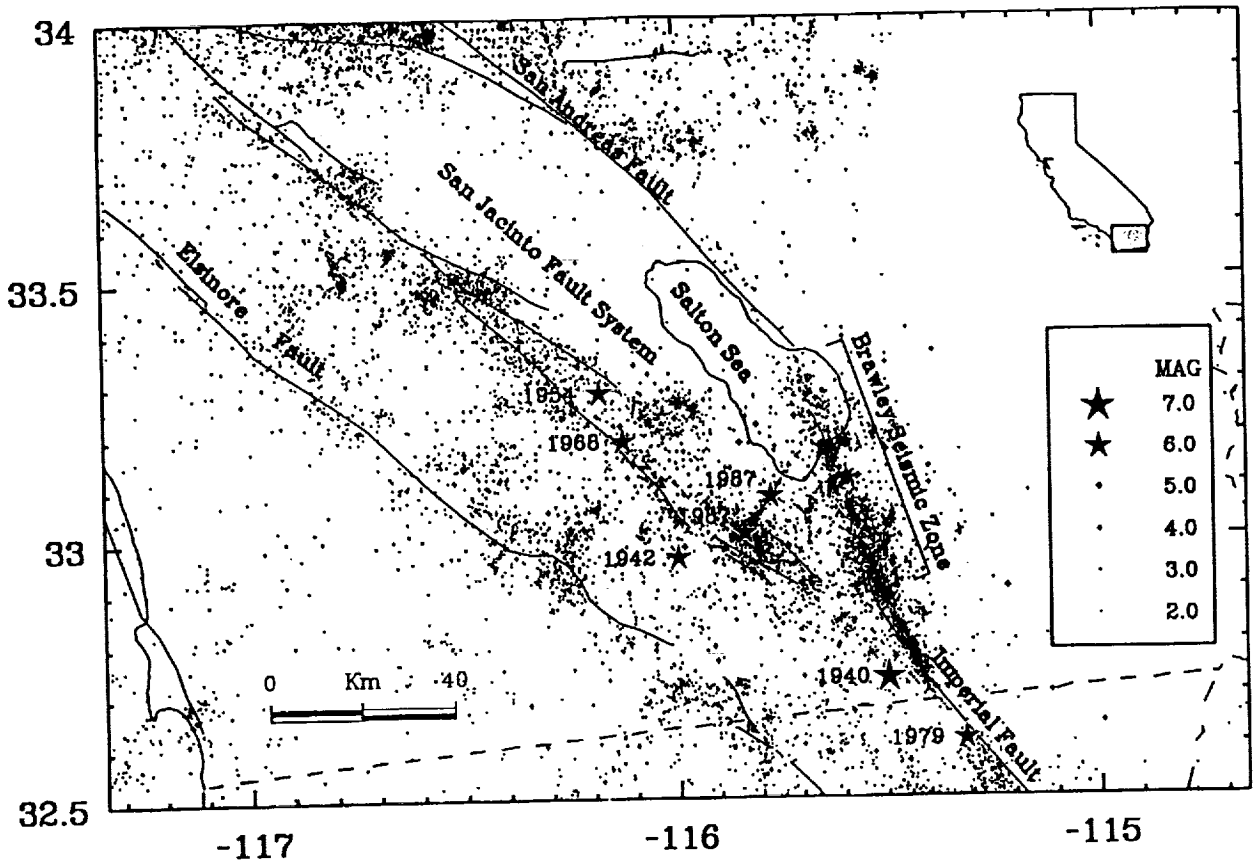

Fig. 1. Major faults and seismicity from 1932 to 1990 (Caltech Catalog) in the Imperial Valley. Large earthquakes are shown as stars. The Brawley Seismic Zone is the region of anomalously high activity between the Imperial and San Andreas faults. Major earthquakes include the 1940 and 1979 events along the Imperial fault, the 1954 and 1968 events along the San Jacinto fault, and the 1987 Superstition Hills earthquake sequence along the Superstition Hills and Elmore Ranch faults.

Conventional geodetic measurements indicate significant displacement across the Imperial Valley, which is inferred to represent interplate deformation. Triangulation data averaged between 1941 and 1986 suggest 4.3 cm/yr right-lateral movement oriented N40°W across the valley [*Snay and Drew*, 1988]. The observed deformation is time dependent, with rates of 6.1, 2.1, and 4.5 cm/yr for the intervals 1941–1954, 1954–1967, and 1967–1979, respectively. The high velocity for the earliest period supports the hypothesis of northwestward strain migration following the 1940 earthquake [*Thatcher*, 1979; *Reilinger*, 1984]. Furthermore, the computed station displacements indicate that north of the Imperial fault, interplate deformation is distributed over a zone at least 50 km wide, whereas to the south, interplate deformation is concentrated within a 20-km-wide band centered along the Imperial fault. Trilateration measurements made by the U.S. Geological Survey from 1973 to 1989 indicate 3.7 ± 0.1 cm/yr right-lateral displacement between stations on opposite sides of the Imperial Valley [*Lisowski et al.*, 1991]. These differential movements are oriented approximately N40°W. No significant change in deformation is observed following the 1979 Imperial Valley earthquake [*Savage et al.*, 1986].

New global plate models (NUVEL-1) predict the Pacific-North American relative velocity averaged over the last several million years to be 4.7 cm/yr oriented N39.6°W at Imperial Valley coordinates (115.5°W, 33.0°N) [*DeMets et al.*, 1987, 1990]. Very long baseline interferometry (VLBI) observations during the 1980's suggest a similar present-day rate [e.g., *Clark et al.*, 1987; *Kroger et al.*, 1987]. The conventional geodetic data in the Imperial Valley indicate a significant fraction of this motion may be distributed along faults in this region.

GPS Observations

The data presented here were obtained in a series of GPS field campaigns in 1986, 1988, and 1989 (Table 1). In all, a total of 32 Imperial Valley stations have been occupied more than once between 1986 and 1989. Here we discuss data collection and processing methods used for each survey. The 1986 and 1988 campaigns are described in more detail by *Larsen* [1991].

The National Geodetic Survey (NGS) began GPS observations in southern California with a 54 station network in 1986; 42 stations were located in or near the Imperial Valley (Figure 2). TI-4100 GPS receivers were used for all data collection. Each of the 20 days of observation were processed independently utilizing the GPS22 software developed at the NGS, with satellite orbit parameters provided by the Naval Surface Weapons Center (NSWC). Station coordinates were obtained from the daily intersite GPS vectors by utilizing the geodetic Dynamic Adjustment Program (DYNAP) [*Drew and Snay*, 1989]. This was one of the first GPS networks established to investigate crustal motion. GPS surveying at this time was still at an "experimental stage." The data collection methods used during 1986 were not suitable

TABLE 1. Reoccupied Stations (1986–1989)

Station Name	Abbreviation	Occupation			
		1986	1988*	1988†	1989
Acute 1934	ACUT	•	•	•	
Alamo	ALAM	•	•	•	•
Black Butte NCMN 1982	BLAC	•	•		•
Brawley 2 rm 5	BRAW	•		•	
Calexico 1954	CALE	•	•		
Calipatria 2	CALI	•			•
Coach	COAC	•	•		
College 1967	COLL	•	•		•
El Centro 2 1959	ELEC	•		•	
Frink 1934	FRIN	•	•	•	•
GLO Corner 1934	GLOC	•	•		
Hamar 2 1967	HAMA	•	•	•	
Holt 1924	HOLT	•		•	
Holtville (Alt) 1934	HLTV	•		•	
Imp 1934	IMPI	•		•	
Imperial 1934	IMPE	•		•	
Junction	JUNC	•		•	•
Kane 1939	KANE	•	•	•	•
L 589 1967	L589	•	•	•	•
Mack 2 1967 bm reset	MACK	•		•	
Mello 3 1967	MELL	•		•	
Monument Peak NCMN 1983	MONU	•			•
Ocotillo NCMN 1982	OCOT	•	•	•	•
Ocotillo 1935	OCTI	•	•	•	•
Offset 217	O217	•	•	•	
Offset 224	O224	•		•	
Offset 227	O227	•		•	
Orient 1939	ORIE	•	•		•
Pinyon Flat	PINY	•		•	
Sandy Beach	SAN1		•		•
T 1226	T122	•		•	
Tamarisk 3 1967	TAMA	•	•		

*Universities.
†NGS.

for obtaining the highest accuracy solutions. In addition, due to a variety of equipment and logistical problems, a significant amount of data was lost. Because of these unfortunate circumstances, the quality of the 1986 data is fairly poor. The positional uncertainties for the 1986 survey are suggested to be approximately 1 ppm (parts per million). This is equivalent to a 5 cm error for a 50-km baseline.

During late February and early March 1988, university GPS crews with assistance from the University Navstar Consortium (UNAVCO) occupied 19 sites in the Imperial Valley, including 15 marks observed in 1986 (Figure 2). The NGS returned to the Imperial Valley the following month and reoccupied 21 of the previously established monuments. TI-4100 receivers were used for all measurements. Data from both surveys were processed independently with the Bernese GPS software package from the University of Bern in Switzerland. For each campaign, the data were combined into one multiday solution. The Cartesian coordinate differences from the university and NGS surveys were adjusted by least squares to obtain station positions for 1988. Satellite orbit parameters were improved with the aid of fiducial observations from Mojave (California), Westford (Massachusetts), and Richmond (Florida), made as part of the Cooperative International GPS Network (CIGNET) [*Chin*, 1988]. The horizontal precision for intersite vectors when orbit improvement techniques are used is about 0.03 ppm [e.g., *Davis et al.*, 1989; *Dong and Bock*, 1989]. This is equivalent to subcentimeter level uncertainty for line lengths less than a few hundred kilometers.

During March 1989, university groups occupied 28 geodetic marks in the vicinity of the Imperial Valley, 19 of which were previously surveyed in 1986 or 1988 (Figure 3). Several new marks were established north of the Salton Sea in the Coachella Valley. While most data were collected with TI-4100 GPS instruments, this campaign differed from previous surveys in that Trimble-4000SD receivers were used at some sites. The field experiment was conducted at a time of anomalously high solar flare activity which created large ionospheric disturbances [*Jackson et al.*, 1989]. The ionosphere creates a frequency dependent delay for the GPS multisignal structure, composed of two carrier phase transmissions at 1575.42 MHz (L1) and 1227.60 MHz (L2) [e.g., *King et al.*, 1985]. For dual-frequency observations (L1 and L2), the ionospheric contribution (error) is removed by an appropriate combination of the two phase observables. However, if only single-frequency measurements are available (either intentionally or due to poor observing conditions), the positioning accuracy of all but the shortest baselines will be seriously degraded. The 1989 phase observations contained a disproportionate number of cycle slips and data gaps, presumably due to the poor ionospheric conditions. The TI-4100 instruments generally collected both the L1 and L2 phase signals, so the ionospheric effect could be eliminated. The Trimble 4000SD receivers, however, experienced significant difficulty maintaining phase-lock on the L2 frequency (it is found that newer Trimble models, specifically the 4000SST, are not as susceptible to solar activity). In fact, between 30% and 60% of the L2 data (Trimble 4000SD) were lost. It is unlikely that the centimeter level accuracy required for this study could be achieved solely with the L1 frequency. Therefore, data collected with Trimble 4000SD instruments were not used, although we are currently working on schemes to utilize these measurements through ionospheric modeling constrained by the

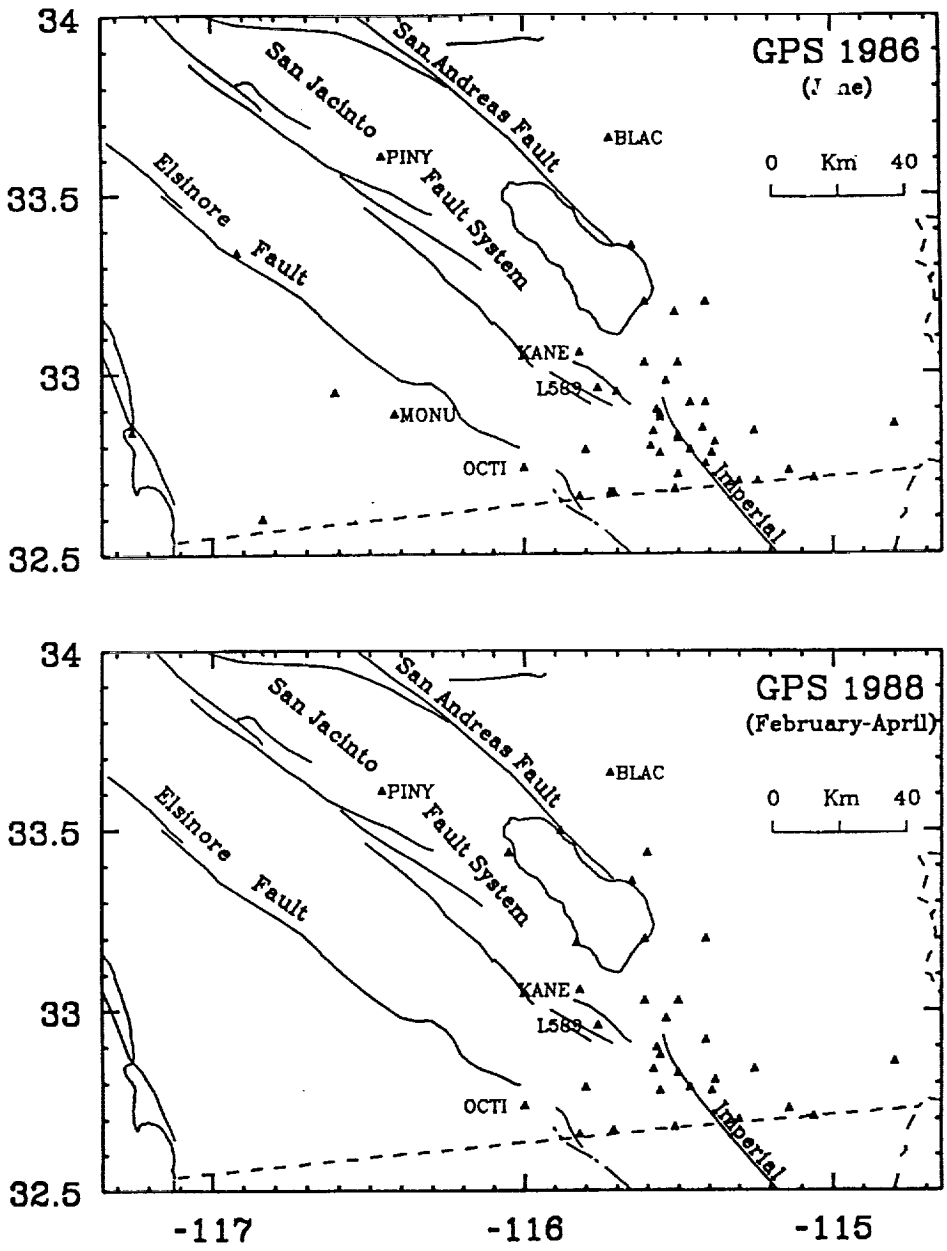

Fig. 2. GPS stations surveyed in 1986 and 1988 (see Table 1). The 1986 campaign was conducted by the National Geodetic Survey and included 42 stations in and near the Imperial Valley. The 1988 observations consisted of two campaigns, the first by university groups in February/March and the second by the National Geodetic Survey in March/April. A total of 32 stations were occupied in 1988, of which 29 were repeat measurements from 1986. Stations mentioned in text are indicated.

dual-frequency TI-4100 data. Continental fiducial phase observations from the CIGNET tracking sites were either nonexistent or of extremely poor quality, presumably due to the poor ionospheric conditions. Therefore, we were unable to apply orbit improvement techniques. A multiday solution was obtained with the Bernese software utilizing the broadcast orbits. Positioning errors with the broadcast ephemerides are believed to be 0.1–1.0 ppm.

GPS Displacements and Error Estimates

GPS displacement vectors for the intervals 1986–1988 and 1988–1989 are shown in Figures 4 and 5 and listed in Tables 2 and 3, respectively. All measurements are made relative to station OCTI. Station OCTI is selected as the reference because it is the site most distant from the 1987 Superstition Hills earthquake sequence occupied in all GPS campaigns.

Formal estimates of GPS uncertainty almost always underestimate variances derived from repeatability studies. We define more realistic errors by multiplying the formal covariance matrix calculated with the GPS solution by an estimated variance factor, which scales as the average baseline length. In general, the measurements reported here are not sufficiently redundant to develop reliable statistics. However, based on those cases where repeat measurements have been made, the errors given in this study appear to represent conservative 1-sigma estimates. For the 1986–1988 displacements, we assume a variance factor so that the average baseline error is 5 cm, or 1 ppm for a 50-km line. This relatively large uncertainty is due to the 1986 survey.

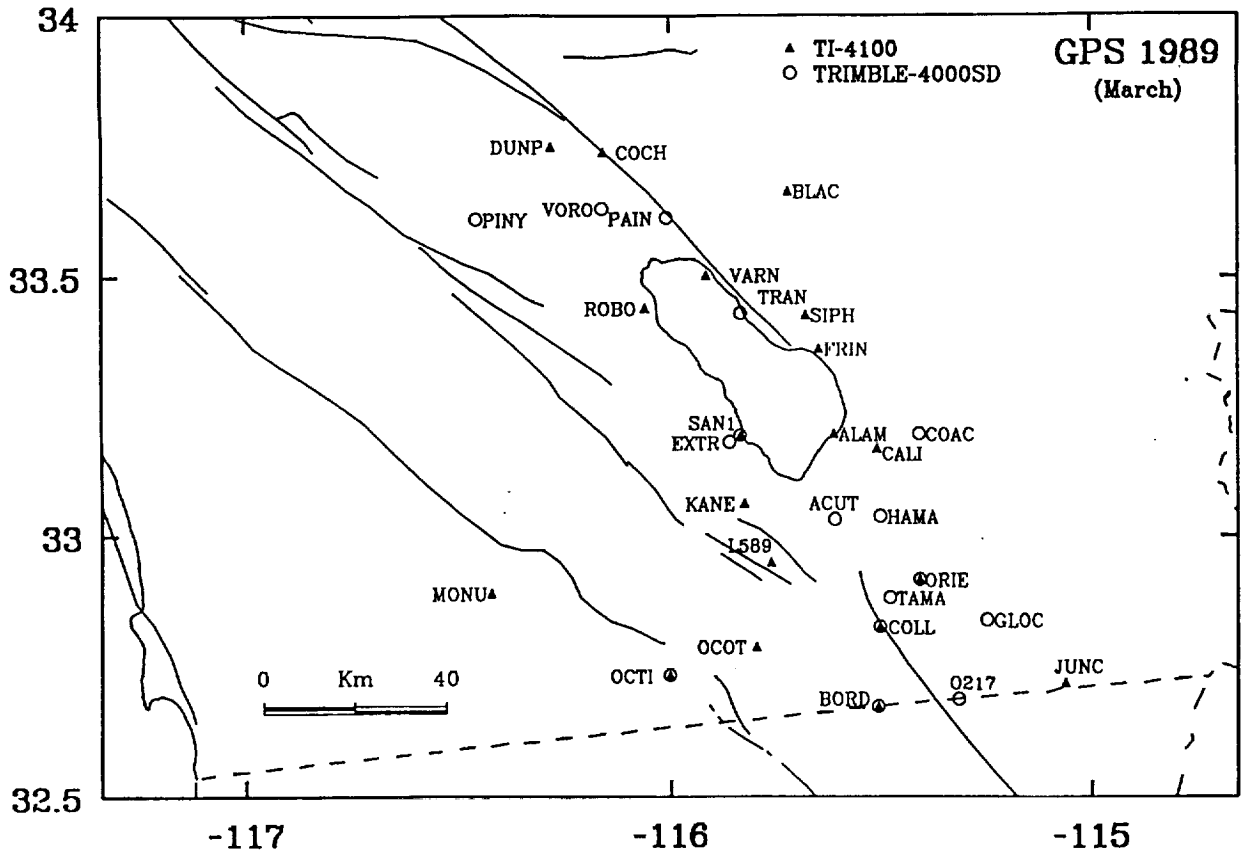

Fig. 3. Imperial Valley GPS stations surveyed in 1989 (see Table 1). TI-4100 GPS receivers (triangles) were used at most sites. Trimble 4000SD receivers (open circles) were also used. Thirty sites were occupied, 10 for the first time. Due to very poor ionospheric conditions, data collected with the Trimble 4000SD receivers are not discussed here.

For the 1988–1989 displacements, the average baseline error is assumed 2 cm, or 0.4 ppm for a 50-km line. The largest component of uncertainty is attributed to the broadcast orbits used for the 1989 solution. In a similar sized network spanning the Santa Barbara channel, S. C. Larsen et al. (Strain accumulation in the Santa Barbara channel: 1970–1988, submitted to *Journal of Geophysical Research*, 1992) found 1–3 cm discrepancies between line-lengths obtained with the broadcast ephemeris and those obtained by utilizing orbit improvement techniques. Our approach for handling uncertainties, albeit somewhat ad hoc, allows for self-consistent relative errors and illustrates the much larger uncertainties in the east-trending direction ($\sim$ 4 times larger than the north-trending errors). This effect is due to the predominantly north-south ground track of the satellite orbits, which significantly improves positional accuracy along this orientation.

Displacements for the 1986–1988 interval (Figure 4) are complicated by the 1987 Superstition Hills earthquake sequence, as well as by large measurement uncertainties. The seismic effects are clearly demonstrated in the GPS vectors; displacements at KANE and L589 approach 0.5 m. Estimates of fault rupture indicate 10 stations near the seismic rupture zone moved at least 5 cm [*Larsen et al.*, 1992]. The displacements are consistent with 130-cm right-lateral slip along the Superstition Hills fault and 30-cm left-lateral slip along the Elmore Ranch fault. Still, there is a considerable component of southeast-trending movement which cannot be explained as seismic deformation or measurement uncertainty. This is evident when the displacements are decomposed into their north- and east-trending components (Figure 6). Decomposing vector displacements into geographic components tends to separate the uncertainties, which are magnified in the longitudinal direction. Each component is plotted as the distance from OCTI on a cross-section trending N50°E, perpendicular to the North American-Pacific relative plate motion (N40°W). Simple dislocation theory [e.g., *Mansinha and Smylie*, 1971] is used to subtract the effect of the 1987 Superstition Hills earthquake sequence from the observed displacement field, following fault models suggested by *Larsen* [1991]. Therefore, Figure 6 represents our best estimate of the nonseismic deformation across the Imperial Valley.

The north-trending 1986–1988 movements clearly exhibit right-lateral displacement; stations to the northeast are offset to the south relative to sites on the other side of the valley. Stations displaying the largest scatter are, for the most part, those sites where the applied seismic correction is greater than 4 cm (Figure 6, open circles). This suggests fault-rupture complexities not represented by the uniform dislocation model used to remove the effects of the 1987 earthquake [*Larsen*, 1991]. The east-trending movements exhibit large scatter with no discernible trend across the valley. This is invariant of the size of the seismic displacement, so the scatter cannot be explained simply as unmodeled seismic effects. Presumably, the large deviations are due to the fairly significant east-trending errors in the 1986 data. This may explain the anomalous vector displacements observed in Figure 4, especially noticeable for those sites near the border east of the Imperial fault.

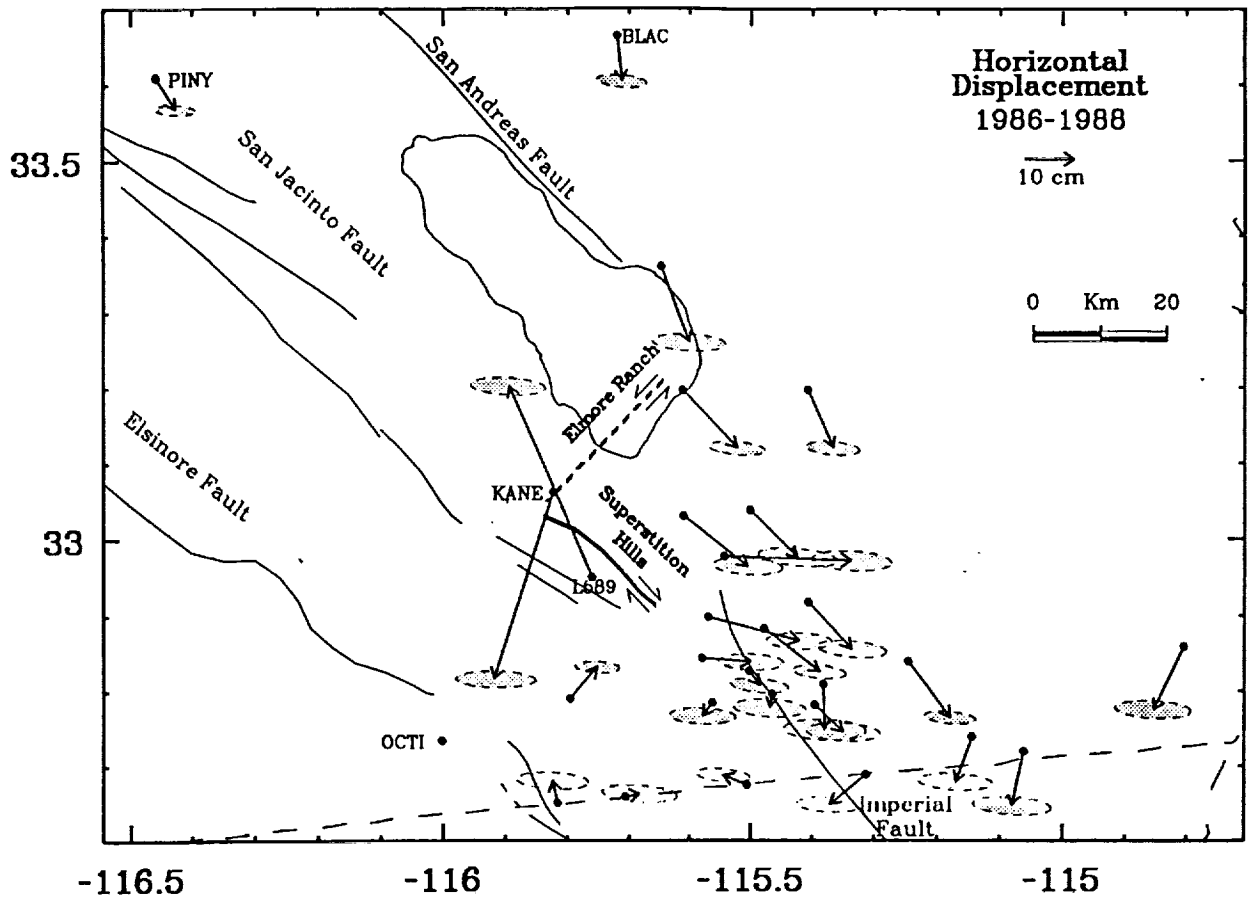

Fig. 4. GPS station displacements for the interval 1986–1988 (1.8 years). Displacements are listed in Table 2. All measurements are made relative to station OCTI. Errors are determined by multiplying the formal uncertainties from the GPS solution by a variance factor so that the average baseline error scales as 1 ppm. The east-trending uncertainties are about 4 times larger than the north-trending uncertainties. Seismically induced displacements from the 1987 Superstition Hills earthquake sequence are most apparent at stations KANE and L589. The large nonseismic displacements are assumed to represent relative motion between the Pacific and North American plates, which is concentrated across the valley.

The nonseismic north-trending GPS displacements indicate an 8.1 ± 1.3 cm offset across the Imperial Valley (Figure 6). This differential movement is calculated by linearly fitting those data furthest to the southwest and northeast. The data errors are increased by 0.33 times the estimated seismic displacements, giving less weight to those stations most affected by the 1987 earthquakes. The east-trending components are not used due to the large data scatter. The 8.1 cm offset is assumed to represent plate-boundary deformation. If we assume a uniform velocity field parallel to the direction of plate motion (N40°W), the observed north-trending offset is equivalent to 5.9 ± 1.0 cm/yr right-lateral movement across the GPS network.

The 1988–1989 station displacements clearly demonstrate right-lateral southeast-trending movement across the Imperial Valley (Figure 5), in spite of the short period between surveys (1 year). Stations furthest to the northeast are displaced approximately 5 cm to the southeast relative to sites on the other side of the valley. The observed motion at some sites (e.g., BLAC) may be attributed to the larger east-trending uncertainties. The 1988–1989 displacements are also decomposed into their north- and east-trending components (Figure 7). Right-lateral differential movement across the GPS network is indicated in both components.

The north-trending offset observed between 1988 and 1989 (Figure 7) is smaller than that from 1986 to 1988 (Figure 6) because of the shorter observation period (1.0 year). However, the more recent measurements are not influenced by seismic activity and contain smaller experimental error. Since the 1988–1989 GPS station coverage is more uniformly distributed across the valley, it is difficult to constrain an absolute differential offset. Instead, the measurements are modeled assuming a semi-infinite right-lateral shear plane at depth representing the Pacific-North American plate margin (Figure 8). The plane is oriented N40°W about coordinates 32.796°N, 115.454°W, almost congruent with the Imperial fault and the axis of the Salton Trough. The upper depth is constrained at 10 km and uniform slip is assumed over the entire shear boundary. *Snay and Drew* [1988] incorporate a similar model to explain triangulation observations between 1941 and 1986, but allow additional slip along the Imperial fault necessitated by their detailed station coverage in this region. More complex models assuming distributed offset along the Imperial, San Andreas, San Jacinto, and Elsinore faults, and within the Brawley Seismic Zone, have been used to model other geodetic measurements in the valley [e.g., *Savage et al.*, 1979]. The measurements presented here are not of sufficient resolution or accuracy (due to the

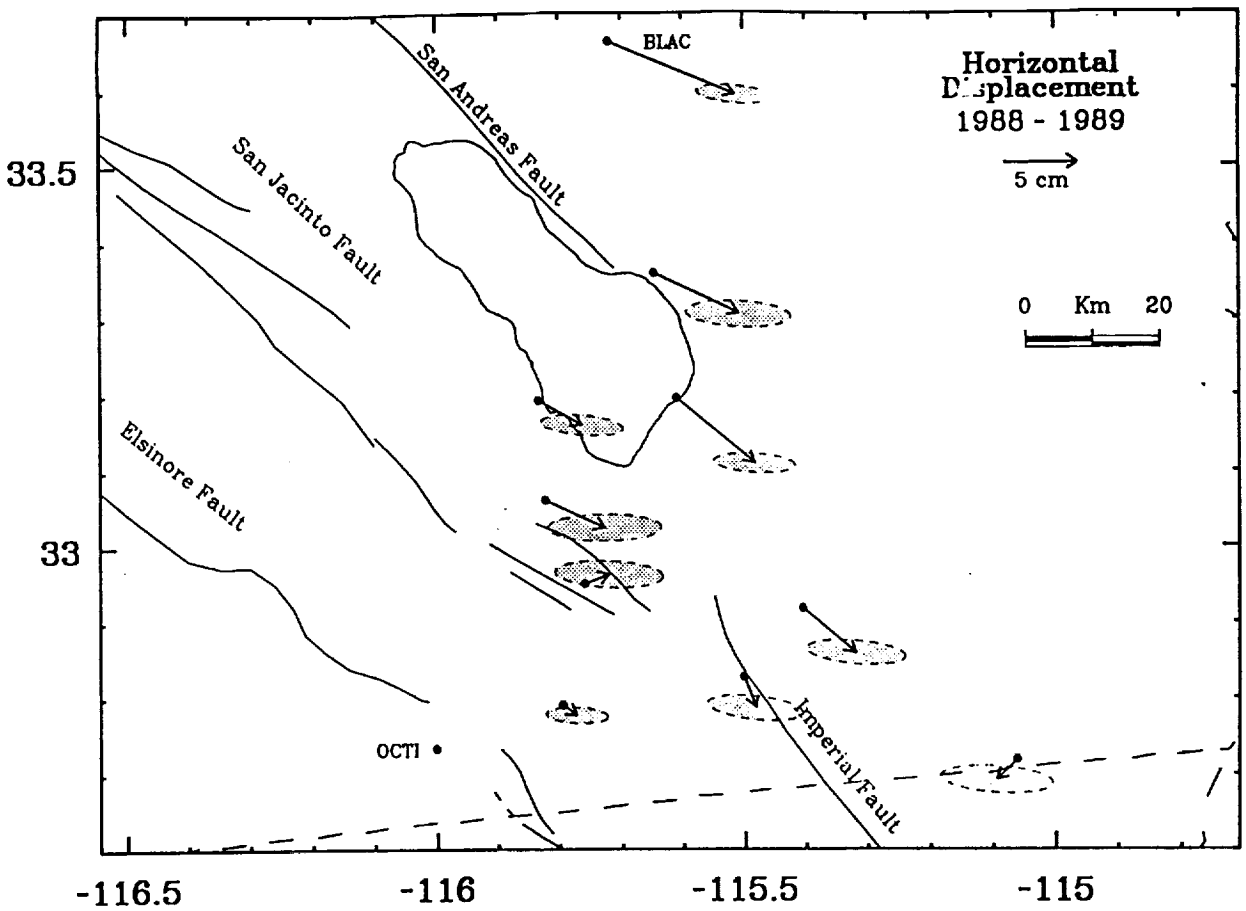

Fig. 5. GPS station displacements for the interval 1988–1989 (1.0 year). Displacements are listed in Table 3. All measurements are made relative to station OCTI. Errors are determined by multiplying the formal uncertainties from the GPS solution by a variance factor so that the average baseline error scales as 0.5 ppm. Stations to the northeast moved about 5 cm southwest relative to stations on the other side of the valley.

TABLE 2. Station Displacements 1986–1988

Station	N, cm	σ_N	E, cm	σ_E
OCTI	0.0	0.0	0.0	0.0
L589	38.1	1.7	−17.2	7.6
KANE	−37.2	1.7	−11.7	8.1
OCOT	6.4	1.1	5.6	4.6
COAC	−11.7	1.3	5.1	5.5
ALAM	−11.7	1.3	11.2	5.8
GLOC	−11.3	1.2	8.5	5.2
BLAC	−9.0	1.2	1.0	5.2
ORIE	−9.2	1.6	8.9	7.3
FRIN	−15.3	1.7	5.8	7.6
CALE	2.0	1.3	−4.9	5.6
TAMA	−8.6	1.3	11.4	5.5
O217	−6.0	1.6	−7.3	6.8
COLL	−3.0	1.4	2.2	6.0
HAMA	−9.3	1.7	9.8	8.2
PINY	−6.2	1.0	4.0	4.1
BRAW	−0.9	1.9	26.2	8.1
HOLT	−5.4	1.8	5.9	7.5
MELL	−2.8	1.8	−0.5	7.5
IMPE	−0.7	1.6	10.1	6.7
IMPI	−4.8	1.6	18.9	6.7
ACUT	−9.9	1.6	13.2	7.2
ELEC	−2.7	1.6	−2.1	6.9
HLTV	−9.0	2.1	0.3	8.4
MACK	−9.1	1.7	−3.4	7.5
O227	4.4	1.7	−0.9	7.4
T122	−12.6	1.8	−6.3	7.8
JUNC	−11.0	1.8	−2.3	7.9
O224	0.6	1.7	3.0	7.9

TABLE 3. Station Displacements 1988–1989

Station	N, cm	σ_N	E, cm	σ_E
OCTI	0.0	0.0	0.0	0.0
OCOT	−0.6	0.5	0.9	2.1
SAN1	−1.6	0.6	3.0	2.8
L589	0.6	0.9	1.7	3.7
BLAC	−3.5	0.6	8.7	2.6
ALAM	−4.4	0.6	5.4	2.8
ORIE	−2.9	0.8	3.6	3.4
FRIN	−2.7	0.8	5.8	3.6
KANE	−1.8	0.9	4.0	3.9
COLL	−2.0	0.8	0.8	3.3
JUNC	−1.3	0.9	−1.4	3.7

short time coverage) to warrant such detail. The 1988–1989 GPS displacement vectors are best constrained by 5.2 ± 0.9 cm/yr plate-boundary deformation. The best fit solution to the observed GPS movements is shown in Figure 7. Additional solutions obtained by varying the depth to the upper boundary of the shear plane between 5 and 15 km suggest displacement rates from 4.4 (5 km) to 6.0 cm/yr (15 km); the minimum residual solution is obtained at 10-km depth (5.2 cm/yr).

Discussion

Deformation Across Valley

The 1986–1988 measurements are concentrated along the Imperial fault (Figure 4). The nonseismic displacements

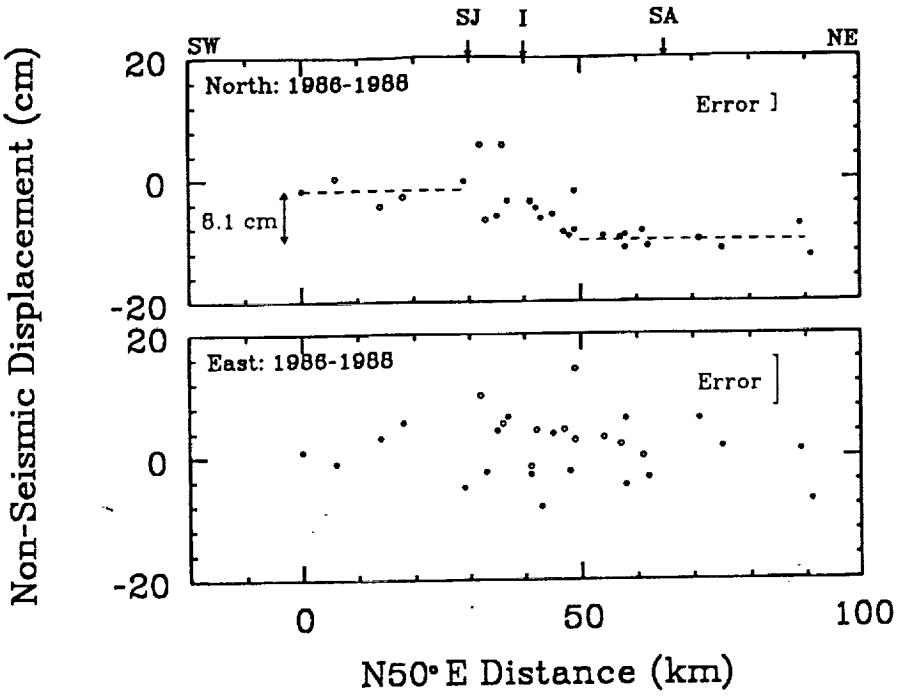

Fig. 6. The north- and east-trending displacement components for the 1986–1988 interval. All distances are relative to OCTI on a cross section trending N50°E, perpendicular to the plate motion (see Figure 8). The effect of the 1987 Superstition Hills earthquake sequence is removed. Open circles indicate stations where the seismic correction is greater than 4 cm. The north-trending offset between stations on opposite sides of the valley is 8.1 cm. The large scatter for the east-trending components is presumably due to errors in the 1986 survey. The average uncertainty for each displacement component is shown.

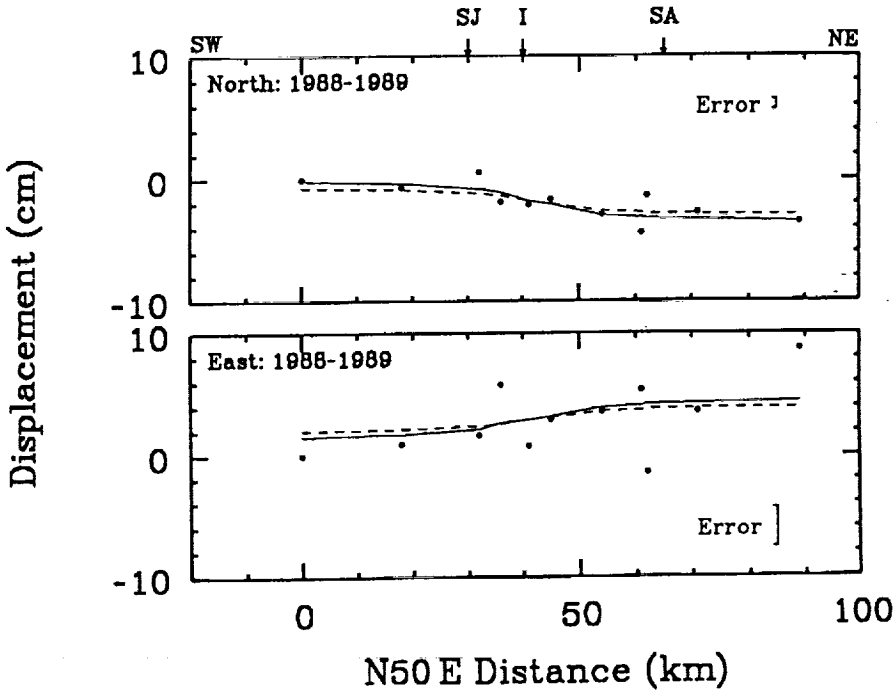

Fig. 7. The north- and east-trending displacement components for the 1988–1989 interval. All distances are relative to OCTI on a cross section trending N50°E, perpendicular to the plate motion direction. The data are best fit by 5.2 cm/yr displacement across the valley (solid line), although a rate of 3.7 cm/yr fit the data nearly as well (dashed line). The average uncertainty for each displacement component is shown.

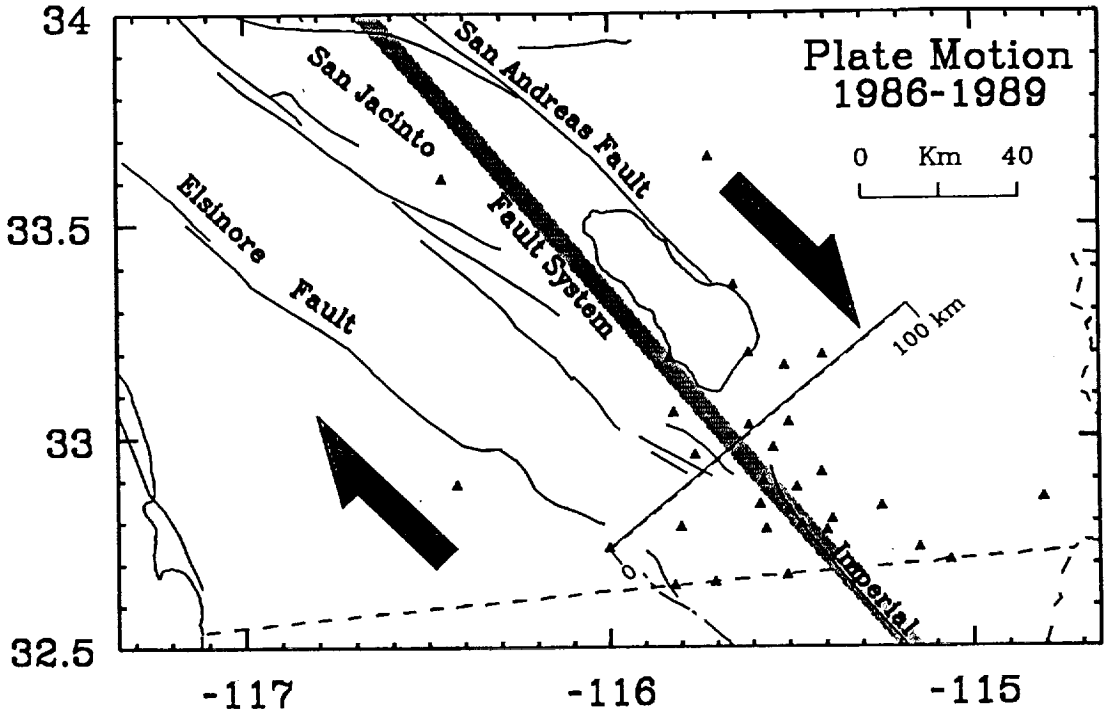

Fig. 8. Shear plane (10-km depth) used to model the 1988–1989 displacements (shaded band); cross section used in Figures 6 and 7; and stations surveyed at least twice between 1986 and 1989. Considerable strain is observed across the GPS network, which is attributed to plate-boundary deformation between the North American and Pacific plates.

TABLE 4. Displacement Rates

Method	Region	Interval	Rate, cm/yr	Reference
GPS	Imperial Valley	1986–1988	5.9 ± 1.0	This study
		1988–1989	5.2 ± 0.9	
Triangulation	Imperial Valley	1941–1986	4.3	*Snay and Drew* [1988]
		1941–1954	6.1	
		1954–1967	2.1	
		1967–1986	4.5	
Trilateration	Imperial Valley	1973–1989	3.7 ± 0.1	*Lisowski et al.* [1991]
VLBI	Salton Trough	1980–1989	3.3 ± 0.1	*Ward* [1990]
	California	1980–1986	$4.0 - 4.8$	*Kroger et al.* [1987]
	Continental	1982–1987	5.1 ± 0.2	*Clark et al.* [1987]
Plate Model	Plate boundary	~ 3 m.y.	4.7 ± 0.1	*DeMets et al.* [1990]

reveal a sharp 15–20 km wide boundary between deformation on either side of the Imperial Valley (Figure 6). This suggests that strain is accommodated exclusively along the Imperial fault in the southern half of the valley. The 1988–1989 measurements are distributed more uniformly throughout the region (Figure 5), and indicate a broader strain-transition zone (Figure 7). This implies that deformation may be occurring along several structures to the north, including the San Andreas, San Jacinto, and Elsinore faults. The same pattern is observed in the conventional geodetic measurements, which indicate concentrated strain in a narrow 20-km-wide zone about the Imperial fault, and diffuse deformation of at least 50 km wide to the north [*Snay and Drew*, 1988; *Lisowski et al.*, 1991].

The GPS obtained rates of deformation across the Imperial Valley, as well as those derived through conventional geodetic techniques, are listed in Table 4. These are compared with the estimated velocity between the Pacific and North American plates (NUVEL-1), and rates derived from VLBI measurements between stations along the western coast of California and within the stable North American continent. Because the 1988–1989 GPS displacements are not affected by seismic deformation, we speculate that this interval yields a more reliable estimate of strain across the Imperial Valley than the 1986–1988 measurements. The 1988–1989 GPS deformation rate is comparable to the plate velocity, suggesting that all plate motion is concentrated across the valley with little or no deformation west of the Elsinore fault. However, this rate is influenced by relatively large measurement error. Significantly smaller rates are indicated by the terrestrial measurements, which require additional slip on faults not spanned by the networks to satisfy the plate velocity.

GPS and trilateration (EDM) provide comparable accuracies, and both are considerably more precise than triangulation. However, the EDM observations span a 15-year period, while only 3 years of GPS coverage are available. Therefore, the trilateration rate should more accurately reflect the deformation in this region, which suggests the GPS measurements overestimate the true displacement. In fact,

TABLE 5. Displacement Rates Across San Andreas Fault

Baseline	Method	Interval	North, cm/yr	East, cm/yr	Fault Parallel, cm/yr
BLAC-PINY	GPS	1986–1988	1.1 ± 0.6		1.4 ± 0.8
	VLBI*	1982–1987	1.8	−1.1	2.1
	VLBI†	1979–1988	1.5	−1.0	1.8
	VLBI‡	1982–1988	1.2	−0.9	1.5
	VLBI§	1980–1989	1.4	−1.1	1.8
BLAC-MONU	GPS	1986–1989	2.5 ± 0.5		3.2 ± 0.6
	VLBI*	1982–1987	2.3	−2.7	3.5
	VLBI†	1979–1988	2.5	−2.5	3.5
	VLBI‡	1982–1988	2.4	−1.8	3.0
	VLBI§	1980–1989	2.2	−2.5	3.3

*Clark et al. [1987].
†Ma et al. [1989].
‡Sauber [1989].
§Ward [1990].

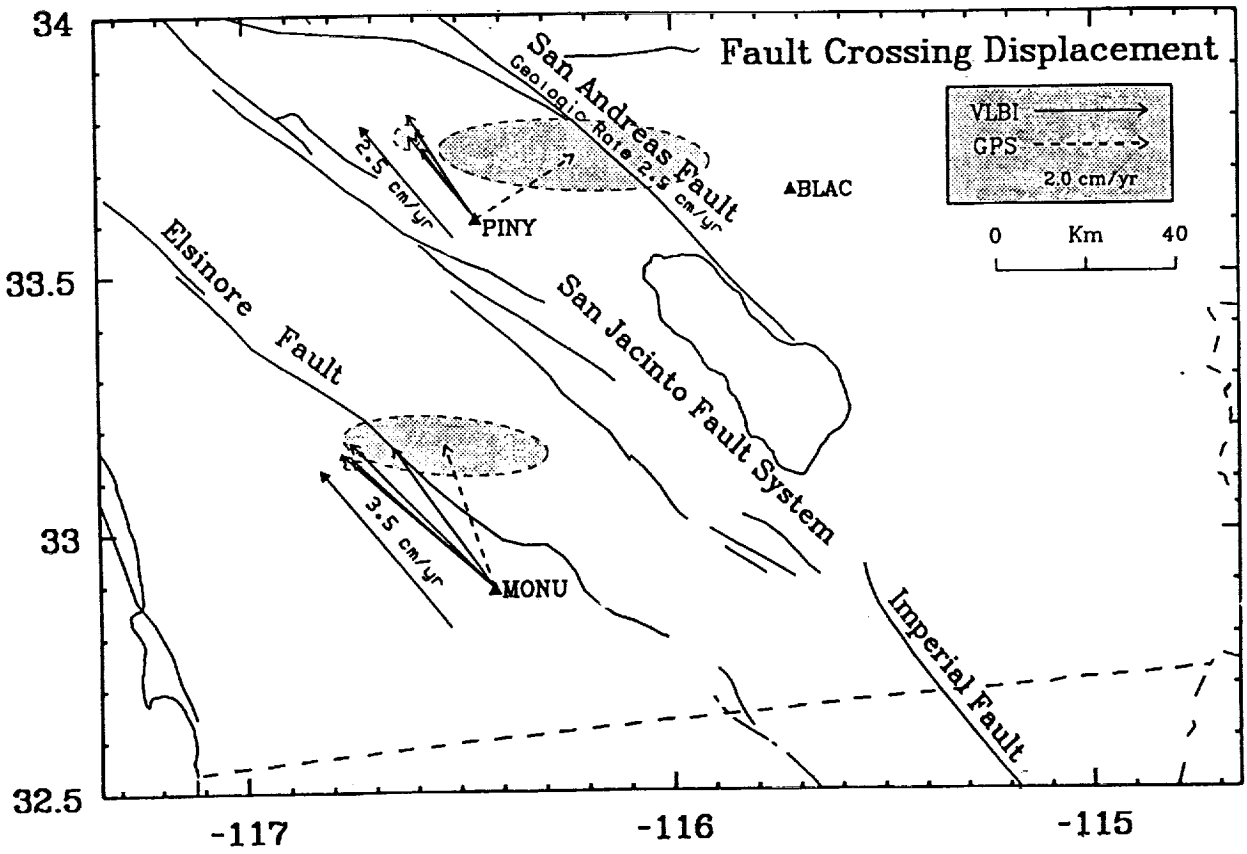

Fig. 9. VLBI (solid arrows) and GPS (dashed arrows) velocities at stations PINY and MONU relative to station BLAC (Table 5). The 3-sigma VLBI uncertainty is from *Ward* [1990]. The GPS vectors contain large east-trending uncertainties. The fault-parallel geodetic velocities across the San Andreas fault are less than geologic estimates.

a 3.7 cm/yr deformation rate fits the 1988–1989 GPS observations nearly as well (Figure 7). An alternate explanation is accelerated deformation between 1986 and 1989. The triangulation data indicate time-dependent displacements. Between 1941 and 1954 the calculated rate is significantly greater than the average between 1941 and 1986, although this is attributed to postseismic effects following the 1940 Imperial Valley earthquake. No increased rate is observed following the 1979 earthquake [*Savage et al.*, 1986]. There is marginal evidence for a regional strain fluctuation (increase) during 1978 and 1979 throughout southern California, but the nature of this apparent deformation is uncertain [*Savage et al.*, 1981, 1986]. Given the large uncertainties for the GPS estimates (~ 1 cm), it is not possible with the available data to distinguish if there has been increased deformation over the last several years.

Earthquake Potential: Imperial and Southern San Andreas Faults

The earthquake recurrence interval along the Imperial fault is estimated using the geodetically determined strain rates. The 1940 Imperial Valley earthquake ruptured the entire length of the Imperial fault. Approximately 3.0- and

4.5-m slip (coseismic plus postseismic) are estimated for the northern and southern segments of the fault, respectively [*Reilinger*, 1984]. Surface offsets were as great as 6 m south of the border with displacements tapering off rapidly to the north [*Trifunac and Brune*, 1970; *Sharp*, 1982]. Surface rupture was confined to the fault north of the border during the 1979 earthquake. Geodetic and strong ground motion modeling suggests an average slip of about 1 m along the 1979 rupture plane, with patches of higher displacement (asperities) [e.g., *Hartzell and Heaton*, 1983; *Archuleta*, 1984; *Reilinger and Larsen*, 1986].

At an observed strain rate of 4–5 cm/yr and per-event ruptures between 1 and 3 m, a 20–75 year earthquake recurrence interval is calculated for the northern Imperial fault. This assumes all strain is released during major seismic episodes. This recurrence rate is comparable to the 32-year earthquake repeat time suggested by *Sykes and Nishenko* [1984] and the $\sim$ 50-year interval predicted by *Anderson and Bodin* [1987].

The relative velocities of three Imperial Valley GPS sites are well constrained from VLBI observations since 1979 [*Clark et al.*, 1987; *Sauber et al.*, 1989; *Ma et al.*, 1989; *Ward*, 1990]. The GPS and VLBI computed deformation rates between BLAC and PINY and between BLAC and MONU are listed in Table 5 and illustrated in Figure 9. Some explanation is needed of the procedure used to determine fault parallel GPS velocities given in Table 5. Only the north-trending GPS displacement components are used because of the large east-trending errors inherent in the 1986 survey. The fault parallel velocities are then calculated assuming right-lateral displacement oriented N40°W (i.e., the measured northward displacement is presumed to be one component of the actual displacement which is oriented parallel to the fault). The VLBI measurements indicate 1.5 to 2.1 cm/yr fault-parallel (right-lateral) displacement across the San Andreas fault (BLAC-PINY) and 3.0 to 3.5 cm/yr across the Imperial Valley (BLAC-MONU). The GPS measurements indicate 1.4 ± 0.8 cm/yr displacement across the fault and 3.2 ± 0.6 cm/yr across the valley (the rate in Table 4 differs, since it represents an average over the entire network). The BLAC-MONU velocities agree with the conventional geodetic measurements of displacement across the valley (3.7 ± 0.1 cm/yr). The fault-crossing displacements (BLAC-PINY), however, are somewhat surprising, since they are less than expected based on geologic evidence. The long-term geomorphological slip rate along the southern San Andreas fault over the last 10,000–30,000 years is estimated between 2.3 and 3.5 cm/yr [*Keller et al.*, 1982; *Weldon and Sieh*, 1985], with 2.5 cm/yr a commonly accepted average [e.g., *Sieh and Williams*, 1990]. The geologic slip rate and radiocarbon dating of Holocene offsets along the fault suggest a recurrence interval of about 300 years with the last major event in 1680 [*Sieh*, 1986]. This logic leads to the conclusion that the potential for a major earthquake along the southern San Andreas fault is high. However, the geodetic evidence reported here indicates a comparatively small strain rate during the last decade. This suggests a decreased earthquake potential for the southern San Andreas fault, assuming the geodetic measurements are indicative of at least the last few hundred years. This decreased seismic potential will be observed either as a longer recurrence interval or less slip per event. The geodetic data are supported by geologic trenching studies, which suggest a decreasing slip rate along the southern San Andreas fault during the past 1000 years [*Sieh*, 1986]. If this is true, the San Jacinto fault should play a more active role in regional tectonics. In fact, the shear strain along the fault determined from EDM observations between 1973 and 1984 is nearly the same as that for networks which lie on the San Andreas fault [*Savage et al.*, 1986]. The two fault systems may alternately assume dominant roles in absorbing plate motions, as is suggested by variable Quaternary slip rates along the San Jacinto fault [*Sharp*, 1981].

CONCLUSIONS

GPS measurements from southern California indicate 5.9 ± 1.0 and 5.2 ± 0.9 cm/yr right-lateral southeast-trending displacement across the Imperial Valley for the intervals 1986–1988 and 1988–1989, respectively. These rates are significantly larger than those obtained from conventional geodetic surveys (3.7 ± 0.1 cm/yr), suggesting the GPS observations may overestimate the true deformation. The earlier measurements contain relatively large errors, and are influenced by the 1987 Superstition Hills earthquake sequence. Regardless, secular deformation is clearly observed for both intervals, and this is attributed to the relative movement between the Pacific and North American plates. There is evidence from VLBI and GPS measurements that the strain accumulation along the southernmost San Andreas fault is smaller than the long-term geologic estimate. This indicates a lower earthquake potential for this segment of the fault than is presently assumed, and suggests that the San Jacinto system plays a more dominant role for relieving strain accumulation in this region.

Acknowledgments. We thank Helen Neugebauer and Bill Strange for providing coordinate solutions from the 1986 NGS GPS survey. This research could not have taken place without the invaluable field support provided by many people. In particular, we thank John Beavan, Lewis Gilbert, Ken Hudnut, James Stowell, Michael Jackson, and Mike Bevis. Reviews by Hiroo Kanamori, Kerry Sieh, Tom Herring, William Prescott, and an anonymous reviewer substantially improved the manuscript. We thank Liz Henderson for formatting the text for *JGR*. This work is supported by U.S. Geological Survey contracts 14-08-0001-G1679, 14-08-001-G1354, and 14-08-0001-G1774, and by NASA grant NAG-5-814.

REFERENCES

Anderson, J.G., and P. Bodin, Earthquake recurrence models and historical seismicity in the Mexicali-Imperial Valley, *Bull. Seismol. Soc. Am.*, *77*, 562–578, 1987.

Archuleta, R.J., A faulting model for the 1979 Imperial Valley earthquake, *J. Geophys. Res.*, *89*, 4559–4585, 1984.

Chin, M., CIGNET report, *GPS Bull.*, Global Positioning System Subcomm. of Comm. VIII, Int. Coord. of Space Tech. for Geod. and Geodyn., Natl. Geod. Surv., Rockville, Md., 1988.

Clark, T.A., D. Gordon, W.E. Himwich, C. Ma, A. Mallama, and J.W. Ryan, Determination of relative site motions in the western United States using Mark III very long baseline interferometry, *J. Geophys. Res.*, *92*, 12,741–12,750, 1937.

Davis, J.L., W.H. Prescott, J.L. Svarc, and K.J. Wendt, Assessment of global positioning system measurements for studies of crustal deformation, *J. Geophys. Res.*, *94*, 13,635–13,650, 1989.

DeMets, C., R.G. Gordon, S. Stein, and D.F. Argus, A revised estimate of Pacific-North America motion and implications for western North America plate boundary zone tectonics, *Geophys. Res. Lett.*, *14*, 911–914, 1987.

DeMets, C., R.G. Gordon, D.F. Argus, and S. Stein, Current plate motions, *Geophys. J. Int.*, *101*, 425–478, 1990.

Dong, D., and Y. Bock, Global Positioning System network analysis with phase ambiguity resolution applied to crustal defor-

mation studies in California, *J. Geophys. Res., 94*, 3949–3966, 1989.

Drew, A.R., and R.A. Snay, DYNAP: software for estimating crustal deformation from geodetic data, *Tectonophysics, 162*, 331–343, 1989.

Elders, W.A., R.W. Rex, T. Meidav, P.T. Robinson, and S. Biehler, Crustal spreading in southern California, *Science, 178*, 15–24, 1972.

Fuis, G.S., W.D. Mooney, J.H. Healey, G.A. McMechan, and W.J. Lutter, Crustal structure of the Imperial Valley region, *U.S. Geol. Surv. Prof. Pap., 1254*, 25–50, 1982.

Hartzell, S.H., and T.H. Heaton, Inversion of strong ground motion and teleseismic waveform data for the fault rupture history of the 1979 Imperial Valley, California, earthquake, *Bull. Seismol. Soc. Am., 73*, 1553–1583, 1983.

Ingle, J.C., Paleobathymetric history of Neogene marine sediments, northern Gulf of California, in *Geology of Peninsular California*, pp. 121–138, Pacific Sections AAPG, SEPM, and SEG, 1974.

Jackson, M., R. Reilinger, M. Bevis, B. Perin, C. Rocken, B. Stephens, and J. Stowell, Impact of ionospheric effects on GPS campaigns in southern California and the South Pacific, *Eos Trans. AGU, 70*, 1049, 1989.

Johnson, C.E., and D.P. Hill, Seismicity of the Imperial Valley, *U.S. Geol. Surv. Prof. Pap., 1254*, 14–24, 1982.

Keller, E.A., M.S. Bonkowski, R.J. Korsch, and R.J. Shlemon, Tectonic geomorphology of the San Andreas fault zone in the southern Indio Hills, Coachella Valley, California, *Geol. Soc. Am. Bull., 93*, 46–56, 1982.

King, R.W., E.G. Masters, C. Rizos, A. Stolz, and J. Collins, *Surveying with GPS, Monograph 9*, School of Surveying, The University of New South Wales, Kensington, Australia, 1985.

Kroger, P.M., G.A. Lyzenga, K.S. Wallace, and J.M. Davidson, Tectonic motion in the western United States inferred from very long baseline interferometry measurements, 1980–1986, *J. Geophys. Res., 92*, 14,151–14163, 1987.

Larsen, S.C., Geodetic measurement of deformation in southern California, Ph.D. thesis, 351 pp., California Institute of Technology, Pasadena, 1991.

Larsen, S.C., R.E. Reilinger, H. Neugebauer, and W. Strange, GPS measurements of deformation associated with the 1987 Superstition Hills earthquake, Imperial Valley, California: Evidence for conjugate faulting, *J. Geophys. Res., 97*, 4885–4902, 1992.

Larson, P.A., H.W. Menard, and S.M. Smith, Gulf of California: A result of ocean-floor spreading and transform faulting, *Science, 161*, 781–784, 1968.

Lisowski, M., J.C. Savage, and W.H. Prescott, The velocity field along the San Andreas fault in central and southern California, *J. Geophys. Res., 96*, 8369–8389, 1991.

Lomnitz, C., F. Mooser, C.R. Allen, J.N. Brune, and W. Thatcher, Seismicity and tectonics of northern Gulf of California region, Mexico: Preliminary results, *Geofis. Int., 10*, 34–48, 1970.

Ma, C., J.W. Ryan, and D. Caprette, Crustal dynamics project data analysis—1988, VLBI geodetic results 1979–1988, *NASA Tech. Memo., 100723*, 1989.

Magistrale, H., L. Jones, and H. Kanamori, The Superstition Hills, California, earthquakes of 24 November, 1987, *Bull. Seismol. Soc. Am., 79*, 239–251, 1989.

Mansinha, L., and D.E. Smylie, The displacement fields of inclined faults, *Bull. Seismol. Soc. Am., 61*, 1433–1440, 1971.

Moore, D.G., and E.C. Buffington, Transform faulting and growth of the Gulf of California since late Pliocene, *Science, 161*, 1238–1241, 1968.

Reilinger, R., Coseismic and postseismic vertical movements associated with the 1940 M7.1 Imperial Valley, California, earthquake, *J. Geophys. Res., 89*, 4531–4537, 1984.

Reilinger, R.E., and S.C. Larsen, Vertical crustal deformation associated with the 1979 M = 6.6 Imperial Valley, California earthquake: Implications for fault behavior, *J. Geophys. Res., 91*, 14,044–14,056, 1986.

Sauber, J., Geodetic measurement of deformation in California, Ph.D. Thesis, Massachusetts Institute of Technology, Cambridge, 1989.

Savage, J.C., W.H. Prescott, M. Lisowski, and N. King, Deformation across the Salton Trough, California, 1973–1977, *J. Geophys. Res., 84*, 3069–3079, 1979.

Savage, J.C., W.H. Prescott, M. Lisowski, and N.E. King, Strain accumulation in Southern California, 1973–1980, *J. Geophys. Res., 86*, 6991–7001, 1981.

Savage, J.C., W.H. Prescott, and G. Gu, Strain accumulation in southern California, 1973–1984, *J. Geophys. Res., 91*, 7455–7473, 1986.

Sharp, R.V., Variable rates of late Quaternary strike slip on the San Jacinto fault zone, southern California, *J. Geophys. Res., 86*, 1754–1762, 1981.

Sharp, R.V., Comparison of 1979 surface faulting with earlier displacements in the Imperial Valley, *U.S. Geol. Surv. Prof. Pap., 1254*, 213–221, 1982.

Sieh, K.E., Slip rate across the San Andreas fault and prehistoric earthquakes at Indio, California (abstract), *Eos Trans. AGU, 67*, 1200, 1986.

Sieh, K.E., and P.L. Williams, Behavior of the southernmost San Andreas fault during the past 300 years, *J. Geophys. Res., 95*, 6629–6645, 1990.

Snay, R.A., and A.R. Drew, Supplementing geodetic data with prior information for crustal deformation in the Imperial Valley, California, Technical Report Series, University of Stuttgart, 30 pp., 1988.

Sykes, L.R., and S.P. Nishenko, Probabilities of occurrence of large plate rupturing earthquakes for the San Andreas, San Jacinto, and Imperial faults, California, 1983–2003, *J. Geophys. Res., 89*, 5905–5927, 1984.

Thatcher, W., Horizontal crustal deformation from historic geodetic measurements in southern California, *J. Geophys. Res., 84*, 2351–2370, 1979.

Trifunac, M.D., and J.N. Brune, Complexity of energy release during the Imperial Valley, California, earthquake of 1940, *Bull. Seismol. Soc. Am., 60*, 137–160, 1970.

U.S. Geological Survey, The Imperial Valley, California, earthquake of October 15, 1979, *U.S. Geol. Surv. Prof. Pap., 1254*, 451 pp., 1982.

Ward, S.N., Pacific-North American plate motions: New results from very long baseline interferometry, *J. Geophys. Res., 95*, 21,965–21,981, 1990.

Weldon, R.J., and K.E. Sieh, Holocene rate of slip and tentative recurrence interval for large earthquakes on the San Andreas fault, Cajon Pass, southern California, *Geol. Soc. Am. Bull., 96*, 793–812, 1985.

S. Larsen, Scientific Software Division, Lawrence Livermore National Laboratory, Livermore, CA 94550.

R. Reilinger, Earth Resources Laboratory, Massachusetts Institute of Technology, Cambridge, MA 02139.

(Received January 30, 1991;
revised January 27, 1992;
accepted February 17, 1992.)

APPENDIX 3

Present-day crustal deformation in the Salton Trough, southern California

by R. Reilinger and S. Larsen

In press in *Scientific Results of the Crustal Dynamics Project*,

Geophys. Mon. Ser., AGU, 1992.

Present-Day Crustal Deformation in the Salton Trough, Southern California

Robert Reilinger
Earth Resources Laboratory
Dept. of Earth, Atmospheric, and Planetary Sciences
Massachusetts Institute of Technology
Cambridge, MA 02139

and

Shawn Larsen
Scientific Software Division
Lawrence Livermore National Laboratory
Livermore, CA 94550

ABSTRACT

Since the late 1970's, NASA's CDP program has supported studies of repeat geodetic measurements of crustal deformation throughout the Salton Trough and surrounding regions. Initial investigations concentrated on existing terrestrial observations to enhance the interpretation of more widely spaced VLBI coverage. More recently, a regional Global Positioning System (GPS) network has been established by a number of university groups in cooperation with state and federal agencies. Major conclusions drawn from these studies include: 1) Geodetically determined deformation for the 1940 (M_S 7.1) and the 1979 (M_L 6.6) Imperial Valley earthquakes, and the 1987 Superstition Hills earthquake sequence (M_S 6.2, 6.6) illustrate the importance of fault slip "asperities", postseismic after-slip, and conjugate faulting within the Salton Trough. We consider the implications of these observations for earthquake hazard assessment.
2) Present-day surface and basement topography reflect, in part, recent tectonic processes and can provide insights into the structural evolution of this area. Specifically, the relationship between geodetically measured seismic and interseismic vertical motions and basement/surface topography is interpreted in terms of the propagation of the Gulf of California rift system into the North American

continent. 3) Repeat GPS and VLBI observations provide evidence for the distribution of strain across the various faults comprising the plate boundary in southern California (Imperial, San Andreas, San Jacinto, Elsinore). These preliminary results are interpreted to imply a lower earthquake potential (i.e., smaller earthquakes and/or longer repeat times) for the southern San Andreas fault than estimated from long-term geologic studies, and correspondingly a higher potential for the San Jacinto and/or Elsinore faults.

INTRODUCTION

The Salton Trough of southern California and northern Mexico is one of the most seismically active regions along the Pacific-North American plate boundary and has been the focus of intense seismic studies by the USGS/Caltech seismic network since 1932. Early geodetic observations were initiated in this area by the National Geodetic Survey (NGS; formerly USC&GS) around the turn of the century. Surveys specifically designed to monitor tectonic deformation were intensified following the 1940 (M_S 7.1) Imperial Valley earthquake and have continued to the present. The U. S. Geological Survey has been monitoring horizontal deformation in this area since the early 1970's. In 1986 NGS initiated Global Positioning System (GPS) measurements in southern California with a high concentration of sites in the Imperial Valley. Subsequently, university, state, and federal groups have collaborated to repeat these GPS measurements and extend coverage both along and across the plate boundary. The combination of intense seismic and geodetic coverage make the Salton Trough an ideal location to study the earthquake deformation cycle, and the mechanics and dynamics of the continental lithosphere in a transition zone from crustal extension to transform faulting. This report reviews our progress in understanding the nature of present-day geodetically observed deformations in the Salton Trough and their relationship to plate boundary processes. The report concentrates primarily on geodetic studies and specifically on research carried out by the authors, and is not meant to be a thorough review of the geology/geophysics of this complex region.

SEISMICITY AND TECTONICS

The Salton Trough is a complex transition zone between crustal spreading in the Gulf of California and right-lateral transform motion along the San Andreas fault (Figure 1) . The trough is characterized by predominantly right-stepping, right-lateral en echelon faults, presumably linked by zones of crustal extension [Lomnitz et al., 1970; Elders et al., 1972]. The trough is 4 - 12 million years old and is filled by up to 15 km of late Cenozoic sediments [Larson et al., 1968; Moore and Buffington, 1968; Ingle, 1974; Fuis et al., 1982]. The structural axis of the Salton Trough and its major fault systems trend to the northwest, roughly parallel to the Pacific-North American plate motion. A large fraction of the relative plate displacement is accommodated across this region.

The Imperial Valley is that section of the Salton Trough south of the Salton Sea. The valley is one of the most seismically active regions in California with much of the activity occurring along the Imperial fault and in the Brawley Seismic Zone (Figure 2). Several large earthquakes have occurred in and near the Imperial Valley since 1940. The Imperial fault ruptured with a M_S 7.1 event in 1940 and a M_L 6.6 event in 1979 [U. S. G. S., 1982]. Segments of the San Jacinto fault system broke with a M_L 6.2 earthquake in 1954 and a M_L 6.5 event in 1968 (Borrego Mountain). The most recent episode of seismic activity occurred along the Superstition Hills segment of the San Jacinto fault system [e.g., Magistrale et al., 1989]. On November 24, 1987, a moderate (M_S 6.2) earthquake occurred along a northeast-trending seismic lineament; 12 hours later a larger event (M_S 6.6) occurred along the northwest-trending Superstition Hills fault. What makes this earthquake sequence particularly interesting is that it occurred within a preexisting GPS network.

Conventional geodetic measurements indicate significant displacement across the Imperial Valley, which is inferred to represent interplate deformation. Triangulation data averaged between 1941 and 1986 suggest 4.3 cm/yr right-lateral movement oriented N40°W across the valley [Snay and Drew, 1988]. The observed deformation is time dependent, with rates of 6.1, 2.1, and 4.5 cm/yr for the intervals 1941-1954, 1954-1967, and 1967-1979, respectively. The high velocity for the

earliest period supports the hypothesis of northwestward strain migration following the 1940 earthquake [Thatcher, 1979; Reilinger, 1984]. Furthermore, the computed station displacements indicate that north of the Imperial fault interplate deformation is distributed over a zone at least 50 km wide, whereas to the south interplate deformation is concentrated within a 20 km wide band centered along the Imperial fault. Trilateration measurements made by the U.S. Geological Survey from 1973 to 1989 indicate 3.7 ± 0.1 cm/yr right-lateral displacement between stations on opposite sides of the Imperial Valley [Lisowski et al., 1991]. These differential movements are oriented approximately N40°W.

New global plate models (NUVEL-1) predict the Pacific-North American relative velocity averaged over the last several million years to be 4.7 cm/yr oriented N39.6°W at Imperial Valley coordinates (115.5°W, 33.0°N) [DeMets et al., 1987; DeMets et al., 1990]. VLBI observations during the 1980's suggest a similar present-day rate [e.g., Clark et al., 1987; Kroger et al. 1987; Argus and Gordon, 1990], as do GPS measurements further south across the Gulf of California [Dixon et al., 1991]. The conventional geodetic data in the Imperial Valley indicate a significant fraction of this motion may be distributed along faults in this region.

COSEISMIC AND POSTSEISMIC DEFORMATION

Considerable information has been obtained from analysis of geodetic observations bracketing major earthquakes along the Imperial Valley segment of the Salton Trough. Horizontal deformations associated with the M_S 7.1, 1940 earthquake have been analyzed by Thatcher (1979) and Snay et al. (1982) and vertical deformations were discussed by Reilinger (1984). The 1979, M_L 6.6 Imperial Valley earthquake was one of the most closely monitored events to have occurred anywhere in the world [U.S.G.S., 1982]. A number of investigators analyzed coseismic and postseismic horizontal strains from triangulation, trilateration, and near fault distance measurements [e.g., Snay et al., 1982; Slade et al., 1984; Crook et al., 1982; Langbein et al., 1983; Cohn et al., 1982]. Reilinger and Larsen (1986) reported vertical deformation from repcated NGS leveling surveys. The 1987 Superstition Hills earthquake sequence is unique in that it occurred within both an existing terrestrial network (USGS EDM) and a GPS network. The terrestrial

observations have been reported by Lisowski and Savage (1988), and the GPS measurements by Larsen et al. (1992).

In this section, we review and illustrate the principal geophysical conclusions drawn from analysis of geodetic measurements of earthquake deformation in the Imperial Valley. These include: 1) Substantial variations in the magnitude of coseismic fault slip indicate the presence of fault "asperities" on the Imperial, Brawley, and Superstition Hills faults. While the Superstition Hills main event apparently initiated near a high-slip area of the fault plane, the 1940 and 1979 earthquakes appear to have initiated near relatively low-slip regions. 2) Significant slip along buried faults within the Brawley Seismic Zone occurred in association with both the 1940 and 1979 events, and during the interseismic period between events. The fault kinematics in the Brawley Seismic Zone imply that much of the strain released by earthquakes on the Imperial fault is transferred to the southern San Andreas fault. 3) Conjugate, secondary faults (northeast-southwest strike) are prevalent in the Salton Trough and appear to be active either before events (1987 earthquake) or during the aftershock sequence (1940, 1979 events). These conjugate faults may play an important role in the strain transfer mechanism between faults (e.g., Hudnut et al., 1989b).

Many of the conclusions listed above are well illustrated by the 1979 event [U.S.G.S., 1982]. In addition to geodetic measurements of this earthquake, Hartzell and Heaton (1983) and Archuleta (1984) used strong ground motion observations to estimate the coseismic slip associated with the 1979 event. Sharp et al. (1982) and Sharp and Lienkaemper (1982) discussed horizontal and vertical offsets accompanying and following the earthquake from field observations and short (less than 250 m) fault crossing leveling lines. Louie et al. (1985) report fault creep measurements along the Imperial and Brawley faults as well as other faults in southern California for the period preceding and following the 1979 event (1967-1983).

Figure 3 shows the location of leveling routes used by Reilinger and Larsen (1986) to investigate vertical deformation associated with the 1979 earthquake. A fault model based on strong ground motion measurements (Figure 4) fits many of the

first order features of the observed vertical deformation. However, significant discrepancies occurred along the southernmost segment of the Imperial fault and in the Brawley Seismic Zone. The most conspicuous departures between observed and predicted elevation changes occur along the Calexico to Niland profile well north of the Imperial fault (between 20 and 30 km on Figure 5a) and west of the Imperial fault along the east-west profile through Calexico (between 4 and 12 km on Figure 5b). Specifically, large subsidence observed within the Brawley Seismic Zone about 15 km north of the Imperial fault is completely absent in the theoretical deformation. This subsidence feature is spatially coherent, extends over a distance of at least 8 km, and has an amplitude comparable to the movements near the Imperial fault crossing. Subsidence occurs entirely within the Brawley Seismic Zone and is associated spatially with the area of most intense aftershock activity for the 1979 earthquake [Reilinger and Larsen, 1986]. Similarly, observed subsidence west of the Imperial fault indicated by the east-west profile through Calexico (Figure 5b), is poorly matched by the theoretical model. As with subsidence in the Brawley Seismic Zone, this subsidence is well defined and extends over a distance of at least 8 km west of the fault. Furthermore, the predicted uplift east of the Imperial fault along this profile appears to be offset approximately 5 km to the east relative to the observed movements. These discrepancies suggest some modifications to the fault model derived from strong ground motion measurements.

Subsidence within the Brawley Seismic Zone suggests significant fault activity well north of the observed 1979 surface faulting. The preferred model based on geodetic and seismic observations involves right-lateral slip on a northwest trending structure and left-lateral slip on a conjugate northeast striking fault [Reilinger and Larsen 1986]. Figure 6a shows the resulting fit to the observed vertical motions by combining the proposed fault slip in the Brawley Seismic Zone with the simpler fault model given in Figure 4; the inset shows a map view of the proposed faults. Slip on the left-lateral fault may have been associated with a M_L 5.8 aftershock [Johnson and Hutton, 1982]. However, no large aftershocks occurred on the hypothesized right-lateral fault, indicating that most of this slip was aseismic. Aseismic slip on a very similar northwest striking fault in the Brawley Seismic Zone was hypothesized to account for postseismic deformations for the 1940 Imperial Valley earthquake [Reilinger, 1984].

Figure 6b shows a comparison between observed and theoretical deformation for the leveling line crossing the Imperial fault east of Calexico. The fault parameters for the simple model shown are given in the figure caption. We emphasize that this model is meant to approximate behavior along the southern end of the Imperial fault (i.e., east of Calexico) and does not represent behavior along the central and northern sections of the fault. The primary differences between this model and our initial model are: 1) The Imperial fault has a dip of 90° as opposed to 80°; 2) Slip terminates 5 km north of the epicenter (i.e., no slip on the southern 5 km of the initial fault model); and 3) Larger slip occurs on the upper 7 km of the fault. While these changes represent significant differences from the model proposed by Archuleta (1984), we note that they are not inconsistent with other interpretations of the strong ground motion data [Hartzell and Heaton, 1983] and that reduced slip on the southernmost segment of the fault is supported by the absence of a surface break along this segment (Figure 3).

This example illustrates the importance of geodetic data for constraining fault models. In addition, the refinements suggested by these data have implications for the mechanics of faulting along the Imperial fault and in the Brawley Seismic Zone. For example, low slip along the southern end of the Imperial fault indicates that the 1979 earthquake initiated on a section of the fault that likely experienced interseismic creep rather than on a high-slip segment (i.e., asperity) [Johnson and Hutton, 1982]. Deformation in the Brawley Seismic Zone illustrates the importance of conjugate fault structures for accommodating interplate deformation. Such fault pairs may represent block-bounding faults; the kinematics of these blocks could provide constraints on the dynamics of plate boundary deformation [e.g., Jackson and Molnar, 1990]. Activity on these northeast-striking conjugate faults may help forecast large earthquakes on the primary northwest-striking faults [Hudnut et al., 1989b]. Furthermore, the nature of faulting in the Brawley Seismic Zone has implications for the mechanism of strain transfer from the Imperial fault to the San Andreas and San Jacinto faults to the north. The substantial right-lateral slip on the proposed northwest-striking fault buried in the Brawley Seismic Zone associated with both the 1979 and 1940 earthquakes suggests that much of the shear strain

released during and following these events was transferred to the southern San Andreas fault.

GEODETIC DEFORMATION AND GEOLOGIC STRUCTURE

In addition to the often large coseismic motions associated with earthquakes, the long history of geodetic observations in the Salton Trough provide information on the more subtle deformations which occur between major events. The particular example discussed here involves subsidence of the Mesquite Basin [Larsen and Reilinger, 1991]. The principal observations we attempt to explain include geodetic estimates of coseismic and interseismic basin subsidence, coseismic vertical offsets on basin bounding faults, topographic basin relief, and fault offsets in the basement inferred from refraction surveys. We interpret these observations to suggest a very young age for the northern Imperial fault and northwestward migration of the Brawley Seismic Zone. We further suggest that this migration may be a manifestation of the propagation of the Gulf of California rift system into the North American continent.

The Mesquite Basin is a subaerial topographic low bounded on the west by the Imperial fault and on the east by the Brawley fault (Figure 3). Maximum basin relief is about 10 m relative to its periphery. Figure 7 shows topography and elevation change profiles derived from NGS leveling surveys across the basin. The 1931-1941 and 1941-1974 elevation changes have been modeled as coseismic and postseismic deformation from the 1940 Imperial Valley earthquake [Reilinger, 1984]. Displacements from 1978-1980 have been ascribed to the 1979 earthquake [Reilinger and Larsen, 1986]. Independent of the particular interpretation, the most striking feature of the leveling data is the similar pattern of subsidence across the Mesquite Basin observed on all three profiles, suggesting that the basin was formed by many episodes of seismic activity similar to the 1940 and 1979 events. As indicated in Figure 7, the total subsidence of the basin for the period 1931-1980 is about 40 cm.

Vertical fault offsets on the Imperial and Brawley faults for the 1940 and 1979 earthquakes ranged from 0 - 30 cm and were concentrated along the section of the

Imperial fault bounding the basin [Sharp, 1982, Sharp et al., 1982]. Additional surface offsets occurred, possibly in association with a 1975 earthquake swarm on the Brawley fault [Sharp, 1976]. In each case, slip was down to the east on the Imperial fault and down to the west on the Brawley fault (i.e., causing basin subsidence).

Perhaps the most puzzling and intriguing aspect of deformation in the Mesquite Basin is the offset pattern in the crystalline basement along the Imperial fault as indicated by refraction measurements [Fuis et al., 1984]. Refraction lines crossing the fault at the three locations shown in Figure 3 indicate decreasing offset from south to north (1000 m, 500 m, 0 m); in all cases down to the east. What makes the basement structure unusual is its opposite arrangement to the 1940 and 1979 seismic surface offsets which increase to the northwest.

Assuming the Mesquite Basin developed from episodes of seismic activity similar to the 1940 and 1979 earthquakes, we use the geodetically observed subsidence, topographic relief, and fault offsets in the basement to place constraints on the age of the basin and, correspondingly, the northern Imperial-Brawley fault system [Larsen and Reilinger, 1991]. About 5 m of seismic and postseismic slip is required to form the 40 cm of subsidence observed between 1931-1980 [Reilinger, 1984; Reilinger and Larsen, 1986]. At a slip rate of 40 mm/yr across the Imperial fault [e.g., Larsen and Reilinger, 1992], 5 m of potential slip will accumulate in 125 years. The basin subsidence rate averaged over this period is therefore 3 mm/yr. At this rate, the 10 m of basin relief will develop in only 3000 years. This suggests that the basin and northern Imperial-Brawley fault system is extremely young compared to the age of the Imperial Valley. However, this young age is a minimum since it does not account for sediment influx into the basin. An upper bound on the age of the northern Imperial fault can be estimated by considering fault offsets in the basement. Although geodetic, geologic, and strong-motion data indicate significant vertical displacements along the northern section of the Imperial fault, apparently insufficient time has elapsed to allow formation of sufficient basement offset to be detected by refraction surveys. Assuming refraction measurements can resolve a basement offset of 300 m at 5 km depth [Fuis et al., 1984], at a subsidence rate of 3 mm/yr, the maximum age of the northern Imperial fault is about 100,000 yrs; again

much younger than the 4-12 million year age of the Imperial Valley. A very young age for the present fault configuration in the valley is supported by analysis of heat flow [Lachenbruch et al., 1985], and geothermal systems [Kasameyer et al., 1984]. These age constraints suggest that the present fault configuration represents the most recent epoch of activity in a rapidly changing fault geometry.

We suggest a scenario for the recent history of the Imperial-Brawley fault system which can account for the anti-correlation between seismic vertical fault offsets observed at the surface and offsets recorded in the basement (i.e., surface offsets increase to the north, basement offsets increase to the south). Although the seismic rupture of the Imperial fault is predominantly strike-slip, the large component of vertical motion along the northern segment of the fault is presumably in response to the en echelon geometry of the Imperial and San Andreas faults. These faults may act as transforms associated with a spreading center beneath the Brawley Seismic Zone [Elders et al., 1972; Johnson, 1979]. If the northern extent of the Imperial fault and the Brawley Seismic Zone, were previously further south, dip slip motion would be expected along this section of the fault. Eventually, a detectable offset would develop in the crystalline basement. As the spreading center migrated to the northwest, so would the vertical movements during seismic events. Although rupture on the fault becomes increasingly strike-slip with age (i.e., to the south), the basement offset equals the integrated offset through time, and therefore increases with age (i.e., to the south). Figure 8 shows a schematic illustration of this model of fault evolution. The Rico fault, which was activated during the 1979 earthquake [Sharp et al., 1982], may be a relic basin bounding fault left behind as the spreading center migrated to the northwest. Similarly, the Sand Hills seismicity lineament may be a remnant of an older segment of the San Andreas fault left dormant with the northwest passage of the Brawley Seismic Zone.

If the Brawley Seismic Zone represents the crustal manifestation of a subcrustal spreading center, and if the local transient phenomenon in the Imperial Valley is representative of more regional processes, we speculate that its northwesterly migration is directly associated with the propagation of the Gulf of California rift system into the North American continent. Understanding the kinematics of the

rapidly changing fault configuration in the valley will help place constraints on the dynamic processes which control the transition from ocean spreading in the Gulf of California to transform motion along the San Andreas fault.

GPS MEASUREMENTS IN THE SALTON TROUGH

The Global Positioning System (GPS) is rapidly becoming one of the most important tools to study tectonic deformation. Signals from earth-orbiting NAVSTAR satellites (NAVigation Satellite Time And Ranging) are inverted to obtain three-dimensional coordinates of geodetic monuments with high precision. For crustal deformation studies, the relative position (or baseline) between stations is often measured. Under optimal conditions the typical accuracy for a 50 km baseline is about 1 cm in the horizontal and 3 cm in the vertical [e.g., Davis et al., 1989]. The accuracy is significantly degraded under poor observing conditions. GPS measurements can be used to monitor the secular deformation associated with plate motion, or to record the rapid strain fluctuations due to seismic and volcanic activity. GPS technology is ideally suited for crustal motion research since, unlike conventional geodesy, intersite visibility is not required, stations can be separated by long distances (> 100 km), and it is possible to measure 3-D deformation.

The Salton Trough is a prime location for GPS studies because of the rapid deformation and intense seismic activity. GPS monitoring was initiated in southern California by the NGS in 1986 with the establishment of a 54 station network; 42 stations were located near the Salton Trough. Since that time, a group of universities together with state and federal agencies (see Table 1 for a list of cooperating institutions) have collaborated to repeat and extend these original measurements with resurveys in 1988, 1989, 1990, and 1991 [Reilinger et al., 1990; de la Fuente et al., 1990; Gilbert et al., 1991]. Figure 9 shows stations established as part of this coordinated effort. The Salton Trough GPS network extends from the Pacific coast, across the Elsinore, San Jacinto, and southern San Andreas faults, east to the California-Arizona border. The network covers roughly 475 km of the plate boundary from the Gulf of California in northern Mexico to just south of the "Big Bend" segment of the San Andreas fault. Snay and Drew (1988) used the 1986 GPS measurements in combination with earlier terrestrial geodetic data to

investigate temporal and spatial variations in regional strain in the Imperial Valley. GPS station displacements from 1986 to 1988 have been discussed by Larsen et al. (1992). These measurements illustrate the effect of the 1987 Superstition Hills earthquake sequence. Larsen and Reilinger (1992) investigated GPS measured deformation for the period 1986-1989 and interpreted the observed station displacements in terms of the relative motion between the North American and Pacific plates. Here, we review some of the more significant results obtained from analysis of these data and present new results derived from preliminary reduction of part of the 1990 GPS campaign.

Analysis of 1986, 1988, and 1990 GPS observations has provided information on the nature of faulting associated with the 1987 Superstition Hills earthquake sequence and regional strain accumulation [Larsen et al., 1992; Larsen and Reilinger, 1992]. The 1987 earthquake sequence occurred spatially and temporally within the Salton Trough GPS network, with 14 stations located within 20 km of the Superstition Hills-Elmore Ranch fault system (Figure 10). This is the first occurrence of a large earthquake within a preexisting GPS network. The 1986 data were processed with the NGS and the 1988/1990 data with the Bernese software packages. Derived station displacements for the period 1986-1988 are shown in Figure 10 (note that the movement of station MOUN was derived from a separate experiment in 1990; See Larsen and Reilinger, 1992 for details). Displacements at three sites within 3 km of the surface rupture approach 0.5 m. Eight additional stations within 20 km of the seismic zone are displaced at least 10 cm. Best-fitting uniform slip models of rectangular dislocations in an elastic half-space indicate 130 cm of right-lateral displacement along the northwest trending Superstition Hills fault and 30 cm left-lateral offset along the conjugate northeast trending Elmore Ranch fault (see Larsen et al., 1992 for details). The geodetic moments are 9.4×10^{25} dyne-cm and 2.3×10^{25} dyne-cm for the Superstition Hills and Elmore Ranch faults respectively, in good agreement with seismic moment estimates. This agreement suggests that after-slip observed along the Superstition Hills fault trace [Bilham, 1989] was confined to the near-surface (i.e., afterslip on a large part of the fault plane would result in a larger geodetic than seismic moment). Distributed slip solutions using Singular Value Decomposition suggest near uniform displacement along the Elmore

Ranch fault and concentrated slip to the northwest and southeast along the Superstition Hills fault [Larsen et al., 1992].

The most prominent feature of the Superstition Hills earthquake sequence is the conjugate relationship exhibited by near-simultaneous ruptures along right-lateral northwest and left-lateral northeast-trending faults. In the context of the Imperial Valley, the northeast-trending structures are termed "cross-faults" [e.g., Hudnut et al., 1989a]. Conjugate and cross-fault seismicity seems to be a fairly typical phenomenon for this region (Figure 2), and may dictate the strain transfer mechanism between faults. The 1981 Westmoreland earthquake (M_L4.1) is a prime example of cross-fault tectonics [Ho-Liu, 1988]. The mainshock and aftershock sequence are clearly mapped onto a northeast-trending lineament. Other examples are associated with the Imperial fault. The largest aftershock (M_L5.8) following the 1979 Imperial Valley earthquake (M_L6.6) was located near the town of Brawley [Johnson and Hutton, 1982]. The focal mechanism and following seismicity suggested left-lateral slip along a vertical northeast-trending fault. As discussed earlier, Reilinger and Larsen (1986) found that rupture along an identical conjugate structure successfully modeled geodetic observations within the Brawley Seismic Zone. A large (M_L5.5) aftershock was also recorded near Brawley following the 1940 earthquake [Neumann, 1942]. Due to the sparse seismic data, neither the mechanism nor location were precisely determined, although we speculate this event occurred along the same northeast-trending feature as the large 1979 aftershock. Of historical interest are Imperial Valley earthquake pairs during 1915 (M_L6.3, M_L6.3) and 1927 (M_L5.8, M_L5.5) [Beal, 1915; Toppozada et al., 1978]. In each case, the second shock followed the first by about 1 hour, contrasting with the 12 hour interval between the 1987 events. It is not known which fault(s) ruptured during these earthquake sequences, but conjugate fault interaction is possible.

Rupture on the Superstition Hills fault was almost certainly triggered by the Elmore Ranch event (occurring 12 hours earlier) suggesting some mechanism of stress transfer between the two faults. Larsen et al. (1992) show that the initial shock generated an increase in the Coulomb failure potential along the Superstition Hills fault, possibly advancing it past its failure threshold. This is seen mostly as a

combination of increased tension (earthquake inducing) countered by left-lateral shear (earthquake inhibiting). The increase is maximized along the northwest boundary of the rupture plane, near the nucleation point of the second event. Presumably rupture began where the applied stress was greatest and then propagated to the southeast. Northwestward rupture is prohibited because the increase in compressive forces tends to inhibit shear failure along this segment of the plane. The magnitude of the Coulomb stress increase near the Superstition Hills epicentral zone is comparable to typical earthquake stress drops (~ 10 bars; Larsen et al., 1992).

The one to several hour delay recorded between events during known and suspected conjugate episodes in the Imperial Valley is significant from an earthquake failure perspective. Figure 11 shows potential scenarios for earthquake ruptures involving conjugate-mainshock interaction, such as that observed for the Superstition Hills events. We assume faults fail by an undefined mechanism when they are at or above some critical stress level. The regional strain acting over several years brings a fault near this critical failure point. A stress increase is induced along part of the fault plane due to rupture on a conjugate structure, which may or may not be sufficient to push the stress state past its critical threshold. In the case of Earthquake 1 (Figure 11a), the stress change caused by the conjugate event is not enough to induce failure. Some form of time-dependent stress transfer onto the fault is activated and eventually the critical level is reached. A mechanism involving postseismic viscous creep along the Elmore Ranch fault has been suggested for the 1987 Superstition Hills sequence [Given and Stuart, 1988]. If this scenario is valid, we would also expect failure modes such as that indicated by Earthquake 2. Here, the instantaneous stress applied to the fault from the conjugate event pushes the stress state past the critical level and rupture is immediate. In this case, failure along the two perpendicular fault planes will occur simultaneously. However, this behavior is not observed in the Imperial Valley. Conjugate episodes characteristically have been separated by one to several hours. This suggests that the critical stress level can be exceeded without immediate failure. Therefore, some time-dependent mechanism must be active on the fault plane. We loosely refer to this as "stress corrosion" (Figure 11b) [e.g., Das and Scholz, 1981]. This does not exclude the occurrence of stress transfer due to non-

seismic deformation. In fact, work hardening along the fault plane during this load transfer may allow the stresses to increase during the time interval between events. In the case of Earthquakes 3 and 4, it is suggested that the critical stress level must be exceeded for a period of one to several hours before failure occurs. Hudnut et al. (1989b) proposed fluid diffusion as an alternate mechanism, whereby the effective normal stress was reduced (made more positive) due to pore-fluid infiltration into the rupture plane, thus increasing the Coulomb failure stress. This process involves action on the fault plane, and cannot be explained by stress transfer alone. Regardless of cause, the temporal and geometric relationship exhibited by conjugate fault interaction is seemingly typical of Imperial Valley tectonics, and is likely an important factor for the prediction of large earthquakes and aftershocks.

In addition to the large displacements attributed to the 1987 earthquakes, repeated GPS observations between 1986 and 1990 indicate considerable strain accumulation across the Salton Trough [Larsen and Reilinger, 1992]. Displacements were computed at 29 stations in and near the trough from 1986-1988, at 11 sites from 1988-1989, and at 22 sites from 1988-1990 (Figures 10, 12, and 13, respectively). The earlier measurements indicate 5.9 ± 1.0 cm/yr right-lateral differential velocity across the trough, although the data are heavily influenced by the 1987 earthquake sequence (this estimate was made after attempting to remove the effects of the earthquakes). The 1988-1989 GPS displacements are best modeled by 5.2 ± 0.9 cm/yr of plate-boundary deformation, but rates calculated from conventional geodetic measurements (3.7 cm/yr; Lisowski et al., 1991) fit the data nearly as well (due to the short time interval between GPS surveys). Figure 13 shows horizontal displacements from 1988 to 1990 based on our preliminary and partial 1990 reduction. These measurements give a preliminary deformation rate across the Imperial Valley of 4.5 ± 0.4 cm/yr. This rate is in better agreement with conventional estimates than our earlier results. Further analysis is required to determine whether the apparent change in strain rate with time is real or an artifact of measurement errors. While our prejudice is towards the latter explanation, we note that large variations in strain rates in the Imperial Valley were reported following the 1940 earthquake [Snay and Drew, 1988]. Substantial improvement in estimates of the distribution of strain across the San Andreas, San Jacinto, and

Elsinore faults will result from inclusion of the remaining 1990 GPS data and from observations made in 1991.

The earthquake recurrence interval along the Imperial fault can be estimated using the geodetically determined strain rates. The 1940 Imperial Valley earthquake ruptured the entire length of the Imperial fault. Approximately 3.0 and 4.5 m slip (coseismic plus postseismic) are estimated for the northern and southern segments of the fault, respectively [Reilinger, 1984]. Geodetic and strong ground motion models suggest an average slip of about 1 m along the 1979 rupture plane, with patches of higher displacement (asperities) [e.g., Hartzell and Heaton, 1983; Archuleta, 1984; Reilinger and Larsen, 1986]. At an observed strain rate of 4 - 5 cm/yr and per-event-ruptures between 1 and 3 m, a 20 - 75 year earthquake recurrence interval is calculated for the northern Imperial fault. This assumes all strain is released during major seismic episodes. This recurrence rate is comparable to the 32 year earthquake repeat time suggested by Sykes and Nishenko (1984) and the ~ 50 year interval predicted by Anderson and Bodin (1987).

The relative velocities of three Imperial Valley GPS sites (BLAC, PINY, MONU) traversing the plate boundary are well constrained from VLBI observations since 1979 [Clark et al., 1987; Sauber et al., 1989; Ma et al., 1989; Ward, 1990]. The GPS and VLBI computed deformation rates between BLAC and PINY and between BLAC and MONU are listed in Table 2 (see Figure 9 for station locations relative to faults). Only the north-trending GPS displacement components are used to estimate GPS fault parallel velocities because of the large east-trending errors inherent in the 1986 data. These fault parallel velocities are calculated assuming right-lateral displacement oriented N40°W (i.e., the measured northward displacement is presumed to be one component of the actual displacement which is oriented parallel to the fault). The VLBI measurements indicate 1.5 to 2.1 cm/yr fault-parallel (right-lateral) displacement across the San Andreas fault (BLAC-PINY) and 3.0 to 3.5 cm/yr across the Imperial Valley (BLAC-MONU). The GPS measurements indicate 1.4 ± 0.8 cm/yr displacement across the fault and 3.2 ± 0.6 cm/yr across the valley. The BLAC-MONU velocities agree with the conventional geodetic measurements of displacement across the valley (3.7 ± 0.1 cm/yr). The

fault-crossing displacements (BLAC-PINY), however, are somewhat surprising since they are less than expected based on geologic evidence. The long-term geomorphic slip rate along the southern San Andreas fault over the last 10,000 - 30,000 years is estimated between 2.3 and 3.5 cm/yr [Keller et al., 1982; Weldon and Sieh, 1985], with 2.5 cm/yr a commonly accepted average [e.g., Sieh and Williams, 1990]. The geologic slip rate and radiocarbon dating of Holocene offsets along the fault suggest a recurrence interval of about 300 years with the last major event in 1680 [Sieh, 1986]. These estimates lead to the conclusion that the potential for a major earthquake along the southern San Andreas fault is high. However, the geodetic evidence reported here indicate a comparatively small strain rate during the last decade. This suggests a decreased earthquake potential for the southern San Andreas fault, assuming the geodetic measurements are indicative of at least the last few hundred years. A decreased seismic potential would be observed either as a longer recurrence interval or less slip per event. This interpretation is supported by geologic trenching studies, which suggest a decreasing slip rate along the southern San Andreas fault during the past 1000 years [Sieh, 1986]. If this is true, the San Jacinto and Elsinore faults should play a more active role in regional tectonics. In fact, the shear strain along the San Jacinto fault determined from EDM observations between 1973 and 1984 is nearly the same as that for networks which lie on the San Andreas fault [Savage et al., 1986]. The two fault systems may alternately assume dominant roles in absorbing plate motions, as is suggested by variable Quaternary slip rates along the San Jacinto fault [Sharp, 1981].

CONCLUSIONS

Analysis of geodetic, geophysical, and geological observations provides information on contemporary tectonic processes and the recent tectonic evolution of the Salton Trough section of the Pacific-North American plate boundary. Studies based on these data have implications for earthquake hazards as well as the mechanics and dynamics of continental deformation. Geodetically determined deformation for the 1940 (M_S7.1) and the 1979 (M_L6.6) Imperial Valley earthquakes, and the 1987 Superstition Hills earthquake sequence (M_S6.2, 6.6) illustrate the importance of fault slip "asperities", postseismic after-slip, and conjugate faulting within the

Salton Trough. Earthquake pairs on conjugate faults appear to be an integral part of Salton Trough tectonics and may provide a means for short-term prediction of major earthquakes and large aftershocks. The relationship between geodetically measured seismic and interseismic vertical motions and geologic structure suggests that the northern Imperial-Brawley fault system is very young compared to the age of the Imperial Valley, and that the Brawley Seismic Zone may be migrating to the northwest. This migration may be related to the propagation of the Gulf of California oceanic rift system into the North American continent. GPS and VLBI observations crossing the southern San Andreas and San Jacinto faults suggest a lower earthquake potential (i.e., smaller earthquakes and/or longer repeat times) for the southern San Andreas fault than derived from longer-term geologic studies, and correspondingly a higher potential for the San Jacinto fault. Continued monitoring of the extensive GPS network in the Salton Trough should provide improved constraints on the distribution of strain accumulation, and the mechanics of continental deformation in this zone of transition from ocean spreading in the Gulf of California to continental transform motion along the San Andreas fault.

ACKNOWLEDGMENTS

We would like to thank many individuals for cooperating on the GPS field work including Bill Strange, Bill Young, John Beavan, Ken Hudnut, Lewis Gilbert, and Mike Bevis in the U.S. and Carlos Aiken, Mark Zeigler, Mauricio de la Fuente, and Javier Gonzalez in Mexico. Reviews by Tim Dixon, ????, Bernard Minster, and an anonymous reviewer substantially improved the paper. This research was supported in part by U.S. Geological Survey contract 14-08-0001-61679 and NASA Grant NAG-5-814.

REFERENCES

Anderson, J. G., and P. Bodin, Earthquake recurrence models and historical seismicity in the Mexicali-Imperial Valley, *Bull. Seismol. Soc. Am, 77,* 562-578, 1987.

Archuleta, R. J., A faulting model for the 1979 Imperial Valley earthquake, *J. Geophys. Res., 89,* 4559-4585, 1984.

Argus, D. F., and R. G. Gordon, Pacific-North American plate motion from very long baseline interferometry compared with motion inferred from magnetic anomalies, transform faults, and earthquake slip vectors, *J. Geophys. Res., 95,* 17,315-17,324. 1990.

Beal, C. H., The earthquake in the Imperial Valley, California, June 22, 1915, *Bull. Seismol. Soc. Am., 5,* 130-149, 1915.

Cohn, S.N., et al., Preearthquake and postearthquake creep on the Imperial fault and the Brawley fault zone, *USGS Prof. Pap. 1254,* 161-168, 1982.

Clark, T. A., D. Gordon, W. E. Himwich, C. Ma, A. Mallama, and J. W. Ryan, Determination of relative site motions in the western United States using Mark III very long baseline interferometry, *J. Geophys. Res., 92,* 12,741-12,750, 1987.

Crook, C.N., R.G. Mason, and P.R. Wood, Geodetic measurements of horizontal deformation on the Imperial fault, *USGS Prof. Pap. 1254,* 182-192, 1982.

Crowell, J. C., and A. G. Sylvester (Eds.), *Tectonics of the Juncture Between the San Andreas Fault System and the Salton Trough: A Guidebook,* 193 pp., University of California, Santa Barbara, California, 1979.

Das, S., and C. H. Scholz, Off-fault aftershock clusters caused by shear stress increase?, *Bull. Seismol. Soc. Am. 71,* 1669-1675, 1981.

Davis, J. L., W. H. Prescott, J. L. Svarc, and K. J. Wendt, Assessment of global positioning system measurements for studies of crustal deformation, *J. Geophys. Res.*, *94*, 13,635-13,650, 1989.

de la Fuente, M., J. J. Gonzalez, D. G. Ziegler, and C. L. V. Aiken, The north Baja, California GPS campaign: First epoch, *EOS, Trans. Am. Geophys. Union, 71*, 478, 1990.

DeMets, C., R. G. Gordon, S. Stein, and D. F. Argus, A revised estimate of Pacific-North America motion and implications for western North America plate boundary zone tectonics, *Geophys. Res. Letts.*, *14*, 911-914, 1987.

DeMets, C., R. G. Gordon, D. F. Argus, and S. Stein, Current plate motions, *Geophys. J. Inter.*, *101*, 425-478, 1990.

Dixon, T. H., G. Gonzalez, S. M. Lichten, D. M. Tralli, G. E. Ness, and J. P. Dauphin, Preliminary determination of Pacific-North America relative motion in the southern Gulf of California using the global positioning system, *Geophys. Res. Lett.*, *18*, 861-864, 1991.

Elders, W. A., R. W. Rex, T. Meidav, P. T. Robinson, and S. Biehler, Crustal spreading in southern California, *Science, 178*, 15-24, 1972.

Fuis, G. S., W. D. Mooney, J. H. Healey, G. A. McMechan, and W. J. Lutter, Crustal structure of the Imperial Valley region, *U.S. Geol. Surv. Prof. Pap., 1254*, 25-50, 1982.

Fuis, G. S., W. D. Mooney, J. H. Healy, G. A. McMechan, and W. J. Lutter, A seismic refraction survey of the Imperial Valley region, California, *J. Geophys. Res.*, *89*, 1165-1189, 1984.

Gilbert, L. E. , S. Larsen, R. E. Reilinger, J. Beavan, K. Hudnut, B. Young, and W. Strange, A comparison of STRC90 and STRC91 campaign results: Strain in the

Coachella Valley, southeastern California, *EOS, Trans. Am. Geophys. Union, 72*, 117, 1991.

Given, D. D., and W. D. Stuart, A fault interaction model for triggering of the Superstition Hills earthquake of November 24, 1987, *Seismol. Res. Letts., 59*, p. 48, 1988.

Hartzell, S. H., and T. H. Heaton, Inversion of strong ground motion and teleseismic waveform data for the fault rupture history of the 1979 Imperial Valley, California, earthquake, *Bull. Seis. Soc. Am., 73*, 1553-1583, 1983.

Ho-Liu, P. H-Y., Modeling regional love waves: Imperial Valley to Pasadena, Ph. D. thesis, California Institute of Technology, Pasadena, 1988.

Hudnut, K. W., L. Seeber, T. Rockwell, J. Goddmacher, R. Klinger, S. Lindvall, and R. McElwain, Surface ruptures on cross-faults in the 24 November 1987 Superstition Hills, California, earthquake sequence, *Bull. Seismol. Soc. Am., 79*, 282-296, 1989a.

Hudnut, K. W., L. Seeber, and J. Pacheco, Cross-fault triggering in the November 1987 Superstition Hills earthquake sequence, southern California, *Geophys. Res. Letts., 16*, 199-202, 1989b.

Ingle, J. C., Paleobathymetric history of Neogene marine sediments, northern Gulf of California, *in Geology of Peninsular California, Pacific Sections AAPG, SEPM, and SEG*, 121-138, 1974.

Jackson, J., and P. Molnar, Active faulting and block rotations in the western Transverse Ranges, California, *J. Geophys. Res., 95*, 22,073-22,087, 1990.

Johnson, C. E., CEDAR-An approach to the computer automation of short-period local seismic networks; seismotectonics of the Imperial Valley of southern California, California Institute of Technology, Ph.D. thesis, 343 pp., Pasadena, 1979.

Johnson, C. E., and L. K. Hutton, Aftershocks and preearthquake seismicity, *U.S. Geol. Surv. Prof. Pap., 1254*, 59-76, 1982.

Kasameyer, P. W., L. W. Younker, and J. M. Hanson, Age of the Salton Sea geothermal system as inferred from the thermal data, *Geol. Soc. Am. Abst., 12*, 458, 1980.

Keller, E. A., M. S. Bonkowski, R. J. Korsch, and R. J. Shiemon, Tectonic geomorphology of the San Andreas fault zone in the southern Indio Hills, Coachella Valley, California, *Geol. Soc. Am. Bull., 93*, 46-56, 1982.

Kroger, P. M., G. A. Lyzenga, K. S. Wallace, and J. M. Davidson, Tectonic motion in the western United States inferred from very long baseline interferometry measurements, 1980-1986, *J. Geophys. Res., 92*, 14,151-14163, 1987.

Lachenbruch, A. H., J. H. Sass, and S. P. Galanis, Jr., Heat flow in southernmost California and the origin of the Salton Trough, *J. Geophys. Res., 90*, 6709-6736, 1985.

Langbein, J., A. McGarr, M.J.S. Johnston, and P.W. Harsh, Geodetic measurements of postseismic crustal deformation following the 1979 Imperial Valley earthquake, California, *Bull. Seismol. Soc. Am., 73*, 1203-1224, 1983.

Larsen, S.C., and R. E. Reilinger, Age constraints for the present fault configuration in the Imperial Valley, California: Evidence for northwestward propagation of the Gulf of California rift system, *J. Geophys. Res., 96*, 10,339-10,346, 1991.

Larsen, S. C., and R. E. Reilinger, GPS measurements of strain accumulation across the Imperial Valley, California: 1986-1989, *J. Geophys. Res.*, in review, 1992.

Larsen, S. C., R. E. Reilinger, H. Neugebauer, W. Strange, GPS measurements of deformation associated with the 1987 Superstition Hills earthquake, Imperial Valley, California: Evidence for conjugate faulting, *J. Geophys. Res.*, in press, 1992a.

Larson, P. A., H. W. Menard, and S. M. Smith, Gulf of California: A result of ocean-floor spreading and transform faulting, *Science, 161*, 781-784, 1968.

Lisowski, M., and J. C. Savage, Deformation associated with the Superstition Hills, California, earthquakes of November 1987, *Seismol. Res. Letts., 59*, p. 35, 1988.

Lisowski, M., J. C. Savage, and W. H. Prescott, The velocity field along the San Andreas fault in central and southern California, *J. Geophys. Res., 96*, 8369-8389, 1991.

Lomnitz, C., F. Mooser, C. R. Allen, J. N. Brune, and W. Thatcher, Seismicity and tectonics of northern Gulf of California region, Mexico: Preliminary results, *Geofis. Int., 10*, 34-48, 1970.

Louie, J.N., C.R. Allen, D.C. Johnson, P.C. Haase, and S.N. Cohn, Fault Slip in southern California, *Bull. Seismol. Soc. Am., 75*, 811-833, 1985.

Ma, C., J. W. Ryan, D. Caprette, Crustal dynamics project data analysis -- 1988, VLBI geodetic results 1979-1988, *NASA Technical Memorandum, 100723*, 1989.

Moore, D. G., and E. C. Buffington, Transform faulting and growth of the Gulf of California since late Pliocene, *Science, 161*, 1238-1241, 1968.

Neumann, F., United States earthquakes, 1940, *U.S. Coast and Geod. Sur. Serial, 647*, 74 pp.,1942.

Nicholson, C., L. Seeber, P. Williams, and L. R. Sykes, Seismic evidence for conjugate slip and block rotation within the San Andreas fault system, southern California, *Tectonics, 89*, 629-648, 1986.

Reilinger, R., Coseismic and postseismic vertical movements associated with the 1940 M7.1 Imperial Valley, California, earthquake, *J. Geophys. Res., 89*, 4531-4537, 1984.

Reilinger, R. E., and S. C. Larsen, Vertical crustal deformation associated with the 1979 M 6.6 Imperial Valley, California earthquake: Implications for fault behavior, *J. Geophys. Res., 91*, 14,044-14,056, 1986.

Reilinger, R. E., J. Beavan, L. Gilbert, S. Larsen, K. Hudnut, C. Aiken, D. Ziegler, W. Strange, M. de la Fuente, J. Gonzalez, J. Stowell, W. Young, G. Doyle, G. Stayner, 1990 Salton Trough-Riverside County GPS network, *EOS, Trans. Am. Geophys. Union, 71*, 477, 1990.

Sauber, J., Geodetic measurement of deformation in California, Ph.D. Thesis, Massachusetts Institute of Technology, 1989.

Savage, J. C., W. H. Prescott, and G. Gu, Strain accumulation in southern California, 1973-1984, *J. Geophys. Res., 91*, 7455-7473, 1986.

Sharp, R. V., Surface faulting in Imperial Valley during the Earthquake swarm of January-February, 1975, *Bull. Seismol. Soc. Am., 66*, 1145-1154, 1976.

Sharp, R. V., Variable rates of late Quaternary strike slip on the San Jacinto fault zone, southern California, *J. Geophys. Res., 86*, 1754-1762, 1981.

Sharp, R. V., Comparison of 1979 surface faulting with earlier displacements in the Imperial Valley, *U.S. Geol. Surv. Prof. Pap., 1254*, 213-221, 1982.

Sharp, R.V., and J.J. Lienkaemper, Preearthquake and postearthquake near-field leveling across the Imperial fault and Brawley fault zone, *USGS Prof. Pap., 1254*, 169-182, 1982.

Sharp, R.V., et al., Surface faulting in the central Imperial Valley, *USGS Prof. Pap. 1254*, 119-144, 1982.

Sieh, K. E., Slip rate across the San Andreas fault and prehistoric earthquakes at Indio, California, *Eos,Trans. Am. Geophys. Union, 67*, p. 1200, 1986.

Sieh, K. E., and P. L. Williams, Behavior of the southernmost San Andreas fault during the past 300 years, *J. Geophys. Res.*, *95*, 6629-6645, 1990.

Slade, M.A., G.A. Lyzenga, and A. Raefskey, Modeling the surface static displacement and fault plane slip for the 1979 Imperial Valley earthquake, *Bull. Seismol. Soc. Am.*, *74*, 2413-2433, 1984.

Snay, R.A., M.W. Cline, and E.L. Timmerman, Horizontal deformation in the Imperial Valley, California, between 1934 and 1980, *J. Geophys. Res.*, *87*, 3959-3968, 1982.

Snay, R. A., and A. R. Drew, Supplementing geodetic data with prior information for crustal deformation in the Imperial Valley, California, *Technical Report Series, University of Stuttgart*, 30 pp., 1988.

Sykes, L. R., and S. P. Nishenko, Probabilities of occurrence of large plate rupturing earthquakes for the San Andreas, San Jacinto, and Imperial faults, California, 1983-2003, *J. Geophys. Res.*, *89*, 5905-5927, 1984.

Thatcher, W., Horizontal crustal deformation from historic geodetic measurements in southern California, *J. Geophys. Res.*, *84*, 2351-2370, 1979.

Toppozada, T. R., D. L. Parke, and C. T. Higgins, Seismicity of California 1900-1931, *Calif. Div. of Mines and Geol Spec. Rep.*, *135*, 39 pp., 1978.

U.S. Geological Survey, The Imperial Valley, California, earthquake of October 15, 1979, *U.S. Geol. Surv. Prof. Pap.*, *1254*, 451 pp., 1982.

Ward, S. N., Pacific-North America plate motions: New results from very long baseline interferometry, *J. Geophys. Res.*, *95*, 21,965-21,981, 1990.

Weldon, R. J., and K. E. Sieh, Holocene rate of slip and tentative recurrence interval for large earthquakes on the San Andreas fault, Cajon Pass, southern California, *Geol. Soc. Am. Bull.*, *96*, 793-812, 1985.

Figure 1. The Salton Trough (hatch pattern) is a transition zone between crustal spreading in the Gulf of California and right-lateral transform motion along the San Andreas fault. This region is divided into the Mexicali Valley south of the U.S. - Mexico border, and the Imperial-Coachella valleys to the north. Map modified from Lachenbruch et al. (1985).

Figure 2. Major faults and seismicity from 1932 to 1990 in the Imperial Valley. Large earthquakes are shown as stars. The Brawley Seismic Zone is the region of anomalously high activity between the Imperial and San Andreas faults. Major earthquakes include the 1940 and 1979 events along the Imperial fault, the 1954 and 1968 events along the San Jacinto fault, and the 1987 Superstition Hills earthquake sequence along the Superstition Hills and Elmore Ranch faults.

Figure 3. Map of the Imperial Valley showing major faults (dashed where inferred) and leveling routes (dotted lines) along which elevation changes have been determined. Heavy lines show primary surface faulting associated with the 1979 earthquake. The epicenter for the 1979 event (star) is also shown. Hatched lines show outline of valley in the United States. Small arrows along Imperial fault indicate locations of fault crossing refraction lines. Abbreviations are: BSZ, Brawley Seismic Zone; MB, Mesquite Basin; IF, Imperial fault; BF, Brawley fault; SAF, San Andreas fault; AF, Algodones fault; SHF, Superstition Hills fault; SMF, Superstition Mountains fault; SJFZ, San Jacinto fault zone; EF, Elsinore fault (base map modified from Crowell and Sylvester, 1979).

Figure 4. Side views of Imperial and Brawley faults showing static slip (m) as reported by Archuleta (1984) (left) and the approximation to this slip used by Reilinger and Larsen (1986). Dot shows hypocenter for 1979 event. (See Reilinger and Larsen [1986] for details.)

Figure 5. Comparison between observed (points) and modeled (line) vertical movements for model shown in Figure 4. Locations of the Imperial fault (IF), and Superstition Hills fault (SHF) crossings are shown. A) Calexico via El Centro to south of Niland. B) East-west line through Calexico.

Figure 6. A) Comparison between observed (points) and theoretical (line) vertical movements for leveling line crossing the Brawley Seismic Zone. Map view of orthogonal faults used in model is shown in inset. Fault parameters: Left-lateral fault: length = 8.6 km, width = 8 km, depth = 2 km, dip = 90°, slip = 1m left lateral; Right-lateral fault: length = 14 km; width = 5 km; depth = 2 km, dip = 70° down to west, slip = 1 m right lateral. B) Comparison between observed (points) and theoretical (line) vertical movements for east-west line through Calexico. Map view of modeled fault relative to benchmarks along leveling route is shown in lower right corner of plot. Fault parameters: length = 23 km, width = 13 km, depth to top of fault = 0 km, dip = 90°, slip = 1 m right-lateral.

Figure 7. Releveling profiles showing vertical movements between El Centro (0 km) and the Salton Sea from 1931 to 1941, 1941 to 1974, and 1978 to 1980 (see Figure 3 for location of leveling route). At the top is the elevation (dashed line). A long wavelength down to the north linear trend is observed in the elevation. The adjusted topography (solid line) is the elevation minus this regional tilt, determined by fitting a straight line to elevation. The Mesquite Basin is clearly defined by the topography. Note the strong correlation between the movement profiles and the surface expression of the Mesquite Basin.

Figure 8. Schematic diagram of past and present fault configurations in the Imperial Valley showing the hypothesized northwesterly migration of the Brawley Seismic Zone.

Figure 9. GPS sites established in and around the Salton Trough between 1986 and 1991 as part of the cooperative Salton Trough-Riverside County project (see Table 1 for participating agencies). Triangles show mobile VLBI stations occupied with GPS.

Figure 10. GPS station displacements for the interval 1986-1988 (1.8 years). All measurements are made relative to station OCTI. Errors are determined by multiplying the formal uncertainties from the GPS solution by a variance factor so that the average baseline error scales as 1 ppm. The east-trending uncertainties are about 4 times larger then the north-trending uncertainties. Seismically induced

displacements from the 1987 Superstition Hills earthquake sequence are most apparent at stations KANE, L589, and MOUN. The large nonseismic displacements are assumed to represent relative motion between the Pacific and North American plates, which is concentrated across the valley. MOUN was resurveyed in a separate campaign in 1990. Station MOUN was disturbed by the earthquake and had to be reset; hence the large uncertainties on its displacement.

Figure 11. Schematic of potential earthquake failure processes in the Imperial Valley. a) Earthquake failure occurs after some critical stress is reached. b) Earthquake failure occurs following a time dependent delay after critical stress is exceeded.

Figure 12. GPS station displacements for the interval 1988-1989 (1.0 years). All measurements are made relative to station OCTI. Errors are determined by multiplying the formal uncertainties from the GPS solution by a variance factor so that the average baseline error scales as 0.5 ppm. Stations to the northeast moved about 5 cm southwest relative to stations on the other side of the valley.

Figure 13. Preliminary GPS horizontal station displacements from 1988-1990. Only part of the 1990 data have been included. These preliminary results suggest about a 4.5 cm/yr deformation rate across the Valley.

Table 1.

SALTON TROUGH GPS PRINCIPAL COOPERATING INSTITUTIONS

UNIVERSITIES/RESEARCH INSTITUTIONS:

- Callifornia Institute of Technology
- Centro de Investigacion Cientifica y Educacion Superior de Ensenada (Mexico)
- Jet Propulsion Laboratory (Pasadena)
- Lamont-Doherty Geological Observatory
- Massachussets Institute of Technology
- University of California, San Diego (Pinyon Flat, La Jolla)
- University of Mexico, Mexico City (Mexico)
- University of Texas, Dallas (Mexico)

CALIFORNIA COUNTY AGENCIES:

- Riverside County Flood Control and Water Conservation District
- San Bernardino County Survey

FEDERAL AGENCIES:

- National Geodetic Survey
- U. S. Geological Survey (Mexico)

Table 2. Displacement Rates Across San Andreas Fault

Baseline	Method	Interval	North (cm/yr)	East (cm/yr)	Fault Parallel (cm/yr)
BLAC-PINY	GPS	1986-1988	1.1 ± 0.6		1.4 ± 0.8
	VLBI[1]	1982-1987	1.8	-1.1	2.1
	VLBI[2]	1979-1988	1.5	-1.0	1.8
	VLBI[3]	1982-1988	1.2	-0.9	1.5
	VLBI[4]	1980-1989	1.4	-1.1	1.8
BLAC-MONU	GPS	1986-1989	2.5 ± 0.5		3.2 ± 0.6
	VLBI[1]	1982-1987	2.3	-2.7	3.5
	VLBI[2]	1979-1988	2.5	-2.5	3.5
	VLBI[3]	1982-1988	2.4	-1.8	3.0
	VLBI[4]	1980-1989	2.2	-2.5	3.3

[1] *Clark et al.* [1987]
[2] *Ma* [1988]
[3] *Sauber* [1989]
[4] *Ward* [1990]

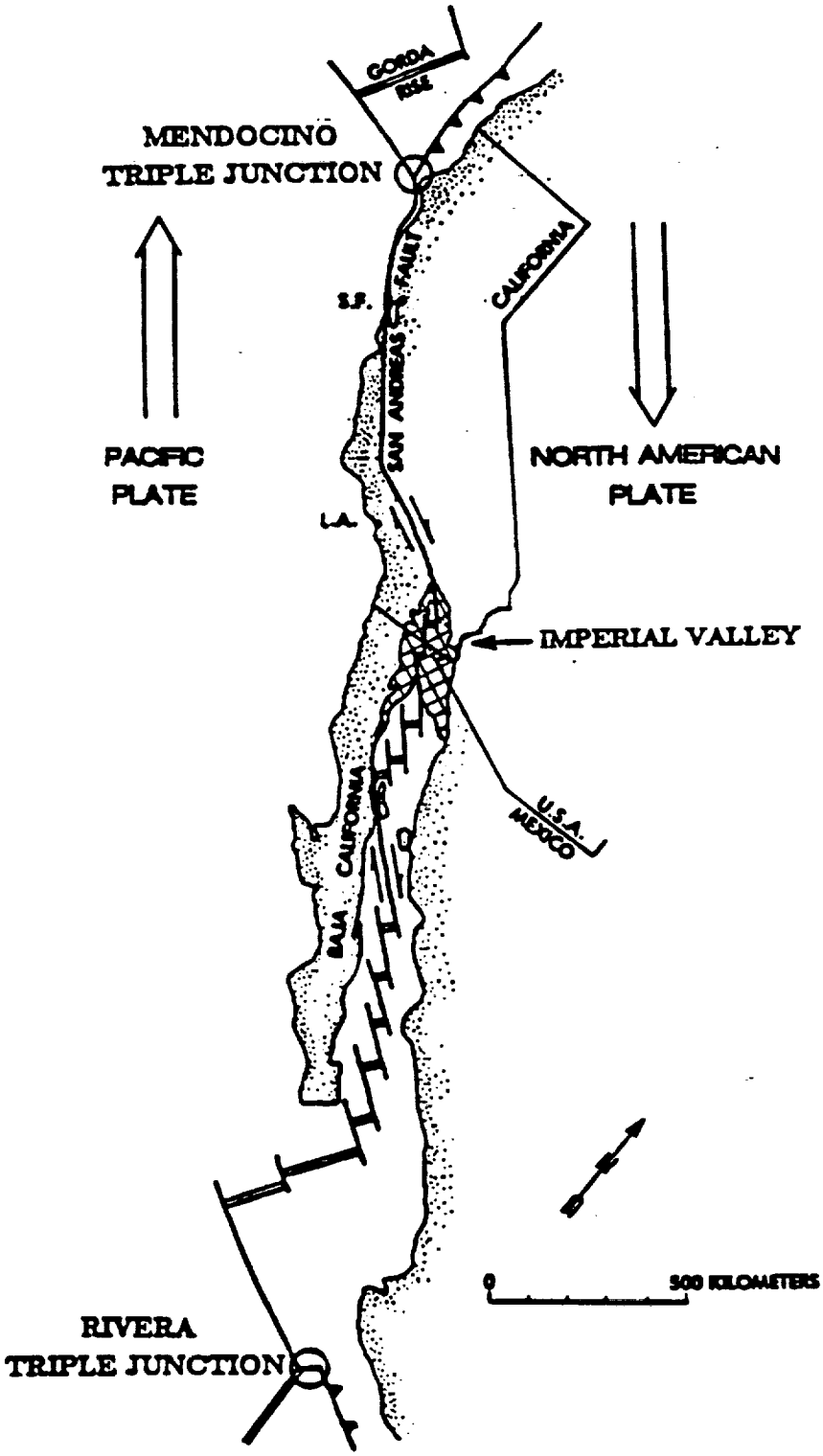
GORDA RISE
MENDOCINO TRIPLE JUNCTION
PACIFIC PLATE
NORTH AMERICAN PLATE
S.F.
SAN ANDREAS FAULT
CALIFORNIA
L.A.
IMPERIAL VALLEY
U.S.A.
MEXICO
BAJA CALIFORNIA
0
500 KILOMETERS
RIVERA TRIPLE JUNCTION

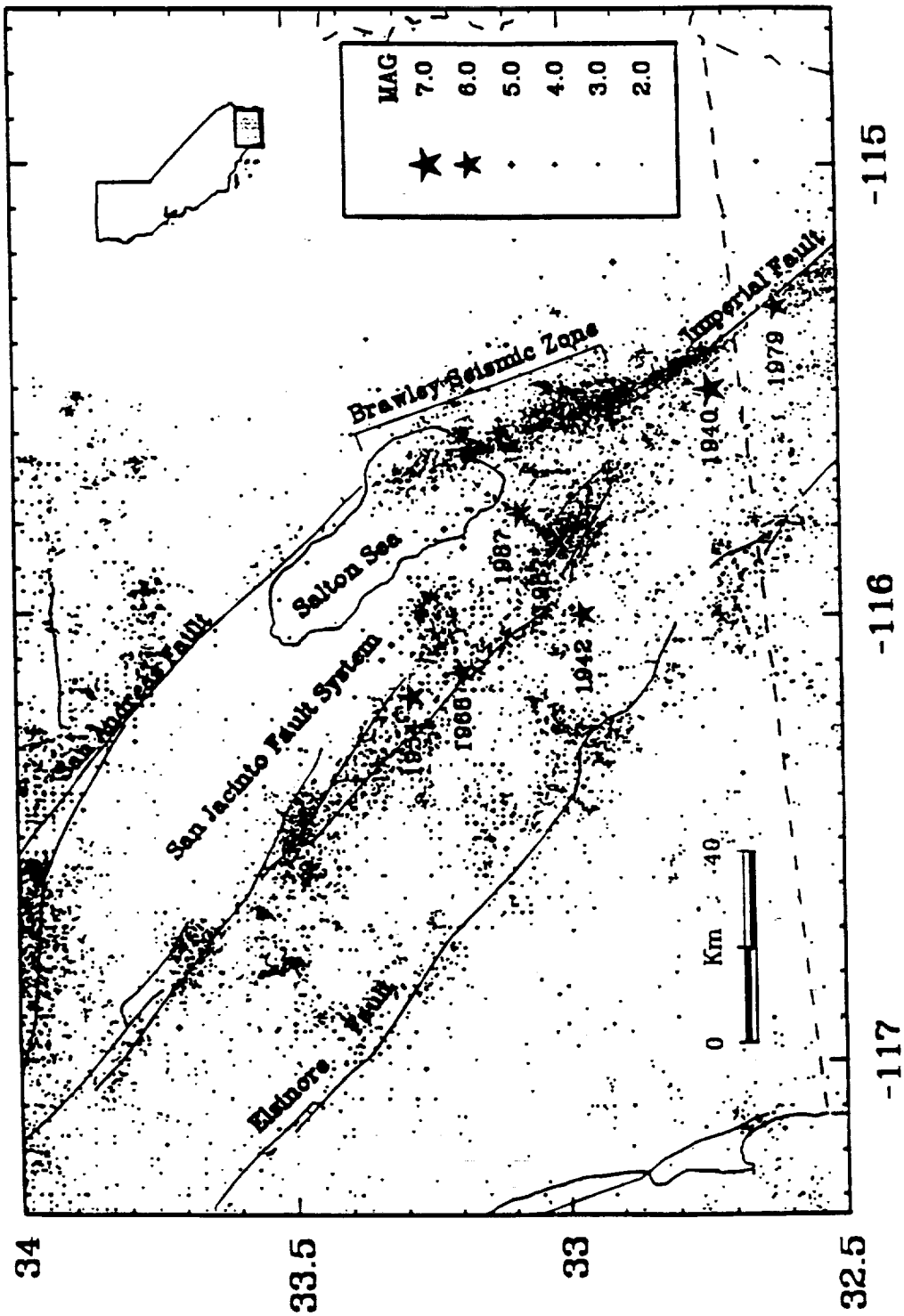
MAG
7.0
6.0
5.0
4.0
3.0
2.0
Brawley Seismic Zone
Imperial Fault
1940
1979
Salton Sea
1987
San Jacinto Fault System
1968
1942
Elsinore Fault
0
Km
40
34
33.5
33
32.5
-115
-116
-117

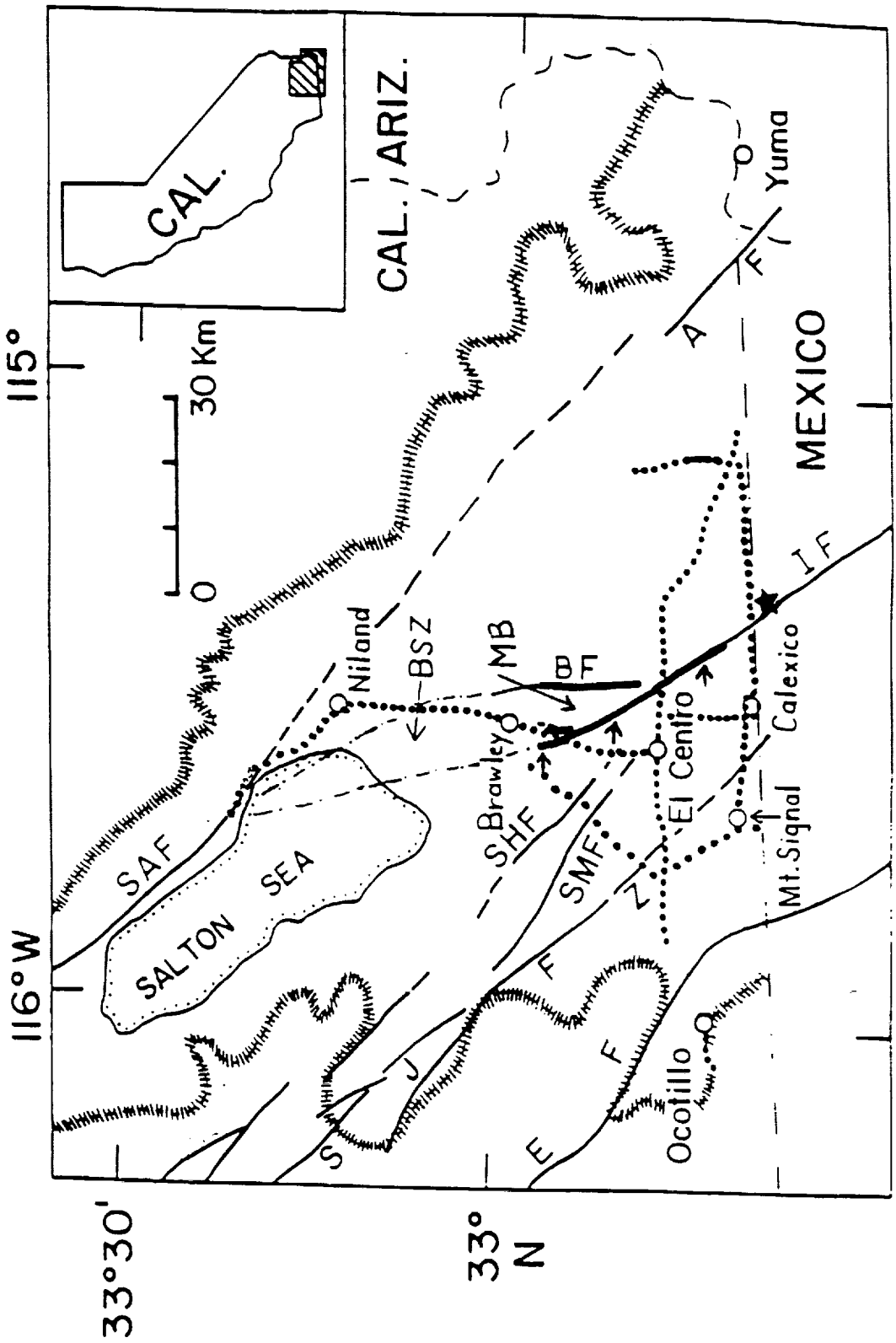
CAL.
CAL. / ARIZ.
30 Km
0
115°
116° W
33°30'
33° N
MEXICO
Yuma
Niland
BSZ
MB
BF
Brawley
SHF
SMF
El Centro
Calexico
IF
Mt. Signal
Ocotillo
SAF
SALTON SEA

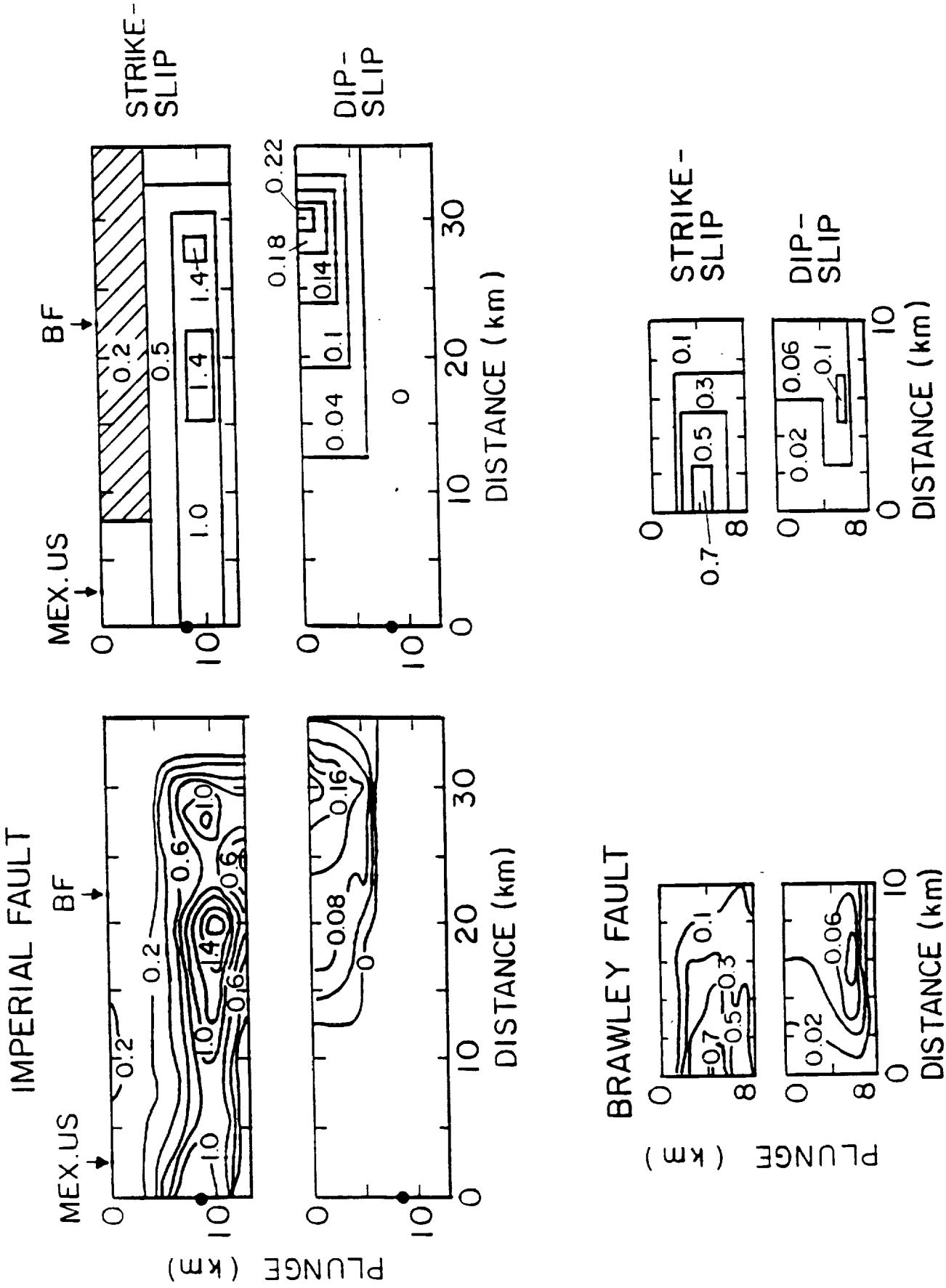
IMPERIAL FAULT
MEX.US
BF
STRIKE-SLIP
DIP-SLIP
PLUNGE (km)
DISTANCE (km)
BRAWLEY FAULT
0
10
20
30
8

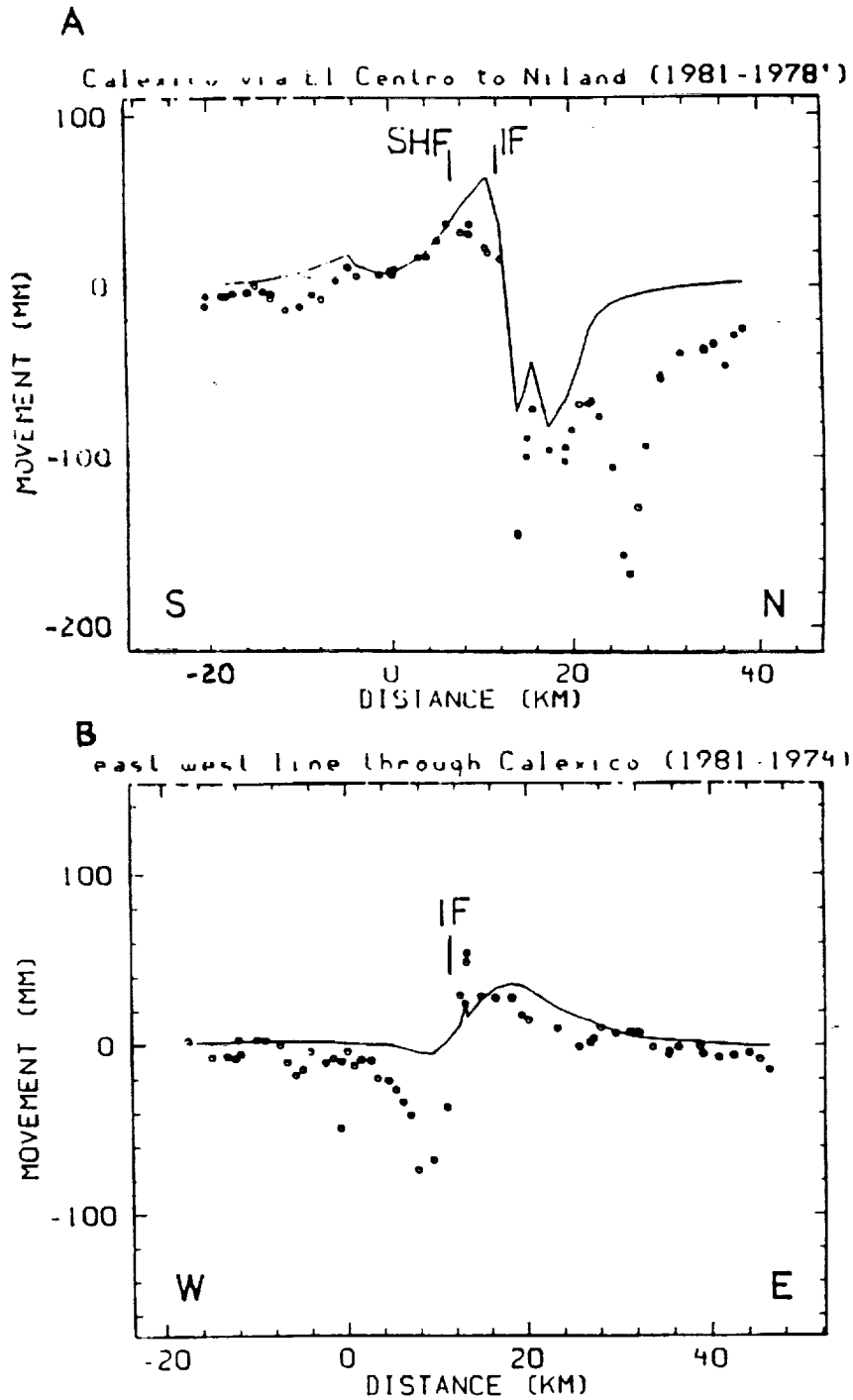
A
Calexico via El Centro to Niland (1981-1978')
100
0
-100
-200
MOVEMENT (MM)
SHF
IF
S
N
-20
0
20
40
DISTANCE (KM)
B
east west line through Calexico (1981-1974)
100
0
-100
MOVEMENT (MM)
IF
W
E
-20
0
20
40
DISTANCE (KM)

A

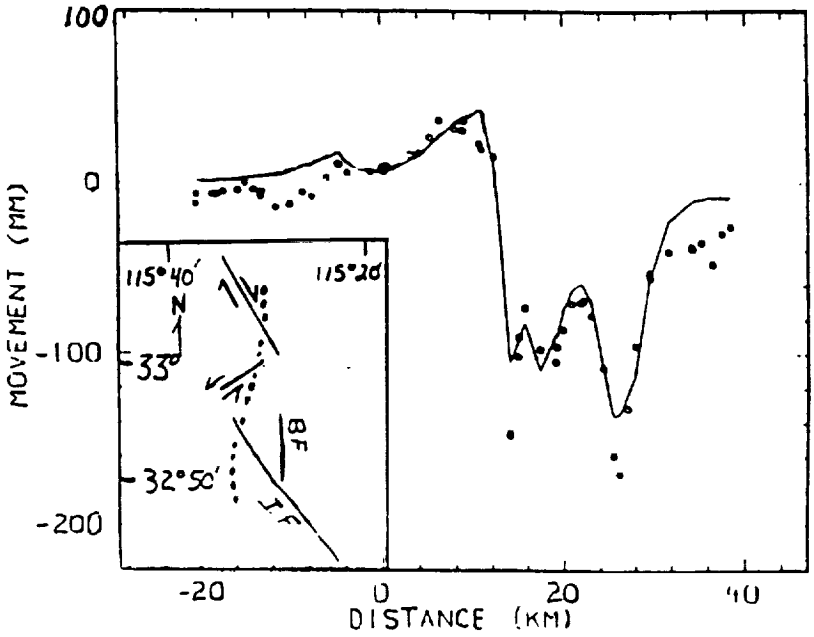
100
0
-100
-200
MOVEMENT (MM)
-20
0
20
40
DISTANCE (KM)
115°40'
115°20'
N
33°
32°50'
BF
IF

B

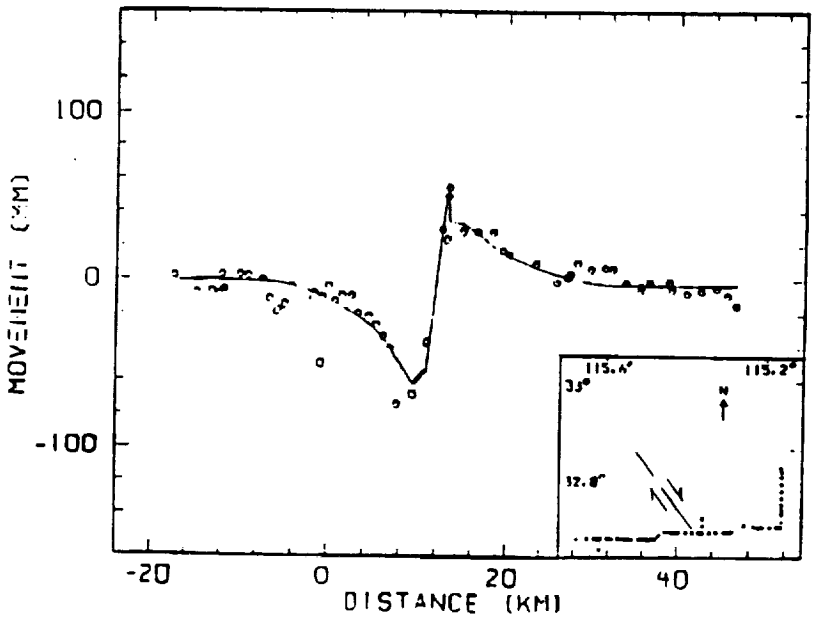
100
0
-100
MOVEMENT (MM)
-20
0
20
40
DISTANCE (KM)
N

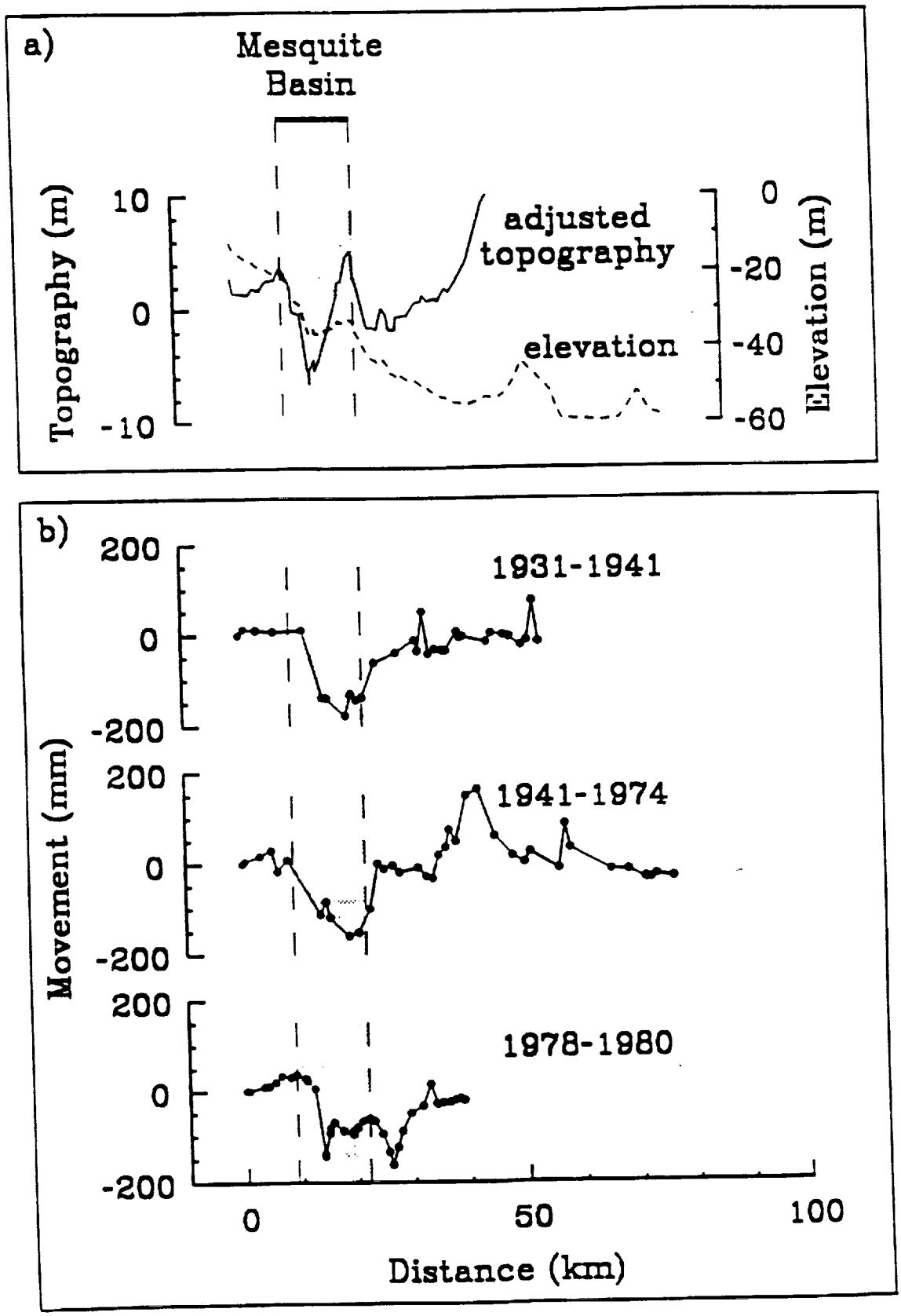
a)
Mesquite
Basin
Topography (m)
10
0
-10
adjusted
topography
elevation
0
-20
-40
-60
Elevation (m)
b)
200
0
-200
1931-1941
1941-1974
1978-1980
Movement (mm)
0
50
100
Distance (km)

17

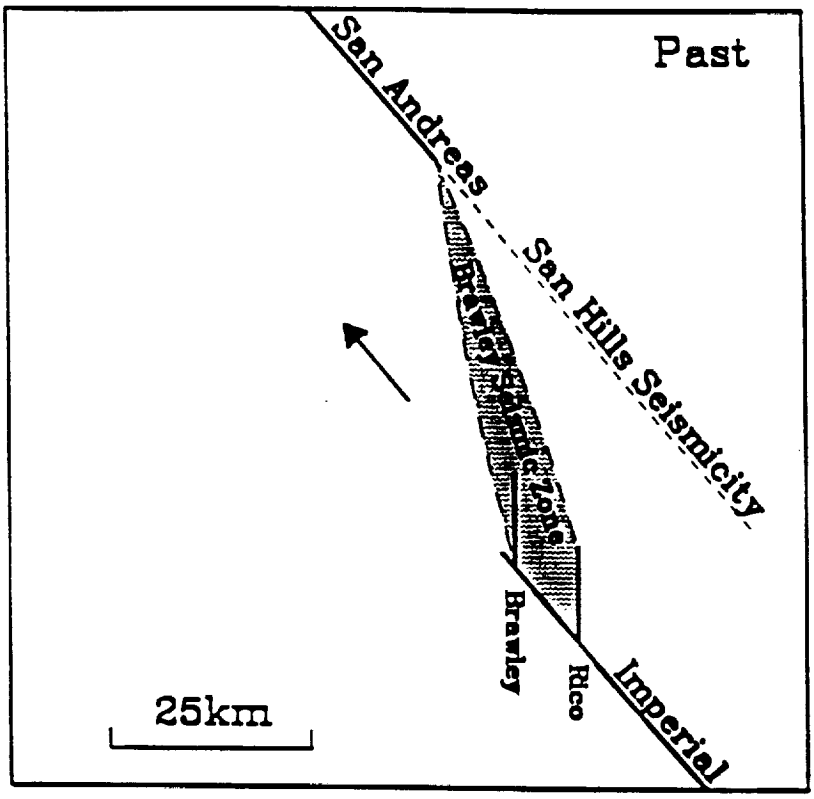
Past
San Andreas
San Hills Seismicity
Brawley Seismic Zone
Brawley
Rico
Imperial
25km

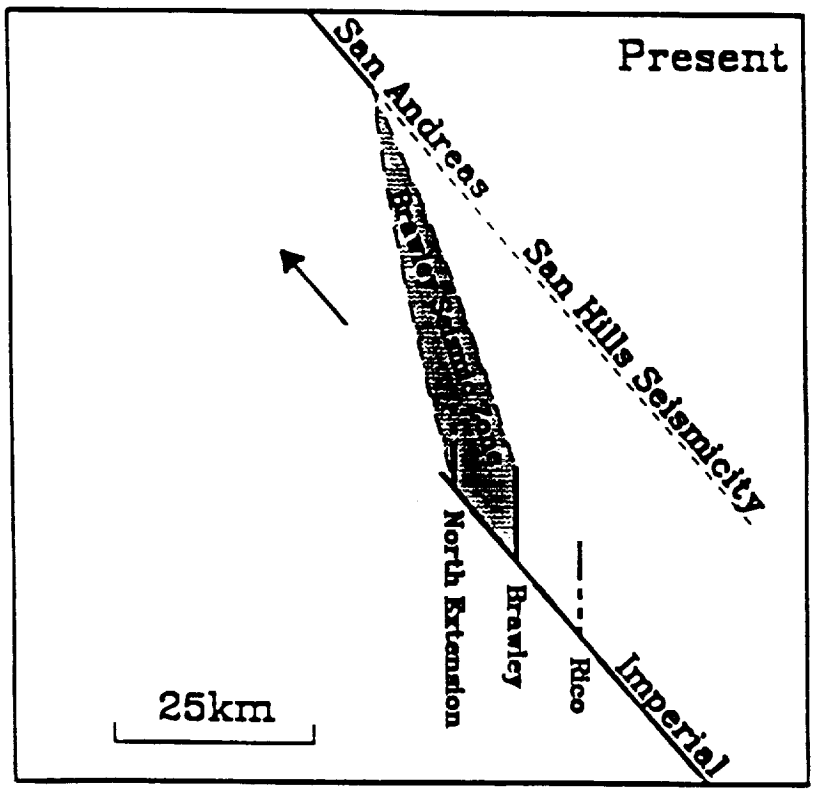
Present
San Andreas
San Hills Seismicity
North Extension
Brawley
Rico
Imperial
25km

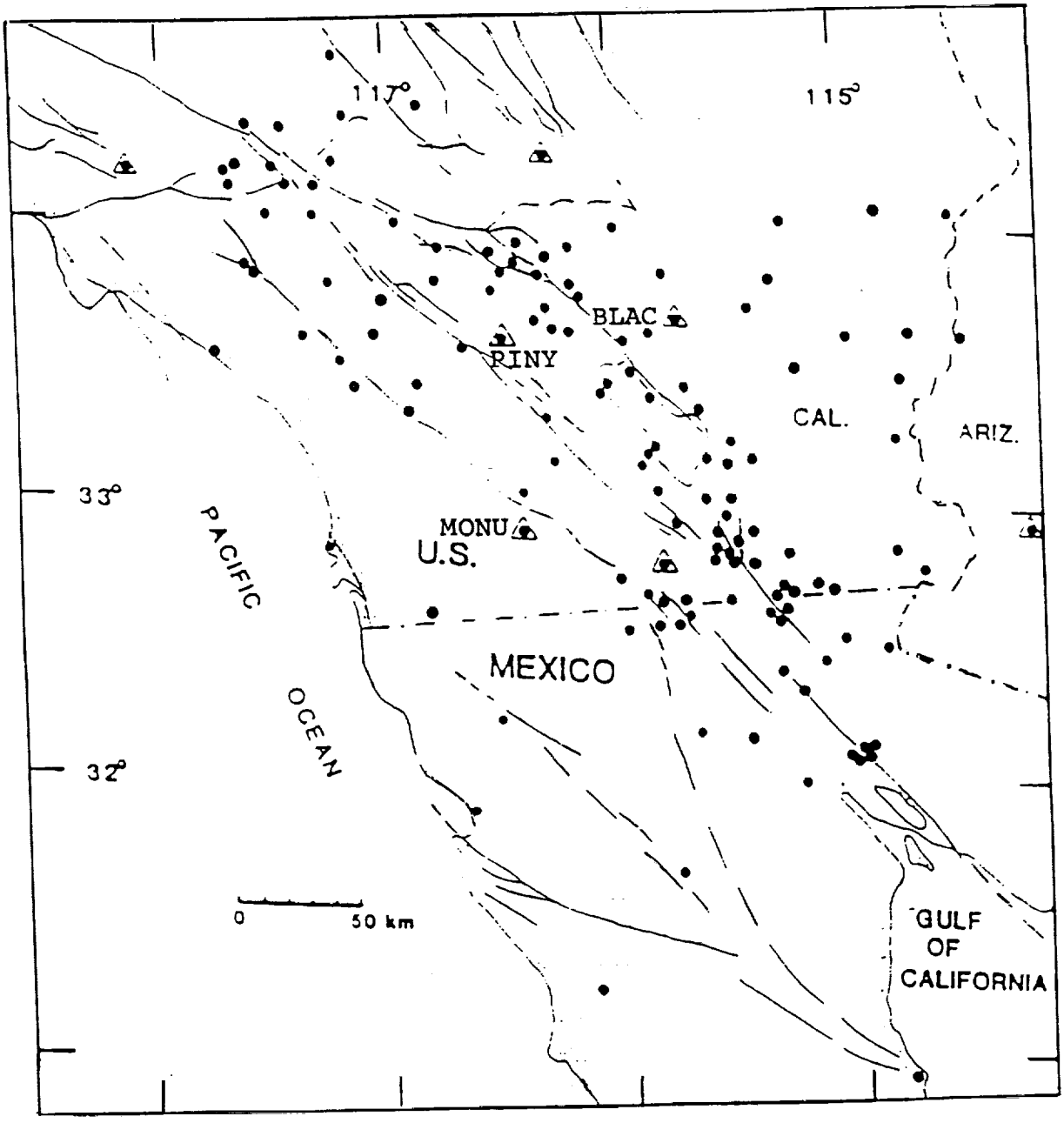
117°
115°
BLAC
RINY
CAL.
ARIZ.
33°
MONU
U.S.
PACIFIC
OCEAN
MEXICO
32°
0
50 km
GULF
OF
CALIFORNIA

9
10

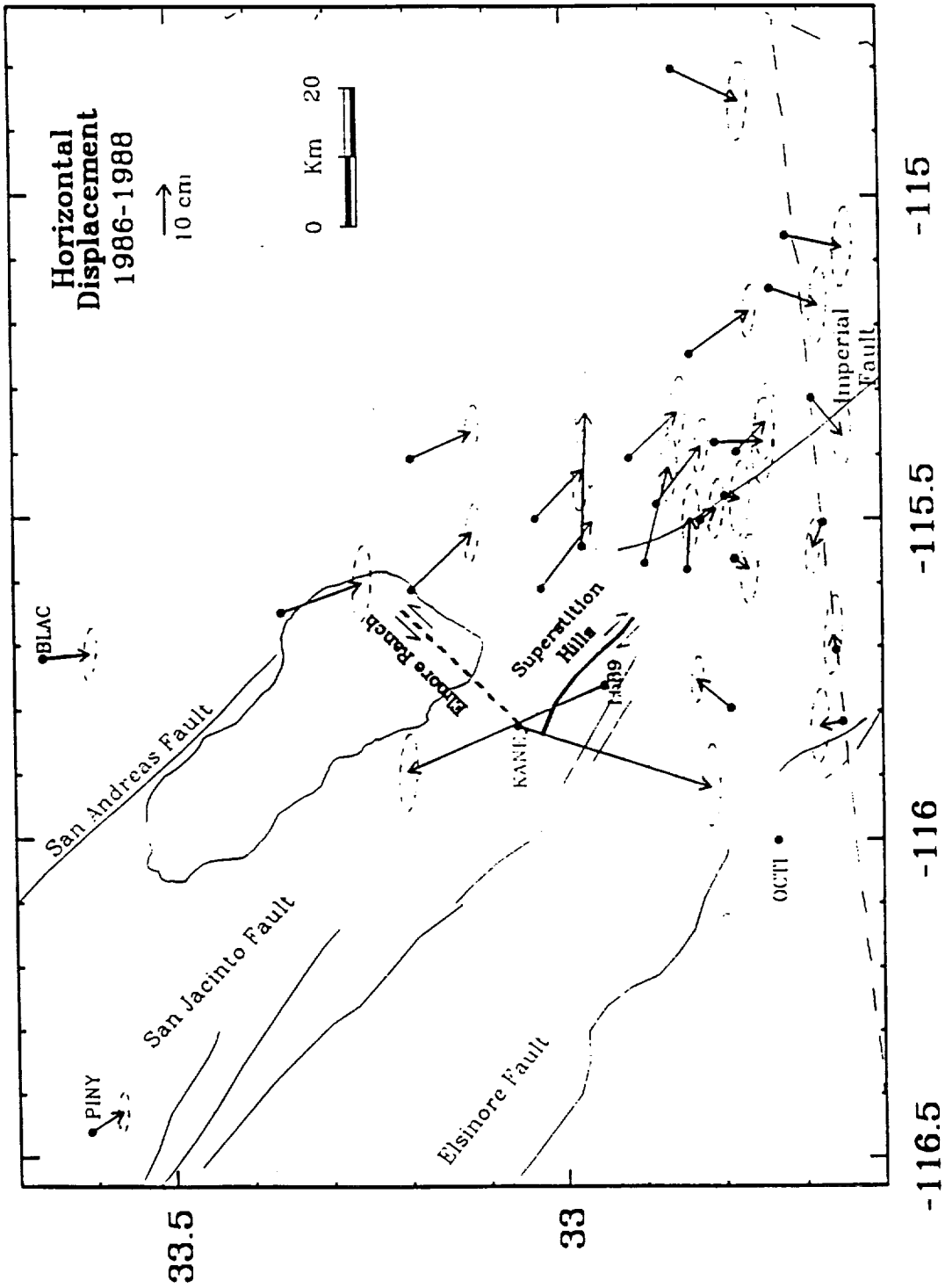
Horizontal
Displacement
1986-1988
10 cm
0 Km 20
BLAC
PINY
San Andreas Fault
San Jacinto Fault
Elsinore Fault
Superstition
Hills
Imperial
Fault
OCTI
-116.5
-116
-115.5
-115
33.5
33

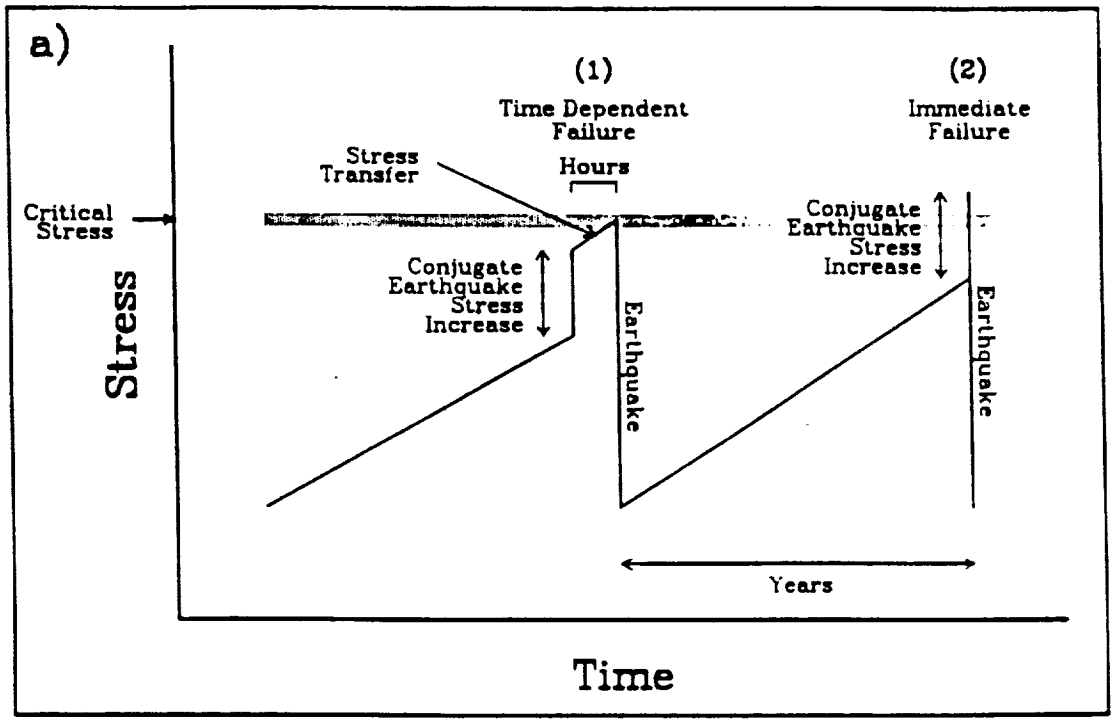
a)
(1)
Time Dependent
Failure
Hours
(2)
Immediate
Failure
Stress
Transfer
Critical
Stress
Conjugate
Earthquake
Stress
Increase
Earthquake
Conjugate
Earthquake
Stress
Increase
Earthquake
Stress
Years
Time

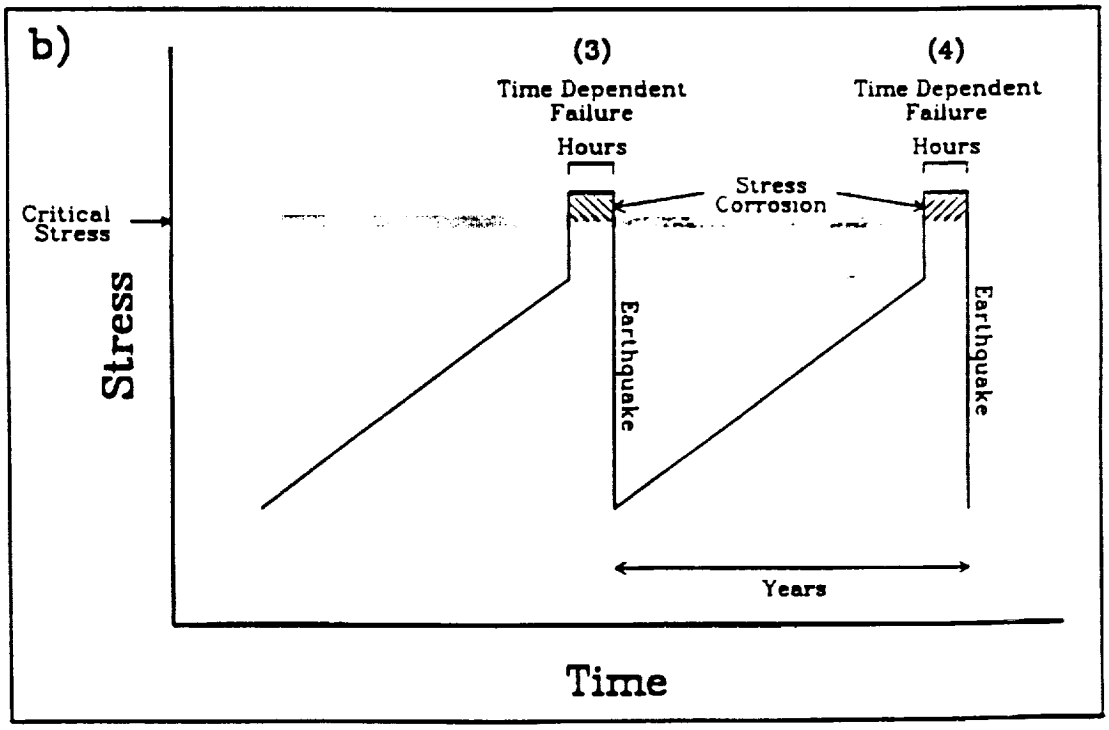
b)
(3)
Time Dependent
Failure
Hours
(4)
Time Dependent
Failure
Hours
Stress
Corrosion
Critical
Stress
Earthquake
Earthquake
Stress
Years
Time

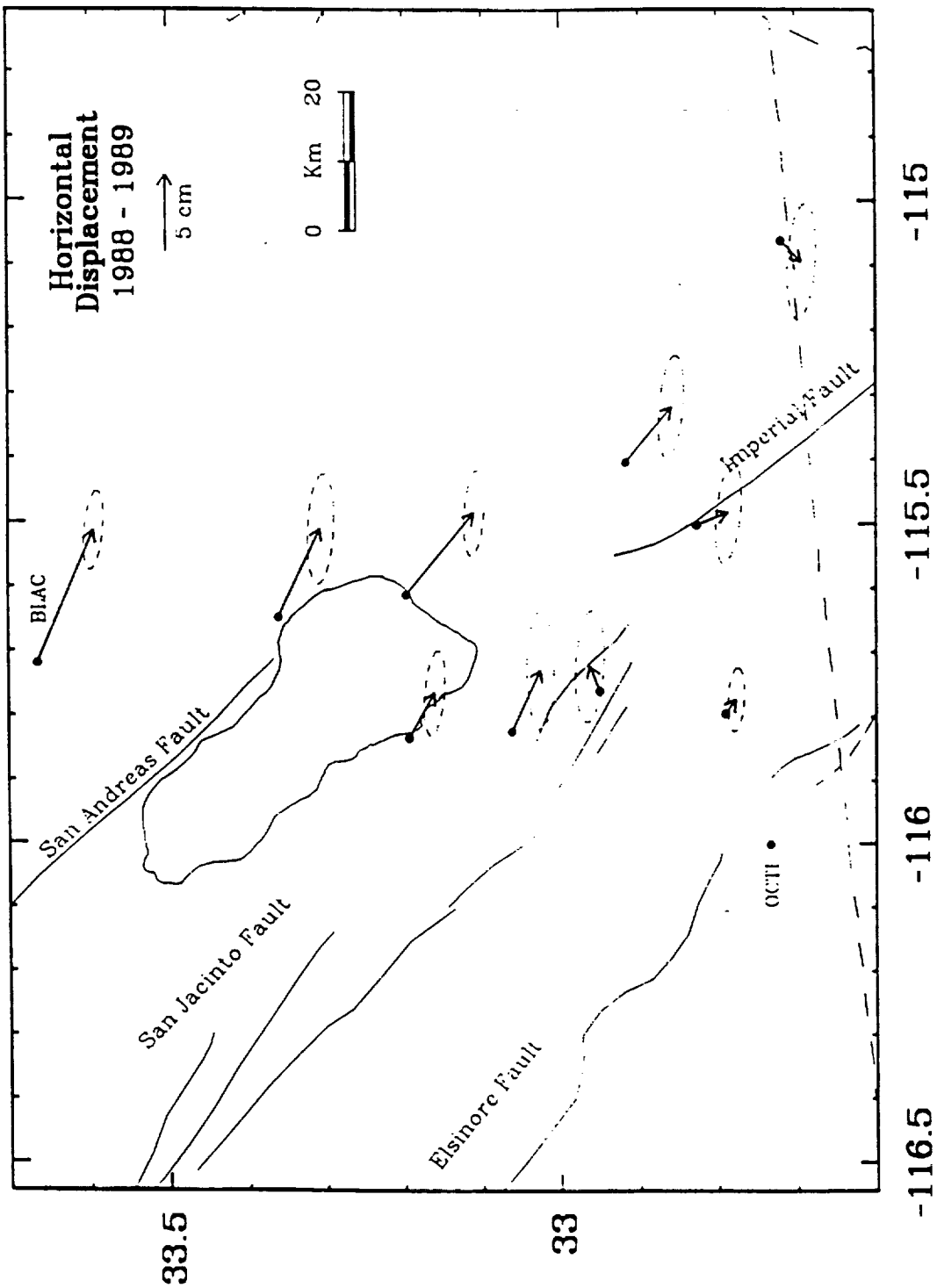
Horizontal
Displacement
1988 - 1989
5 cm
0 Km 20
BLAC
San Andreas Fault
San Jacinto Fault
Elsinore Fault
Imperial Fault
OCTI
33.5
33
-116.5
-116
-115.5
-115

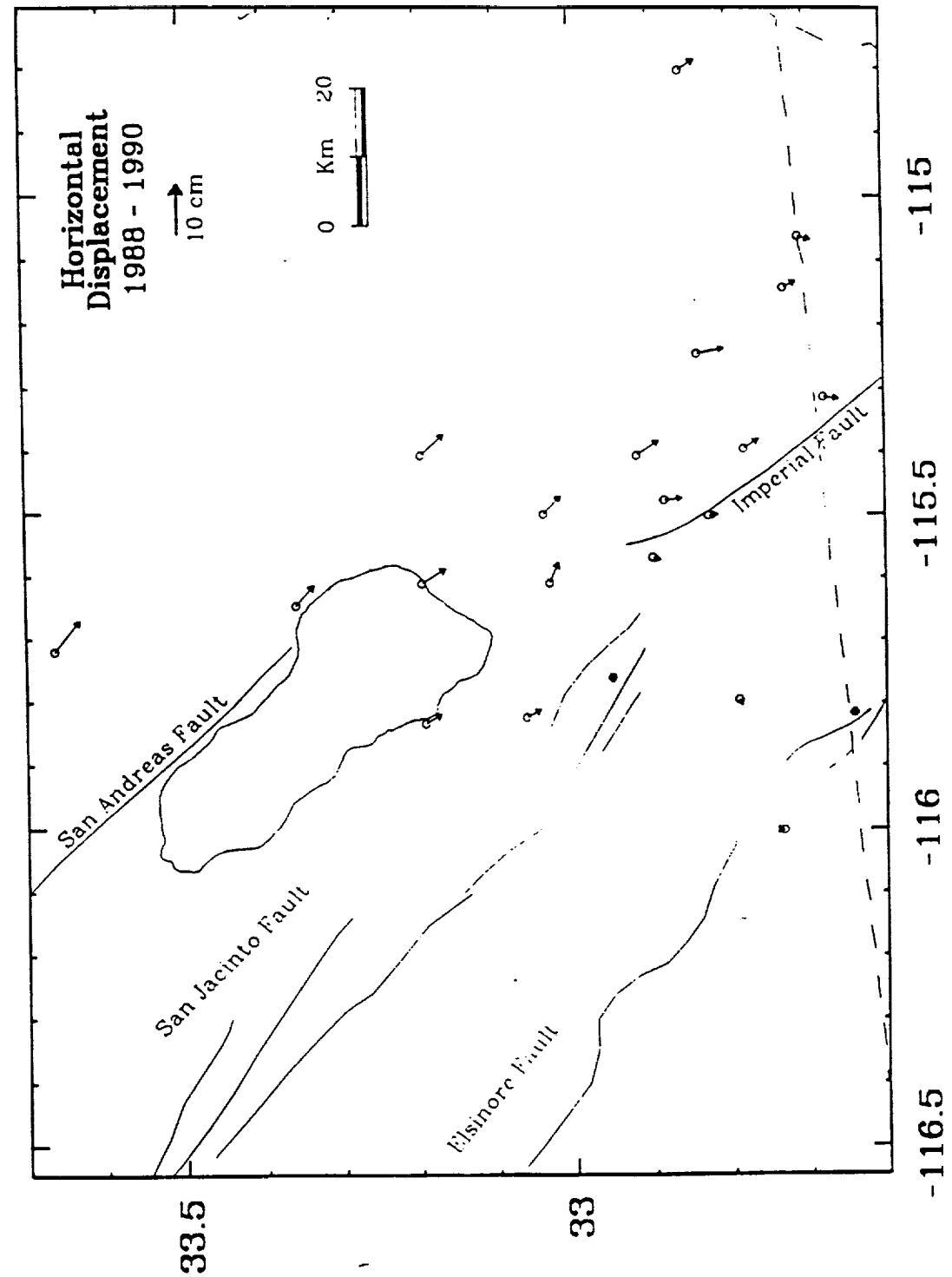
Horizontal
Displacement
1988 - 1990
10 cm
0 Km 20
San Andreas Fault
San Jacinto Fault
Elsinore Fault
Imperial Fault
33.5
33
-116.5
-116
-115.5
-115

APPENDIX 4

Oceanic transform earthquakes with unusual mechanisms or locations: Relation to fault geometry and state of stress in the adjacent lithosphere

by C. J. Wolfe, E. A. Bergman, and S. C. Solomon

Submitted to *J. Geophys. Res.*, 1992.

OCEANIC TRANSFORM EARTHQUAKES WITH UNUSUAL MECHANISMS OR LOCATIONS: RELATION TO FAULT GEOMETRY AND STATE OF STRESS IN THE ADJACENT LITHOSPHERE

CECILY J. WOLFE, ERIC A. BERGMAN[1], AND SEAN C. SOLOMON

Department of Earth, Atmospheric, and Planetary Sciences, Massachusetts Institute of Technology, Cambridge, Massachusetts

Submitted to *Journal of Geophysical Research*

March 1992

[1]Now at U.S. Geological Survey, National Earthquake Information Center, Golden, Colorado

ABSTRACT

On oceanic transforms, most earthquakes are expected to occur on the principal transform displacement zone (PTDZ) and to have strike-slip mechanisms consistent with transform-parallel motion. We conducted a search for transform earthquakes departing from this pattern on the basis of source mechanisms and locations taken from the Harvard centroid moment tensor catalogue and the Bulletin of the International Seismological Centre, respectively. Events with unusual mechanisms occur on several transforms. We have determined the source mechanisms and centroid depths of 10 such earthquakes on the St. Paul's, Marathon, Owen, Heezen, Tharp, Menard, and Rivera transforms from inversions of long-period body waveforms. Relative locations of earthquakes along these transforms have been determined with a multiple-event relocation technique. Much of the anomalous earthquake activity on oceanic transforms is associated with complexities in the geometry of the PTDZ or the presence of large structural features that may influence slip on the fault. Reverse-faulting earthquakes occur at a compressional bend in the Owen transform in the area of Mount Error and at the St. Paul's transform near St. Peter's and St. Paul's Rocks. A normal-faulting earthquake on the Heezen transform is located at the edge of a pull-apart basin marking an extensional offset of the fault. Normal-faulting earthquakes along the Tharp, Menard, and Rivera transforms may also be related to extensional offsets. Some events with unusual mechanisms occur outside of the transform fault zone, however, and do not appear to be related to fault zone geometry. For instance, earthquakes with mechanisms indicating reverse-faulting on ridge-parallel fault planes are located near the ridge-transform intersections of the St. Paul's and the Marathon transforms. Possible additional contributors to the occurrence of anomalous earthquakes include recent changes in plate motion, differential lithospheric cooling, and the development of a zone of weakness along the fault zone, but we do not find strong evidence to confirm the influence of these processes.

INTRODUCTION

Since *Sykes's* [1967] study of earthquakes on mid-ocean ridges confirmed the transform fault hypothesis [*Wilson*, 1965], the mechanisms of most earthquakes along oceanic transforms have been generally well-explained by a simple model. Such earthquakes are expected to have strike-slip mechanisms consistent with transform motion, to have vertical fault planes, and to occur on the principal transform displacement zone (PTDZ). A corollary of this standard model, from the classical theory of faulting, is that the direction of the most compressive principal stress, σ_1, is horizontal and makes an angle of 30° to 45° to the strike of the fault [*Anderson*, 1951]. Two current lines of research, however, suggest that this model bears closer scrutiny. First, studies of earthquake characteristics and fault mechanics along oceanic [*Prothero and Reid*, 1982; *Tréhu and Solomon*, 1983; *Bergman and Solomon*, 1988] and continental transforms [e.g., *Segall and Pollard*, 1980; *Sibson*, 1985; 1986; *McNally et al.*, 1989; *Saucier et al.*, 1991] have shown that bends or offsets in the fault can strongly affect the state of stress and pattern of earthquake faulting near such features. Second, there is increasing evidence that at least some oceanic and continental transforms act as weak zones relative to the adjacent lithosphere and that the stress state near the fault departs from classical theory [*Zoback et al.*, 1987; *Mount and Suppe*, 1987; *Wilcock et al.*, 1990].

Recent studies of individual oceanic transforms with high-resolution bathymetric mapping, side-scan sonar imaging, and observations from submersibles have revealed complex fault geometries and structures within the transform domain [*Fox and Gallo*, 1984, 1986]. Extensional or compressional jogs (bends or offsets) in the PTDZ have been documented along several transforms [e.g., *Macdonald et al.*, 1979, 1986; *Lonsdale*, 1986; *Gallo et al.*, 1986]. Microearthquake experiments conducted with ocean bottom seismometers have indicated patterns of seismicity and fault plane solutions consistent with the presence of extensional relay zones along the Rivera [*Prothero and Reid*, 1982] and Orozco [*Tréhu and Solomon*, 1983] transforms. Large earthquakes occurring near compressional fault jogs on the Kane and Vema transforms in the Atlantic have been

shown to consist of primary strike-slip events and secondary events with reverse faulting mechanisms [*Bergman and Solomon*, 1988].

Studies of continental strike-slip faults have illustrated the importance of fault geometry on the pattern of faulting. Jogs in stike-slip faults are known to produce uplift or subsidence along the fault, depending of whether the sense of the jog is compressional or extensional [*Sylvester*, 1988; *Bilham and King*, 1989; *Anderson*, 1990]. Numerical models of strike-slip faults that are offset or contain bends show that such geometry can considerably alter the state of stress [*Segall and Pollard*, 1980; *Saucier et al.*, 1991]. For instance, the thrust faulting component to the mechanism of the Loma Prieta earthquake has been attributed to the event's location at a local bend in the San Andreas fault in the Santa Cruz Mountains [*McNally et al.*, 1989]. Earthquake rupture can be stopped by both compressional and extensional fault jogs [*Segall and Pollard*, 1980; *Sibson*, 1985, 1986].

The orientation of stresses in central California, as inferred from borehole breakout data, off-fault focal mechanisms, and the trends of active reverse faults and thrust-related anticlines along the fault system, indicate that σ_1 is nearly perpendicular to the San Andreas fault within only a few kilometers of the fault zone [*Zoback et al.*, 1987; *Mount and Suppe*, 1987; *Jones*, 1988]. Such an orientation differs from that of the stress field farther (~100 km) from the fault. The lack of a heat flow anomaly across the San Andreas fault requires that shear stresses acting on the fault plane be low, less than about 20 MPa [*Brune et al.*, 1969; *Lachenbruch and Sass*, 1980]. These results, and a small predicted component of convergence between the Pacific and North-American plates, have led to the suggestion that plate motion along the San Andreas is decoupled by a weak fault zone into a low-stress, strike-slip component along the fault and a high-stress, compressional component off the fault [*Zoback et al.*, 1987; *Mount and Suppe*, 1987].

The orthogonality of ridge-transform plate boundaries suggests that oceanic transforms are also comparatively weak. A perpendicular ridge-transform-ridge configuration minimizes the energy dissipated along the plate boundary if the transform is a zone of weakness, i.e., if stresses resisting plate separation along the ridge axis are larger than the shear stresses along the transform

[*Lachenbruch and Thompson*, 1972; *Froidevaux*, 1973]. Curvature of the ridge-axis neovolcanic zone toward the transform fault as the ridge-transform intersection is approached is also consistent with ridge-axis stresses being several times larger than shear stresses on the transform [*Phipps Morgan and Parmentier*, 1984]. Fracture zone bathymetry and magnetic anomalies indicate that oceanic transforms are zones of weakness that adjust to changes in plate motion and can be deformed by compression or extension [*Menard and Atwater*, 1968]. In a microearthquake experiment along the active transform portion of the Kane Fracture Zone, *Wilcock et al.* [1990] observed that while the PTDZ was inactive during the experiment seismic activity near the base of the southern transform valley wall was characterized by normal faulting, with the axis of least compressive stress, σ_3, oriented perpendicular to the transform. Such a stress-state is consistent with the hypothesis that the transform acts as a zone of weakness.

To investigate further the nature of shear stress and deformation in the vicinity of oceanic transform faults, we have conducted a global search of large ($m_b \geq 4.5$) earthquakes on and near oceanic transforms for those events with unusual source mechanisms and locations. From an initial examination of the Harvard catalogue of centroid moment tensor (CMT) solutions [*Dziewonski et al.*, 1981], we identified transform earthquakes with mechanisms differing from the expected model of strike-slip motion on a vertical fault. We limit the present study to seven transforms on which we found anomalous earthquakes suitable for further study using an inversion of long-period body waveforms [*Nabelek*, 1984]. To provide better constraints on the pattern of seismicity and its relation to fault geometry, we relocated earthquakes along these transforms with a multiple-event relocation technique [*Jordan and Sverdrup*, 1981]. We consider the implications of these results for the standard fault model for transform slip, for the importance of geometrical irregularities in the fault trace, and for the state of stress near and along transforms.

A Search for Events with Anomalous Mechanisms

The search of the Harvard CMT catalogue for 1977-1989 for oceanic transform events with

mechanisms differing significantly from the prediction of the standard model was conducted as follows. Earthquake epicenters from the catalogue of the International Seismological Centre (ISC) for 1964-1989 served to define the geometry of the ridge-transform system. Transforms are identified by the trend of ISC epicenters and strike-slip mechanisms with the expected sense of motion. For large-offset transforms, on which there is a significant amount of earthquake activity, this means of identification is adequate. Figure 1 shows a sample map of earthquake epicenters and CMT mechanisms along the active portion of the Eltanin Fracture Zone, made up of three transforms along the Pacific-Antarctic plate boundary; several anomalous normal-faulting mechanisms are evident in this region. We excluded from this study areas where the ridge approaches a trench or a continent (e.g., the Gulf of California and the Gulf of Aden). There is possible bias in the search procedure in that earthquakes that displayed normal faulting mechanisms and occurred near the ridge-transform intersection with one or both nodal planes oriented parallel to the ridge axis were assumed to be related to the spreading process.

We identified 15 large-offset oceanic transform faults where earthquakes with anomalous mechanisms occurred during the 13-year study interval (we include the Udintsev transform in this list, where an anomalous strike-slip earthquake occurred in 1990). The mechanisms vary from reverse, to normal, to strike-slip with the wrong sense of slip for transform motion. Only 10 of these earthquakes (occurring on seven transforms) are well-enough recorded to permit body-waveform inversion. Table 1 lists the source parameters derived for these earthquakes. The CMT source parameters of other anomalous transform earthquakes are listed in Table 2. Figure 2 shows the location of the seven transforms that we have investigated in detail.

WAVEFORM INVERSION

In centroid-moment tensor analysis [*Dziewonski et al.*, 1981; *Dziewonski and Woodhouse*, 1983] long-period digital data are inverted for the six independent components of the moment tensor, as well as centroid origin time and location. The inversion includes all seismic phases that

arrive at a station prior to the arrival of Rayleigh or Love waves (for earthquakes having moments greater than about $1x10^{25}$ dyne cm long-period mantle waves are included). Data are filtered to exclude periods less than 45 s and do not constrain shallow centroid depths. In addition, for shallow earthquakes the components of the moment tensor corresponding to a vertical dip-slip or horizontal thrust mechanism are the least well resolved.

We have refined the mechanisms and centroid depths of the anomalous transform earthquakes using an inversion of long-period teleseismic P and SH waveforms [*Nabelek*, 1984] from stations of the World-Wide Standardized Seismograph Network (WWSSN). Because long-period WWSSN instruments have peak responses at 15-s period, this inversion can usually constrain the centroid depth and the vertical dip slip or horizontal strike-slip component of shallow earthquakes [*Nabelek*, 1984]. (However, CMT solutions are more sensitive to data at longer periods and better describe the seismic moment.) For 13 earthquakes, there is a good azimuthal distribution of stations with clear P and S arrivals on WWSSN analogue records. WWSSN records were digitized and corrected for differences in magnification and epicentral distance as described by *Bergman et al.* [1984]. Global Digital Seismic Network (GDSN) S-wave data were included when necessary to improve SH coverage. In a few cases, additional P-wave coverage was gained by using broad-band seismograms constructed by combining long-period and short-period GDSN data in the frequency domain [*Harvey and Choy*, 1982]. For such a construction we used a procedure similar to that of *Ekström* [1989]; short-period data were resampled at 0.2 s and broad-band data were filtered with a 3-pole band-pass Butterworth filter with corner frequencies at 0.015 Hz and 1.0 Hz.

The source parameters in the inversion are centroid depth, double couple mechanism, seismic moment, and the source time function (STF). The number of elements in the STF, taken as a series of overlapping triangles, is assigned prior to inversion and represents an additional parameter to be tested. In some cases the event is parameterized as two point sources or as a unilateral, horizontally propagating rupture along the strike of one of the nodal planes. For the latter situation a rupture velocity of 3.5 km/s is assumed. Values for the attenuation parameter t*

[*Futterman*, 1962] are taken to be 1.0 s for long-period P-waves and 4.0 s for long-period S-waves .

The assumed source velocity structure has an effect on the inversion results, in that takeoff angles of the rays and delay times of depth phases depend on the source structure. For slow-slipping transforms, we adopted the velocity structure used by *Bergman and Solomon* [1988], which was based on the refraction studies of *Bowen and White* [1986] and *Louden et al.* [1986] of the Vema transform (Table 3). For fast-slipping transforms, data on the velocity structure are limited: a study at the Orozco transform [*Tréhu and Purdy*, 1984] found anomalous velocity structure associated with relict ridge features and normal oceanic crust to the south of the transform. A model for normal oceanic crust (Table 3) was used for the source region along fast-slipping transforms.

Body-wave modelling has proven useful in determining the centroid depths of earthquakes in a number of tectonic settings, but the uncertainty in depths determined with this method is often difficult to establish. Discussions of the errors in determining centroid depths can be found in *Nabelek* [1984], *Huang et al.* [1986], *Stein and Wiens* [1986], *Goff et al.* [1987], and *Bergman and Solomon* [1988]. Factors such as signal-to-noise (S/N) ratio, station distribution, mechanism, and depth of faulting can all influence the magnitude of uncertainties.

For all events, we conducted a series of inversions with the depth fixed at values spanning a wide range; at each depth we solved for the remaining source parameters. The alignment between observed and synthetic seismograms and the length of the STF are both critical elements in this process. Seismograms are checked for proper alignment during each inversion, and STF lengths are chosen so that the final element tends toward zero amplitude. Our estimates of centroid depths are based on the interval over which the residual variance, given by the weighted mean squared difference between the observed and synthetic waveforms divided by the data variance (weighted mean squared observed waveforms), is minimized [*Huang et al.*, 1986]. While *Huang et al.* [1986] developed formal estimates of depth resolution using a statistical approach, *Bergman and Solomon* [1988] suggest that the range in centroid depth over which the residual variance varies by

no more than a small percentage of the data variance also allows a simple yet conservative estimate of the uncertainty in centroid depth. The presence of distinguishable depth phases provides another important constraint on centroid depths. However, apparent depth phases can be generated by either surface reflections from a simple source at a greater depth or a source at shallower depth with a complex STF. Within a range of minimum residual variance, we prefer solutions for which the STF is single-peaked and matches depth phases.

The results of the waveform inversions are given in Table 1. The inversions for individual events are discussed in Appendix A.

EARTHQUAKE RELOCATIONS

We applied a multiple-event relocation technique [*Jordan and Sverdrup*, 1981] to study the pattern of seismicity in the vicinity of unusual transform events. The advantage of a multiple-event relocation is its ability to reduce the effect of path-correlated noise on the relative locations of earthquakes within a small region. In the hypocentroidal decomposition method of *Jordan and Sverdrup* [1981], an inversion for the relative locations between events (the cluster vectors) is performed first, and then the global position of the average location of events within a cluster (the hypocentroid) is determined. This technique has advantages over other methods for multiple-event location in that it does not require fixing a master event and it makes full use of all available data.

This method is well suited for studying the relative locations of oceanic events with teleseismic data [*Jordan and Sverdrup*, 1981; *Bergman and Solomon*, 1990; *Wiens and Petroy*, 1990]. As with the single earthquake location problem, the epicentroid can be biased by errors in the theoretical travel times and uneven station distribution. *Bergman and Solomon* [1990] found by comparison with epicenters from a local ocean bottom seismograph network that the teleseismic epicentroid of a cluster of events on the northern Mid-Atlantic Ridge may be biased systematically to the north by as much as 15 km because of the concentration of stations in North America and Europe. The relative pattern of multiple-event locations tends to be less affected by such

systematic error, although station distribution for individual events still affects the axis orientation and aspect ratio of confidence ellipses, and errors may be significant for earthquakes with few arrivals in a single quadrant.

The ISC catalogue for January 1964-March 1989 was searched for earthquakes near each of the transforms of interest. We excluded events that could not be reliably located, for example events with fewer than 7 arrival times or events with data in less than three azimuth quadrants. Details of the data selection and inversion procedures, including the travel time calculation, ellipticity correction, and weighting of the data, were generally as described in *Bergman and Solomon* [1990]. The stations in the inversion were constrained to be within epicentral distances of 20° to 98°. Focal depths were fixed at 10 km below sea level. The relocation procedure drops data with residuals greater than 10 s in the first iteration and then uses 3 s as a maximum residual. The relocation procedure is repeated so that data with large relative errors can be flagged and omitted in the next inversion for relative location, although all such data are included in the final hypocentroidal inversion.

The absolute positions of relocated earthquakes are plotted in Figures 3-9. The relative positions of relocated earthquakes, including 95% confidence ellipses, are shown in Appendix B.

TRANSFORM FAULTS WITH UNUSUAL EARTHQUAKE MECHANISMS AND LOCATIONS

The anomalous transform mechanisms analyzed in this study occurred on seven oceanic transform faults along both slow- and fast-spreading ridges (Figure 2). In this section we present a synthesis of earthquake mechanisms and relocated epicenters on these oceanic transforms and of the relation of the earthquake characteristics to the geometry and structure of the transform fault zone.

Owen Transform

The Owen transform offsets the Carlsberg Ridge and the Sheba Ridge by 300 km. The present plate configuration was established at 10 My B.P., when magnetic anomalies indicate that spreading in the Gulf of Aden commenced [*Laughton et al.*, 1970; *Cochran*, 1981]. The boundary of a magnetic quiet zone, marking the limit of recent spreading on the Sheba Ridge, is presently located about 150 km from the ridge [*Cochran*, 1981], only halfway along the transform. *Stein and Cochran* [1985] argue on the basis of basement depths and heat flow measurements that the Error Ridge complex and the Sharbithat Ridge complex, which border the magnetic quiet zone, were formed by rifting of old oceanic lithosphere during the early stages of opening of the Gulf of Aden. Changes in the trend of the inactive limbs of the fracture zone are also observed near its intersection with Error Ridge [*Matthews*, 1966; *Cochran*, 1981] and Sharbithat Ridge [*Whitmarsh*, 1979].

Three earthquakes with unusual mechanisms have occurred on the southwestern portion of the transform fault zone in the vicinity of Error Ridge (Figure 3): the thrust-faulting event of July 7, 1986, the vertical dip-slip (or low-angle strike-slip) event of July 29, 1983, and the September 29, 1986, event having a strike-slip mechanism with an unusual fault orientation. In relocating earthquakes using the multiple-event technique, the assumption that P waves have traveled similar paths begins to break down at inter-event distances larger than perhaps 200-300 km. We therefore divided the large area around the southwestern ridge-transform intersection into three regions, and we relocated subsets of earthquakes on the ridge, at the ridge-transform intersection, and on the central portion of the transform (Appendix B, Figures B1-B3). The earthquakes of July 29, 1983, July 7, 1986, and September 29, 1986, are given as events 6, 8, and 13, respectively, in Figure B2. The September 29, 1986, earthquake is one of a series of aftershocks (events 12-15 in Figure B2) northwest of the large (M_o=2x10^{25} dyn cm) strike-slip main event of September 17, 1986 (event 11 in Figure B2). Three earthquakes occurred after the July 7, 1986, earthquake (events 9 and 10 in Figure B2, and event 14 in Figure B1), two on the transform, one on the ridge. Body

waveform inversions for the July 29, 1983, and July 7, 1986, earthquakes are given in Appendix A (Figures A1 and A2).

In the vicinity of the ridge-transform intersection, the earthquake epicenters and the bathymetry indicate an apparent compressional jog (Figure 3), although the transform in this area may be made up of several faults accommodating slip. To the northeast of the jog, the slip vectors of the strike-slip mechanisms and the epicenters follow a linear trend defining the transform fault zone. The July 29, 1983, and September 17, 1986, earthquakes, located near the intersection of the transform with the jog, both have one nodal plane on which horizontal slip would be in the expected direction of transform motion. The mechanism of the September 29, 1986, aftershock, however, is incompatible with expected transform motion. The orientation of both nodal planes of the July 7, 1986, reverse-faulting earthquake are rotated clockwise from the transform-parallel direction, a sense that is consistent with slip occurring at a compressional jog. The orientation of the maximum horizontal compressive stress indicated by the anomalous mechanism of the earthquake of July 29, 1983, is similar to that for most strike-slip events along the transform. The orientation of σ_1 for the September 29, 1986, earthquake indicates transform-perpendicular compression.

St. Paul's Transform

The three large equatorial transforms, the St. Paul's, the Romanche, and the Chain, offset the Mid-Atlantic Ridge by about 630, 940, and 300 km, respectively. In the central and eastern portion of the St. Paul's transform are at least three volcanically-active extensional relay zones [*Schilling et al.*, 1987]. A notable feature of this transform is the presence of St. Peter's and St. Paul's Rocks (hereafter referred to as just St. Paul's Rocks), a small group of nonvolcanic islets. While previous studies place the islets along a transverse ridge on the northern boundary of the transform, a revised bathymetric map indicates that the transform divides this feature (Figure 4). Studies have shown that St. Paul's Rocks consist mostly of mylonitized peridotite and hornblendite and are likely an upper-mantle-derived intrusion [e.g., *Melson et al.*, 1972]. Recent

volcanism is postulated to have occurred north of St. Paul's Rocks, where an alkali basalt associated with Quaternary sediments and carrying mylonitized ultramafic xenoliths was dredged [*Sinton*, 1979].

Several earthquakes with unusual mechanisms and locations are found in the area around St. Paul's Rocks (Figure 4). Because the study area is large, we have relocated events in three smaller subsets, with one group containing the area of the ridge north of the transform intersection and two groups covering the western part of the transform. As can be seen directly in the elongation of the confidence ellipses (Figures B4-B6), the distribution of stations for these events gives poorest epicentral resolution in the northwest to southeast direction. Events with anomalous locations (on October 11, 1973, November 14, 1982, and October 12, 1985) or CMT mechanisms (on September 20, 1986, April 20, 1988, and December 23, 1988) were selected for further study using waveform inversion. Data are not yet available for the earthquake of December 30, 1989, but this event had a small moment (7×10^{23} dyn cm) and likely cannot be analyzed by body-waveform inversion with WWSSN data.

The orientation of the greatest horizontal compressive stress indicated by the mechanisms of the two reverse-faulting earthquakes of September 20, 1986, and December 23, 1988, are similar, although rotated to more nearly perpendicular to the transform than the directions given by the strike-slip events. We postulate that these earthquakes may be associated with a small compressional jog in the vicinity of St. Paul's Rocks and that the presence of anomalous structure has an influence on fault motion. Further information is needed on the fault geometry and transform structure near St. Paul's Rocks before this conjecture can be evaluated. The April 20, 1988, reverse-faulting earthquake shows a fault plane striking parallel to the ridge, and the direction of maximum horizontal compressive stress is transform-parallel (σ_2 is perpendicular to the transform); this event was followed by a series of aftershocks (events 32, 33, 34, and 35 in Figure B5). The mechanism of the unusual strike-slip event of December 30, 1989, is consistent with a maximum horizontal compressional stress that is transform-parallel in this region (and σ_3 perpendicular to the transform).

Seismic activity outside of the transform fault zone (Figure 4) between longitudes 29° and 30° W could be the result of the anomalous stresses in the vicinity of St. Paul's Rocks. The anomalous locations of the larger events, however, are more likely the result of travel time errors. For instance, the off-transform location of the October 11, 1973, earthquake (event 16 in Figure B5) is strongly influenced by data from only two stations in the southern hemisphere; the event has a complicated source time function, which introduces large picking errors. The October 12, 1985, earthquake (event 27 in Figure B5) has a long source time function; picking errors could again be large. The November 14, 1982, earthquake (event 24 in Figure B5), with a simple STF, provides stronger evidence for deformation occurring outside the transform fault zone, slightly to the north of St. Paul's Rocks.

Marathon Transform

Between the Fifteen Twenty Fracture Zone and the Vema Fracture Zone, the Mid-Atlantic Ridge is offset by two smaller transforms, the Mercurius, which offsets the ridge by 45 km at 12° 10' N, and the Marathon, which offsets the ridge by 80 km at 12° 40' N [*Collette et al.*, 1979, 1980, 1984]. An anomalous reverse-faulting earthquake occurred on September 22, 1985, near the Marathon transform (Figure 5).

The ridge segments to the immediate north and south of the transform do not display recent seismic activity. Activity on the transform is limited to the ridge-transform intersections, an area along the central portion of the transform, and a sequence of events to the southeast of the transform valley (Figure 5). The anomalous thrust earthquake of September 22, 1985, was the first in a series of five events (9-13 in Figure B7) that occurred over a 4-day period on the southern transverse ridge. The period of the water reverberations in the P waveforms is consistent with a shallow water depth of 2-3 km.

Heezen and Tharp Transforms

The Heezen and Tharp transforms are two large-offset transforms on the fast-spreading Pacific-Antarctic plate boundary, which is called the East Pacific Rise to the north and the Pacific-Antarctic Ridge to the south of these fracture zones. The Heezen and Tharp transforms are closely spaced (100 km), offset the ridge by 350 and 650 km, respectively, and collectively constitute most of the transform portions of the Eltanin Fracture Zone (Figure 1). The seismic history of the Eltanin system has been investigated by *Stewart and Okal* [1983], who suggested that seismic slip from 1920-1981 was about one tenth that predicted by plate motion models. They attributed the deficit to a lack of larger earthquakes, since there have been few earthquakes with M_S greater than 6 and none with M_S greater than 7.

Earthquakes with extensional mechanisms occur along both the Heezen and the Tharp transforms. Figure 6 shows relocated events along a central portion of the Heezen transform. A normal-faulting earthquake occurred on the transform on February 17, 1978 (event 11 in Figure B8), and another occurred in a trough north of the transform on August 16, 1984 (event 17 in Figure B8). Figure 7 shows relocated events along a central portion of the Tharp transform. A normal-faulting earthquake occurred on the transform on October 10, 1982 (event 21 in Figure B9). The May 27, 1989, normal-faulting earthquake is considered an intraplate event.

The earthquakes of February 17, 1978, and May 27, 1989, were suitable for body waveform inversion (Figures A11 and A12). The August 16, 1984, earthquake on the Heezen transform and the October 10, 1982, earthquake on the Tharp display dilatational first motions on many short-period seismograms, consistent with the normal-faulting mechanisms indicated by CMT analysis.

A multibeam survey of a portion of the Heezen transform [*Lonsdale*, 1986] helps to identify the tectonic framework of the extensional events. Between 125° W and 126° W, there are three extensional offsets of the fault trace, with two of the offsets forming deep pull-apart basins [*Lonsdale*, 1986] (Figure 8). The February 17, 1978, earthquake was located near the easternmost offset. The August 16, 1984, event occurred off the Heezen transform; a recent multibeam and

side-scan sonar imaging survey of this area shows a transform-parallel trough that extends from the ridge (P. Lonsdale, personal communication, 1991).

The area of the Tharp transform near the epicenter of the October 10, 1982, normal-faulting earthquake has not been mapped with multibeam bathymetry. Because the pattern of earthquake seismicity is similar to that along the Heezen, however, we suggest that an extensional offset may be present along the Tharp transform in the vicinity of the epicenter.

Menard Transform

The Menard transform, north of the Eltanin system, is a large-offset transform on the fast-spreading Pacific-Antarctic plate boundary. Bathymetric and geophysical data for this transform are given by *Molnar et al.* [1975]. A normal-faulting earthquake occurred along this transform on May 15, 1987 (Figure 9).

A seismicity gap about 50 km long occurs to the west of the anomalous event (event 28 in Figure B10). Waveform inversion for the May 15, 1987, earthquake is given in Figure A13. The direction of maximum horizontal compressive stress of the normal-faulting earthquake is similar to that of the strike-slip earthquakes.

Multibeam data from a recent survey indicate that a small extensional offset may be present at 116° W, where two parallel troughs, offset of by 1-2 kilometers, overlap (P. Lonsdale, personal communication, 1991). The bathymetry within the Menard transform does not indicate the presence of a large extensional offset similar to that along the Heezen transform.

Rivera Transform

The current plate configuration at the Rivera transform was established around 3.5 My. B.P., when spreading was abandoned on the Mathematician Ridge and transferred to the Pacific-Cocos Rise [*Klitgord and Mammerickx*, 1982]. An abrupt change in orientation and tectonic character

occurs mid-way along the transform near longitude 107.5° W. West of this area, seismicity is more diffuse, bathymetry exhibits greater relief, and several subparallel valleys are suggested, although it is not known how slip is being accommodated [*Ness and Lyle*, 1991]. Teleseismically recorded earthquakes are generally smaller and more frequent in the western area, and there is a greater tendency for swarms to occur [*Prothero and Reid*, 1982]. *DeMets and Stein* [1990] find that the azimuths of the transform strike and earthquake slip vectors west of 108.3 ° W are systematically rotated by several degrees clockwise relative to the azimuths predicted by the Pacific-Rivera Euler vector. An extensional offset of the transform has been identified at 108° W on the basis of bathymetry and an en echelon pattern of microearthquakes [*Prothero and Reid*, 1982]. *Prothero and Reid* [1982] found a second en echelon offset of microearthquakes west of 109° W, possibly indicating another extensional relay.

Figure 10 shows relocated earthquakes ($m_b \geq 4.5$) and mechanisms along a portion of the western Rivera transform. As seen in Figure B11, epicentral confidence ellipses are elongated in the northeast-southwest direction due to the lack of arrivals to the southwest, and the location uncertainty in this direction is large. While most earthquake epicenters and mechanisms are consistent with the expected transform motion, to the west of 109° W some earthquake epicenters appear to lie north of the transform. This pattern occurs near the area where *Prothero and Reid* [1982] report an en echelon pattern of microearthquake epicenters.

Several earthquakes with anomalous mechanisms are located west of 109° W. The normal-faulting earthquake of September 21, 1977, occurred in the seismically active inner corner of the rise-transform intersection. In addition, three earthquakes with predominantly strike-slip mechanisms but with the strike directions of the probable fault planes rotated clockwise from the expected transform direction occurred on May 8, 1983. These earthquakes are a part of a sequence of about 15 events that span a 3-day period. The May 9, 1983, earthquake having a strike-slip mechanism with an anomalous fault dip is the largest event in this sequence (M_o=4.2x10^{25} dyn cm). The earthquake of February 17, 1984, is located to the east of a short offset of the rise axis, a region where deformation may be more complex than simple strike-slip motion [*Lonsdale*, 1991].

The mechanism of this earthquake also shows a strike direction of the probable fault plane that is rotated clockwise from the expected direction of transform slip. Current bathymetric information does not permit a clear association of the unusual pattern of epicenters and mechanisms with morphologic features and physical processes.

CENTROID DEPTHS

Centroid depths of strike-slip earthquakes along the St. Paul's transform and the two reverse-faulting earthquakes near St. Paul's Rocks may be compared with results for other large earthquakes [*Engeln et al.*, 1986; *Bergman and Solomon*, 1988] and for microearthquakes [*Francis et al.*, 1978; *Wilcock et al.*, 1990] on slow-slipping transforms. In contrast, centroid depths are not well-resolved on the Heezen and Menard transforms because of the poor P-wave signal-to-noise ratios and the sparse sampling of waveforms. The age offset of the Owen transform is not fully developed, because oceanic crust generated by spreading on the Sheba ridge to the north extends only halfway along the transform, so the depth of seismic faulting cannot be simply related to thermal models.

From body waveform modelling *Engeln et al.* [1986] reported centroid depths along Atlantic transforms from 2-7 km below the seafloor and suggested that earthquake faulting is limited by the 600° C isotherm. *Bergman and Solomon* [1988] disputed this result and found that centroid depths on such transforms are generally 7-10 km, consistent with a nominal limiting isotherm of 900° $\pm$ 100° C. The centroid depths of 10-14 km that we determine for earthquakes along the St. Paul's transform are in agreement with the conclusions of *Bergman and Solomon* [1988]. To estimate the value of the isotherm limiting earthquake faulting we follow the method of *Bergman and Solomon* [1988]: we average the isotherms in adjoining lithospheric plates, in which temperatures are calculated from a standard plate-cooling model [*Parsons and Sclater*, 1977]. The depth extent of faulting is assumed to be twice the centroid depth. The presence of volcanically active relay zones within the transform and the lack of magnetic anomaly information on age offset,

however, complicate specification of a thermal model. For a constant half-spreading rate of 16 mm/yr [*DeMets et al.*, 1990] and a fault offset of 630 km, the hypothesis that the depth of faulting is limited by the 900° C isotherm is sustained (Figure 11a). If the fault offset is shortened to 300 km by postulating that volcanically active relay zones have thermal structures similar to fully developed ridge segments, the limiting isotherm may be as high as 1000° C (Figure 11b).

The depths of microearthquakes are typically somewhat shallower than the inferred maximum depths of faulting of large earthquakes. *Francis et al.* [1978], from a microearthquake experiment at the eastern intersection of the St. Paul's transform and the Mid-Atlantic Ridge, found that earthquakes occurred in two depth intervals: shallow shocks at 0-1 km depth mostly occurred as small swarms on the ridge axis, while events clustered near 7 km depth occurred on the active transform. *Wilcock et al.* [1990] reported microearthquake focal depths along the Kane transform of 3-6 km near the ridge-transform intersection and 5-9 km in the transform fault zone distant from the intersection.

DISCUSSION

The mechanisms of transform earthquakes provide important information about mechanical processes occurring along the transform. In this section we evaluate the possible processes contributing to the occurrence of such events by comparing the characteristics of anomalous earthquakes to be expected from each process against our observations.

Importance of Fault Geometry and Structure

Bends or offsets in strike-slip faults are capable of generating anomalous stresses in the adjoining blocks, producing uplift or subsidence, and influencing the pattern of faulting [e.g., *Segall and Pollard*, 1980; *Sibson*, 1985, 1986; *Bilham and King*, 1989; *McNally et al.*, 1989; *Anderson*, 1990; *Saucier et al.*, 1991]. Previous studies [*Prothero and Reid*, 1982; *Tréhu and*

Solomon, 1983; *Bergman and Solomon*, 1988] have shown that anomalous patterns of seismicity can also occur at bends or offsets in oceanic transforms. The observations of this study provide additional evidence that the presence of complex fault geometry and structure can influence the pattern of earthquake locations and mechanisms along oceanic transforms. Such irregularities in fault geometry can be expected to arise from a variety of processes influencing the temporal evolution of the PTDZ (e.g., changes in plate motion, diapiric rise of altered blocks of lower crustal or upper mantle material, volcanic construction, fault-normal compression or extension, variability in ridge axes accretion, small deviations of transform strike from the ideal small circle).

At the western ridge-transform intersection of the Owen transform, as noted above, bathymetry, earthquake epicenters, and the presence earthquakes with anomalous mechanisms indicate the existence of a compressional fault jog (Figure 3). The interaction of the active transform with Error Ridge, anomalous structure inherited from the opening of the Gulf of Aden, may account for the complex fault geometry.

At the St. Paul's transform, the reverse-faulting earthquakes occurring near St. Paul's Rocks (Figure 4) may be associated with a compressive fault jog, similar to the case at the Owen transform. Elemental and isotopic chemistry, mineralogy, and geothermometry of islet samples suggest that St. Paul's Rocks may be a relict of sub-continental mantle, left behind in the opening of the Atlantic and subsequently emplaced as surface blocks [*Bonatti*, 1990]. While complexities in fault geometry may be responsible for the present deformation near St. Paul's Rocks, it is less likely that fault geometry was the principal cause for the original emplacement of this feature. Rapid ascent from depths $\geq$ 30 km and emplacement in the solid state are suggested by the presence of mantle-equilibrated primary assemblages in the form of augen within a variably recrystallized mylonite matrix [*Melson et al.*, 1972]. Uplifted blocks have been found on the walls of many transforms; petrologic investigations suggest that these blocks are made up of gabbro or peridotite that originated in the lower crust or upper mantle [e.g., *Bonatti*, 1978; *Bonatti and Hamlyn*, 1978].

Along the Pacific-Antarctic plate boundary, the normal-faulting earthquakes occurring on the

Heezen, Tharp, and Menard transforms appear to be associated with extensional jogs in the trace of the PTDZ. At the Heezen transform, a normal-faulting earthquake occurred on the border of an extensional offset (Figure 6), possibly reflecting a normal fault at the edge of a pull-apart basin. Normal-faulting earthquakes on the Tharp (Figure 7) and the Menard (Figure 9) transforms may also be associated with extensional offsets.

At the western ridge-transform intersection of the Rivera transform, a normal-faulting earthquake and several strike-slip events with anomalously striking fault planes have occurred (Figure 10). Earthquake epicenters appear offset to the northeast of the expected transform location, although the constraint on locations in the direction perpendicular to the transform is weak. An extensional offset of the Rivera transform may occur west of 109° W. Alternatively, the earthquakes with anomalous mechanisms may reflect internal deformation of the Rivera plate .

Fox and Gallo [1984] argue that higher strain rates and the juxtaposition of thinner lithosphere will allow relay zones to develop more easily along transforms at fast-spreading ridges. In accord with this hypothesis, extensional relay zones have been mapped along a number of other transforms along the East Pacific Rise, including the Tamayo [*Macdonald et al.*, 1979], the Orozco [*Tréhu and Solomon*, 1983; *Madsen et al.*, 1986], the Clipperton [*Gallo et al.*, 1986], and the Siqueiros [*Fornari et al.*, 1989] transforms, and the Quebrada, Discovery, Gofar, Wilkes, and Garrett transforms on the Pacific-Nazca spreading center [*Lonsdale*, 1989]. (A recent compilation of transforms known to have extensional relay zones can be found in *Fornari et al.* [1989].) The CMT catalogue does not include events with normal-faulting mechanisms along these transforms. An anomalous strike-slip earthquake, having a sense of slip opposite that expected for transform motion, occurred along the right-stepping Gofar transform (Table 2), but this earthquake is probably associated with one of two small left-stepping offsets south of the Gofar [*Lonsdale*, 1989].

The lack of teleseismically observable normal-faulting earthquakes along most of the fastest-slipping transforms may be because many of these extensional relay zones occur as intra-transform spreading centers. At fast-spreading rates, such relays would not be expected to display significant

seismicity at teleseismic distances. Crustal thinning and magmatic activity (either intrusive or extrusive) within the extending region of the transform could yield anomalously high temperatures, at most a thin seismogenic layer, and thus a paucity of observable activity. The presence of amphibolite-facies metamorphic rocks collected in the vicinity of the pull-apart at 125.7° W on the Heezen transform provide indirect evidence for limited magmatic intrusion associated with crustal thinning [*Lonsdale*, 1986].

Extensional offsets may also have an influence on the rate of release of seismic moment along fast-slipping transforms. The maximum moment of transform earthquakes appears to decrease and the moment-rate deficit increase with increasing spreading rate [*Burr and Solomon*, 1978; *Kawasaki et al.*, 1985]. The presence of fault offsets could inhibit rupture of long fault segments and limit the maximum moments of earthquakes, although it is not clear how fault offsets would affect the total moment release. The thermal and compositional effects of offsets could also be important.

Influence of Changes in Spreading Direction

Changes in plate motion may lead to the occurrence of earthquakes with anomalous mechanisms by altering fault geometry and by introducing a component of compression or extension along the fault. For instance, along the Pacific-Nazca plate boundary, a recent small clockwise rotation is inferred to have created intra-transform spreading centers within large-offset, right-stepping transforms [*Lonsdale*, 1989]. Others have suggested that recent plate motion changes have occurred along the Rivera, Eltanin, and St. Paul's transforms [*Lonsdale*, 1986; *Schilling*, 1987; *DeMets and Stein*, 1990]. We examine whether these changes appear to have been a significant influence in the occurrence of earthquakes with anomalous mechanisms and locations.

The Pacific-Rivera magnetic lineations show that the rise crest has progressively rotated 5-15° in a clockwise direction in the last 5 My [*DeMets and Stein*, 1990], putting the left-stepping Rivera transform in compression. This change in spreading direction is compatible with the apparent

rotation of stresses toward transform-perpendicular compression inferred from the anomalous strike-slip earthquakes near the ridge-transform intersection. Such a change would tend to destroy extensional relay zones along the left-stepping transform, although at least one such relay zone has been suggested on the basis of seismicity and bathymetry.

Recent plate motion changes at the Eltanin may explain the occurrence of several earthquakes with normal-faulting mechanisms. Magnetic anomalies north of the Heezen transform show a 10° clockwise rotation of spreading in the past 4 My, which would put the right-stepping transform in extension in the more recent past and would favor the development of extensional offsets [*Lonsdale*, 1986], similar to the situation along the Pacific-Nazca plate boundary.

The normal-faulting mechanisms along the Eltanin fault system and at the Menard transform may also reflect regional stresses caused by plate motion changes. Minor internal plate deformation in the past 20 My near this region of the Pacific-Antarctic plate boundary has been suggested to explain the possible mismatch of fracture zones from plate reconstructions [*Stock et al.*, 1991]. Analysis of bathymetric and magnetic data [*Molnar et al.*, 1975; *Lonsdale*, 1986] and of geoid data [*Mayes et al.*, 1990] demonstrates the evolution of spreading direction in the past: the spacing between the Heezen and Tharp fracture zones decreased by 100 km due to changes in the spreading direction along the Pacific-Antarctic spreading center about 20-35 My ago. The destruction of small, left-offsetting fracture zones and the creation of many small, right-offsetting fracture zones occurred during this counterclockwise change in plate motion [*Molnar et al.*, 1975], consistent with the view that transforms, particularly along fast-spreading rises, are zones of weakness that can adjust readily during plate motion changes [*Menard and Atwater*, 1968]. Regional deformation may explain the occurrence of normal-faulting earthquakes with similar orientation both along the transforms and in intraplate settings, such as south of the Tharp transform.

A survey of the Mid-Atlantic Ridge north of the St. Paul's transform [*Schilling*, 1987; *Schilling et al.*, 1987] revealed that the morphologic grain changed orientation from about N340-350°E to 0° over the past 0.2 My and that the ridge has propagated northward from the transform, perhaps in

response to a clockwise change in spreading direction and rotation of the fracture zone, as proposed by *Bonatti and Crane* [1982] for the Vema transform. The change in ridge orientation may explain the ridge-perpendicular compressive stresses indicated by earthquakes with unusual mechanisms near the western ridge-transform intersection. *Schilling* [1987] has suggested that this clockwise change in orientation may have led to the development of extensional relay zones in the transform.

In summary, there is some indication that changes in plate motion are responsible for the occurrence of anomalous earthquake activity along some oceanic transforms, but further evidence is required to support this hypothesis.

Thermal Stresses

Thermal stresses generated by the differential cooling of oceanic lithosphere have been suggested as a primary cause of oceanic intraplate earthquakes, on the basis of the pattern of earthquake source characteristics with depth and seafloor age [*Bratt et al.*, 1985; *Parmentier and Haxby*, 1986]. Two-dimensional models of thermal stresses predict large, ridge-parallel extensional stresses near the ridge-transform intersection [*Sandwell*, 1986; *Haxby and Parmentier*, 1988]. It has also been proposed that fracture zones form in response to such ridge-parallel extension [*Collette*, 1974; *Turcotte*, 1974]. The presence of earthquakes with mechanisms indicating that the least compressive horizontal stress is ridge-parallel in the vicinity of the ridge-transform intersections of the St. Paul's and Marathon transforms are thus consistent with a controlling influence by thermal stresses. A quantitative analysis comparing a larger set of earthquake data with appropriate three-dimensional models of thermal stress near oceanic transforms is necessary to provide a rigorous test of this hypothesis.

Evidence for a Weak Fault

As noted earlier, some oceanic and continental transforms appear to act as zones of weakness, with low shear stresses on the fault and a horizontal principal stress oriented in a nearly fault-normal direction in the lithosphere adjacent to the fault [*Zoback et al.*; 1987; *Mount and Suppe*, 1987; *Wilcock et al.*, 1990]. In this section, we consider whether transform earthquakes with anomalous mechanisms provide additional evidence for the presence of a weak fault zone.

On the St. Paul's and Marathon transforms, shallow reverse-faulting events with ridge-parallel fault strikes occur near the ridge-transform intersections. A strike-slip event with an unusual orientation occurred near the site of the reverse-faulting event at the St. Paul's transform. The mechanisms of these earthquakes indicate transform-perpendicular extension near the ridge-transform intersection. Near St. Paul's Rocks, on the other hand, the reverse-faulting focal mechanisms imply that the horizontal stresses are rotated toward transform-perpendicular compression. Differences in fault geometry and structure may account for this difference in the ordering of principal stresses. In the area of the compressive fault jog at the Owen transform, an anomalous strike-slip earthquake indicating transform-perpendicular compression occurred as an aftershock to an earthquake with mechanism compatible with transform-parallel motion. At the Eltanin transform, several normal-faulting earthquakes show an orientation of stresses similar to that of a normal-faulting intraplate earthquake that occurred 100 km south of the Tharp transform (Figure 1) and thus are more likely a response to a regional stress field. Earthquakes with anomalous strike-slip mechanisms near the Rivera transform indicate a stress field tending toward transform-perpendicular compression.

We see no strong evidence in these data to support the view that oceanic transforms are generally weaker than the surrounding lithosphere on the basis of a systematic perturbation to the regional stress field. Neither do the observations invalidate this hypothesis, however. The mechanisms of the large anomalous earthquakes in this study appear to be dominated by factors other than a systematically reduced strength on the transform. We note that no anomalous large

earthquakes were found on the Kane transform, where the microearthquake experiment of *Wilcock et al.* [1990] found several events within the transform valley indicative of extension perpendicular to the transform.

CONCLUSIONS

A number of large earthquakes with mechanisms or locations inconsistent with simple models have occurred near large-offset oceanic transform faults. Much of the earthquake activity can be associated with complex fault geometry or large structural features that apparently influence slip on the fault. Compressional fault jogs associated with anomalous structures are likely responsible for earthquakes with unusual mechanisms on the Owen and St. Paul's transforms. A normal-faulting earthquake on the Heezen transform occurs at the edge of an extensional offset, and other normal-faulting earthquakes on transforms along the East-Pacific Rise may likewise be associated with extensional offsets.

Several other factors may contribute to the occurrence of such earthquakes, but we do not find strong evidence to support their influence. Recent changes in plate motion, suggested to have occurred at the Eltanin, Rivera, and St. Paul's transforms, could contribute to the presence of anomalous earthquakes by influencing fault geometry or the state of stress along the fault. Thermal stresses near ridge-transform intersections may lead to earthquakes having reverse-faulting mechanisms characterized by a ridge-parallel least compressive stress; events with such mechanisms are seen near the ridge-transform intersections of the St. Paul's and Marathon transforms. While some earthquakes show evidence for a nearly transform-perpendicular orientation of one of the principal horizontal stresses, consistent with a weak fault zone, our results do not resolve whether oceanic transforms are generally weaker than surrounding lithosphere.

APPENDIX A: EARTHQUAKE SOURCE MECHANISMS FROM BODY WAVEFORM INVERSION

In this appendix we present the details of long-period P and SH waveform inversion for the 13 transform earthquakes listed in Table 1. The orientation (strike/dip/slip) of each double couple mechanism is presented according to the convention of *Aki and Richards* [1980]. Centroid depths are given relative to the seafloor.

July 29, 1983, Owen transform (Figure A1)

Waveform inversion for this event indicates a mechanism of 214/89/298, similar to the CMT solution of 37/71/44 [*Dziewonski et al.*, 1984], and consistent with either predominantly dip-slip motion on a nearly vertical fault oriented approximately parallel to the transform or primarily right-lateral strike-slip motion on a northeasterly-dipping low-angle fault. Vertical short-period records at KEV and CHG were examined to confirm the polarity of the first pulses. The SH-wave data for this event provide strong constraints on the unusual mechanism. The minimum residual occurs for centroid depths between 6 and 16 km.

July 7, 1986, Owen transform (Figure A2)

The earthquake of July 7, 1986, on the Owen transform is the largest event (M_0=3.7x10^{25} dyn cm) in the catalogue of anomalous transform events. There is good coverage of the focal sphere, and the waveforms are best fit by a reverse-faulting solution (238/36/095) at a centroid depth of 4 km. This source mechanism is similar to the CMT solution of 242/42/098 [*Dziewonski et al.*, 1987*b*]. Solutions constrained to be shallower or deeper than 4 km have jagged source time functions and higher rms residual variances. P wave reverberations indicate a water depth of 4 km.

October 11, 1973, St. Paul's transform (Figure A3)

On October 11, 1973, the ISC reported two events separated by approximately 10 s. The earlier, smaller event falls on the map trend of transform activity while the later, larger event occurred off-trend (Figure 4 and events 15 and 16 in Figure B5). The unusual character of these locations made body-waveform analysis of these events desirable. For the smaller event, we could not resolve a mechanism, and we fixed the parameters to those of a conventional strike-slip event. For the larger event, we parameterized the STF as a horizontal rupture along the nodal plane striking at 264°. Minimization of the rms residual indicates a centroid depth in the range 9-15 km, consistent with apparent depth phases in P waves at ESK, IST, and JER.

November 14, 1982, St. Paul's transform (Figure A4)

Our analysis shows that this earthquake involved almost purely strike-slip faulting, although the probable fault plane appears to depart from the vertical. This event is well-fit by a simple STF at 9-13 km centroid depth. Our solution of 86/66/172 is in good agreement with the CMT solution of 85/90/180 [*Dziewonski et al.*, 1983*a*].

October 12, 1985, St. Paul's transform (Figure A5)

For this earthquake we parameterized the STF as a horizontal rupture along the nodal plane striking at 76°. Analysis of waveform data indicates a predominantly strike-slip mechanism. The minimum residual occurs at 7-13 km centroid depth. The STF length of 17 s is unusually long for an event of moment 4×10^{25} dyn cm (Figure 9), and the relatively high level of low-frequency excitation indicated by free oscillation amplitudes indicates that this is a slow earthquake (T.H. Jordan, personal communication, 1991). Our mechanism solution of 76/72/174 is in good agreement with the CMT solution of 83/75/179 [*Dziewonski et al.* 1986*b*].

September 20, 1986, St. Paul's transform (Figure A6)

Although this earthquake is located along the trend of principal seismic activity, a thrust mechanism (246/60/090) is reported in the Harvard CMT catalogue [*Dziewonski et al.*, 1987*b*]. Despite the small moment of this event, we were able to obtain good P and SH coverage of the focal sphere. The mechanism (227/53/50) obtained from body waveform inversion contains a small strike-slip component; this strike-slip motion is in the expected direction for transform slip if the southward-dipping nodal plane is the fault plane. The overall fit as described by the rms residual displays a distinct minimum over the centroid depth range 12-16 km.

April 20, 1988, St. Paul's transform (Figures A7 and A8)

Our reverse-faulting solution of 189/52/107 differs somewhat from the CMT solution of 196/78/108 [*Dziewonski et al*, 1989*b*], which has a steeper dip. The discrepancy may be attributed to the poor signal-to-noise ratio for this small event. The identification of the first pulse is ambiguous in the long-period P-wave data (Figure A7), but compressional first motions, consistent with a thrust mechanism, are confirmed in the vertical short-period waveforms (Figure A8). For the short-period P-wave synthetics, a value of 0.6 s is taken for t*, and the mechanism is that from long-period waveform inversion. A centroid depth of 8 km is required by long-period data and also provides a good fit to the short-period data. Water reverberations indicate a seafloor depth of about 2.5 km.

December 23, 1988, St. Paul's transform (Figure A9)

The Harvard CMT catalogue lists a reverse-faulting mechanism of 245/57/094 for this earthquake [*Dziewonski et al.*, 1989*c*]. Inversion of body waveforms from WWSSN records indicates a mechanism of 228/56/072, a similarly reverse-faulting solution but with different strike and slip angles from the CMT solution. Our preferred centroid depth is in the range of 7-11 km,

on the basis of both the residual variance and the observed fit to the waveforms. The small first SH arrivals at WES and BLA provide constraints on the strike of the source mechanism.

September 9, 1985, Marathon transform (Figure A10)

Our mechanism solution for this event is 140/54/051, corresponding to primarily reverse faulting on a fault oblique or orthogonal to the transform. The CMT reverse-faulting solution is 196/31/111 [*Dziewonski et al*, 1986*a*]. The polarity was found to be reversed on ZOBO (SH). This is a well-fit shallow event, with a centroid depth of 3-5 km, as required by a minimization of the rms residual.

February 17, 1978, Heezen transform (Figure A11)

Although coverage is sparse and the signal-to-noise ratio is low, the combination of both P and S waveforms suggests a mechanism of 241/16/301, which has a smaller dip and a larger strike-slip component than the CMT mechanism of 256/34/287 [*Dziewonski et al.*, 1987*c*]. The best-fitting centroid depth ranges from 8-14 km, but P wave coverage is poor. The predicted polarity of P-wave first motions is in agreement with short-period records.

May 27, 1989, Tharp transform (Figure A12)

Our normal-faulting solution of 275/59/287 is similar to the CMT mechanism of 258/57/277 [*Dziewonski et al.*, 1990*b*]. Examination of short-period records shows that this event has a precursor that is not evident in the long-period records, although high noise levels exist on long-period records prior to the onset of the P wave of the main event. Our best-fitting centroid depth is approximately 10 km, but the P-wave signal-to-noise ratio is poor.

May 15, 1987, Menard transform (Figure A13)

We find a normal-faulting mechanism of 50/37/247, in agreement with the CMT solution of 53/37/260 [*Dziewonski et al.*, 1988*b*]. The dilatational first motions are confirmed by examination of short-period vertical records. Centroid depth is within the range 7-11 km, but the P-wave signal-to-noise ratio is low.

September 21, 1977, Rivera transform (Figure A14)

We find a normal-faulting mechanism of 353/35/291. The CMT mechanism is 346/72/254 [*Dziewonski et al.*, 1987*a*]. The preferred centroid depth is 4 km, but the P-wave signal-to-noise ratio is low.

APPENDIX B: EARTHQUAKE RELOCATIONS

In this appendix we show in Figures B1-B11 the relative locations of events along and near the oceanic transforms discussed in this study. Relative locations are found using the method of *Jordan and Sverdrup* [1981] in the manner described in the text.

Acknowledgements

We thank Jim Cochran, Peter Hunter, Peter Lonsdale, and Jean-Guy Schilling for providing survey data for individual transforms. We also thank Geoff Abers, Göran Ekström, and Tom Jordan, and Bob Woodward for helpful information, and Marcia McNutt for contributing support for this project. This research was supported by the National Science Foundation under grant EAR-9004750 and the National Aeronautics and Space Administration under grant NAG-5-814.

REFERENCES

Aki, K., and P.G. Richards, *Quantitative Seismology: Theory and Methods*, vol. 1, p. 114, W.H. Freeman, New York, 1980.

Anderson, E.M., *The Dynamics of Faulting and Dyke Formation with Applications to Britain*, 2nd ed., Oliver and Boyd, Edinburgh, 206 pp., 1951.

Anderson, R.S., Evolution of the northern Santa Cruz Mountains by advection of crust past a San Andreas fault bend, *Science, 249*, 397-401, 1990.

Bergman, E.A., and S.C. Solomon, Source mechanisms of earthquakes near mid-ocean ridges from body waveform inversion: Implications for the early evolution of oceanic lithosphere, *J. Geophys. Res., 89*, 11,415-11,441, 1984.

Bergman, E. A., and S. C. Solomon, Transform fault earthquakes in the North Atlantic: Source mechanisms and depth of faulting, *J. Geophys. Res., 93*, 9027-9057, 1988.

Bergman, E. A., and S. C. Solomon, Earthquake swarms on the Mid-Atlantic Ridge: Products of magmatism or extensional tectonics?, *J. Geophys. Res., 95*, 4943-4965, 1990.

Bergman, E.A., J.L. Nabelek, and S.C. Solomon, An extensive region of off-ridge normal-faulting earthquakes in the southern Indian Ocean, *J. Geophys. Res.*, 89, 2425-2443, 1984.

Bilham, R., and G. King, The morphology of strike-slip faults: Examples from the San Andreas fault, California, *J. Geophys. Res., 94*, 10,204-10,216, 1989.

Bonatti, E., Vertical tectonism in oceanic fracture zones, *Earth Planet. Sci. Lett., 37*, 369-379, 1978.

Bonatti, E., Subcontinental mantle exposed in the Atlantic Ocean on St. Peter-Paul islets, *Nature, 345*, 800-802, 1990.

Bonatti, E., and K. Crane, Oscillatory spreading explanation of anomalously old uplifted crust near oceanic transforms, *Nature, 300*, 343-345, 1982.

Bonatti, E., and P.R. Hamlyn, Mantle uplifted block in the western Indian ocean, *Science, 201*, 249-251, 1978.

Bowen, A.N., and R.S. White, Deep-tow seismic profiles from the Vema transform and ridge-transform intersection, *J. Geol. Soc. London, 143*, 807-817, 1986.

Bratt, S.R., E.A. Bergman, and S.C. Solomon, Thermoelastic stress: How important as a cause of earthquakes in young oceanic lithosphere?, *J. Geophys. Res., 90*, 10,249-10,260, 1985.

Brune, J. N., T. L. Henyey, and R. F. Roy, Heat flow, stress, and rate of slip along the San Andreas Fault, California, *J. Geophys. Res., 74*, 3821-3827, 1969.

Burr, N.C., and S.C. Solomon, The relationship of source parameters of oceanic transform earthquakes to plate velocity and transform length, *J. Geophys. Res., 83*, 1193-1205, 1978.

Cochran, J.R., The Gulf of Aden: Structure and evolution of a young ocean basin and continental margin, *J. Geophys. Res., 86*, 263-287, 1981.

Cochran, J.R., Somali Basin, Chain Ridge, and origin of the Northern Somali Basin gravity and geoid low, *J. Geophys. Res., 93*, 11,985-12,008, 1988.

Collette, B.J., Thermal contraction joints in a spreading seafloor as origin of fracture zones, *Nature, 251*, 299-300, 1974.

Collette, B.J., A.P. Slootweg, and W. Twigt, Mid-Atlantic Ridge crest topography between 12° and 15° N, *Earth Planet. Sci. Lett., 42*, 103-108, 1979.

Collette, B.J., J. Verhoef, and A.F.J. de Mulder, Gravity and a model of the median valley, *J. Geophys., 47*, 91-98, 1980.

Collette, B.J., A.P. Slootweg, J. Verhoef, and W.R. Roest, Geophysical investigations of the floor of the Atlantic Ocean between 10° and 38°N (Kroonvlag-project), *Proceedings of the Koninklijke Nederlandse Akademie van Wetenschappen, B, 87*, 1-76, 1984.

Dauphin, J.P., and G.E. Ness, Bathymetry of the gulf and peninsular province of the Californias, *Mem. Am. Assoc. Pet. Geol., 47*, 21-23, 1991.

DeMets, C., and S. Stein, Present-day kinematics of the Rivera plate and implications for tectonics in southwestern Mexico, *J. Geophys. Res., 95*, 21,931-21,948, 1990.

DeMets, C., R.G. Gordon, D.F. Argus, and S. Stein, Current plate motions, *Geophys. J. Int., 101*, 425-478, 1990.

Dziewonski, A.M., and J.H. Woodhouse, An experiment in systematic study of global seismicity: Centroid-moment tensor solutions for 201 moderate and large earthquakes in 1981, *J. Geophys. Res.*, *88*, 3247-3271, 1983.

Dziewonski, A.M., T.A. Chou, and J.H. Woodhouse, Determination of earthquake source parameters from waveform data for studies of global and regional seismicity, *J. Geophys. Res.*, *86*, 2825-2852, 1981.

Dziewonski, A.M., A. Friedman, D. Giardini, and J.H. Woodhouse, Global seismicity of 1982: Centroid-moment tensor solutions for 308 earthquakes, *Phys. Earth Planet. Inter.*, *33*, 76-90, 1983*a*.

Dziewonski, A.M., J.E. Franzen, and J.H. Woodhouse, Centroid-moment tensor solutions for April-June 1983, *Phys. Earth Planet. Inter.*, *33*, 243-249, 1983*b*.

Dziewonski, A.M., J.E. Franzen, and J.H. Woodhouse, Centroid-moment tensor solutions for July-September 1984, *Phys. Earth Planet. Inter.*, *34*, 1-8, 1984.

Dziewonski, A.M., J.E. Franzen, and J.H. Woodhouse, Centroid-moment tensor solutions for October-December 1984, *Phys. Earth Planet. Inter.*, *39*, 147-156, 1985.

Dziewonski, A.M., J.E. Franzen, and J.H. Woodhouse, Centroid-moment tensor solutions for July-September 1985, *Phys. Earth Planet. Inter.*, *42*, 205-214, 1986*a*.

Dziewonski, A.M., J.E. Franzen, and J.H. Woodhouse, Centroid-moment tensor solutions for October-December 1985, *Phys. Earth Planet. Inter.*, *43*, 185-195, 1986*b*.

Dziewonski, A.M., G. Ekström, J.E. Franzen, and J.H. Woodhouse, Global seismicity of 1977: Centroid-moment tensor solutions for 471 earthquakes, *Phys. Earth Planet. Inter.*, *45*, 11-36, 1987*a*.

Dziewonski, A.M., G. Ekström, J.E. Franzen, and J.H. Woodhouse, Centroid-moment tensor solutions for July-September 1986, *Phys. Earth Planet. Inter.*, *46*, 305-315, 1987*b*.

Dziewonski, A.M., G. Ekström, J.E. Franzen, and J.H. Woodhouse, Global seismicity of 1978: Centroid-moment tensor solutions for 512 earthquakes, *Phys. Earth Planet. Inter.*, *46*, 316-342, 1987*c*.

Dziewonski, A.M., G. Ekström, J.E. Franzen, and J.H. Woodhouse, Global seismicity of 1980: Centroid-moment tensor solutions for 515 earthquakes, *Phys. Earth Planet. Inter., 50*, 127-154, 1988*a*.

Dziewonski, A.M., G. Ekström, J.H. Woodhouse, and G. Zwart, Centroid-moment tensor solutions for April-June 1987, *Phys. Earth Planet. Inter., 50*, 215-225, 1988*b*.

Dziewonski, A.M., G. Ekström, J.E. Franzen, and J.H. Woodhouse, Global seismicity of 1982 and 1983: Additional centroid-moment tensor solutions for 553 earthquakes, *Phys. Earth Planet. Inter., 53*, 17-45, 1988*c*.

Dziewonski, A.M., G. Ekström, J.H. Woodhouse, and G. Zwart, Centroid-moment tensor solutions for October-December 1987, *Phys. Earth Planet. Inter., 54*, 10-21, 1989*a*.

Dziewonski, A.M., G. Ekström, J.H. Woodhouse, and G. Zwart, Centroid-moment tensor solutions for April-June 1988, *Phys. Earth Planet. Inter., 54*, 199-209, 1989*b*.

Dziewonski, A.M., G. Ekström, J.H. Woodhouse, and G. Zwart, Centroid-moment tensor solutions for October-December 1988, *Phys. Earth Planet. Inter., 57*, 179-191, 1989*c*.

Dziewonski, A.M., G. Ekström, J.H. Woodhouse, and G. Zwart, Centroid-moment tensor solutions for January-March 1989, *Phys. Earth Planet. Inter., 59*, 233-242, 1990*a*.

Dziewonski, A.M., G. Ekström, J.H. Woodhouse, and G. Zwart, Centroid-moment tensor solutions for April-June 1989, *Phys. Earth Planet. Inter., 60*, 243-253, 1990*b*.

Dziewonski, A.M., G. Ekström, J.H. Woodhouse, and G. Zwart, Centroid-moment tensor solutions for October-December 1989, *Phys. Earth Planet. Inter., 62*, 194-207, 1990*c*.

Dziewonski, A.M., G. Ekström, J.H. Woodhouse, and G. Zwart, Centroid-moment tensor solutions for October-December 1990, *Phys. Earth Planet. Inter., 68*, 201-204, 1991.

Ekström, G., A very broad band inversion method for the recovery of earthquake source parameters, *Tectonophysics, 166*, 73-100, 1989.

Engeln, J. F., D. A. Wiens, and S. Stein, Mechanisms and depths of Atlantic transform earthquakes, *J. Geophys. Res.*, 91, 548-577, 1986.

Fornari, D.J., D.G. Gallo, M.H. Edwards, J.A. Madsen, M.R. Perfit, and A.N. Shor, Structure

and topography of the Siqueiros transform fault system: Evidence for the development of intra-transform spreading centers, *Mar. Geophys. Res., 11*, 263-300, 1989.

Fox, P.J., and D.G. Gallo, A tectonic model for ridge-transform-ridge plate boundaries: Implications for the structure of oceanic lithosphere, *Tectonophysics, 104*, 205-242, 1984.

Fox, P.J., and D.G. Gallo, The geology of North Atlantic transform plate boundaries and their aseismic extensions, in *The Geology of North America*, vol. M, *The Western North Atlantic Region*, edited by P.R. Vogt and B.E. Tuckolke, pp. 157-172, Geological Society of America, Boulder, Colo., 1986.

Francis, T. J. G., I.T. Porter, and R.C. Lilwall, Microearthquakes near the eastern end of St. Paul's Fracture Zone, *Geophys. J. R. Astron. Soc., 53*, 201-217. 1978.

Froidevaux, C., Energy dissipation and geometric structure at spreading plate boundaries, *Earth Planet. Sci. Lett., 20*, 419-424, 1973.

Futterman, W.I., Dispersive body waves, *J. Geophys. Res., 67*, 5279 -5291, 1962.

Gallo, D., P.J. Fox, and K.C. Macdonald, A Sea Beam investigation of the Clipperton transform fault: The morphotectonic expression of a fast-slipping transform boundary, *J. Geophys. Res., 91*, 3455-3467, 1986.

Goff, J.A., E.A. Bergman, and S.C. Solomon, Earthquake source mechanisms and transform fault tectonics in the Gulf of California, *J. Geophys. Res., 92*, 10,485-10,510, 1987.

Harvey, D., and G.L. Choy, Broad-band deconvolution of GDSN data, *Geophys. J. R. Astron. Soc., 69*, 659-668, 1982.

Haxby, W.F., and E.M. Parmentier, Thermal contraction and the state of stress in the oceanic lithosphere, *J. Geophys. Res., 93*, 6419-6429, 1988.

Huang, P.Y., and S.C. Solomon, Centroid depths and mechanisms of mid-ocean ridge earthquakes in the Indian Ocean, Gulf of Aden, and Red Sea, *J. Geophys. Res., 92*, 1361-1382, 1987.

Huang, P.Y., and S.C. Solomon, Centroid depths of mid-ocean earthquakes: Dependence on spreading rate, *J. Geophys. Res., 93*, 13,445-13,447, 1988.

Huang, P.Y., S.C. Solomon, E.A. Bergman, and J.L. Nabelek, Focal depths and mechanisms of Mid-Atlantic Ridge earthquakes from body waveform inversion, *J. Geophys. Res., 91*, 579-598, 1986.

Jones, L., Focal mechanisms and the state of stress on the San Andreas Fault in southern California, *J. Geophys. Res.*, 8869–8891, 1988.

Jordan, T.H., and K.A. Sverdrup, Teleseismic location techniques and their applications to earthquake clusters in the south-central Pacific, *Bull. Seismol. Soc. Am., 71*, 1105-1130, 1981.

Kawasaki, I., Y. Kawahara, I. Takata, and N. Kosugi, Mode of seismic moment release at transform faults, *Tectonophysics, 118*, 313-327, 1985.

Lachenbruch, A. H., and J. H. Sass, Heat flow and energetics of the San Andreas fault zone, *J. Geophys. Res., 85*, 6185-6222, 1980.

Lachenbruch, A. H., and G. A. Thompson, Oceanic ridges and transform faults: Their intersection angles and resistance to plate motion, *Earth Planet. Sci. Lett., 15*, 116-122, 1972.

Laughton, A.S., R.B. Whitmarsh, and M.T. Jones, The evolution of the Gulf of Aden, *Phil. Trans. Roy. Soc. London, Ser. A., 267*, 227-266, 1970.

Lonsdale, P., Tectonic and magmatic ridges in the Eltanin fault system, south Pacific, *Mar. Geophys. Res., 8*, 203-242, 1986.

Lonsdale, P., Segmentation of the Pacific-Nazca spreading center, 1° N-20° S, *J.Geophys. Res., 94*, 12,197-12,225, 1989.

Lonsdale, P., Structural patterns of the Pacific floor offshore of peninsular California, *Mem. Am. Assoc. Pet. Geol., 47*, 87-125, 1991.

Louden, K.E., R.S. White, C.G. Potts, and D.W. Forsyth, Structure and seismotectonics of the Vema Fracture Zone, Atlantic Ocean, *J. Geol. Soc. London, 143*, 795-805, 1986.

Macdonald, K.C., K. Kastens, S. Miller, and F.N. Spiess, Deep-tow studies of the Tamayo transform fault, *Mar. Geophys. Res., 4*, 37-70, 1979.

Macdonald, K. C., D. A. Castillo, S. P. Miller, P. Fox, K.A. Kastens, and E. Bonatti, Deep-tow studies of the Vema Fracture Zone, 1: Tectonics of a major slow slipping transform fault and its

intersection with the Mid-Atlantic Ridge, *J. Geophys. Res., 91*, 3334-3354, 1986.

Madsen, J.A., P.J. Fox, and K.C. Macdonald, Morphotectonic fabric of the Orozco transform fault: Results from a Sea Beam investigation, *J. Geophys. Res., 91*, 3439-3454, 1986.

Mammerickx, J., S.M. Smith, I.L. Taylor, and T.E. Chase, Topography of the South Pacific, Map, Scripps Inst. Oceanogr., Univ. Calif., San Diego, 1975.

Matthews, D.H., The Owen Fracture Zone and the northern end of the Carlsberg Ridge, *Phil. Trans. Roy. Soc. London, Ser. A, 259*, 172-197, 1966.

Mayes, C.L., L.A. Lawver, and D.T. Sandwell, Tectonic history and new isochron chart of the South Pacific, *J. Geophys. Res., 95*, 8543-8568, 1990.

McKenzie, D.P., The relation between fault plane solutions for earthquakes and the directions of the principal stresses, *Bull Seismol. Soc. Am., 59*, 591-601, 1969.

McNally, K.C., T. Lay, M. Protti-Quesada, G. Valensise, D. Orange, and R.S. Anderson, Santa Cruz Mountains (Loma Prieta) earthquake, *Eos Trans. AGU, 70*, pp. 1463, 1467, 1989.

Melson, W. G., S.R. Hart, and G. Thompson, St. Paul's rocks, equatorial Atlantic: Petrogenesis, radiometric ages and implications on sea-floor spreading, *Geol. Soc. Am., Mem., 132*, 241-272, 1972.

Menard, H.W., and T. Atwater, Changes in direction of sea floor spreading, *Nature, 219*, 463-467, 1968.

Minster, J.F., T.H. Jordan, P. Molnar, and E. Haines, Numerical modelling of instantaneous plate tectonics, *Geophys. J. R. Astron. Soc., 36*, 541-576, 1974.

Molnar, P., T. Atwater, J. Mammerickx, and S.M. Smith, Magnetic anomalies, bathymetry and the tectonic evolution of the South Pacific since the late Cretaceous, *Geophys. J. R. Astron. Soc.*, 40, 383-420, 1975.

Mount, V. S. and J. Suppe, State of stress near the San Andreas fault: Implications for wrench tectonics, *Geology, 15*, 1143-1146, 1987.

Nabelek, J.L., Determination of earthquake source parameters from inversion of body waves, Mass. Inst. Technol., Ph.D. thesis, Cambridge, 346 pp., 1984.

Ness, G.E., and M.W. Lyle, A seismo-tectonic map of the gulf and peninsular province of the Californias, *Mem. Am. Assoc. Pet. Geol., 47*, 71-77, 1991.

Parmentier, E.M., and W.F. Haxby, Thermal stresses in the oceanic lithosphere: Evidence from geoid anomalies at fracture zones, *J. Geophys. Res., 91*, 7193-7204, 1986.

Phipps Morgan, J., and E.M. Parmentier, Lithospheric stress near a ridge-transform intersection, *Geophys. Res. Lett., 11*, 113-116, 1984.

Prothero, W.A., and I.D. Reid, Microearthquakes on the East Pacific Rise at 21° N and the Rivera Fracture Zone, *J. Geophys. Res., 87*, 8509-8518, 1982.

Sandwell, D.T., Thermal stress and the spacing of transform faults, *J. Geophys. Res., 89*, 6405-6417, 1986.

Saucier, F.J., E.D. Humphreys, and R.J. Weldon, Stress near geometrically complex strike-slip faults: Application to the San Andreas at Cajon Pass, southern California, *J. Geophys. Res.*, in press, 1992.

Schilling, J.-G., CONRAD 28-06, unpublished cruise report, Lamont-Doherty Geol. Obs., Columbia Univ., New York, 1987.

Schilling, J.-G., B. McCully, and H. Bougault, Mid-Atlantic Ridge volcanism in the equatorial region (3°S-5°N) (abstract), *Eos Trans. AGU, 68*, 1508, 1987.

Segall, P., and D.D. Pollard, Mechanics of discontinuous faults, *J. Geophys. Res., 85*, 4337-4350, 1980.

Sibson, R.H., Stopping of earthquake ruptures at dilational fault jogs, *Nature, 316*, 248-251, 1985.

Sibson, R.H., Rupture interaction with fault jogs, in *Earthquake Source Mechanics, Geophys. Monogr. Ser., 37*, edited by S. Das, J. Boatwright, and C. H. Scholz, pp. 157-167, AGU, Washington, D. C., 1986.

Sinton, J. M., Ultramafic inclusions and high-pressure xenocrysts in submarine basanitoid, equatorial Mid-Atlantic Ridge, *Contrib. Mineral. Petrol., 70*, 49-57, 1979.

Stein, C.A., and J.R. Cochran, The transition between Sheba Ridge and Owen Basin: Rifting of

old oceanic lithosphere, *Geophys. J. R. Astron. Soc., 81*, 47-74, 1985.

Stein, S., and D.A. Wiens, Depth determination for shallow teleseismic earthquakes: Methods and results, *Rev. Geophys., 24*, 806-832, 1986.

Stewart, L.M., and E.A. Okal, Seismicity and aseismic slip along the Eltanin Fracture Zone, *J. Geophys. Res., 88*, 10,495-10,507, 1983.

Stock, J.M., K.M. Marks, and F.R. Schult, Mismatch of fracture zones across the Pacific-Antarctic Ridge (abstract), in *AGU 1991 Fall Meeting, Eos Trans. AGU, 72, suppl.*, p. 444, 1991.

Sykes, L. R., Mechanism of earthquakes and nature of faulting on the mid-oceanic ridges, *J. Geophys. Res., 72*, 2131-2153, 1967.

Sylvester, A.G., Strike-slip faults, *Geol. Soc. Am. Bull., 100*, 1666-1703, 1988.

Tréhu, A.M., and G.M. Purdy, Crustal structure in the Orozco transform zone, *J. Geophys. Res., 89*, 1834-1842, 1984.

Tréhu, A.M., and S.C. Solomon, Earthquakes in the Orozco transform zone: Seismicity, source mechanisms, and tectonics, *J. Geophys. Res., 88*, 8203-8255, 1983.

Turcotte, D.L., Are transform faults thermal contraction cracks?, *J. Geophys. Res., 79*, 2573-2577, 1974.

Wiens, D.A., and D.E. Petroy, The largest recorded earthquake swarm: Intraplate faulting near the Southwest Indian Ridge, *J. Geophys. Res., 95*, 4735-4750, 1990.

Wilcock, W. S. D., G. M. Purdy, and S. C. Solomon, Microearthquake evidence for extension across the Kane transform fault, *J. Geophys. Res., 95*, 15,439-15,462, 1990.

Wilson, J.T., A new class of faults and their bearing on continental drift, *Nature, 207*, 343-347, 1965.

Whitmarsh, R.B., The Owen Basin off the southeast margin of Arabia, *Geophys. J. R.. Astron. Soc., 58*, 441-470, 1979.

Zoback, M. D., M. L. Zoback, V. S. Mount, J. Suppe, J. P. Eaton, J. H. Healy, D. Oppenheimer, P. Reasenberg, L. Jones, C. B. Raleigh, I. G. Wong, O. Scotti, and C.

Wentworth, New evidence on the state of stress of the San Andreas fault system, *Science, 238*, 1105-1111, 1987.

E.A. Bergman, U.S. Geological Survey, P.O. Box 25046, Mail Stop 967, Denver Federal Center, Denver, CO 80225.

S.C. Solomon, Department of Earth, Atmospheric, and Planetary Sciences, Room 54-522, Massachusetts Institute of Technology, Cambridge, MA 02139.

C.J. Wolfe, Department of Earth, Atmospheric, and Planetary Sciences, Room 54-822, Massachusetts Institute of Technology, Cambridge, MA 02139.

FIGURE CAPTIONS

Figure 1. Earthquake epicenters (ISC) and CMT mechanisms for earthquakes along the Eltanin fault system on the Pacific-Antarctic plate boundary. Epicenters are depicted by dots; mechanisms are equal-area projections of the lower focal hemisphere, with compressional quadrants shaded. The Eltanin system is made up of the Heezen and Tharp transforms and a transform identified as Fracture Zone VI by *Molnar et al.* [1976].

Figure 2. Location of the seven transforms considered in this study. Locations of the earthquakes along these transforms with anomalous mechanisms and for which we have performed body waveform inversion are shown as filled circles. Also shown are plate boundaries and continents, in Mercator projection.

Figure 3. Earthquake locations and mechanisms along the southwestern portion of the Owen transform. Bathymetry is adapted from *Cochran* [1988]; 1-km contour interval. Mount Error is at about 10.3° N, 56.2° E and reaches depths less than 1 km. The southeastern portion of Error Ridge includes both Mount Error and the elongate high at about 11° N, 56.2° E. Suggested plate boundary geometry is shown as a stippled line. The northeastern transform boundary is taken as a small circle about the African-Indian Euler vector, and arrows denote relative plate motion directions [*DeMets et al.*, 1990]. Epicenters are of relocated events from January 1964-March 1989. The mechanisms of the earthquakes of July 29, 1983, and July 7, 1986, are from this study. All other mechanisms are from the Harvard CMT catalogue. Tic marks denote the azimuth of the maximum compressive horizontal stress, under the assumption that the P-axis and T-axis correspond to the axes of maximum and minimum principal stress, respectively. This assumption may not always be valid [*McKenzie*, 1969].

Figure 4. Earthquake locations and mechanisms along the western portion of the St. Paul's transform. Bathymetric contours are from the General Bathymetric Chart of the Oceans (GEBCO) Digital Atlas, as supplied by the British Oceanographic Data Centre, Bidston, U.K.,

March 1992; 1-km contour interval, Mercator projection. The location of the December 30, 1989, event is from the ISC. Mechanisms of earthquakes on October 11, 1972, November 14, 1982, October 12, 1985, September 20, 1986, April 20, 1988, and December 23, 1988, are from this study. Mechanisms of the events on September 14, 1971 and April 11, 1972 are from *Engeln et al.* [1986]. Mechanisms of other events are taken from the Harvard CMT catalogue. Crosses show the location of the Mid-Atlantic Ridge and its intersection with the St. Paul's transform, as given by *Schilling* [1987]. The transform boundary is taken as a small circle about the South American-African Euler vector [*DeMets et al.*, 1990]. See Figure 3 for further details.

Figure 5. Earthquake locations and mechanisms along the Marathon transform. Bathymetry is from *Collette et al.* [1984]; 1-km contour interval, Mercator projection. The mechanism of the September 22, 1985, earthquake is from this study. The June 9, 1987, mechanism is from the Harvard CMT catalogue. The transform boundary is taken as a small circle about the South American-African Euler vector [*DeMets et al.*, 1990]. See Figure 3 for further details.

Figure 6. Earthquake locations and mechanisms along the central portion of the Heezen transform. Bathymetry is adapted from *Lonsdale* [1986]; 1-km contour interval. The mechanism of the earthquake of February 17, 1978, is from this study. All other mechanisms are from the Harvard CMT catalogue. See Figure 3 for further details.

Figure 7. Earthquake locations and mechanisms along a portion of the Tharp transform. Bathymetry is adapted from *Lonsdale* [1986]; 1-km contour interval. The mechanism of the May 27, 1989, earthquake is from this study. Other earthquake mechanisms are from the Harvard CMT catalogue. The epicenter of the May 27, 1989, earthquake is taken from the ISC catalogue. See Figure 3 for further details.

Figure 8. Geologic sketch map of the Heezen transform from *Lonsdale* [1986], oblique projection.

Figure 9. Earthquake locations and mechanisms along the Menard transform. Bathymetry is adapted from *Mammerickx et al.* [1975]; contours are in thousands of fathoms, with a 100-

fathom contour interval and the 1500-fathom contour dashed. The mechanism of the May 15, 1987, earthquake is from this study. Other earthquake mechanisms are from the Harvard CMT catalogue. The transform boundary is taken as a small circle about the Pacific-Antarctic Euler vector [*DeMets et al.*, 1990]. See Figure 3 for further details.

Figure 10. Earthquake locations and mechanisms along the western Rivera transform. Bathymetry is adapted from *Dauphin and Ness* [1991]; 1-km contour interval. Plate boundary is taken from *Ness and Lyle* [1991], who identify possible fault lineations on the basis of bathymetry and seismicity. Arrows denote relative plate motion directions [*DeMets and Stein*, 1991]. See Figure 3 for further details.

Figure 11. Centroid depths of earthquakes along the St. Paul's transform. (a) Thermal model derived for an offset of 630 km and an age difference of 39 Ma. (b) Thermal model derived for an offset of 300 km and an age difference of 19 Ma. See text for further details.

Figure A1. Observed (solid lines) long-period P and SH waveforms from the earthquake of July 29, 1983, compared with synthetic waveforms (dashed lines) generated from the best-fitting point source model found from body waveform inversion. Waveforms from GDSN stations (MAJO, NWAO, and BCAO) are plotted at the scale shown in the lower right. P and SH radiation patterns are shown on the lower focal hemisphere (equal-area projection). For SH waves, compression corresponds to positive motion as defined by *Aki and Richards* [1980]. All amplitudes are normalized to an epicentral distance of 40° and a WWSSN instrument magnification of 1500; the amplitude scales correspond to the waveforms that would be observed on an original seismogram from such an instrument. The two vertical lines show the portion of each time series used in the inversion. Open circles denote dilatational first motions, filled circles denote compressional first motions, and crosses denote emergent arrivals.

Figure A2. Observed P and SH waveforms from the earthquake of July 7, 1986, compared with synthetic waveforms generated from the best-fitting point source model found from body waveform inversion. See Figure A1 for further details.

Figure A3. Observed P and SH waves from the earthquake of October 11, 1973, compared with

synthetic waveforms generated for a source model with two point sources. The parameters of the first, smaller, event were fixed in the inversion; the source parameters of the second event are found from body waveform inversion. The radiation pattern of the larger subevent is shown. See Figure A1 for further details.

Figure A4. Observed P and SH waveforms from the earthquake of November 14, 1982, compared with synthetic waveforms generated from the best-fitting point source model found from body waveform inversion. See Figure A1 for further details.

Figure A5. Observed P and SH waveforms from the earthquake of October 12, 1985, compared with synthetic waveforms generated from the best-fitting point source model found from body waveform inversion. See Figure A1 for further details.

Figure A6. Observed P and SH waveforms from the earthquake of September 20, 1986, compared with synthetic waveforms generated from the best-fitting point source model found from body waveform inversion. ANTO is a GDSN station. See Figure A1 for further details.

Figure A7. Observed P and SH waveforms from the earthquake of April 20, 1988, compared with synthetic waveforms generated from the best-fitting point source model found from body waveform inversion. GRFO is a GDSN station. See Figure A1 for further details.

Figure A8. Observed short-period P waveforms from the earthquake of April 20, 1988, compared with synthetic waveforms generated from the mechanism found from long-period body waveform inversion. All data are from GDSN stations. See Figure A1 for further details.

Figure A9. Observed P and SH waveforms from the earthquake of December 23, 1988, compared with synthetic waveforms generated from the best-fitting point source model found from body waveform inversion. See Figure A1 for further details.

Figure A10. Observed P and SH waveforms from the earthquake of September 22, 1985, compared with synthetic waveforms generated from the best-fitting point source model found from body waveform inversion. ZOBO is a GDSN station. See Figure A1 for further details.

Figure A11. Observed P and SH waveforms from the earthquake of February 17, 1978, compared with synthetic waveforms generated from the best-fitting point source model found

from body waveform inversion. SNZO is a GDSN station. See Figure A1 for further details.

Figure A12. Observed P and SH waveforms from the earthquake of May 27, 1989, compared with synthetic waveforms generated from the best-fitting point source model found from body waveform inversion. AFI is a GDSN station. See Figure A1 for further details.

Figure A13. Observed P and SH waveforms from the earthquake of May 15, 1987, compared with synthetic waveforms generated from the best-fitting point source model found from body waveform inversion. CTAO and ANMO are GDSN stations. See Figure A1 for further details.

Figure A14. Observed P and SH waveforms from the earthquake of September 21, 1977, compared with synthetic waveforms generated from the best-fitting point source model found from body waveform inversion. See Figure A1 for further details.

Figure B1. Relative locations of earthquakes (1964-March 1989) on the Carlsberg Ridge south of the Owen transform. For each earthquake the relative location is indicated by the event number, the 95% confidence ellipse for the cluster vector is shown, and the change in relative position from the starting (ISC) location is indicated by a line. The position of the average location of events within a cluster (the hypocentroid) is indicated by a cross. The distance scales are in kilometers north and east of the hypocentroid. Events are numbered in chronological order.

Figure B2. Relative locations of earthquakes near the southwestern intersections of the Owen transform and the Carlsberg Ridge. See Figure B1 for further details.

Figure B3. Relative locations of earthquakes on the central portion of the Owen transform. See Figure B1 for further details.

Figure B4. Relative locations of earthquakes on the Mid-Atlantic Ridge near its intersection with the western portion of the St. Paul's transform.

Figure B5. Relative locations of earthquakes on the western portion of the St. Paul's transform (ISC locations west of 29° W). See Figure B1 for further details.

Figure B6. Relative locations of earthquakes on the western portion of the St. Paul's transform (ISC locations between 28° W and 29° W). See Figure B1 for further details.

Figure B7. Relative locations of earthquakes at the Marathon transform and the adjacent segments

of the Mid-Atlantic Ridge. See Figure B1 for further details.

Figure B8. Relative locations of earthquakes on a central portion of the Heezen transform. See Figure B1 for further details.

Figure B9. Relative locations of earthquakes on a central portion of the Tharp transform. See Figure B1 for further details.

Figure B10. Relative locations of earthquakes on the Menard transform. See Figure B1 for further details.

Figure B11. Relative locations of earthquakes ($m_b \geq 4.5$) on the a portion of the Rivera transform. See Figure B1 for further details.

TABLE 1. Epicentral Data and Source Parameters from Body-Waveform Inversion

Date	Origin Time[a],UT	Latitude[a], °N	Longitude[a], °E	m_b[a]	M_S[a]	M_o[b]	Mechanism[c]	Depth[d], km	STF[e], s
			Carlsberg Ridge: Owen Transform						
Sept. 29, 1983	18:03:59.8	10.45	56.91	5.7	5.0	2.0×10^{24}	214/89/298	11	4
Sept. 7, 1986	16:26:56.5	10.31	56.81	6.2	6.1	3.7×10^{25}	238/36/095	4	8
			Mid-Atlantic Ridge: St. Paul's Transform						
Oct. 11, 1973	2:07:51.8	0.52	-29.47	5.9		6.2×10^{25}	264/82/183	12	11
Oct. 14, 1982	17:29:24.7	0.99	-29.07	5.1	5.2	9.0×10^{24}	86/66/172	11	5
Oct. 12, 1985	22:20:42.8	0.87	-29.90	5.4	5.9	4.2×10^{25}	76/72/174	10	17
Sept. 20, 1986	1:31:14.2	0.88	-29.25	5.4	4.8	1.8×10^{24}	227/53/050	14	3
Apr. 4, 1988	4:25:36.7	0.97	-30.27	5.8	5.4	2.7×10^{24}	189/52/107	8	3
Dec. 23, 1988	21:49:09.1	0.77	-29.41	5.7	5.5	6.0×10^{24}	228/56/072	9	4
			Mid-Atlantic Ridge: Marathon Transform						
Sept. 22, 1985	18:23:12.9	12.52	-44.31	5.6	5.5	4.2×10^{24}	140/54/051	4	4
			Pacific-Antarctic Ridge: Heezen Transform						
Feb. 17, 1978	1:40:03.1	-55.71	-125.24	5.7	5.2	2.4×10^{24}	241/16/309	11	3

				Pacific-Antarctic Ridge: Tharp Transform					
May 27, 1989	3:01:24.7	-55.24	-133.14	5.5	5.7	1.5×10^{25}	275/59/287	12	7
				East Pacific Rise: Menard Transform					
May 15, 1987	13:49:14.6	-49.91	-115.3	5.5	4.7	1.9×10^{24}	50/37/247	9	2
				East Pacific Rise: Rivera Transform					
Sept. 21, 1977	13:15:58.2	19.97	-109.26	5.5		4.9×10^{24}	353/35/291	4	6

a. Epicentral data, m_b, and M_S are from the ISC.

b. Seismic moment in units of dyn cm.

c. Strike/dip/slip, in degrees, using the convention of *Aki and Richards* [1980].

d. Depth of centroid below the seafloor.

e. Duration of the source time function (STF).

TABLE 2. Epicentral Data and CMT Source Parameters of Additional Unusual Transform Earthquakes

Date	Origin Time[a], UT	Latitude[a], °N	Longitude[a], °E	M_o[b]	Mechanism[c]	Source
			East Pacific Rise: Gofar Fracture Zone			
Oct. 8, 1980	20:19:47.0	-4.87	-106.15	4.55×10^{24}	280/72/197	*Dziewonski et al.* [1988*a*]
			Pacific-Antarctic Ridge: Heezen Transform			
Aug. 16, 1984	15:30:59.8	-55.40	-123.75	1.57×10^{24}	257/63/268	*Dziewonski et al.* [1985]
			Pacific-Antarctic Ridge: Tharp Transform			
Oct. 10, 1982	17:44:45.2	-54.73	-130.54	6.18×10^{23}	246/54/250	*Dziewonski et al.* [1988*c*]
			Pacific-Antarctic Ridge: Fracture Zone VI			
Sept. 17, 1982	11:08:31.7	-54.55	-136.86	6.65×10^{23}	287/61/298	*Dziewonski et al.* [1983*a*]
			Pacific-Antarctic Ridge: Udintsev Transform			
Nov. 1, 1990	1:56:44.6	-56.00	-143.19	8.04×10^{23}	264/90/180	*Dziewonski et al.* [1991]
			Pacific-Antarctic Ridge: Unnamed Transform			
May 28, 1977	15:10:13.6	-65.04	175.71	4.16×10^{24}	153/46/129	*Dziewonski et al.* [1987*a*]

			Southeast Indian Ridge: Unnamed Transform			
June 20, 1983	22:41:57.3	-42.82	83.57	4.97×10^{23}	247/49/134	*Dziewonski et al.* [1983*b*]
			Southeast Indian Ridge: Unnamed Transform			
May 5, 1988	23:35:34.7	-49.82	115.38	4.03×10^{24}	112/69/130	*Dziewonski et al.* [1989*b*]
			Southwest Indian Ridge: Discovery II Transform			
Aug. 17, 1977	10:41:40.3	-40.95	42.70	8.00×10^{23}	145/58/070	*Dziewonski et al.* [1987*a*]
			Carlsberg Ridge: Owen Transform			
Sept 29, 1986	7:10:37.7	10.58	57.05	7.47×10^{23}	242/72/167	*Dziewonski et al.* [1987*b*]
			Juan de Fuca: Blanco Transform			
Oct. 17, 1987	8:12:21.4	43.30	-126.65	1.52×10^{24}	28/90/078	*Dziewonski et al.* [1989*a*]
Jan. 11, 1989	12:23:33.1	44.60	-129.69	4.52×10^{23}	140/48/262	*Dziewonski et al.* [1990*a*]
			Mid-Atlantic Ridge: St. Paul's Transform			
Dec. 30, 1989	20:16:02.2	1.00	-30.15	6.85×10^{23}	304/90/000	*Dziewonski et al.* [1990*c*]

a. Epicentral data, m_b, and M_S are from the ISC, expect that data for the earthquake of Nov. 1, 1990, are from the National Earthquake Information Center's Preliminary Determination of Epicenters.

b. Seismic moment in units of dyn cm.

c. Strike/dip/slip, in degrees, using the convention of *Aki and Richards* [1980].

TABLE 3. Seismic Velocity Models Assumed for Source Regions

Layer	Thickness, km	V_P, km/s	V_S, km/s	ρ, g/cm^3
		Fast-slipping transforms		
1	variable	1.5	0.0	1.0
2	6.0	6.4	3.7	2.8
3	half-space	8.1	4.6	3.4
		Slow-slipping transforms		
1	variable	1.5	0.0	1.0
2	2.2	4.3	2.5	2.5
3	2.6	5.9	3.4	2.6
4	half-space	8.1	4.6	3.4

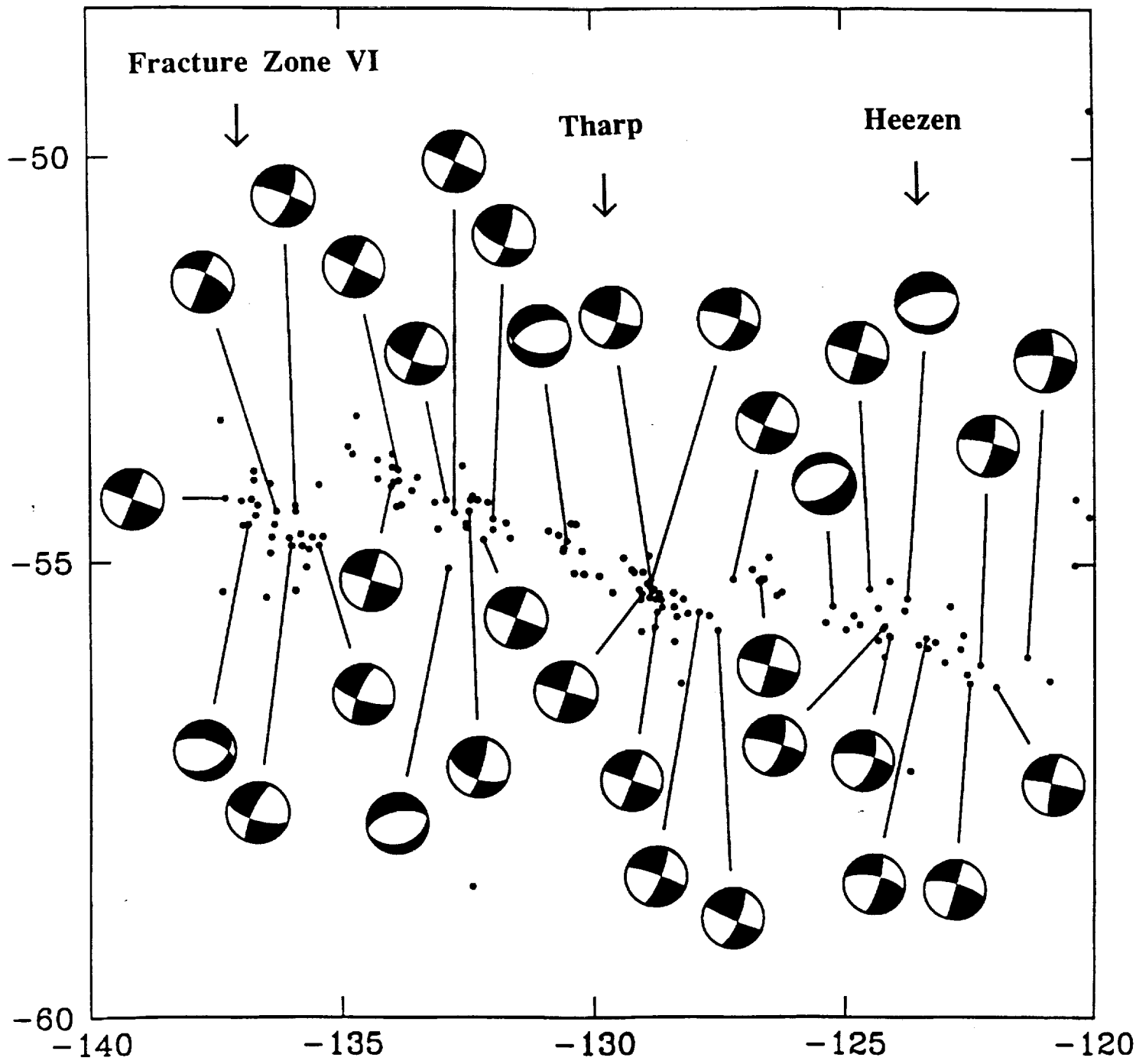

Figure 1

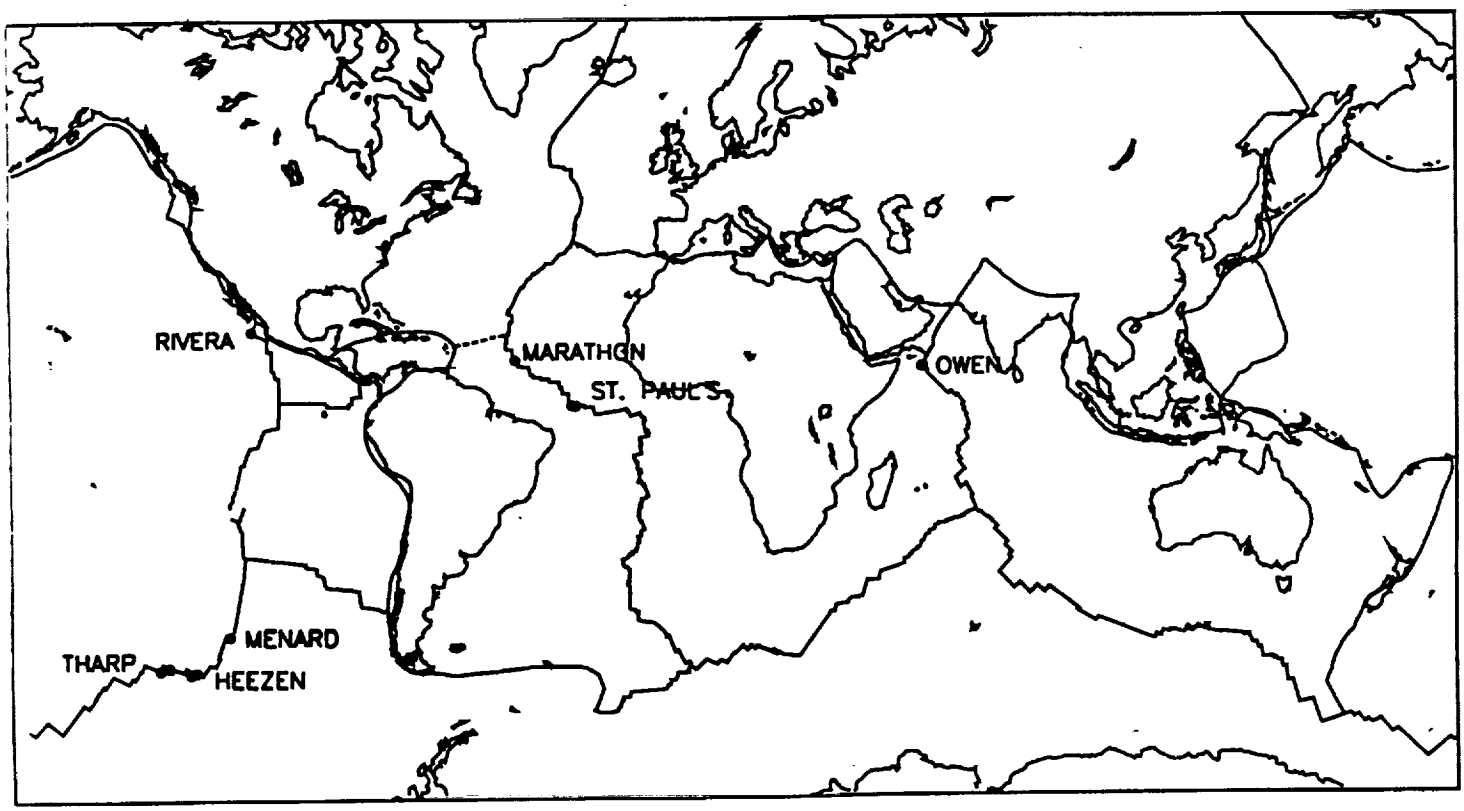

Figure 2

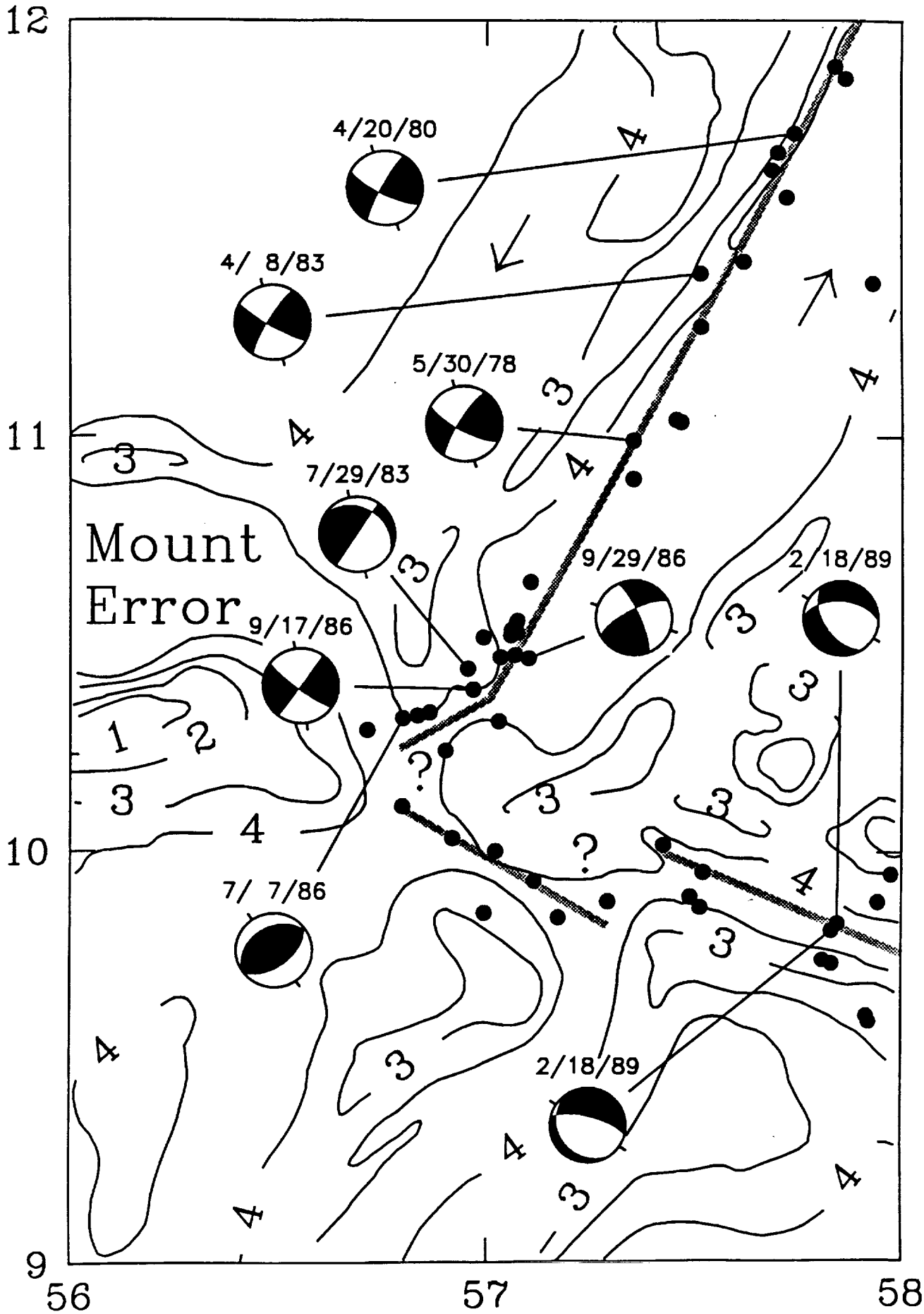
12
11
10
9
56
57
58
4/20/80
4/ 8/83
5/30/78
7/29/83
9/17/86
9/29/86
2/18/89
7/ 7/86
2/18/89
Mount
Error
1
2
3
4
?

Figure 3

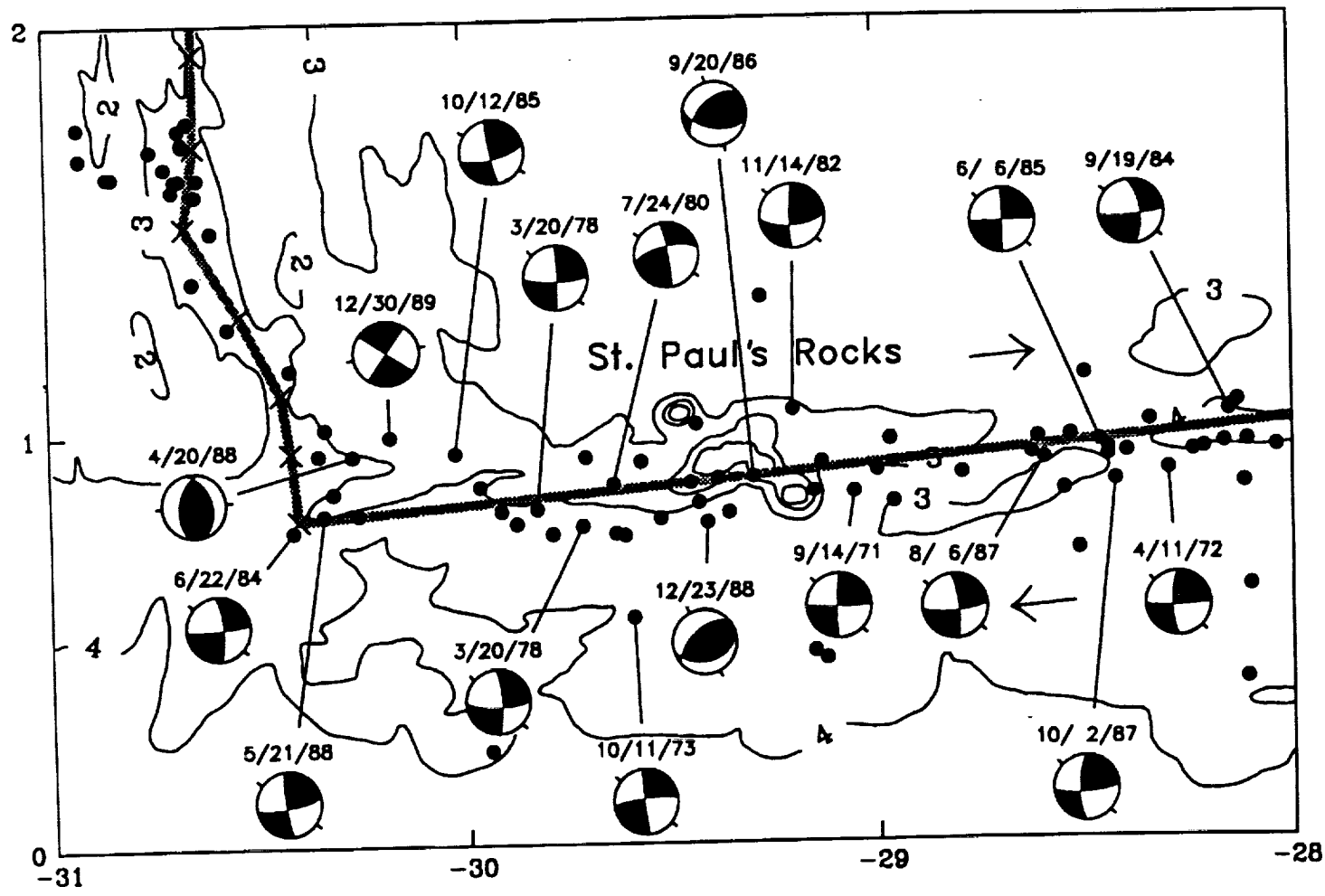
9/20/86
10/12/85
11/14/82
6/ 6/85
9/19/84
7/24/80
3/20/78
12/30/89
St. Paul's Rocks
4/20/88
6/22/84
9/14/71
8/ 6/87
4/11/72
12/23/88
3/20/78
5/21/88
10/11/73
10/ 2/87
2
1
0
-31
-30
-29
-28

Figure 4

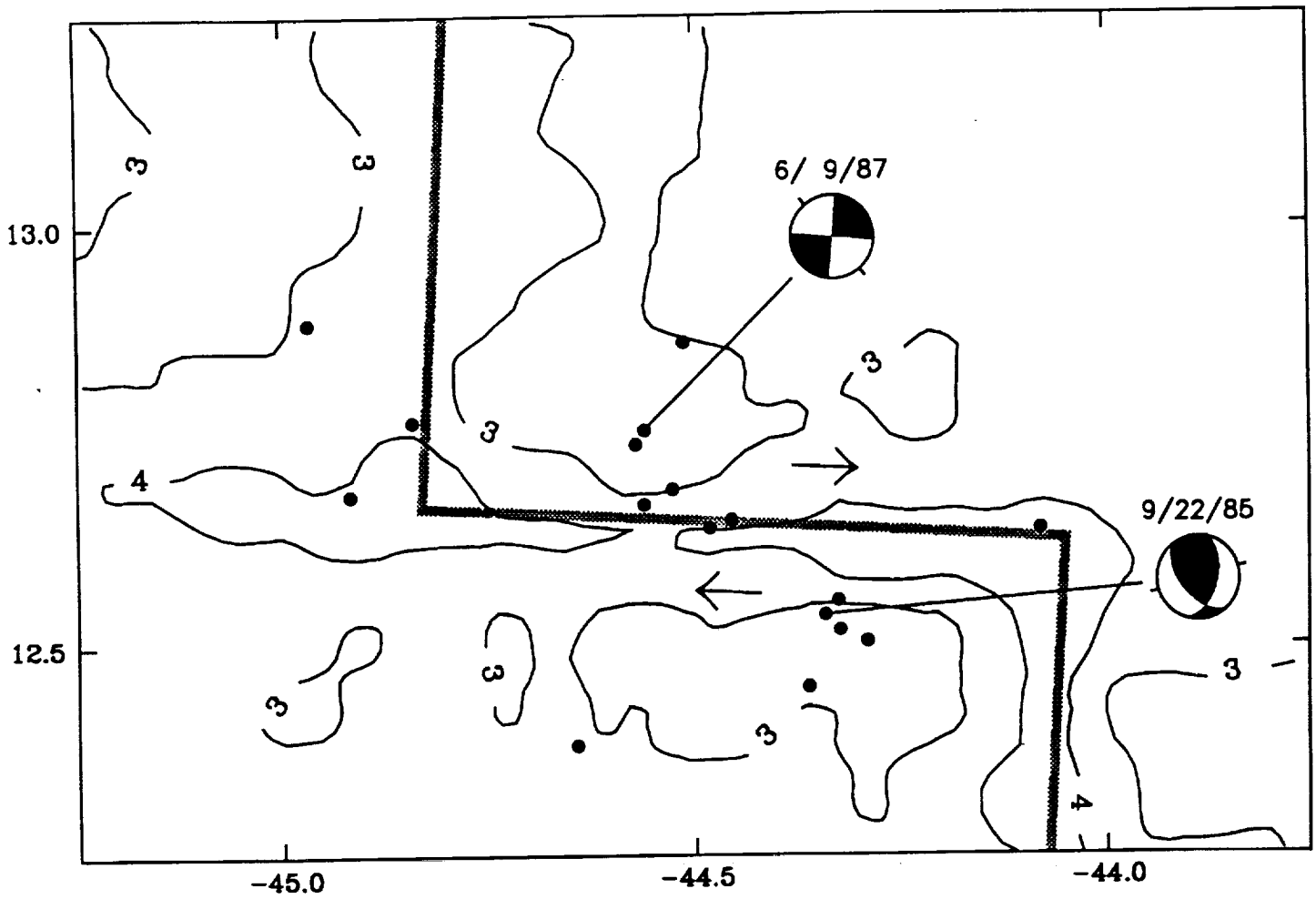

Figure 5

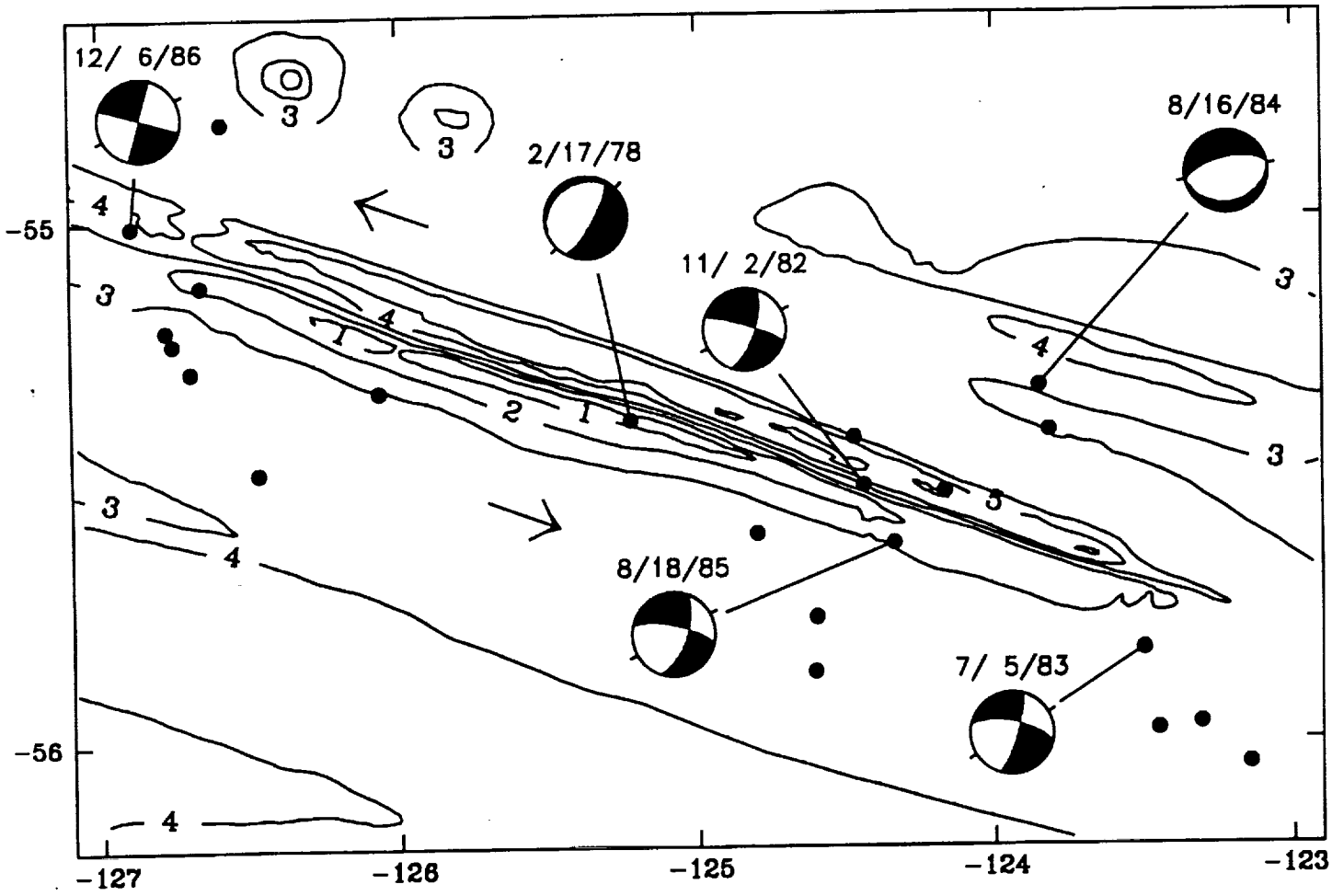
12/ 6/86
2/17/78
8/16/84
11/ 2/82
8/18/85
7/ 5/83
3
4
2
1
-55
-56
-127
-126
-125
-124
-123

Figure 6

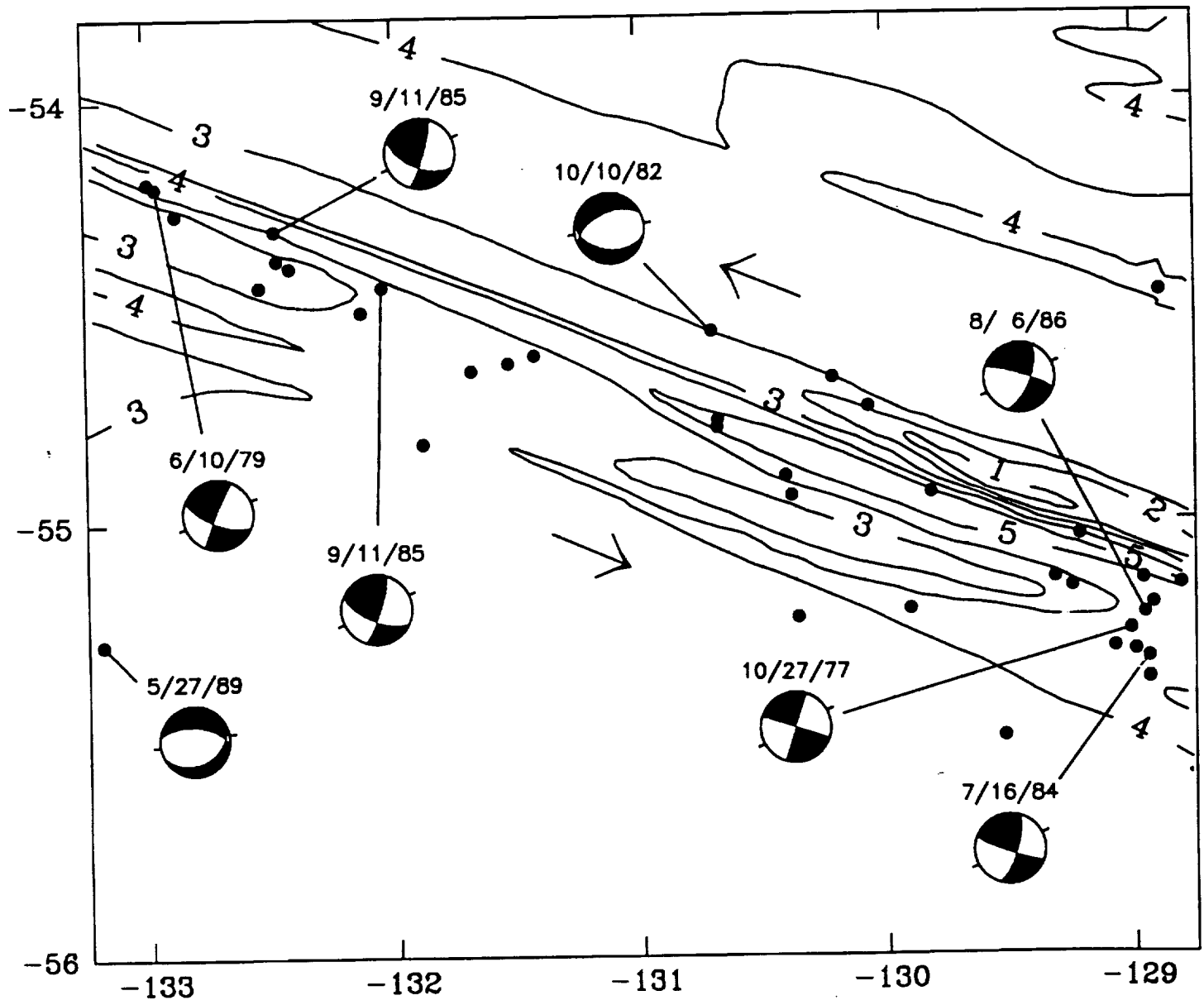
9/11/85
10/10/82
8/ 6/86
6/10/79
9/11/85
5/27/89
10/27/77
7/16/84
4
3
4
3
4
3
4
3
1
2
3
5
5
4
-54
-55
-56
-133
-132
-131
-130
-129

Figure 7

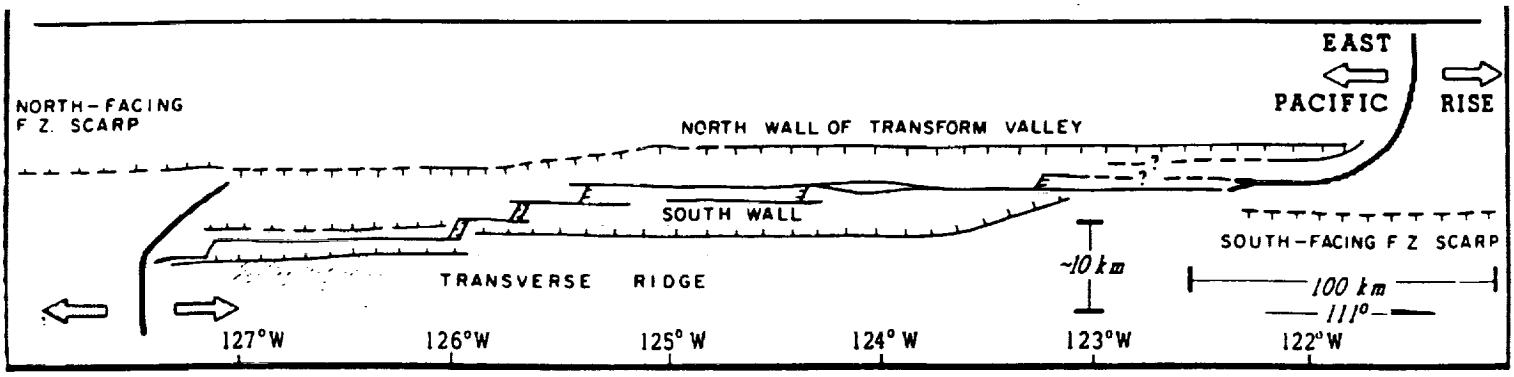
EAST
PACIFIC
RISE
NORTH-FACING
F Z. SCARP
NORTH WALL OF TRANSFORM VALLEY
SOUTH WALL
SOUTH-FACING F Z SCARP
~10 km
100 km
111°
TRANSVERSE RIDGE
127°W
126°W
125° W
124° W
123°W
122°W

Figure 8

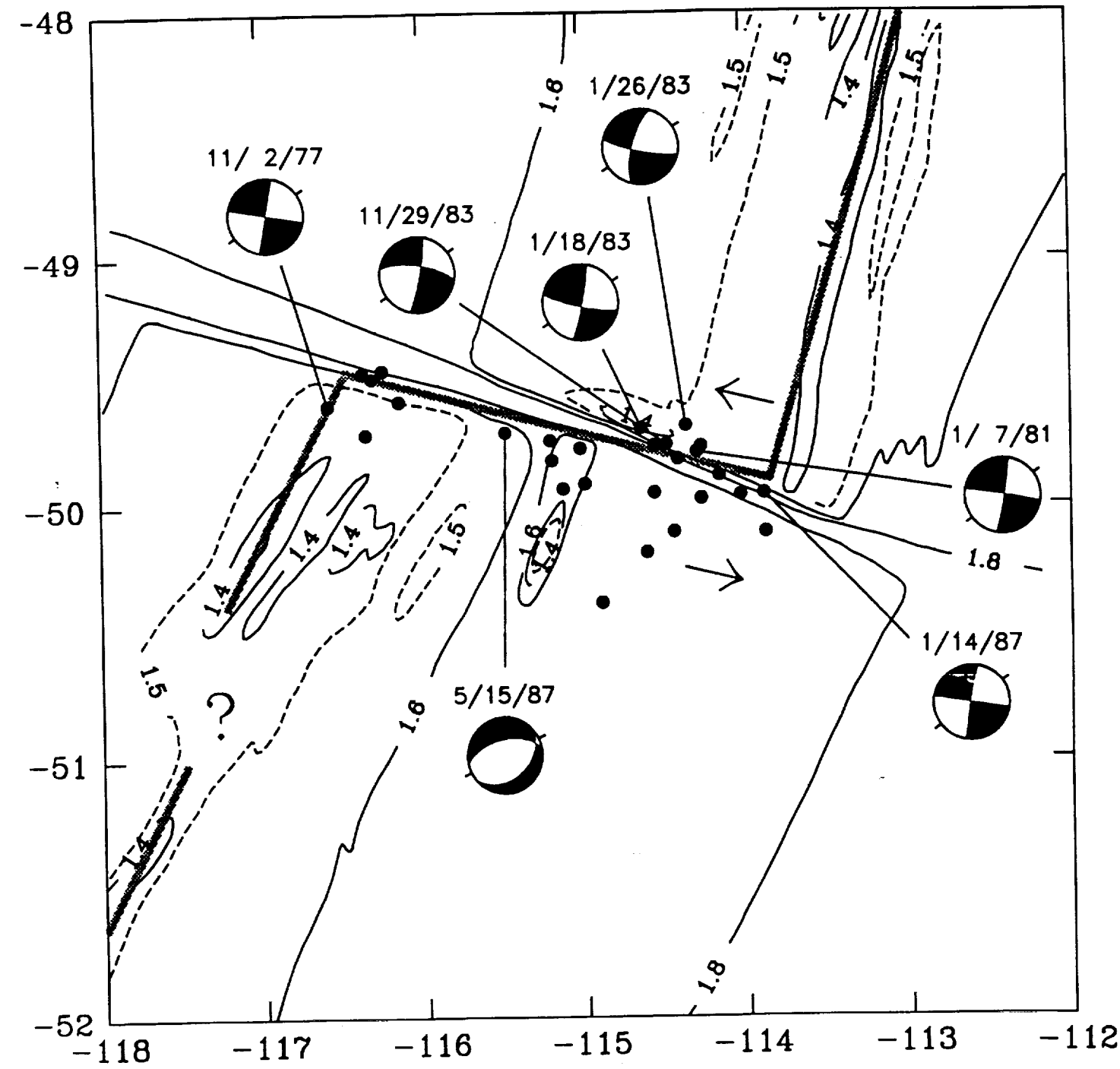
-48
-49
-50
-51
-52
-118
-117
-116
-115
-114
-113
-112
11/ 2/77
11/29/83
1/18/83
1/26/83
1/ 7/81
1/14/87
5/15/87
1.4
1.5
1.6
1.8
?

Figure 9

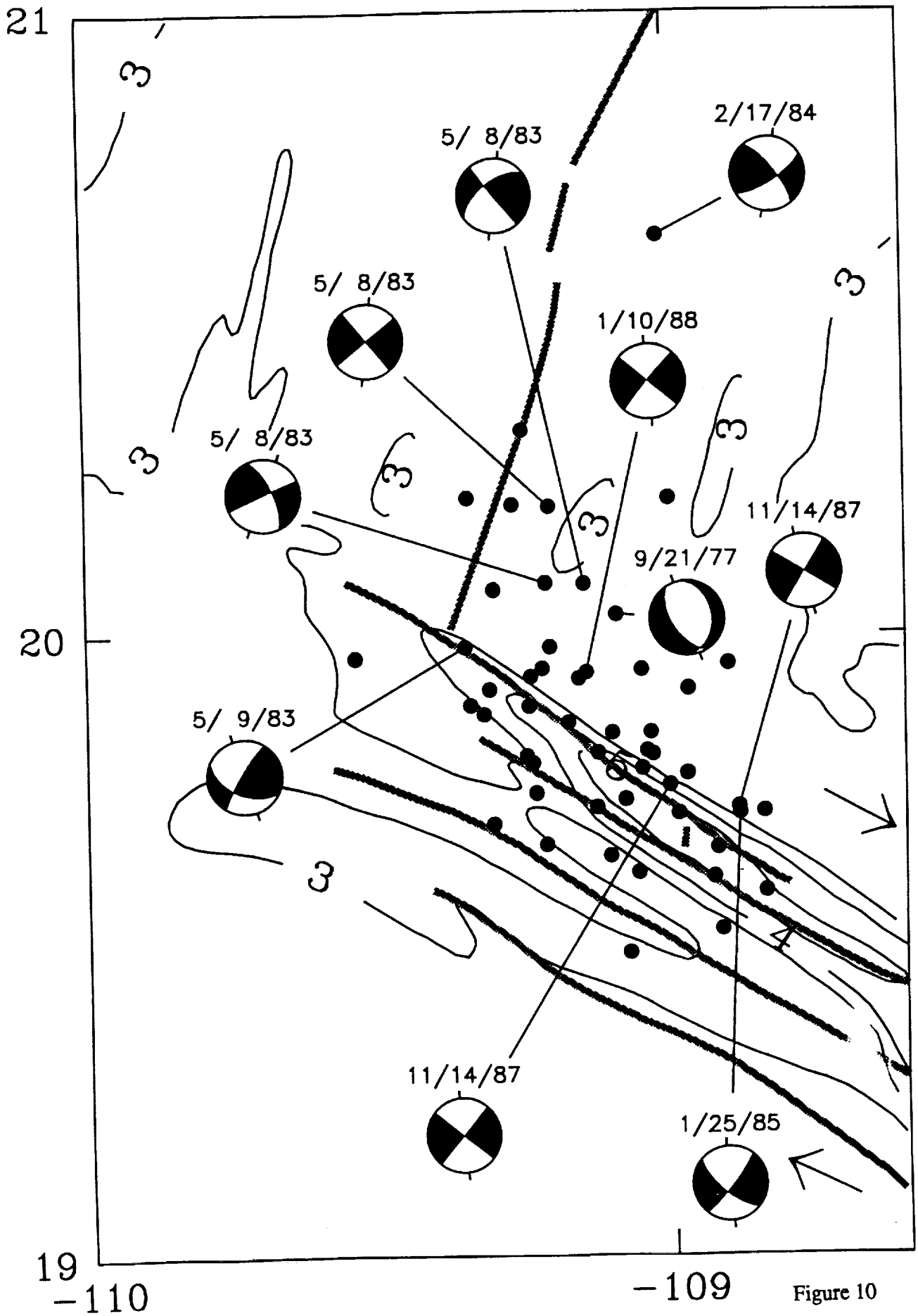
21
20
19
−110
−109
5/ 8/83
2/17/84
5/ 8/83
1/10/88
5/ 8/83
11/14/87
9/21/77
5/ 9/83
11/14/87
1/25/85
3
3
3
3
3
3
3
3
4

Figure 10

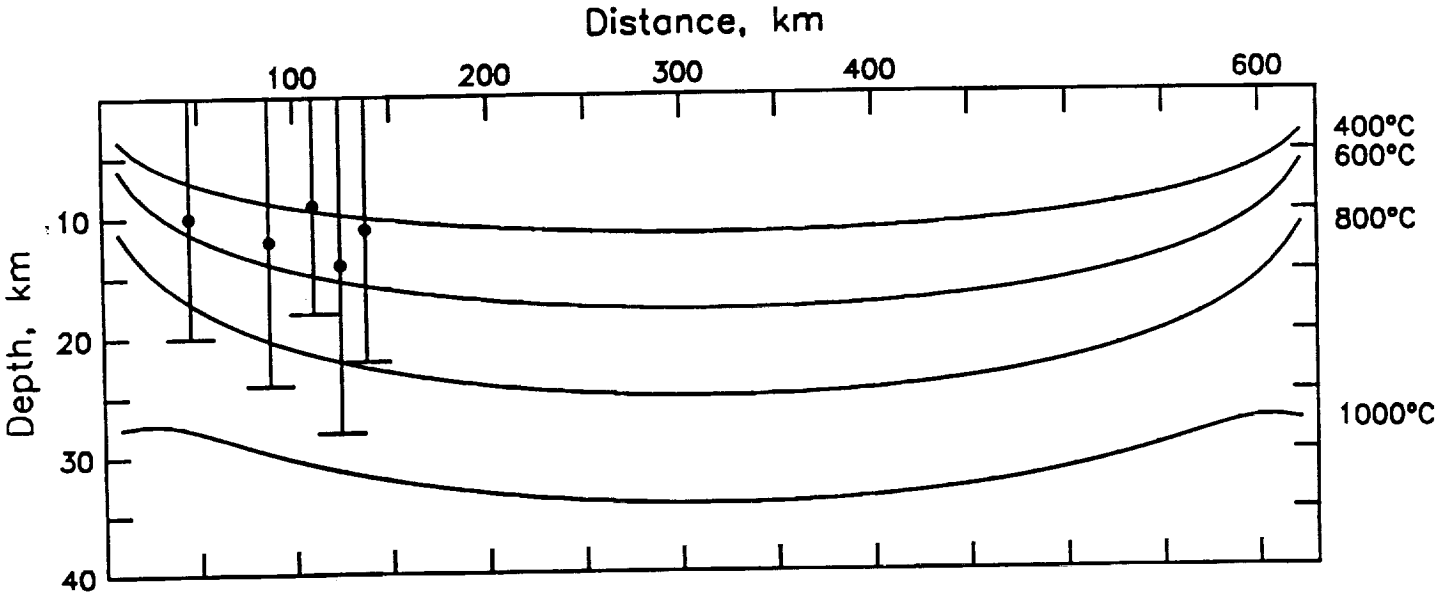
Distance, km
100
200
300
400
600
Depth, km
10
20
30
40
400°C
600°C
800°C
1000°C

Figure 11a

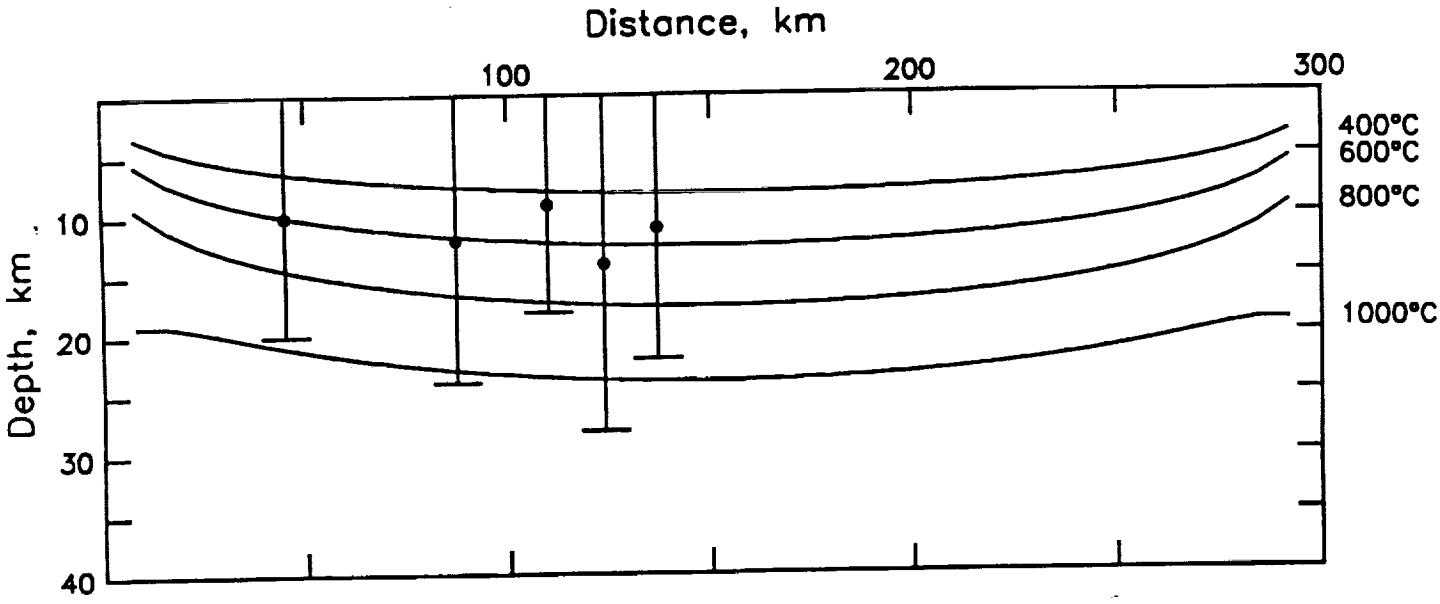
Distance, km
100
200
300
Depth, km
10
20
30
40
400°C
600°C
800°C
1000°C

Figure 11b

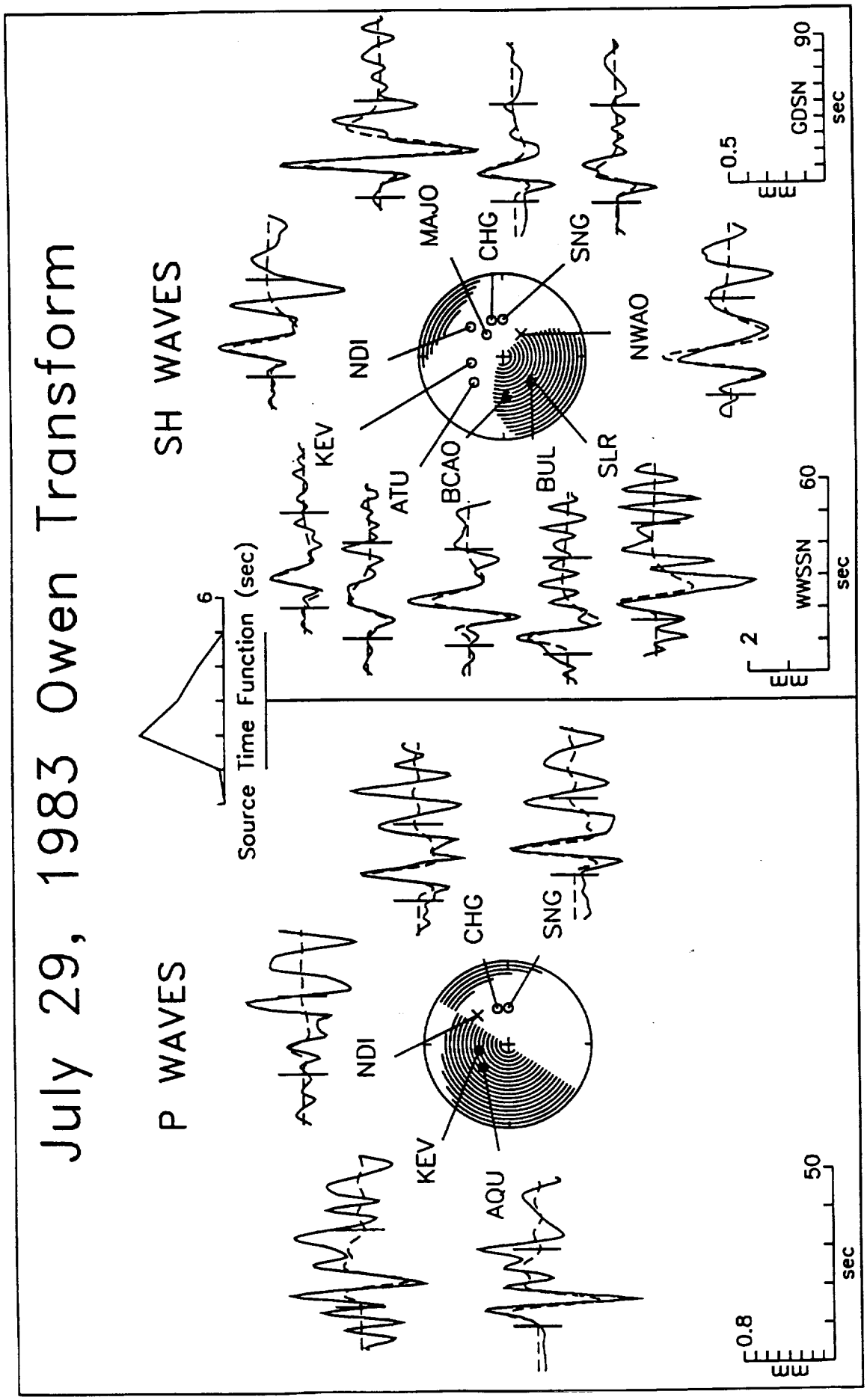
July 29, 1983 Owen Transform
P WAVES
SH WAVES
Source Time Function (sec)
6
KEV
NDI
ATU
BCAO
MAJO
CHG
BUL
SNG
SLR
NWAO
AQU
0.8
50
sec
2
60
WWSSN
0.5
90
GDSN

Figure A1

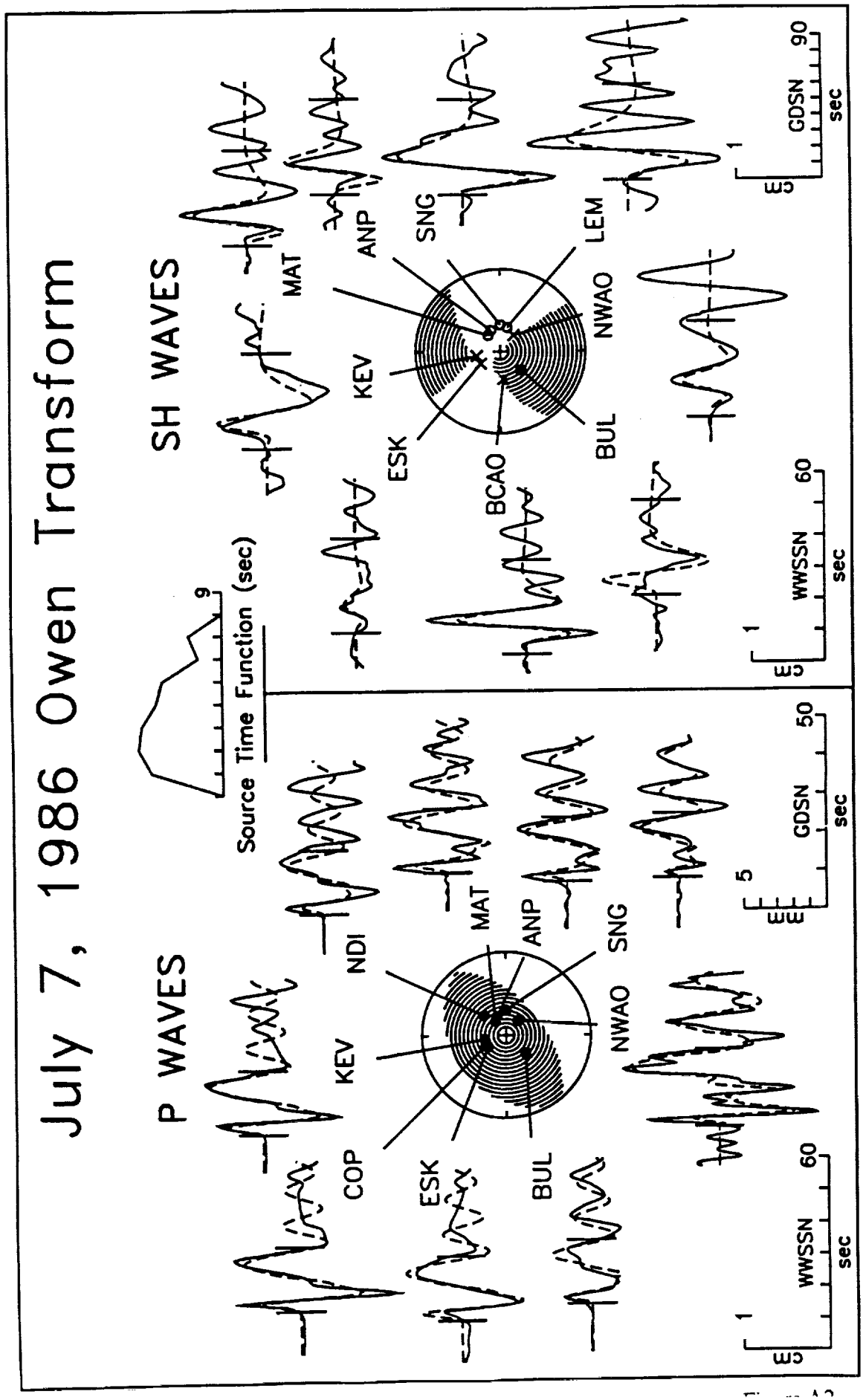
July 7, 1986 Owen Transform
P WAVES
SH WAVES
Source Time Function (sec)
9
COP
KEV
NDI
ESK
MAT
BUL
ANP
NWAO
SNG
BCAO
LEM
WWSSN
GDSN
sec
1
60
5
50
90

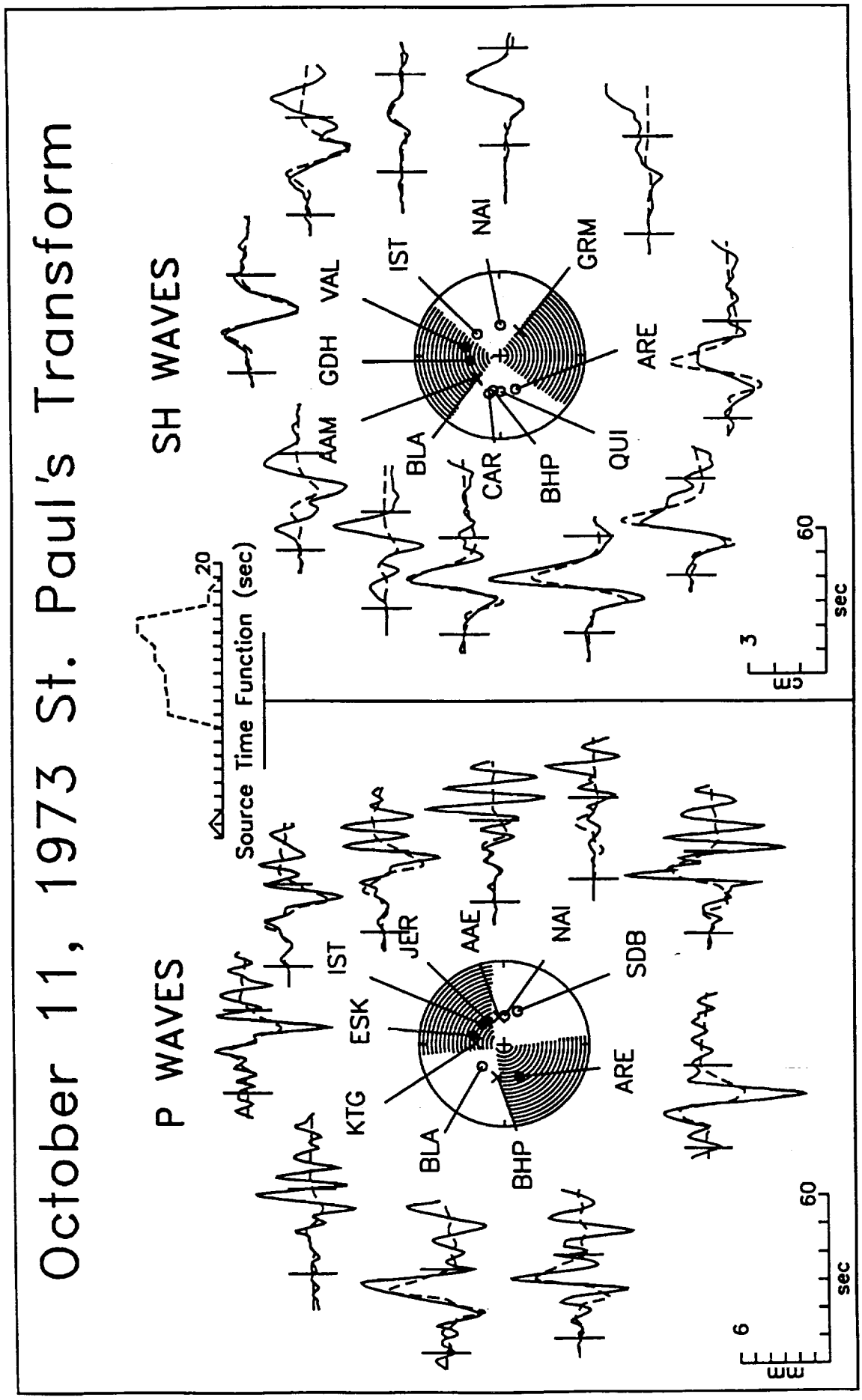
October 11, 1973 St. Paul's Transform
P WAVES
SH WAVES
Source Time Function (sec)
20
AAM
GDH
VAL
IST
BLA
CAR
NAI
BHP
QUI
GRM
ARE
KTG
ESK
JER
AAE
SDB
3
60
sec
6
60
sec

Figure A3

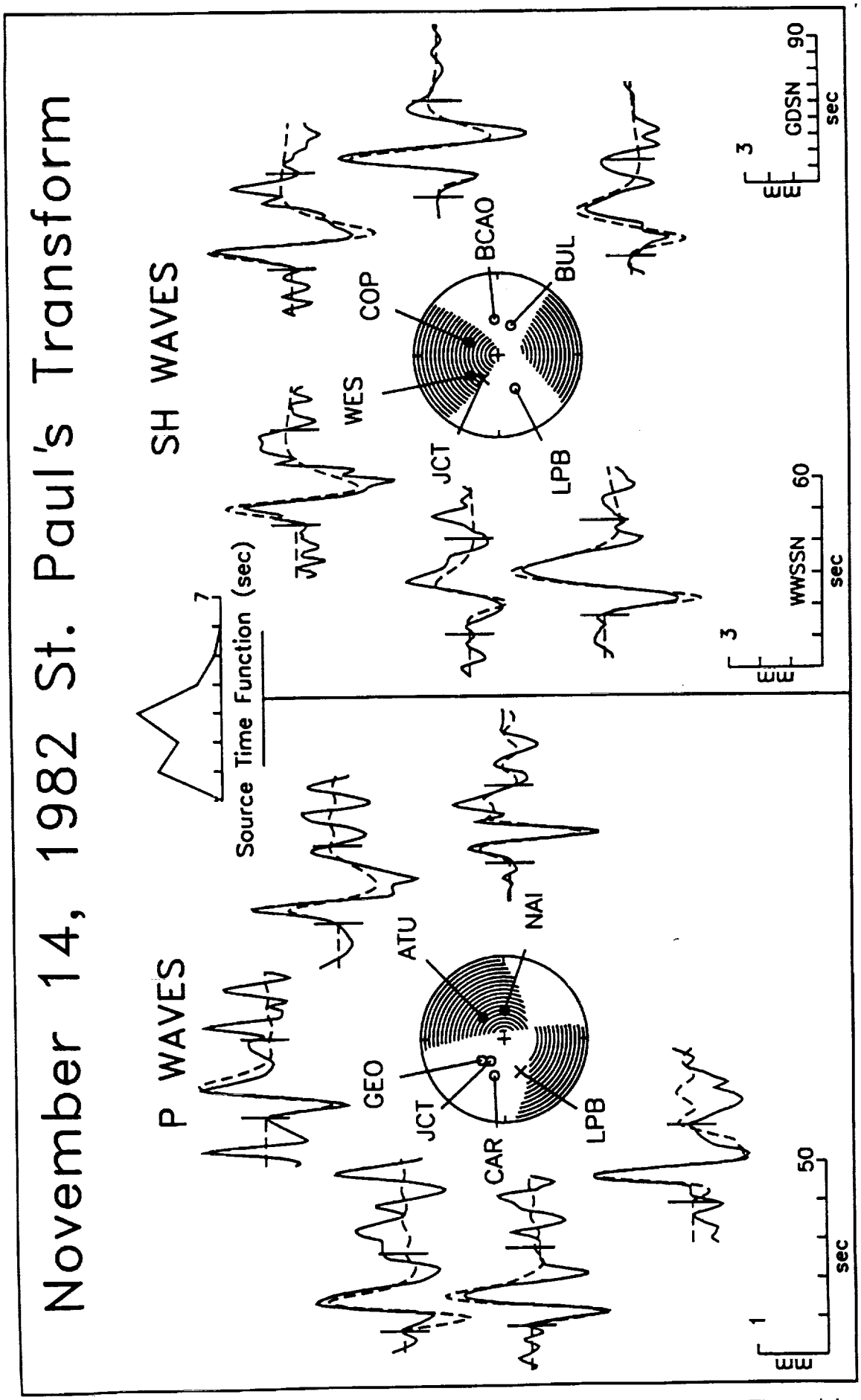
November 14, 1982 St. Paul's Transform
P WAVES
SH WAVES
Source Time Function (sec)
7
GEO
ATU
NAI
JCT
CAR
LPB
WES
COP
BCAO
BUL
JCT
LPB
1
50
sec
3
WWSSN
60
sec
3
GDSN
90
sec

Figure A4

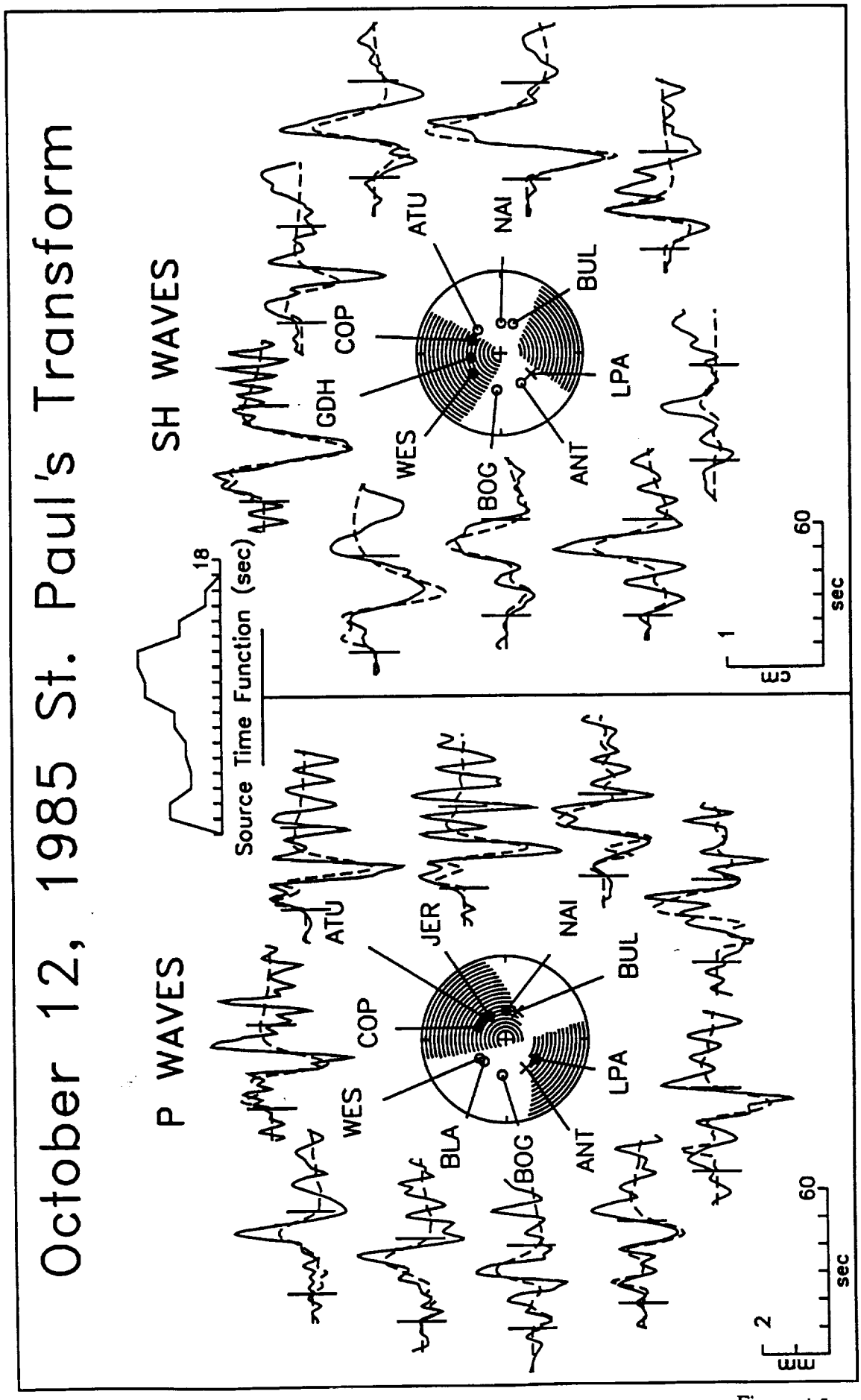
October 12, 1985 St. Paul's Transform
P WAVES
SH WAVES
Source Time Function (sec)
18
WES
COP
ATU
JER
NAI
BUL
LPA
ANT
BOG
BLA
GDH
2
60
sec
1
60
sec

Figure A5

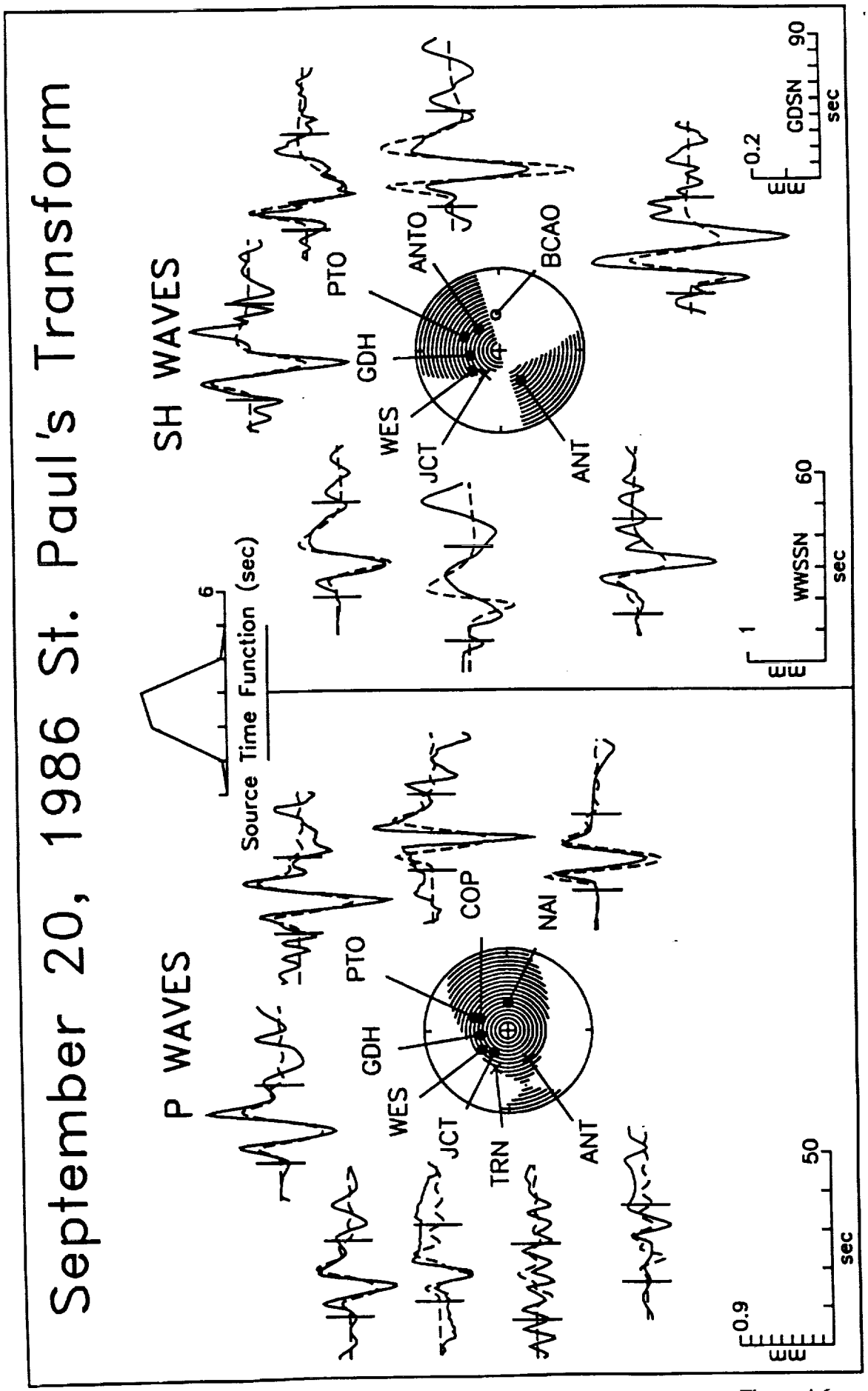
September 20, 1986 St. Paul's Transform
P WAVES
SH WAVES
Source Time Function (sec)
6
PTO
GDH
WES
JCT
TRN
ANT
COP
NAI
ANTO
BCAO
0.9
50
sec
1
WWSSN
60
sec
0.2
GDSN
90
sec

Figure A6

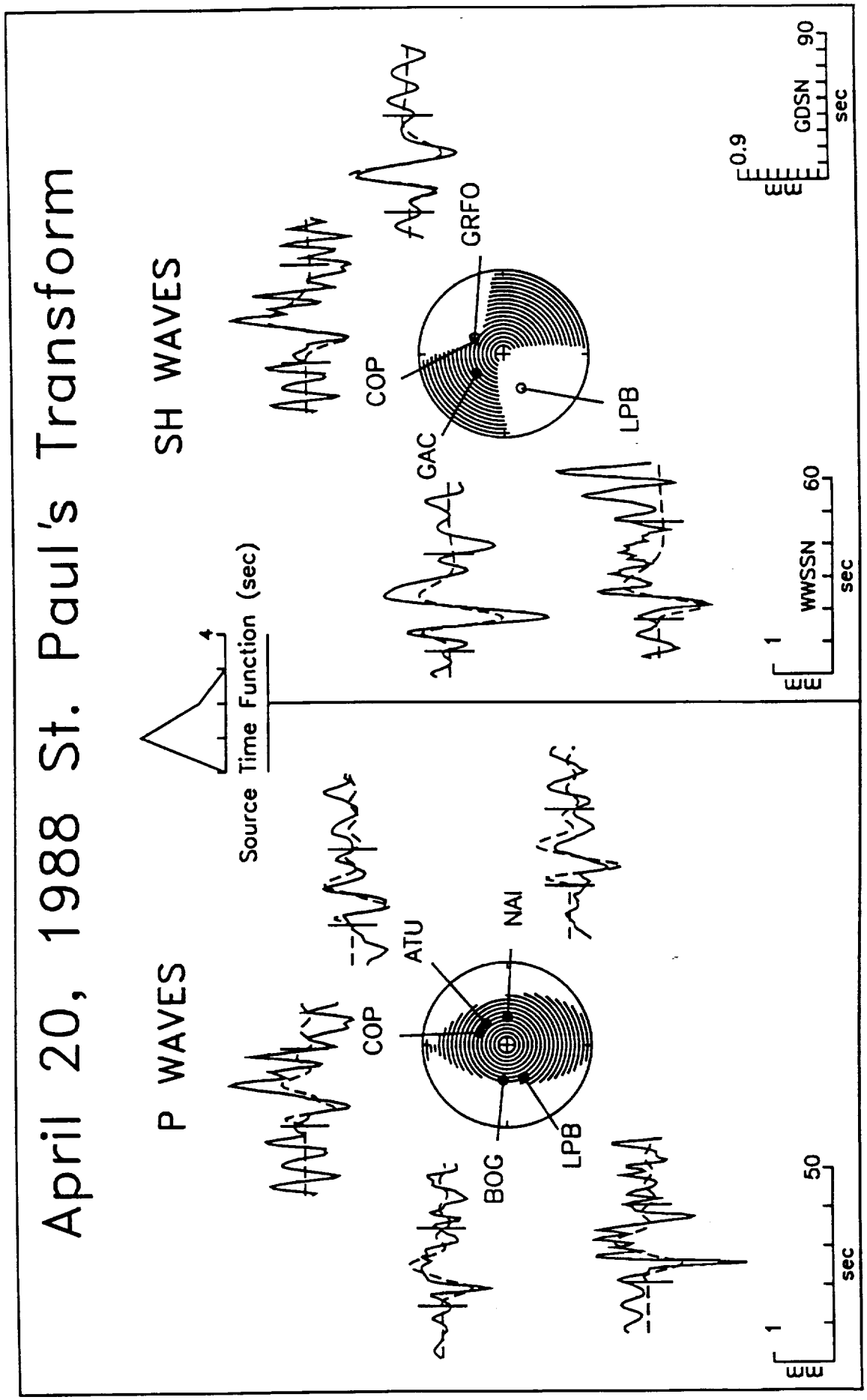
April 20, 1988 St. Paul's Transform
P WAVES
SH WAVES
Source Time Function (sec)
4
COP
ATU
NAI
BOG
LPB
GAC
GRFO
LPB
1
50
sec
1
WWSSN
60
sec
0.9
GDSN
90
sec

Figure A7

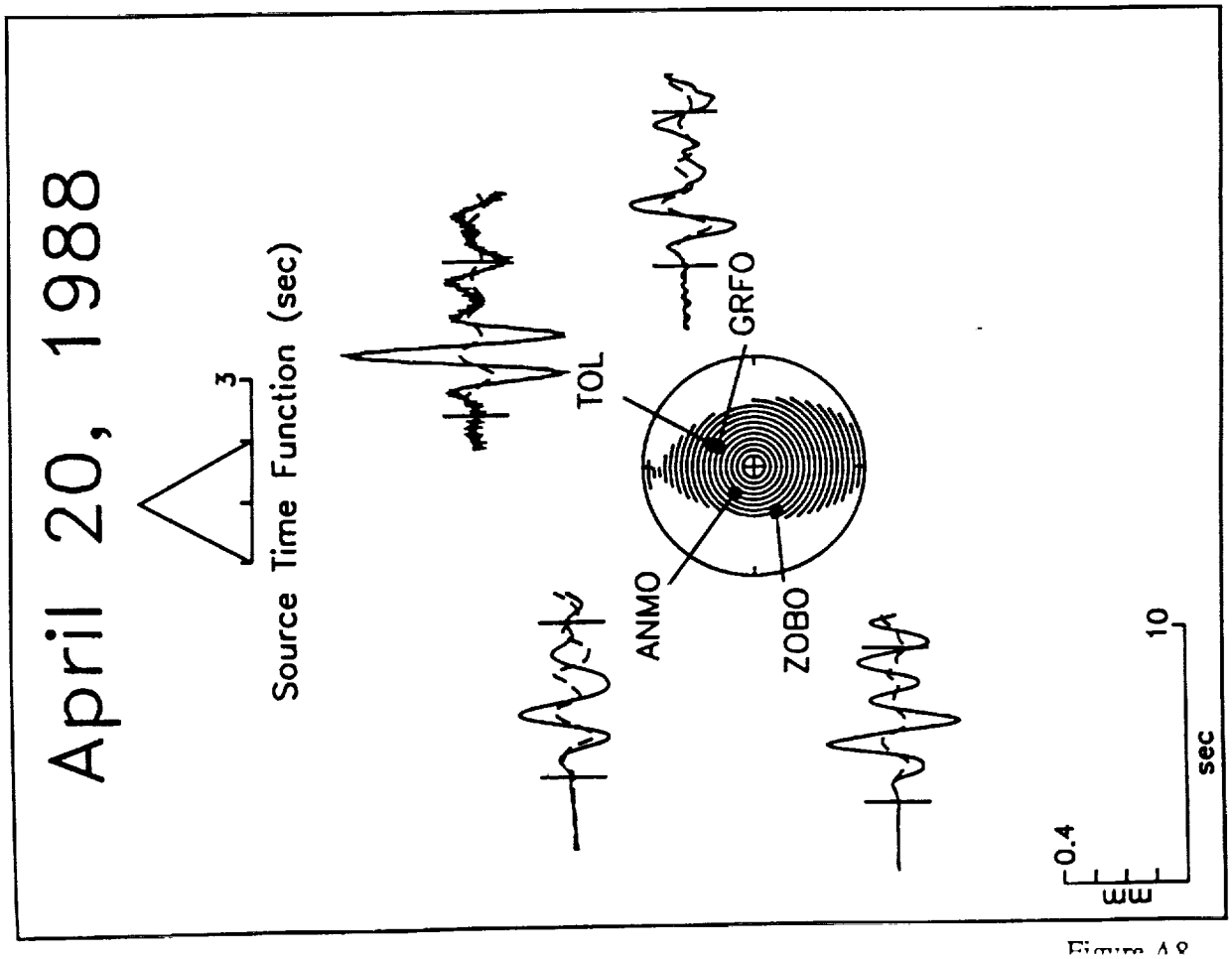
April 20, 1988
Source Time Function (sec)
3
TOL
GRFO
ANMO
ZOBO
0.4
10
sec

Figure A8

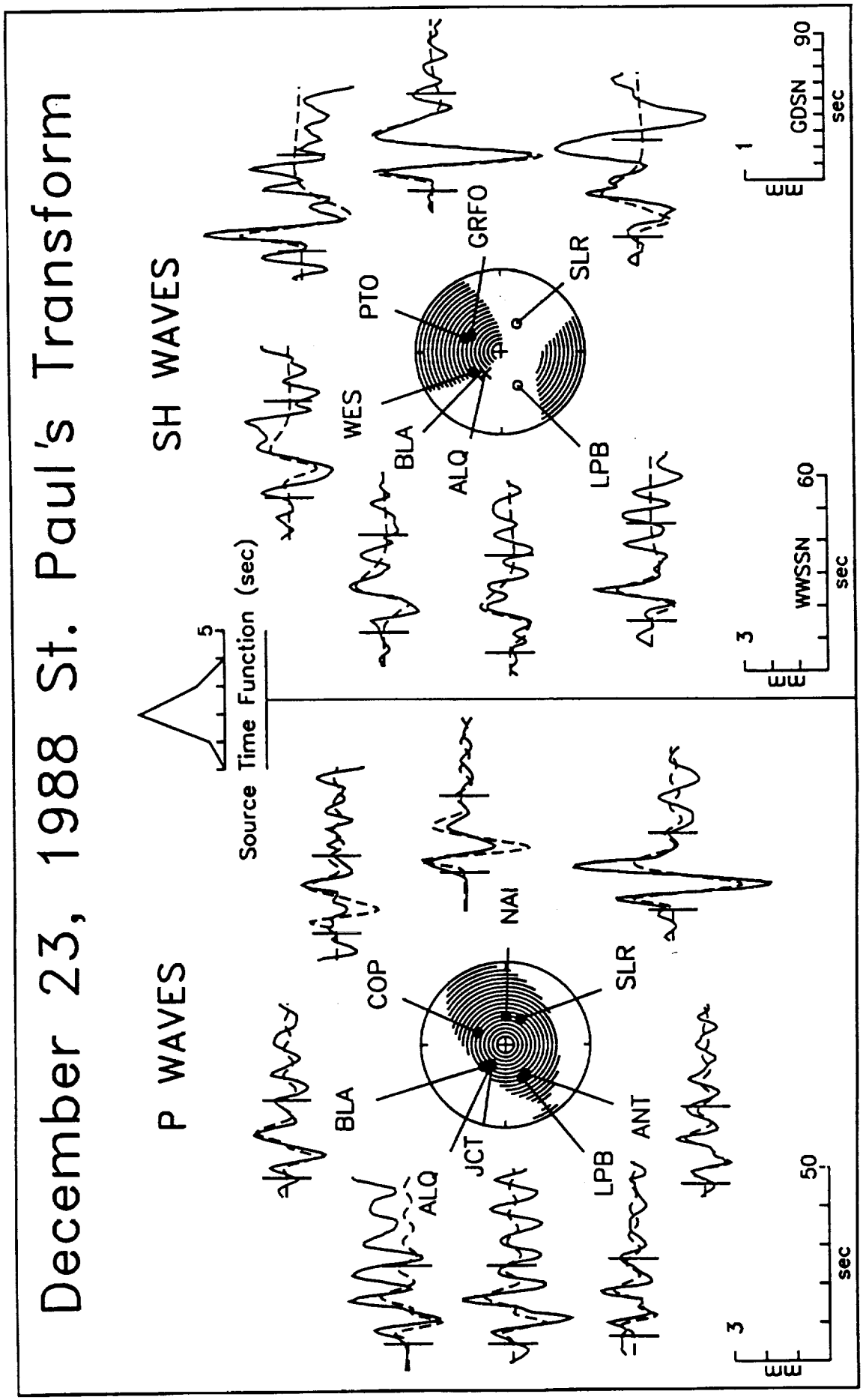
December 23, 1988 St. Paul's Transform
P WAVES
SH WAVES
Source Time Function (sec)
5
BLA
COP
NAI
ALQ
JCT
LPB
ANT
SLR
WES
PTO
BLA
ALQ
GRFO
SLR
LPB
3
50
sec
3
WWSSN
60
sec
1
GDSN
90
sec

Figure A9

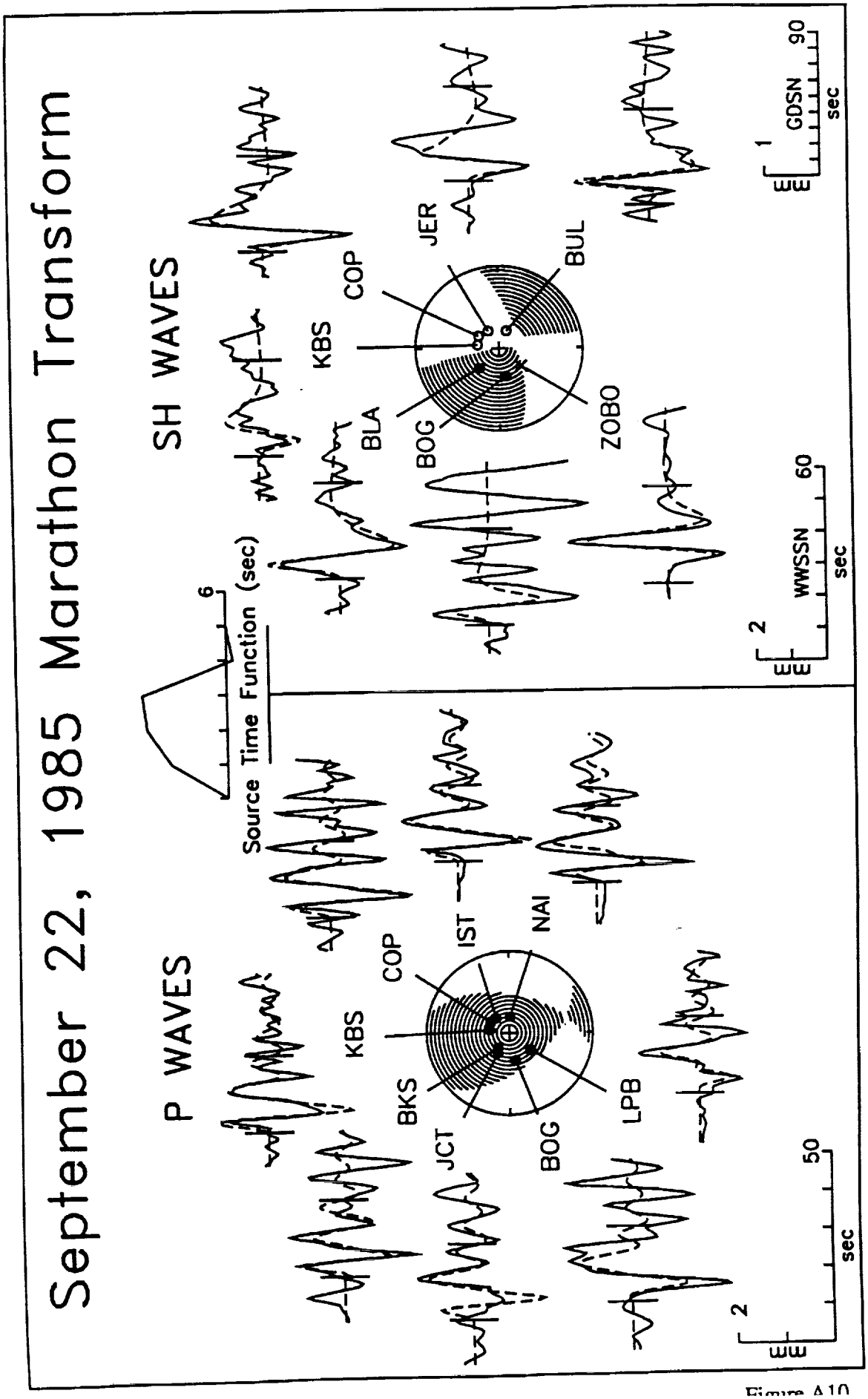
September 22, 1985 Marathon Transform
P WAVES
SH WAVES
Source Time Function (sec)
6
KBS
COP
IST
NAI
BKS
JCT
BOG
LPB
BLA
KBS
COP
JER
BUL
BOG
ZOBO
2
50
sec
2
WWSSN
60
sec
1
GDSN
90
sec

Figure A10

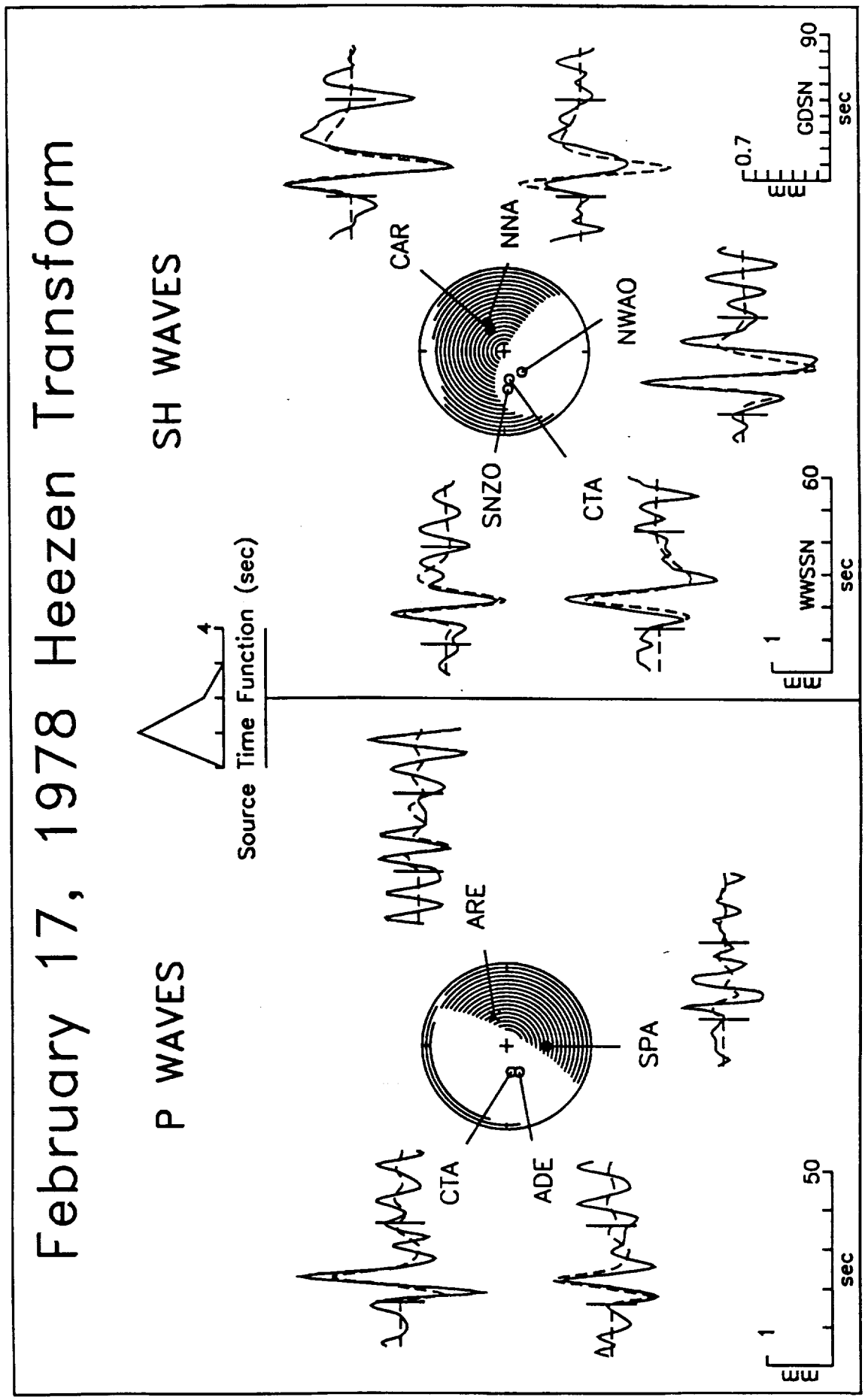
February 17, 1978 Heezen Transform
P WAVES
SH WAVES
Source Time Function (sec)
4
CTA
ADE
ARE
SPA
CAR
SNZO
NNA
CTA
NWAO
1
50
sec
1
WWSSN
60
sec
0.7
GDSN
90
sec

Figure A11

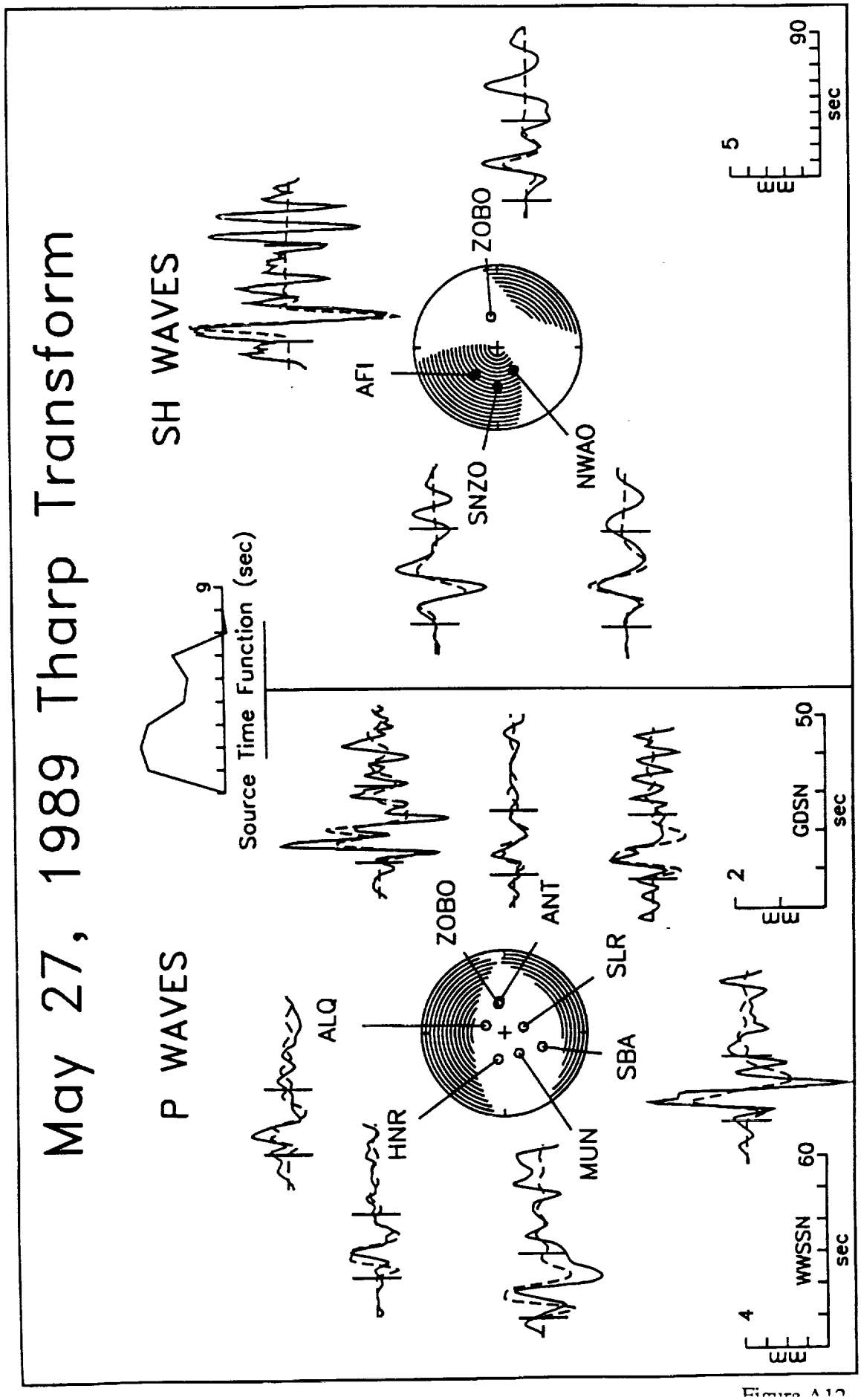
May 27, 1989 Tharp Transform
P WAVES
SH WAVES
Source Time Function (sec)
9
ALQ
HNR
ZOBO
ANT
SBA
SLR
MUN
AFI
SNZO
ZOBO
NWAO
4
WWSSN
60
sec
2
GDSN
50
sec
5
90
sec

Figure A12

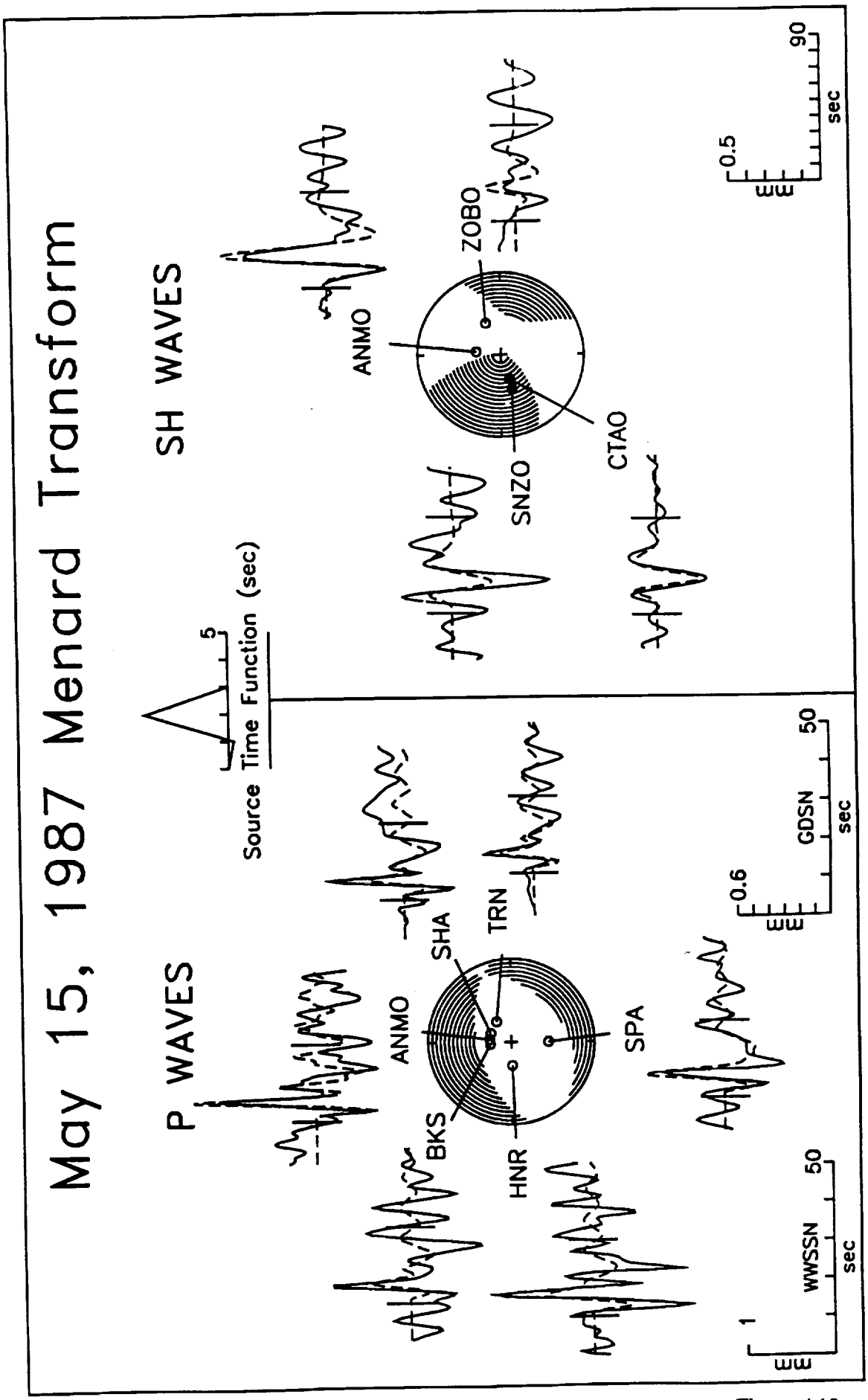
May 15, 1987 Menard Transform
P WAVES
SH WAVES
Source Time Function (sec)
5
ANMO
BKS
SHA
TRN
HNR
SPA
ZOBO
SNZO
CTAO
WWSN
GDSN
sec
1
50
0.6
0.5
90

Figure A13

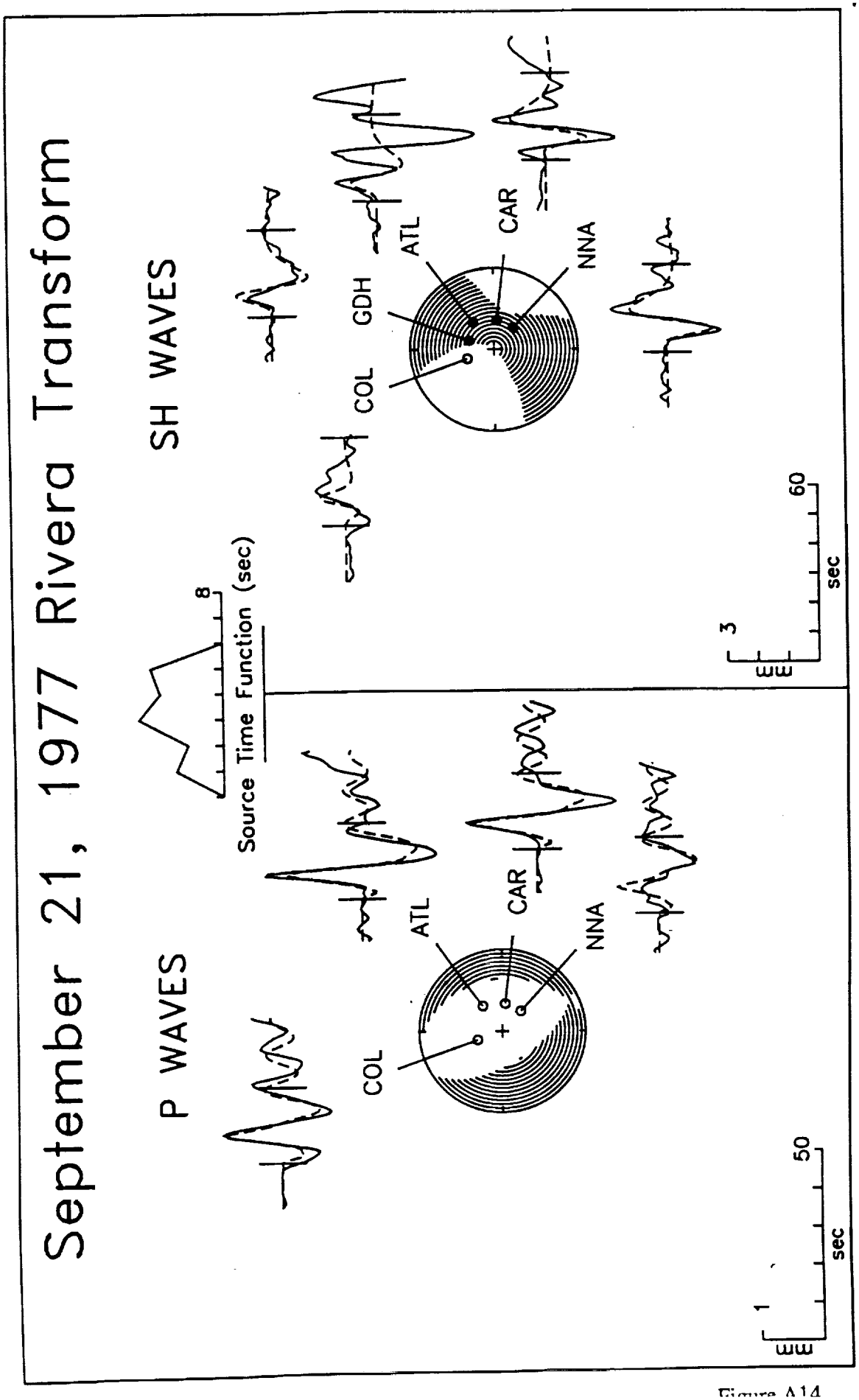
September 21, 1977 Rivera Transform
P WAVES
SH WAVES
Source Time Function (sec)
8
COL
ATL
CAR
NNA
GDH
1
50
sec
3
60
sec

Figure A14

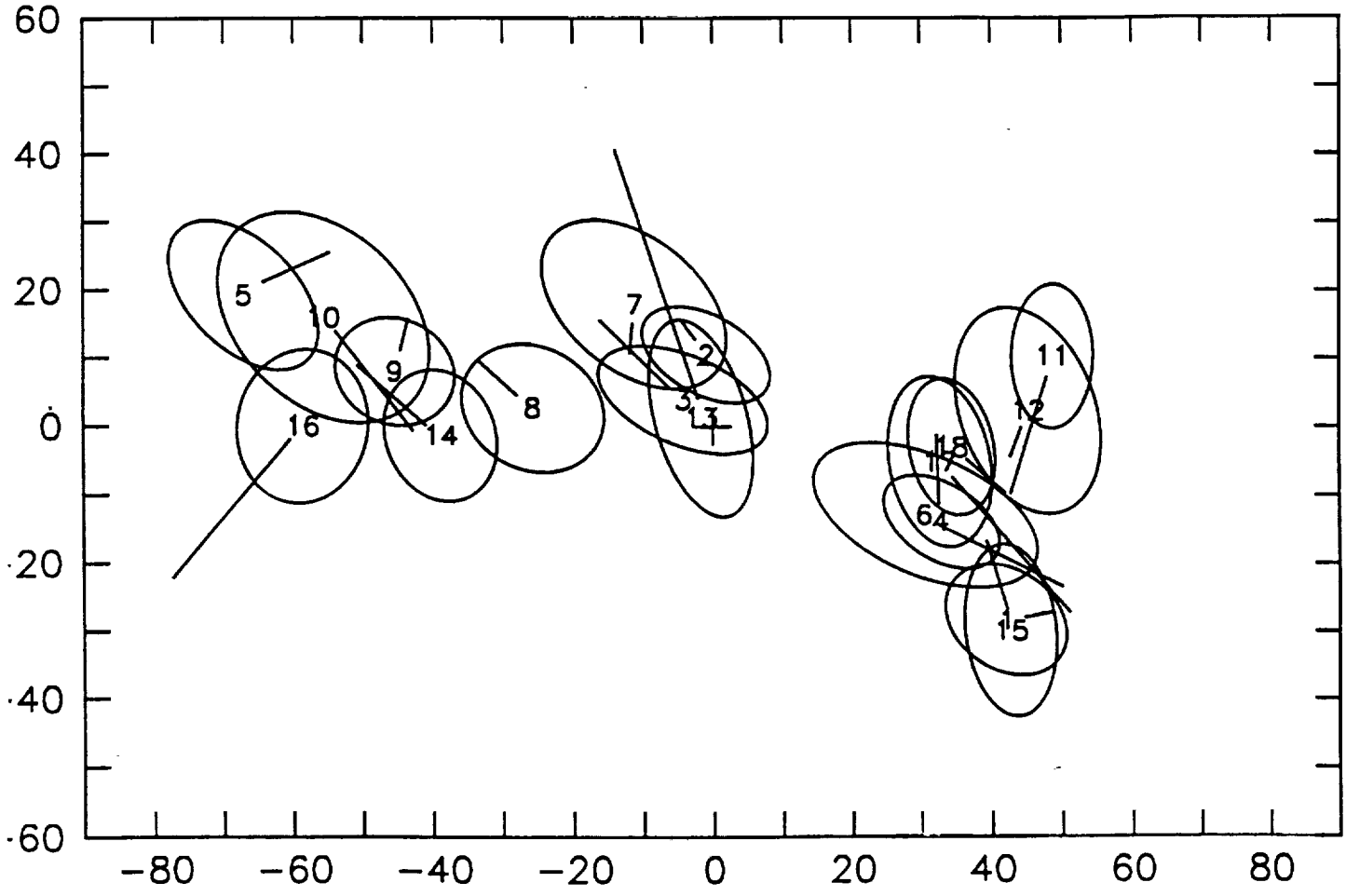
60
40
20
0
-20
-40
-60
-80
-60
-40
-20
0
20
40
60
80
5
10
9
16
14
8
7
2
3
13
11
12
18
17
64
15

Figure B1

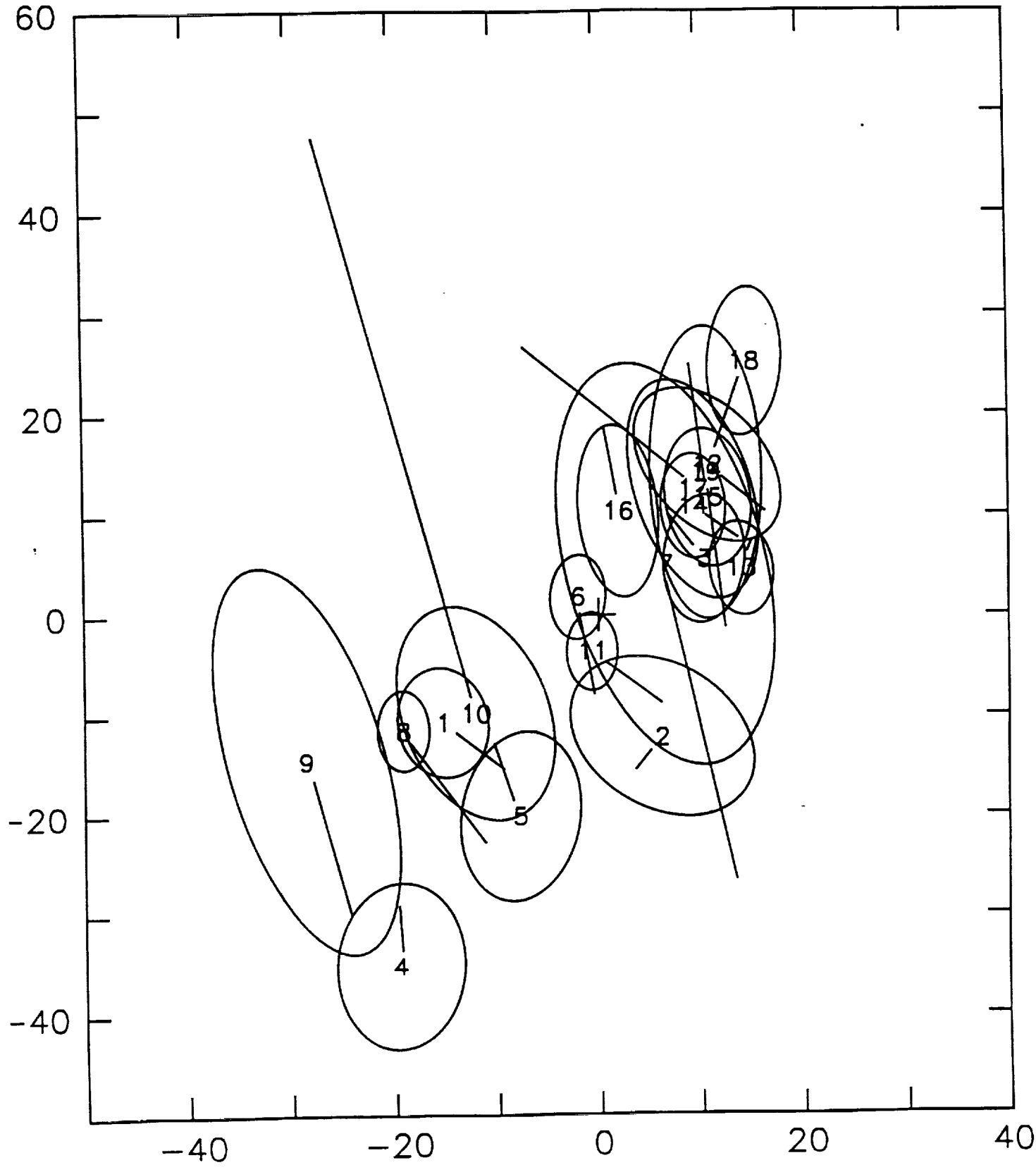

Figure B2

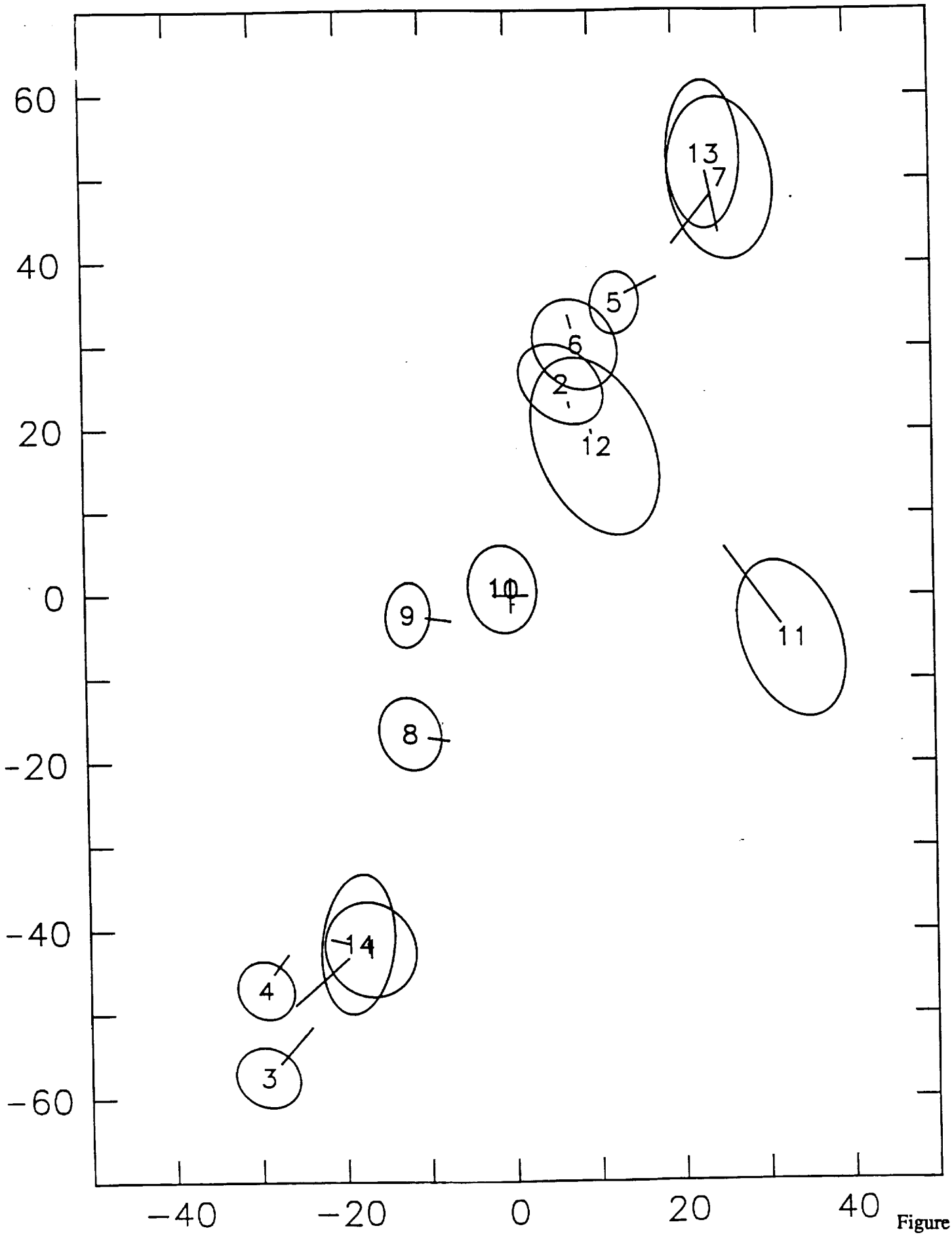

Figure B3

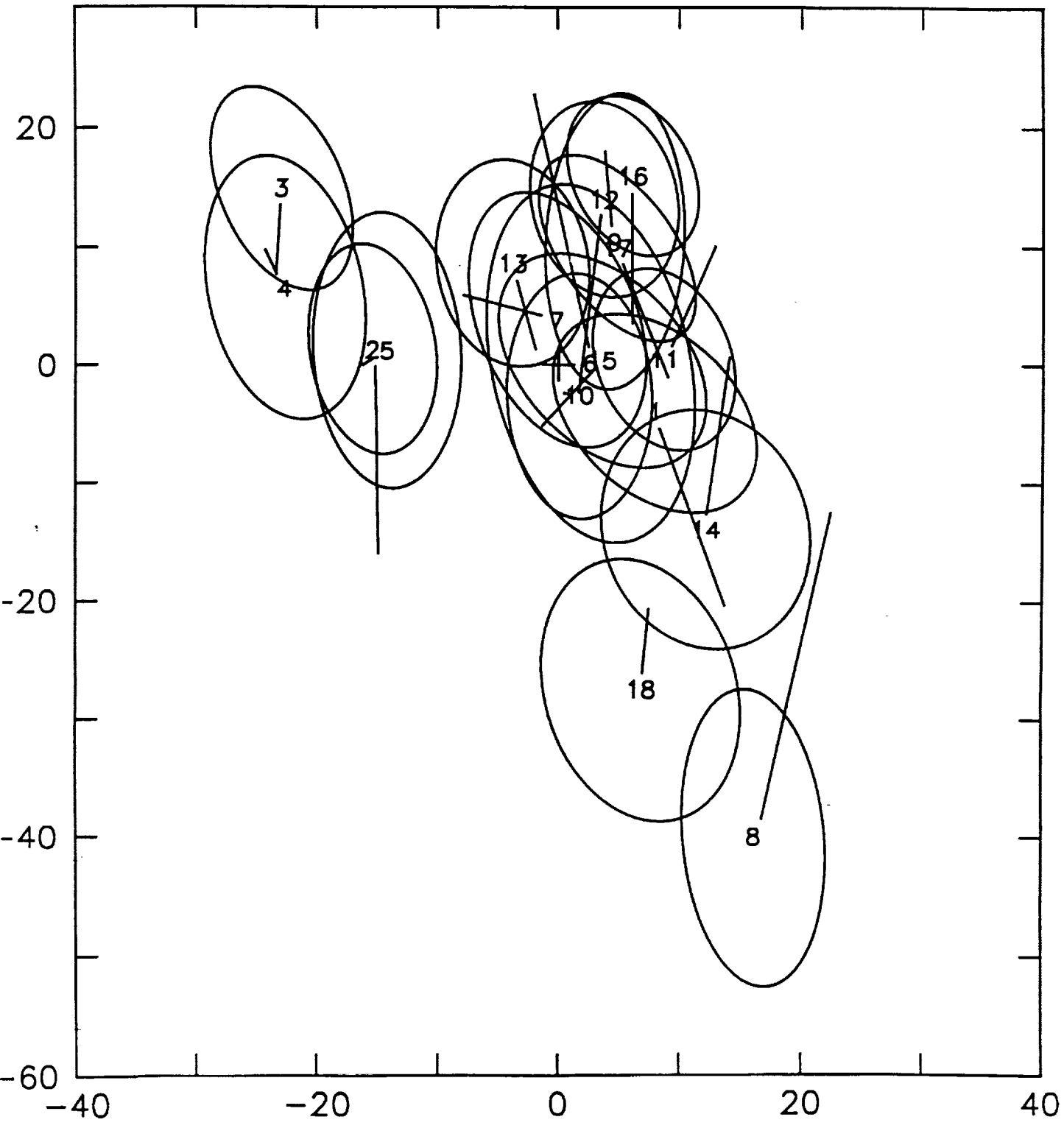

Figure B4

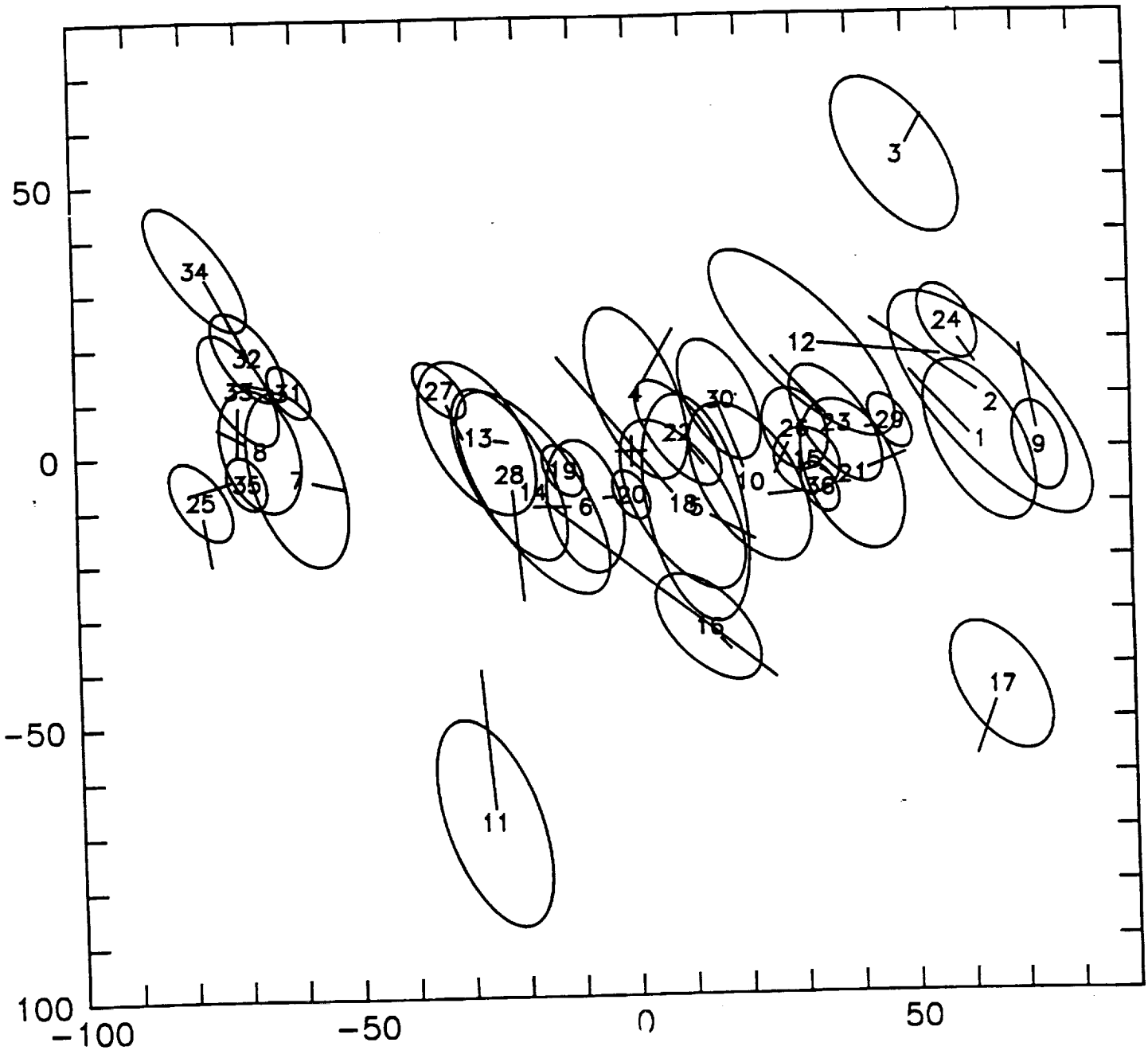
50
0
-50
100
-100
-50
0
50
3
34
32
31
27
13
4
30
12
24
2
1
9
8
35
7
25
28
19
14
6
20
18
22
10
16
17
11

Figure B5

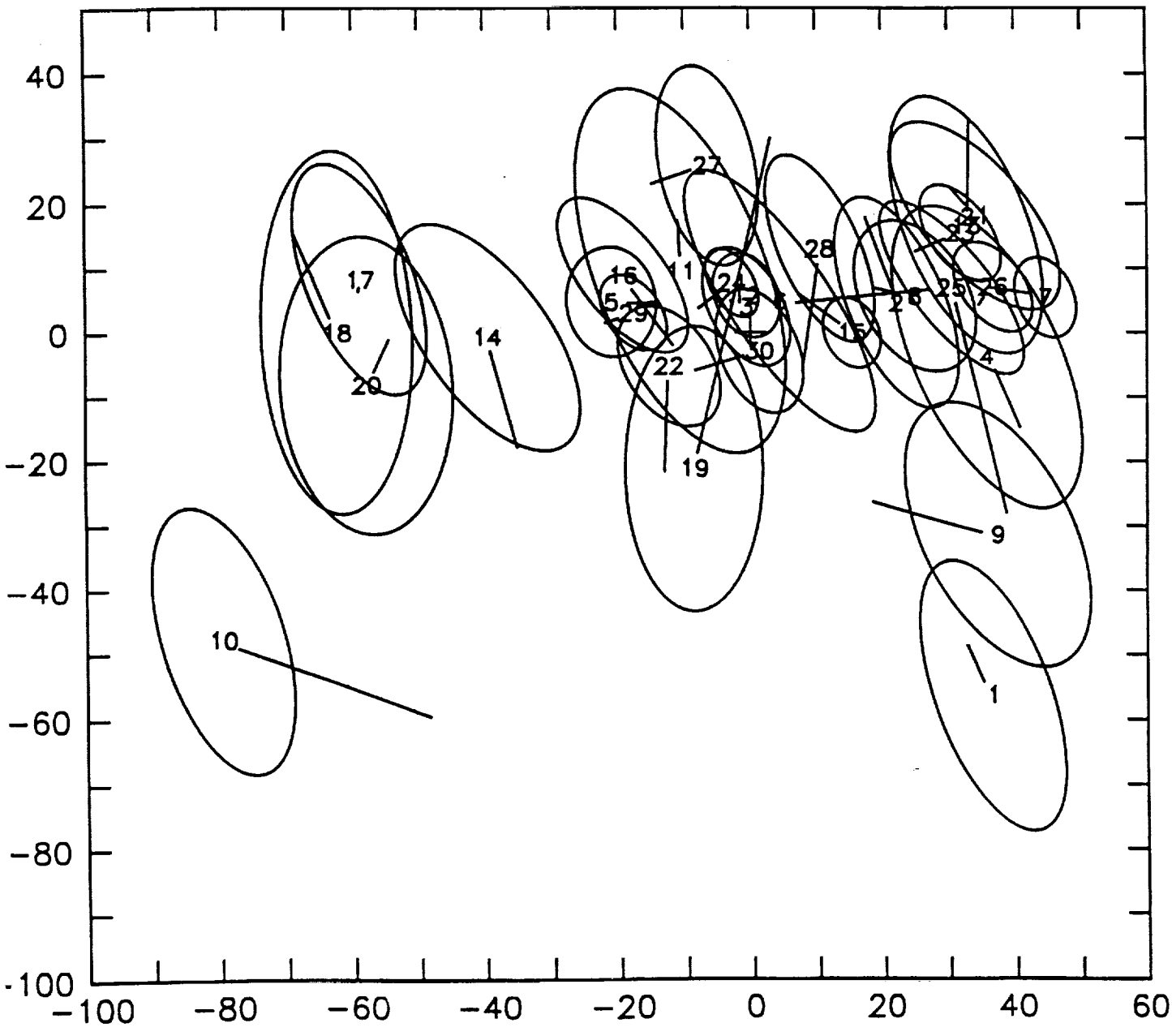
40
20
0
-20
-40
-60
-80
-100
-100
-80
-60
-40
-20
0
20
40
60
1,7
18
20
14
16
5
29
27
11
24
13
28
22
30
19
15
26
25
6
7
4
21
23
9
10
1

Figure B6

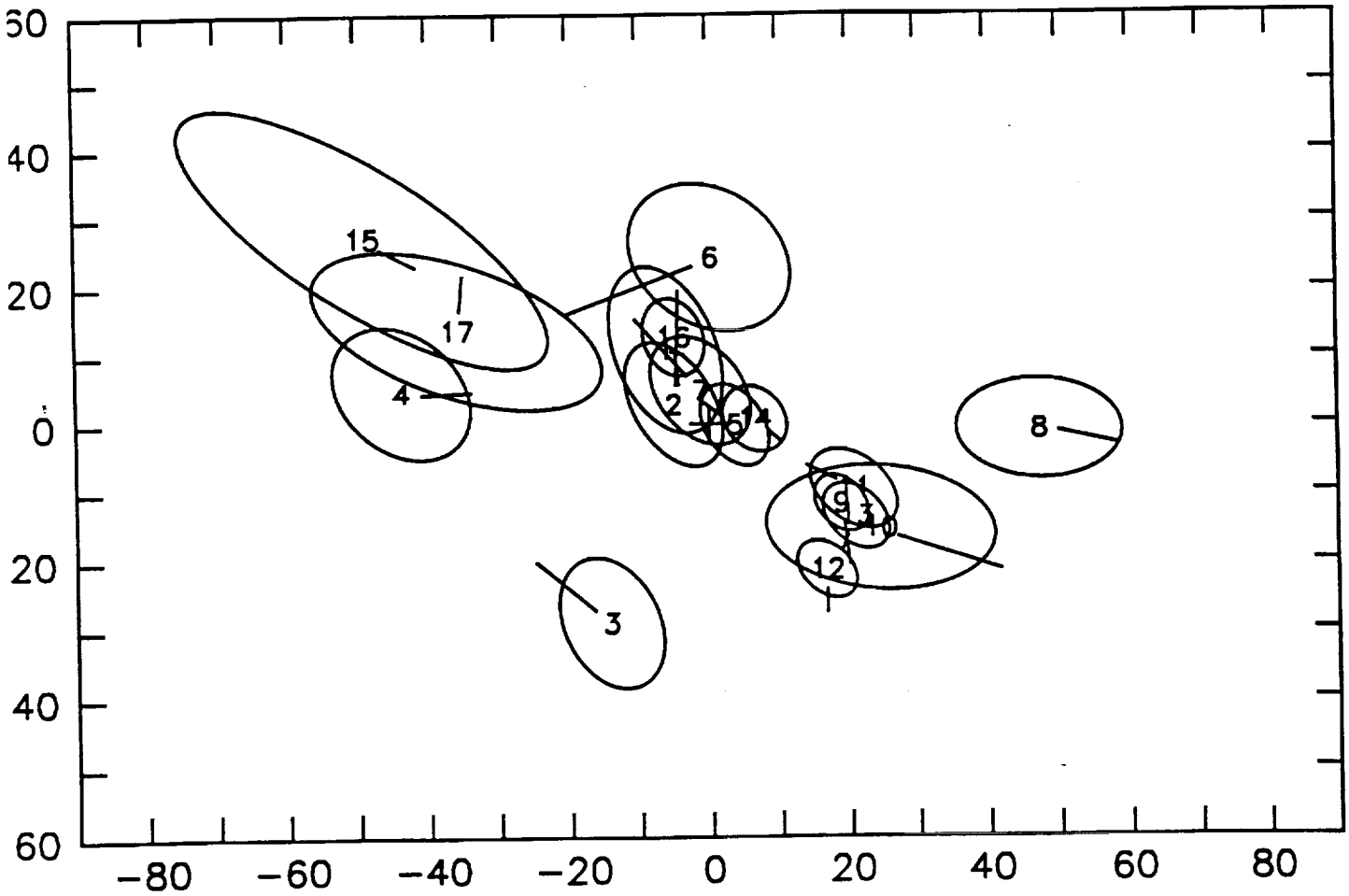
60
40
20
0
20
40
60
-80
-60
-40
-20
0
20
40
60
80
15
17
4
6
16
2
5
14
8
9
3
10
12
3

Figure B7

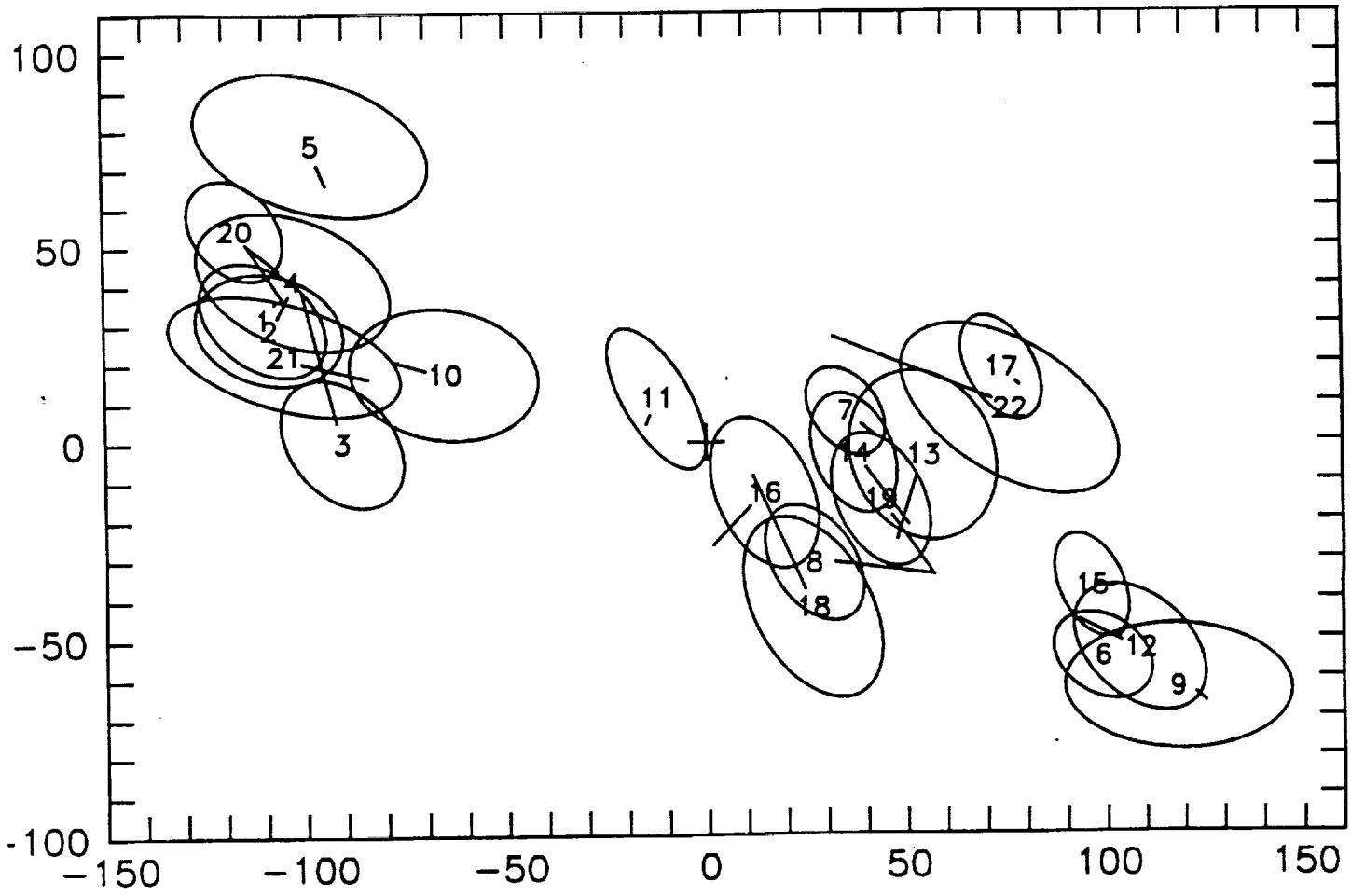
100
50
0
-50
-100
-150
-100
-50
0
50
100
150
5
20
4
1
2
21
10
3
11
7
14
13
17
22
16
19
8
18
15
6
12
9

Figure B8

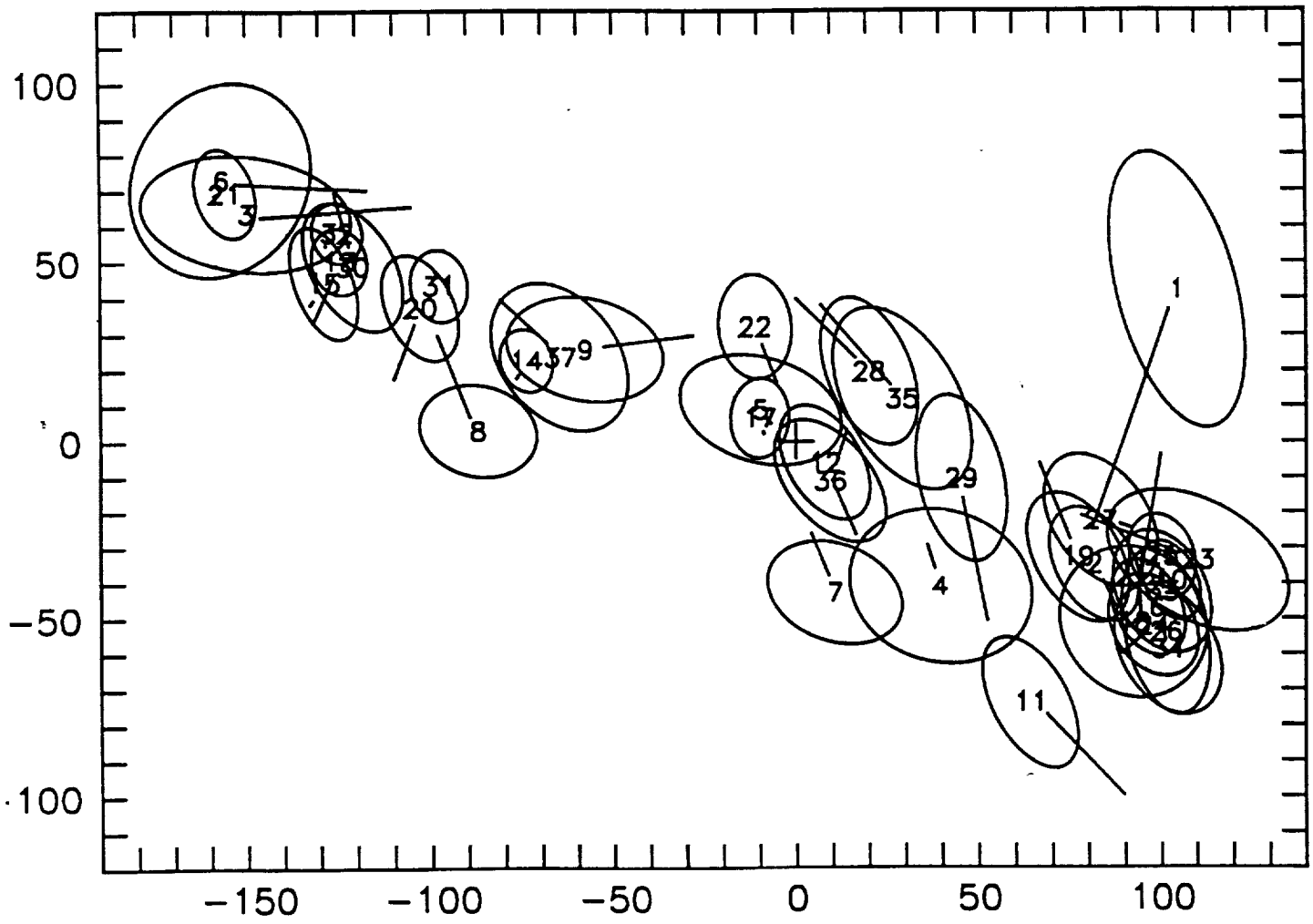

Figure B9

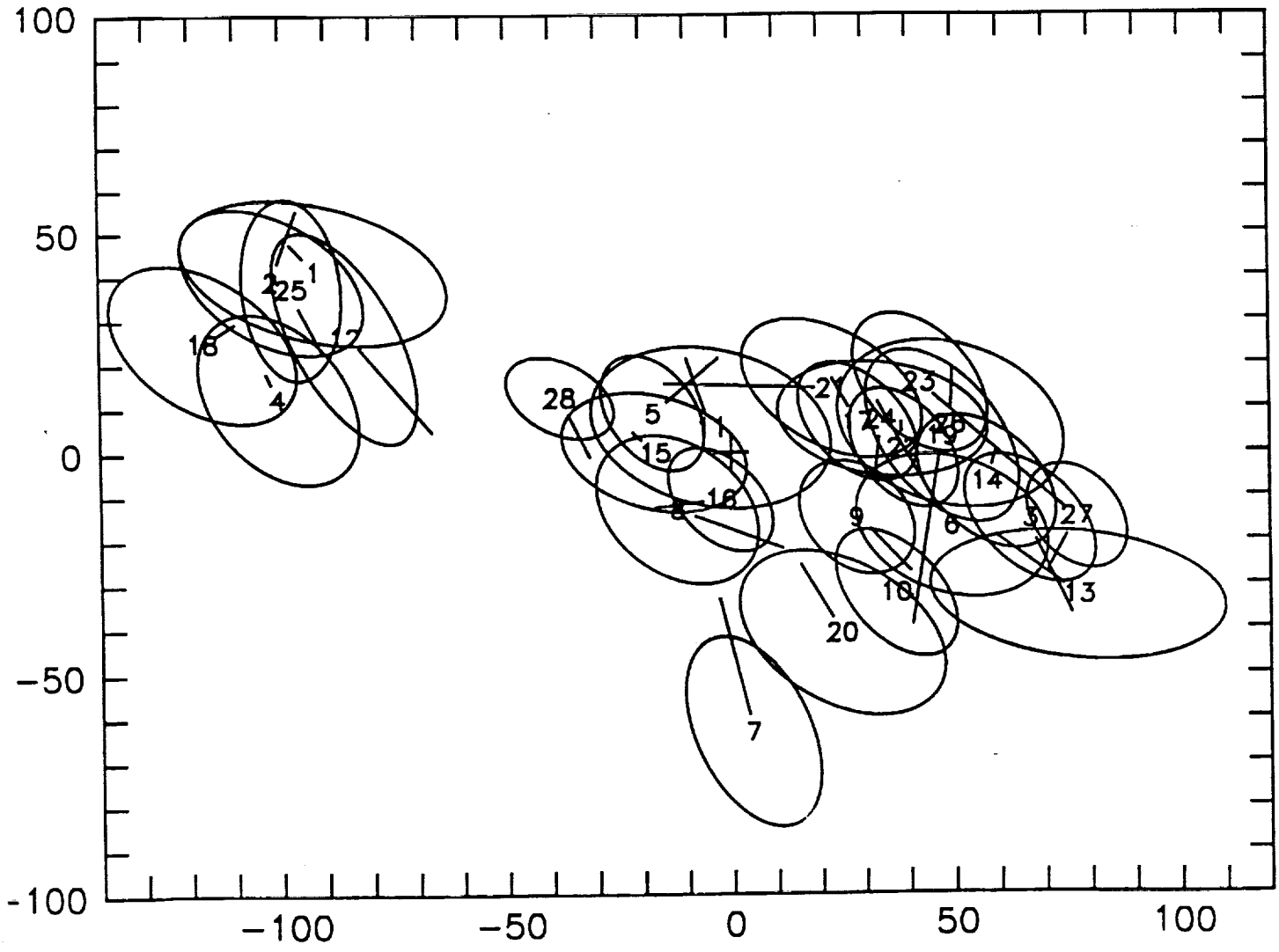
100
50
0
-50
-100
-100
-50
0
50
100
1
2
25
18
4
12
28
5
11
15
16
21
23
24
26
14
9
6
3
27
13
10
20
7

Figure B10

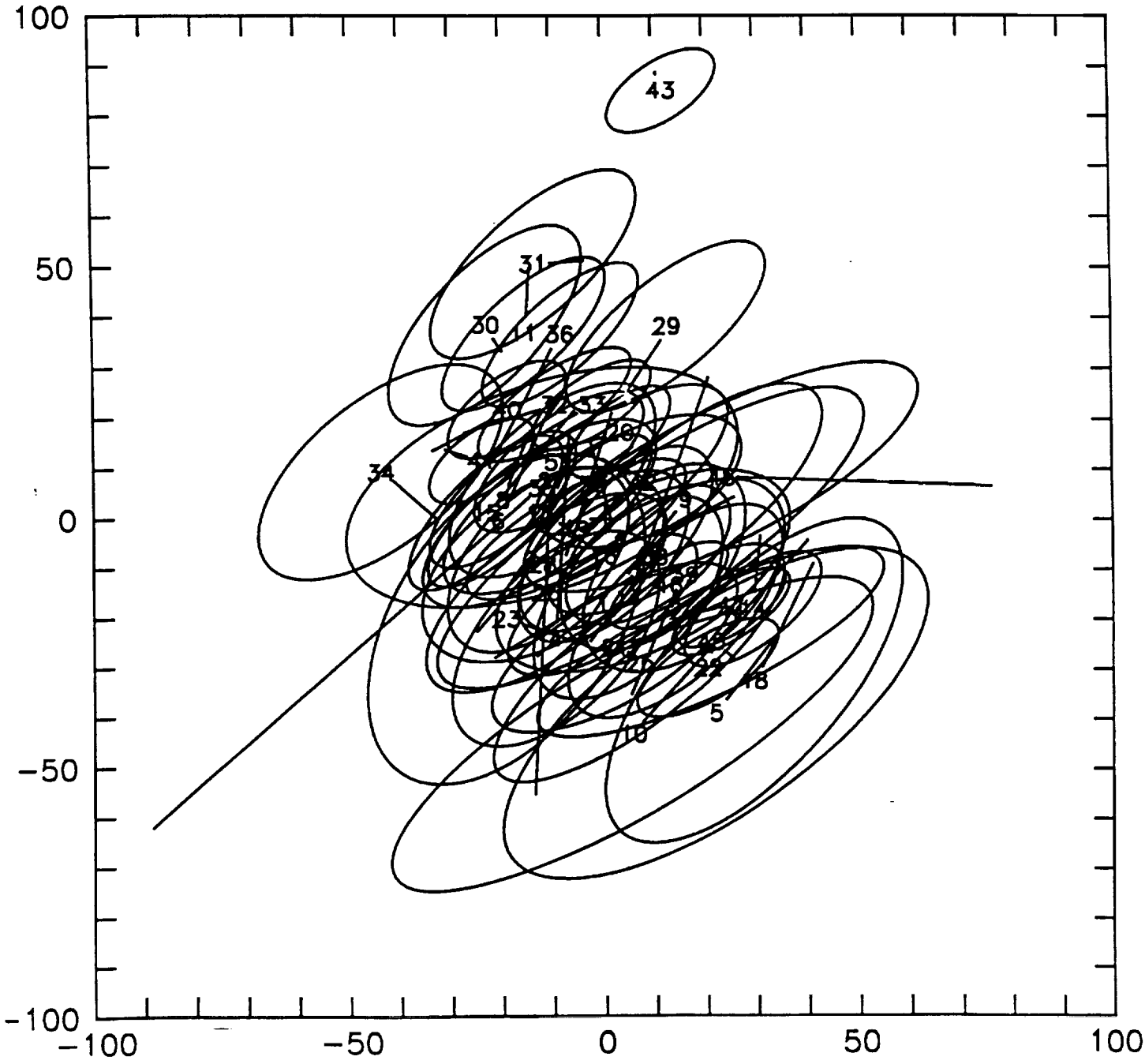

Figure B11

APPENDIX 5

Crustal strain and the 1992 Mojave Desert earthquakes

By J. Sauber, S. C. Solomon, and W. Thatcher

Abstract submitted to *1992 Fall Meeting, Eos Trans. Amer. Geophys. Un.*, 1992.

Crustal Strain and the 1992 Mojave Desert Earthquakes

Jeanne Sauber (Geodynamics Branch, NASA/GSFC, Greenbelt, MD 20771; 301-286-8586; sauber@redoubt.gsfc.nasa.gov)
Sean C. Solomon (Carnegie Instit. of Washington, Washington, DC 20015)
Wayne Thatcher (U.S.G.S., Menlo Park, CA 94025)

The occurence of the June 1992 Landers($M = 7.4$) and Big-Bear($M = 6.5$) earthquakes and the earlier Joshua Tree earthquake($M = 6.1$), east of the big-bend section of the San Andreas fault, has highlighted the importance of understanding deformation within the Mojave block and its relation to deformation in the surrounding region. With these objectives, we have reexamined the implications of geodetic measurements from the region of the Landers earthquake rupture zone, as well as results from VLBI measurements that span and are distributed within the Pacific - North American plate boundary zone. On the basis of triangulation/trilateration measurements (1934-1982), the rate of strain across the central Mojave faults has been estimated to be $\dot{\gamma} = 0.16 \pm 0.03$ μstrain/yr, with the maximum right-lateral shear strain occurring on a plane oriented N41°W. The leading hypothesis that accounted for this rate of strain between the Helendale and Camp Rock faults was that elastic strain had been accumulating that would eventually be released as a large earthquake. The occurrence of a major strain releasing event which resulted in up to 6.7 m of slip confirms this hypothesis and suggests that the central Mojave faults are still favorably oriented to accommodate strain. If the short-term strain rate estimated from the geodetic data is similiar to the average strain rate between major events, such large earthquakes would occur infrequently (approximately every 700 years for the repeat of a similar type event). The VLBI results show that the big-bend region represents a transition from the dominantly transform boundary in southernmost California to transcurrent motion on the San Andreas fault in central and northern California and extension in the Basin and Range province. The average velocities of the VLBI stations east of the big-bend (MOJA and DEAD), as well as OVRO (north of the Garlock fault), relative to stable North America, are approximately 8-12 mm/yr at N30-60°W. These geodetic results, along with geologic evidence, suggest that slip on the northwest-striking faults of the central Mojave are kinematically related to strike-slip motion on the right-lateral faults that bound the region of extensional tectonics in the southern Basin and Range province. Further support for this interpretation comes from the observation that aftershocks from the Landers and Joshua Tree earthquakes extended from the San Andreas fault south of San Gorgonio Pass to the central Mojave and northward to the Panamint Valley fault zone.